INCLUSIVE HIGH-$p_\perp$ $b\bar{b}$ CROSS SECTION MEASUREMENT AT $\sqrt{s} = 1.96$ TeV

A Dissertation

Submitted to the Graduate School
of the University of Notre Dame
in Partial Fulfillment of the Requirements
for the Degree of

Doctor of Philosophy

by

Eugene Galyaev, B.S., M.S.

Neal Cason, Director

Graduate Program in Physics
Notre Dame, Indiana
November 2006

INCLUSIVE HIGH-$p_\perp$ $b\bar{b}$ CROSS SECTION MEASUREMENT

AT $\sqrt{s} = 1.96$ TeV

Abstract

by

Eugene Galyaev

The Run II physics program at the Tevatron started in the spring of 2001 with protons and antiprotons colliding at an energy of $\sqrt{s} = 1.96$ TeV, and is continuing with about 1.2 fb^{-1} of data currently collected by the CDF and DØ experiments. A measurement of the b-jet cross section as function of jet transverse momentum $p_\perp$ has been performed using 312 pb^{-1} of DØ data. The results for this measurement were obtained and are presented herein. A neural network algorithm was used to identify b jets.

This work is dedicated to my family - my mom Margarita, my dad Nikolai, and my brother Alex. You have inspired me and passed on to me everything that I am, and I hope this recent product of my study will make you all proud and will allow me to carry on the scientific tradition in our family to a yet higher mark.

I love you very much.

It is not the possession of truth, but the success which attends the seeking after it, that enriches the seeker and brings happiness to him.

Max Karl Ernst Ludwig Planck, Physicist

CONTENTS

FIGURES

TABLES

ACKNOWLEDGMENTS

This dissertation is the most significant milestone of a path over which I have traveled most of my life. It started in the 6th grade in Middle School in my hometown of Protvino, Russia, with a tour over the Institute for High Energy Physics. I had the first chance in my life to meet so many nice and friendly people from over the world doing Physics together. My imagination was captivated by complex yet exciting tasks these people were facing. That was probably the moment I decided to give a shot at joining this wonderful and rich world of particle physics. I am grateful to all of the people who have helped me along my path to this goal.

My journey of a physicist started at the Department of Physics in Moscow State University. I wish to thank my mentors for inspiring me further as I was learning the skills that now give me confidence and pride in my work and everyday life. I express my special gratitude to my first academic advisor, Sergey P. Denisov - a knowledgeable and accomplished scientist, a wonderful administrator and an attentive and incredibly talented teacher. I also wish to thank everyone at MSU and IHEP for helping me build my first practical, hands-on skills doing real physics analysis.

To those I started graduate school with at The University of Notre Dame, I could not have picked a better group of people. I would like to thank them all for helping in innumerable ways during some difficult years, I could not have done it without them. Specifically, I want to thank Ryan Hooper, Aaron Couture, Arthur

Teymurazyan, and all of my fellow students for sharing with me the ups and downs in the complicated life of a graduate student.

I cannot possibly express in full my gratitude to my advisor, Professor Neal Cason. He has always been there to listen, attend and advise me not only with my academic tasks, but with all of the aspects of my life in the United States. With all my heart I thank Neal for being very patient and wise, and letting me choose my own way, and being there to help me through it. Especially I am grateful to Neal for helping me get seriously involved in the CFT work at DØ. He would always take the time to listen whenever I needed to discuss something and allowed me a lot of freedom in the research I wanted to do. For all his help to me in preparation of this dissertation and with multitude of aspects of my life here in the United States, I am very grateful to Neal.

In general, all of the comments and directions I have received from the QCD and b-Id groups during my years at DØ have been of great help. To all of the people in the DØ QCD and b-Id groups: thank you. Furthermore, I would like to thank Don Lincoln for taking me under his wing and helping me with countless aspects of this analysis. I could not possibly have that priceless first-hand experience if not all the valuable time and knowledge invested in me by Don. He is a brilliant scientist, a great mentor and a wonderful person. Without Don's assistance I would not have become an experimentalist and the person I am now.

I would like to thank several individuals for helping me in a multitude of ways while I was at DØ. Gordon Watts, Avto Kharchilava, Yuri Gershtein, Drew Alton, Ariel Schwartzman and Jadwiga Warchol - I can't thank you all enough for all your help and encouraging comments.

My very special gratitude goes to my dearest life partner, Vaida, for understanding me, supporting me in all of my life's pursuits, and sharing the ups and downs of

our lives together. Thank you for being patient, for taking care of numerous aspects of our lives while I was doing my best to finish this dissertation. I also thank our mischievous cat Lucky for keeping me awake and upbeat during those late hours of writing.

Finally, I wish to express my gratitude to the Department of Energy, the University of Notre Dame, and all of the institutions and organizations from around the globe whose collective efforts made DØ a reality. To the thousands of people working hard on multitude of hardware and software, administrative and financial aspects of physics at Fermilab, who I have never met, and likely will never ever meet, thank you!

CHAPTER 1

INTRODUCTION

There are many things in nature that surround us in our everyday lives. Since the very beginning people have been curious about the world they live in, and out of this curiosity science was born. Some of the most basic questions a scientist can ask about pretty much anything are: "how big is it?", or "how long does it last?" Among these questions there is another fundamental question asking "from what is it made?" Perhaps since before the times of Leucippus and Democritus, many philosophers and scientists have been trying to approach this question by looking for the most of simplistic nature's building blocks, which combined produce all of the diversity of shapes around us. Modern science has answered this question to a remarkable degree. By the beginning of the twentieth century, scientists had determined that all visible matter in the universe was indeed made of atoms. Dmitri Mendeleev had invented and explained the periodic table of elements. While the table did not list every element that can be found in nature, and new ones have since been manufactured, this was a major success that led to great progress in answering the above fundamental question. Some scientists believed that atoms were entirely indivisible, but nobody had yet applied enough energy to fragment them and see what they were made of. Chemical reactions typically involve energies of less than a few eV (electron Volts) per atom, which is not enough to break atoms apart.

In their early x-ray studies scientists have reached energies of keV (10^3 eV) but this was still insufficient to break atoms. By then there were numerous hints that atoms might be composite and divisible. The electron and other forms of radiation were discovered before the end of the nineteenth century. In the early part of the twentieth century, scientists learned that atoms contained electrons and a positively charged nucleus. The discovery of the atomic nucleus required slamming atoms with other particles that had kinetic energies of several MeV (10^6 eV). This experiment required the use of highly energetic natural radiation that was also discovered near the turn of the century. By the mid 1930s, scientists determined that matter was made of three distinct types of particles: electrons, protons, and neutrons. Much of this knowledge came from scattering experiments, the most famous of which was done in Ernest Rutherford's laboratory and led him to publication of his atomic model in 1911. By scattering naturally occurring α particles off thin gold foil, he found that gold atoms have hard cores at their centers. The energy of α particles used in that experiment was about 6 MeV.

With this energy, α particle probes could easily penetrate the atom, but not the nucleus. Discovering protons and neutrons in the nucleus required similar energies, but smaller target nuclei. To probe the subatomic structure any deeper required higher energies, far beyond what natural radiation found on Earth can provide. While extremely energetic, cosmic rays discovered in 1930's are not a good probe either, primarily due to their scarcity. Exploring the nature of electrons, protons, and neutrons requires particle accelerators. Using primarily the results of accelerator-based experiments, physicists in the twentieth century have emerged with the Standard Model of particle physics. In the Standard Model, the electron is a fundamental particle, but the neutron and proton are composites made of indivisible *quarks* and *gluons*. As the energy frontier moves forward, scientists will probe

these particles at even smaller distance scales always asking: "from what is it made? " References to all of these discoveries and much more can be found in [1]. Following the tradition set by Rutherford, modern-day scientists are probing the structure of the proton at the smallest distances they can attain to get to the bottom of the "from what is it made? " question.

1.1 Thesis Overview

In order to understand the structure and context in which this dissertation is written, some introductory words must be said about the main goal and contents of this manuscript.

The Standard Model theory of particle physics was developed in the 1960's and describes the fundamental particles and their interactions in nature. This model consists of a set of gauge theories, and its main theses and features are described in Chapter 2. It has been extremely successful since its development and many experimental measurements have been found to be consistent with Standard Model predictions.

The analysis described in this thesis measures the cross section for b-jet production, where b-quarks contained within the collimated streams of particles are one of the fundamental particles of the Standard Model. The described events are the products of proton-antiproton ($p\overline{p}$) collisions. The data describing these events are produced at the Tevatron $p\overline{p}$ collider, and collected using the DØ detector, both of which are described in Chapter 3. The mechanics of event selection made by the detector hardware, or *triggering*, is covered in Chapter 4. The definitions and particulars of measuring particle jets are explained in Chapter 5.

The measurement is made by identifying (or *tagging*) jets associated with the b-quarks through a convolution of methods summarized in Chapter 6. A Neural

Network operating with several process-specific signatures was used to identify jets of interest.

The detailed discussion of the analysis used to obtain the experimental results is given in Chapter 7, and assessing the associated systematic uncertainties and comparison to computer-simulated and previous b-jet cross section measurements is done in Chapter 8.

This analysis provides an insight into b quark production mechanisms, and is a strong test for the Standard Model. By using jets rather than a specific hadron decay mode for the measurement we ascertain that there is no dependence on branching fractions that often are needed to be measured experimentally. The data preselections allow us to primarily pick out leading order production mechanisms and thus to test a specific part of QCD. The measurement also supplies top quark and Higgs searches with a useful feedback. Since it is also true that there are possible physics mechanisms which might generate enhanced b-quark production at high transverse momentum (for instance, some hypothetical heavy-mass object preferentially decaying into quarks of the third generation), this analysis might be able to reveal those mechanisms which otherwise remain hidden, being overshadowed by the more common light-quark and gluon production in inclusive jet studies.

CHAPTER 2

GENERAL THEORETICAL AND EXPERIMENTAL ASPECTS

The main theoretical concerns within the context of this dissertation are the Standard Model theory in general, and Quantum Chromodynamics (QCD) in particular. Within QCD, several concepts including quark masses, asymptotic freedom, heavy flavor production and cross sections are discussed. Details and experimental handles on practical cross section measurements as well as the general motivation for this study are given in this chapter.

2.1 The Standard Model

All of the matter in the universe is built with, and governed by four types of interactions. There are four corresponding forces: gravitational, strong, electromagnetic, and weak. Since the early 1960s, there have been many fundamental changes in our understanding of the universe, its building blocks and physics laws. There were many remarkable theoretical ideas proposed, including local gauge invariance allowing us to treat weak and electromagnetic interactions as two distinct manifestations of one more fundamental electroweak interaction. The gauge invariance principle was also applied to strong interactions, leading to creation of a quite comprehensive theory called Quantum Chromodynamics (QCD), which nowadays is inseparable from the electroweak theory [2].

Combining the multitude of theoretical and experimental results, a mathematical model that explains all of the particle physics effects observed to date has emerged. This model is called the Standard Model (SM). As its building blocks, SM uses elementary particles grouped into two classes: *bosons* (particles that transmit forces) and *fermions* (particles that make up matter). Thus, the Standard Model is a set of gauge theories describing the strong, weak and electromagnetic interactions. Many tests of the Standard Model have been performed and thus far none has shown that the Standard Model is incorrect. However, mysteries still remain. The most feeble force in nature, gravity, cannot be accommodated in the current Standard Model. Also, the Higgs boson, the last building block of the Standard Model, so far has evaded detection [2].

It is impossible to describe a particle physics theory without mentioning the basic building blocks of the Standard Model of particle interactions in more detail. Basically, the Standard Model treats particles as field excitations above a certain vacuum ground state. The particles are categorized into three groups based on their spin: *fermions* have spin 1/2; *gauge bosons* with spin 1; and bosons with spin 0 (the elusive *Higgs* particle mentioned above). Despite the fact that the fermions are responsible for the representation of matter, some members of this group in the SM can be massless. Furthermore, the fermion sector of the SM can be further categorized into the leptons (ℓ) and quarks (q). The leptons and quarks can also be further differentiated into one of three families (or *generations*) based on their physical properties. The various interactions which govern their features and dynamics originate from the three forces: electromagnetic, strong, and weak, represented by their corresponding boson mediators. The photon γ mediates the electromagnetic (EM) force, the W and Z bosons are responsible for the weak, and the gluons g mediate the strong force. All of these mediators form the *gauge boson*

group. These building blocks of the Standard Model are illustrated in Figure 2.1. Mathematical constructs known as *symmetry groups* are used to further facilitate the SM description.

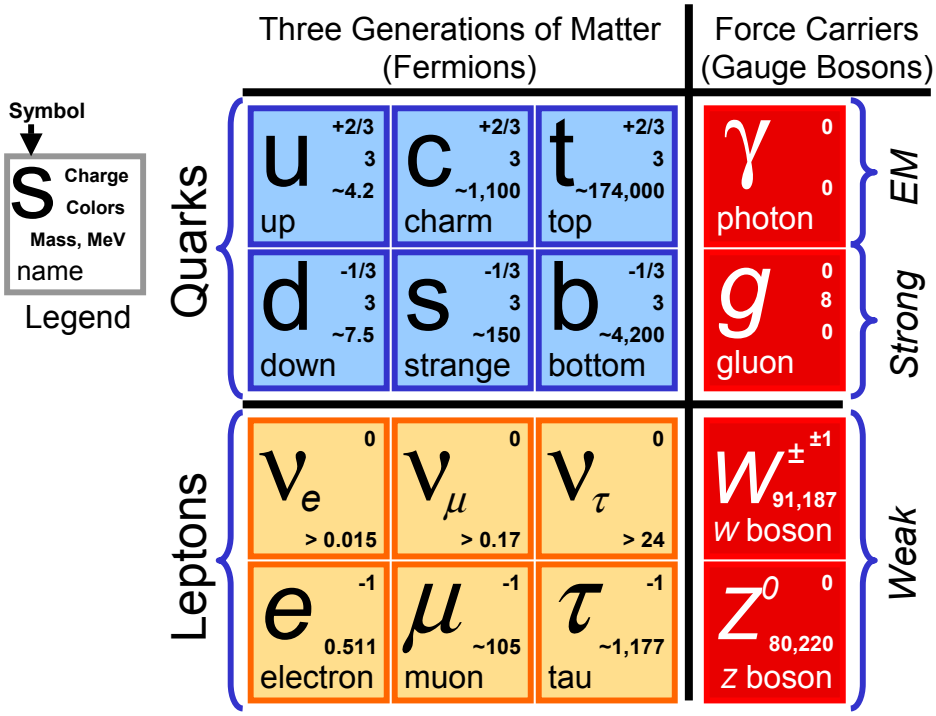

Figure 2.1. The Standard Model (SM) building blocks.

For instance, we can immediately notice one of the symmetries by looking at the fermion sector: all fermions have anti-particles associated with them. For example, the positron e^+ and anti-neutrino $\overline{\nu}_e$ are the anti-particles of the electron e and the electron neutrino ν_e, respectively. For the Standard Model, the gauge symmetry group is $SU(3) \times SU(2)_L \times U(1)$, where $SU(3)$ is the symmetry group describing the strong interaction and $SU(2)_L \times U(1)$ the symmetry group describing the electroweak interaction. In this formalism, $SU(2)_L$ involves left-handed fermions only (hence the

L subscript). The quarks and gluons also have additional degrees of freedom called *color charge*. There are three color charges typically referred to as red, green and blue. While each quark can have one of the three different color charges, antiquarks carry one of the three *anticolors*. With the color charge included, the total number of fermions in the Standard Model is forty eight [3].

The vector gauge bosons that mediate the forces between these particles are required by the local gauge invariance to be massless. The bosons that carry the electroweak force, namely, two charged particles, W^+ and W^-, and one neutral particle Z^o, interact with themselves through the triple gauge couplings. This produces three massless mediators, but experiment shows such a description to be incorrect. The weak nuclear force has short interaction distance, behaving as if the gauge bosons are very heavy. In order to make a gauge invariant theory work for the weak nuclear force, theorists had to introduce heavy gauge bosons in a way that wouldn't destroy the consistency of the quantum theory in general. The way to make such introduction was a mechanism where massless gauge bosons acquire mass by interacting with a scalar field called the Higgs field. In the resulting theory gauge bosons become massive yet allow for all of the attractive properties of a gauge invariant theory. Through the Higgs mechanism, the $W^{\pm}$ and Z bosons obtain non-zero masses by *spontaneous symmetry breaking* of the $SU(2)_L \times U(1)$ symmetry group. During the 1960s Sheldon Glashow, Abdus Salam, and Steven Weinberg independently discovered that they could construct a gauge-invariant theory of the weak force, provided that they also included the electromagnetic force described by Quantum Electrodynamics (QED) [2].

The $SU(3)$ element of the group structure is used to describe the strong interactions which adhere quarks together. Strong interactions within the Standard Model intercede by massless gluons. Strongly interacting particles are called *hadrons*, which

in turn can be classified further into *mesons* (quark-antiquark states) and *baryons* (three quark states). Strong interactions of color charges are described by Quantum Chromodynamics (QCD) [4].

Since its gradual formation during the 1960s, the Standard Model had a striking success by not only accurately incorporating observed phenomena known to date, but also correctly predicting a broad range of discoveries later determined to be true by precision experiments. These notable accomplishments include the prediction of the existence of the W and Z bosons as well as their masses, which were later experimentally verified. Another example of the accuracy of the Standard Model is the prediction of the top quark, which was discovered and its properties measured in the middle of the 1990s both by the CDF and DØ collaborations at Fermilab [5, 6, 7, 8].

Despite all of the accord with experimental data, there are issues not addressed by the Standard Model. One issue is that there are over twenty free parameters within the Standard Model, which are introduced absolutely arbitrarily. To agree with observations, some of these parameters must be related to other parameters with a very high precision [5].

Another issue is the Higgs mechanism, which gives masses to the various particles. While the Higgs mechanism is an important piece to the Standard Model, many aspects of it still remain a mystery. For instance, the Higgs mechanism predicts the existence of a new particle with spin 0 called the *Higgs boson*, which has not yet been observed despite extensive searches conducted for several decades now. Perhaps another and one of the most obvious flaws of the Standard Model is that it does not incorporate gravity in a consistent quantum mechanical way. The force that holds the Earth in its orbit around the sun, and is inherently incorporated in our everyday lives is not fully addressed within the theory which is supposed to be self-

sufficient and explain everything. In the past there were many theoretical models attempting to address the issue of gravity, most of which are impossible to test with currently existing or foreseeable experimental techniques. The mystery of quark and lepton proliferation into generations, and their masses varying greatly with other properties somehow remaining unchanged, imposes another question without an answer. The only way to address these and many other questions is to go beyond the Standard Model formalism, and look for any manifestation of new physics, which could in turn, enhance our understanding of the Universe by extending the existing theoretical model.

2.2 Electroweak Theory

The electroweak theory, for which Sheldon Glashow, Abdus Salam, and Steven Weinberg shared the 1979 Nobel Prize in Physics, originated from attempts to produce a self-consistent theory for the weak force, analogously to quantum electrodynamics (QED), the successful quantum theory of the electromagnetic force developed during the 1940s. There were two basic requirements for such theory. First, such a theory should be gauge invariant, so it would behave in the same way at different points in space and time. Second, it should be re-normalizable, which means to have a finite number of infinitely large parameters which can be set equal to the measured experimental values [2].

The existence of the electroweak interaction was experimentally established in two stages. The first stage was the discovery of neutral currents in neutrino scattering by the Gargamelle collaboration in 1973. The second stage was accomplished in 1983 by the UA1 and the UA2 collaborations that discovered the W and Z gauge bosons in proton-antiproton collisions at the Super Proton Synchrotron [3].

Electroweak theory is a gauge theory for the $SU(2)_L U(1)_Y$ group, where $SU(2)_L$

is the gauge group for the weak interaction. The $U(1)_Y$ group, however, is not the gauge group of the electromagnetic interactions but of hypercharge Y, defined as $Y = 2(Q - I_3)$. Here I_3 is the third component of weak isospin and Q is the electric charge. As it was mentioned in Section 2.1, the weak force interacts only with left handed quarks and leptons. These form doublets which are represented by columns in Figure 2.1. The right-handed components are singlets which are unaffected by the weak interaction.

The gauge bosons of the group (B, W^1, W^2 and W^3) are all massless. The masses of the physically observed W and Z bosons are generated through the Higgs mechanism. A scalar Higgs field is introduced in order to spontaneously break the symmetry of the group. The coupling of the gauge bosons with the Higgs field results in the massive $W^{\pm}$ bosons and the Z boson. It also results in the entangling of the $SU(2)$ and $U(1)$ groups as the Z boson and the photon appear to be linear combinations of the massless B and W^3 bosons. This is shown by equations (2.1) and (2.2), where θ_W is the weak mixing angle [2].

$$Z = \cos\theta_W W^3 - \sin\theta_W B \tag{2.1}$$

$$\gamma = \cos\theta_W B + \sin\theta_W W^3 \tag{2.2}$$

Transitions of quarks across generations are possible via the weak interaction, as the weak eigenstates of the quarks are represented by superpositions of the mass eigenstates of the physical quarks. The mechanism of mixing of the mass and weak eigenstates is described by the Cabibbo-Kobyashi-Maskawa (CKM) matrix, and is discussed in more detail in [2].

2.3 Quantum Chromodynamics

Quantum chromodynamics is the theory of strong interactions, governed by fundamental force describing the interactions of the quarks and gluons found in nucleons

(such as the proton and the neutron). QCD is a quantum field theory of a specific kind called a non-abelian (non-abelian groups are a special kind of group elements of which do not always commute) gauge theory. The most fundamental concept of QCD is that hadronic matter is made of quarks. The idea of quarks emerged from the need to find physical manifestations for the $SU(3)$ symmetry group describing the flavor, and observed in the spectrum of the lowest-mass mesons and baryons [12]. The quark hypothesis allowed for treatment of these observed baryons as three-quark states. The quark constituents of baryons are forced to have half-integral spin in order to account for spins of the low-mass baryons. By this logic, the quarks within spin $\frac{3}{2}$ baryons are then in a symmetrical state of space, spin, and flavor. However, according to Fermi-Dirac statistics, the baryon wave function must be totally asymmetric. To resolve this dilemma, in the Standard Model quarks have been given an extra internal degree of freedom, namely color. In this new index, particles in nature have to be composed of either a colored and an anti-colored particle, or three differently colored particles. This additional quantum number could lead to proliferation of states, so the color hypothesis has to be superimposed with an additional requirement that only color singlet states can exist in nature, and no physical color states ever occur. This important addition assures Pauli principle preservation.

Due to the non-abelian nature of QCD, the gauge mediators interact with each other at three-point and four-point vertices. Eight mediating gluons have to be introduced in order to accommodate all the color couplings and to preserve local gauge invariance. Gauge invariance allows us to re-define the quark fields independently at any point in space and time without changing the physical content of the theory. The strength of the strong interaction is specified by the strong coupling parameter α_s [4]. This parameter decreases with increasing $|Q^2|$, the absolute squared

four-momentum transfer in the particle collision. If g_s is the strong charge,

$$\alpha_s = \frac{g_s^2}{4\pi} \simeq 0.1 \tag{2.3}$$

The quarks are manifested by the gauge field four-spinors ψ_i, where i runs from 1 to 3 and represents the quantum number for the color. For each of the quark flavors, the basic QCD Lagrangian is given by [3, 4]:

$$\mathcal{L} = -\frac{1}{4} F^{\alpha}_{\mu\nu} F^{\alpha,\mu\nu} + i\overline{\psi}(\gamma^\mu D_\mu - mI)\psi \tag{2.4}$$

$$F^a_{\mu\nu} = \partial_\mu A^a_\nu - \partial_\nu A^a_\mu - g_s f^{abc} A^b_\mu A^c_\nu \tag{2.5}$$

$$D_\mu = \partial_\mu I + i g_s T^a A^a_\mu \tag{2.6}$$

where ψ and A^a are the quark and gluon fields, I is the unit matrix and T^a are the generator matrices. f^{abc} define the Lie algebra [9] of the $SU(3)$ group and are called *structure constants*. The indices a, b and c run from 1 to 8 and represent the eight combinations of possible gluon color states. The above Lagrangian defines the quark and gluon propagators. The Feynman rules for the propagators and interaction vertices are derived directly from this Lagrangian.

Structure constants are defined through the generator matrices t_j of dimension 3×3 in the following way: $[t_b, t_c] = i f^{abc} t_a$. In case of the abelian theory such as QED structure constants would disappear due to commutative properties of the generators t_i.

If the strength α_s is sufficiently small, which is the case for values of $|Q^2|$ greater than a few GeV^2 (so-called *asymptotic freedom*), one can use perturbation theory (pQCD) to reliably calculate the cross sections predicted by QCD. This approach does not work in case of smaller $|Q^2|$ values. The center of mass energy of the Tevatron, $\sqrt{s} = 1.96$ TeV, is sufficient enough to allow precise tests of QCD predictions, especially for the production of bottom and charm quarks.

2.3.1 Parton Model and Perturbative QCD

Initially, the idea of the parton model was the concept of the presence of quarks as elementary constituents inside hadrons. To describe distributions of these constituents or *partons* inside hadrons, probability density functions are used. These functions describe fractions of momentum carried by constituents and are known as *structure functions*. The revised parton model historically grew out as a developed explanation of the observed effect of *scaling*. In deep inelastic scattering (DIS) processes with large values of $|Q^2|$ and energy loss ν scaling was manifested by an experimental observation of the structure function

$$F_2\left(Q^2, \nu\right) \quad = \quad F_2\left(\frac{Q^2}{\nu}\right) \tag{2.7}$$

to be dependent on (or "scaled") the ratio

$$x = \frac{Q^2}{2M\nu} \tag{2.8}$$

for any $|Q^2|$, as was originally suggested by J. D. Bjorken. The revised parton model is essentially a generalization of the momentum approximation. We assume that any physically observed hadron is made up of constituent particles, its "partons, which are quarks and gluons. At high energy, we neglect the masses of hadrons and partons compared to the scale $|Q^2|$ of the DIS.

When momentum transfer between partons $|Q^2|$ is sufficiently large, the cross section for quark-quark or gluon-gluon interactions can be expanded in α_s in series:

$$\sigma \quad = \quad \alpha_s^2(\sigma_0 + \alpha_s\sigma_1 + \alpha_s^2\sigma_2 + ...) \tag{2.9}$$

It is conventional to refer to calculations up to σ_0 term as to leading order (LO), and to σ_1 term calculations as to next to leading order (NLO) calculations.

When calculating cross sections, the inclusion of higher order Feynman diagrams (for example, the one shown in Figure 2.3) the virtual fermion loops appear in the

propagators, which leads to the divergences of the series. In order to retain the predictive powers of the theory, these divergences are classified in two main classes, and dealt with differently.

One class of such infinite integrals is called *ultraviolet divergences*. They are characterized by the fact that no constraint is imposed on the virtual momentum involved in the gluon loop, which leads to integrals behaving as $\int^{\infty} \frac{dp}{p}$ and diverging logarithmically.

Other divergences are caused by emission of gluons by a quark, and are known as *infrared* or *collinear* divergences. When calculating the amplitude for the cross section, the terms $[E_q E_g (1 - \cos\theta_{qg})]^{-1}$ appear. In case of the quark energy E_q vanishing or $\cos\theta_{qg} \approx 0$ these terms produce infrared or collinear divergences, respectively. A comprehensive description of pQCD is given in [10].

2.3.2 Asymptotic Freedom

Unfortunately, there is no simple intuitive explanation of the property of asymptotic freedom in QCD. There are however two types of arguments aimed to simplify this apparently perturbative concept [4]. They describe the phenomenon either as a dielectric or a paramagnetic effect. The first approach suggests that the emission of virtual gluons by quarks causes the color they carry to discharge into surrounding vacuum. The color charges overlap, leading to reduction of the color force at short distances, which causes asymptotic freedom. The second line of argument describes asymptotic freedom as a paramagnetic effect due to the spin of gluons. In the following explanation we confine ourselves to the first type of argument. In QCD, the leading order quark production processes, as are shown in Figure 2.2, are modified by higher order loop diagrams in which the loops consist of quarks or gluons (Figure 2.3). The effect of these loops causes the net color charge of the quark to be

screened, which affects the coupling α_s of other quarks and gluons to the particular net color charge:

$$\alpha_s(|Q^2|) = \frac{\alpha_s(m_Z^2)}{1 + (\alpha_s(m_Z^2)/12\pi)\,(11N_c - 2n_f)\ln(|Q^2|/m_Z^2)} \tag{2.10}$$

Here, m_Z is a reference scale, in this case the Z mass, N_c is the number of colors, and n_f is the number of flavors participating in the process at the given $|Q^2|$, for a certain re-normalization scheme. Since in the Standard Model $N_c = 3$ and $n_f = 4$ for $b\bar{b}$ production and for the most common renormalization schemes, the term $11N_c - 2n_f$ is positive. Thus, these loops have an effect which is the reverse of screening: it increases the effective coupling with higher $|Q^2|$. When transferred momentum gets very high, the quarks and gluons decouple and behave like almost free particles.

The loop corrections made to the gluon propagator, as discussed in 2.3.1, produce UV divergences [4]. These divergences are dealt with by means of *renormalization*. In essence, renormalization is subtraction at some renormalisation scale μ, which appears inside a logarithm for the renormalised quantities. The couplings, masses and felds are redefined by renormalization in such manner that causes infinite quantities to cancel at their corresponding order. For interactions at a four-momentum scale Q (where $|Q| \gg \mu$) this results in the coupling constant depending on a logarithmic term of Q^2/μ^2 which satisfies the differential equation:

$$\frac{\partial \alpha_s(Q^2)}{\partial \ln(Q^2)} = \beta\left(\alpha_s\left(Q^2\right)\right) \tag{2.11}$$

We can think of the perturbative expansion of β in terms of α_s and determine β_0, knowing the number of colors N_c and number of flavors whose mass threshold is below the four-momentum scale, n_f:

$$\beta(\alpha) = -\beta_0\alpha^2 + \mathcal{O}(\alpha^3) + ... \tag{2.12}$$

$$\beta_0 = \frac{11N_c - 2n_f}{12\pi} \tag{2.13}$$

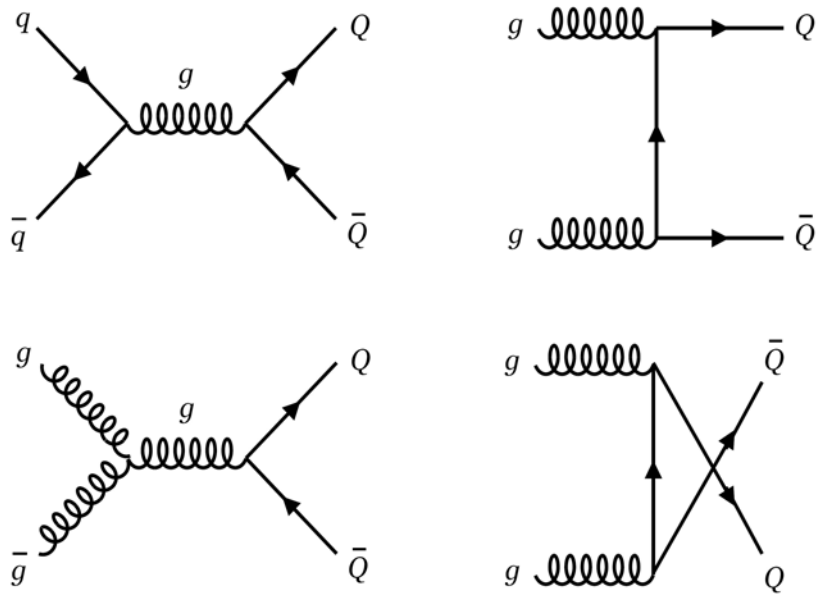

Figure 2.2. Feynman diagrams for leading order heavy quark production.

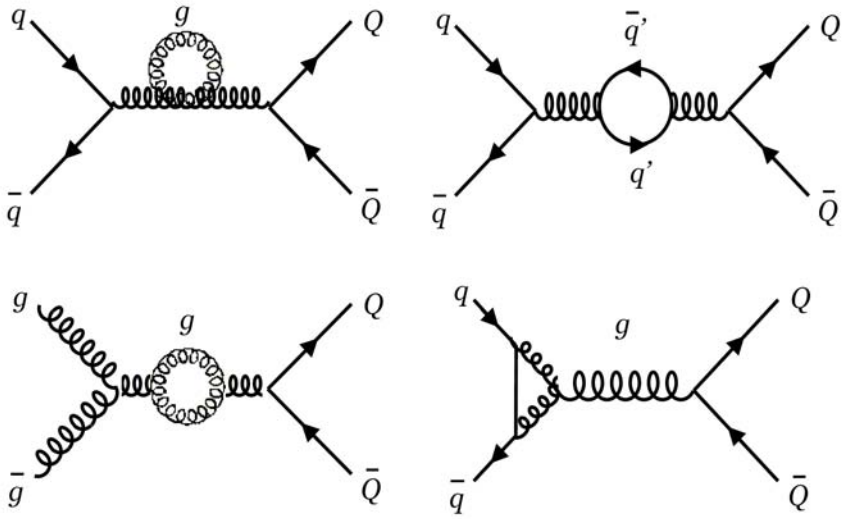

Figure 2.3. Some higher order diagrams for heavy quark production with loops in the gluon propagator.

The negative sign of β shows that the coupling strength of strong interactions α_s gets smaller with higher $|Q^2|$. If α_s is sufficiently small ($|Q^2|$ higher than a few GeV^2), perturbation theory can be used to reliably calculate cross sections predicted by QCD. This method cannot be applied in the case of smaller $|Q^2|$ values. The center of mass energy of the Tevatron, $\sqrt{s} = 1.96$ TeV, is high enough to allow precise measurements of the QCD predictions, especially for the production of bottom and charm quarks.

2.3.3 Quark Masses

Unlike the leptons, quarks obey the confinement principle, and are not observed as free particles. Due to that fact, quark masses cannot be measured in a direct experiment, but must be determined indirectly through their influence on hadron properties. As a result, the values of the quark masses depend on precisely how they are defined. There can be proposed many definitions of equal strength [4]. In practice, an easily measurable set of physical quantities such as masses of hadrons, is computed. Then quark masses are varied until the agreement with the existing calculation is reached. From the point of view of the QCD Lagrangian, the quark mass is just another parameter like the coupling constant. The mass parameters in the QCD Lagrangian (2.4) depend on the renormalization scheme used to define the theory, and also on the scale parameter μ. The most commonly used renormalization scheme for QCD perturbation theory is the so-called "modified minimal subtraction" ($\overline{MS}$) scheme [10].

At the limit of quark masses taken to be zero, the QCD lagrangian is chirally symmetric. This symmetry is spontaneously broken by dynamic symmetry breaking mechanism, and explicitly broken by the masses of quarks [11]. The non-perturbative scale of dynamical chiral symmetry breaking, Λ_χ, is around 1 GeV. It

is conventional to call quarks heavy if $m > \Lambda_\chi$, and explicit chiral symmetry breaking dominates, and light if $m < \Lambda_\chi$, and spontaneous chiral symmetry breaking dominates. According to this characterization, the c, b, and t quarks are heavy, and the u, d and s quarks are light. The mass computations for light quarks involve an expansion in m_q at the limit $m_q = 0$, whereas for heavy quarks, they involve an expansion in m_q/Λ_χ at $m_q = \infty$. The perturbative corrections for masses are largest for the s and c quarks, which are the heaviest light quark and the lightest heavy quark, respectively [12].

At high energies or short distances, non-perturbative effects such as chiral symmetry breaking are not important, and one can evaluate mass-dependent effects using pQCD to extract the masses of quarks. QCD computations are usually performed using the $\overline{MS}$ scheme at a scale $\mu \gg \Lambda_\chi$, and give the $\overline{MS}$ *running* mass $\overline{m}(\mu)$. At short distances the dependence μ of $m(\mu)$ can be determined using renormalization equations.

2.4 Heavy Flavor Production

Hard processes have a large scale in the calculation. That makes pQCD applicable: high momentum transfer Q^2, high mass m, high transverse momentum $p_\perp$, and since $m_q \neq 0$, heavy quark production are all *hard* processes. Under the condition of asymptotic freedom, we can perceive the proton-antiproton interaction as a set of parton-parton interactions [3]. The cross section in the QCD parton model (for $A \rightarrow\leftarrow B$ collision where $AB = p\overline{p}$) can be written [4]:

$$\sigma\left(S\right) = \sum_{i,j} \int dx_i dx_j \hat{\sigma}_{ij}\left(x_i p_A, x_j p_B, \mu_R, \mu_F, \alpha_s(\mu_R)\right) F_i^A(x_i, \mu_F) F_j^B(x_j, \mu_F) \quad (2.14)$$

where $S = Q^2$ is the parton total center-of-mass energy squared. The $F_{i,j}$ are the momentum densities, or structure functions (Subsection 2.3.1). These momentum densities depend on a factorization scale μ_R, analogous to μ. The Parton Model

perceives the proton as a composite of three almost free constituents - partons, with no interactions between them. Therefore, scattering occurs on a single, free and effectively massless parton. The $\hat{\sigma}_{ij}$ here is the short distance cross section, which can be represented by perturbative expansion in α_s:

$$\hat{\sigma}_{ij}((x_1 x_2 S), m^2, \mu^2) = \sigma_0 c_{ij}^{(0)} + 4\pi\alpha_s \left[c_{ij}^{(1)} + \ln\left(\frac{\mu^2}{m^2}\right) \bar{c}_{ij}^{(1)} \right] + \mathcal{O}\left(\alpha_s^2\right) \qquad (2.15)$$

with c_{ij} evaluated analytically as well as from the numerical fit [13]. The total cross section for b-quark production results from the sum of all short distance cross sections for the contributing processes.

2.4.1 Jet Cross Sections

The experimental signature for a b production event is two $p_\perp$-balanced jets in the detector [4]. A typical double-jet event is shown in Figure 2.4. The Feynman diagrams for several of the leading order processes for b production are shown in Figure 2.2, and some of the possible higher order diagrams in Figure 2.3. However, there is a fraction of events with higher jet multiplicity, where jets may have come from either radiative corrections to the leading order processes (where there were two quarks or two gluons in the initial state), or a new class of processes in which a quark and a gluon are in the initial state. Some possible diagrams showing such next to leading order corrections are shown in Figure 2.5. However, in this analysis we are studying the production of b-jets instead of the production of b-quarks. The main difference is that studies oriented on the b-quark production are focused on the properties of the quark itself. The present analysis is an example of *jet-based* studies, where the main interest is in the energy of the jet that contains one or more heavy quarks, and not in the fraction of the energy carried by these quarks. The explicit measurement of b-quark production is experimentally complicated, as colliding partons produce collinear gluons *en masse*, and taking their contributions

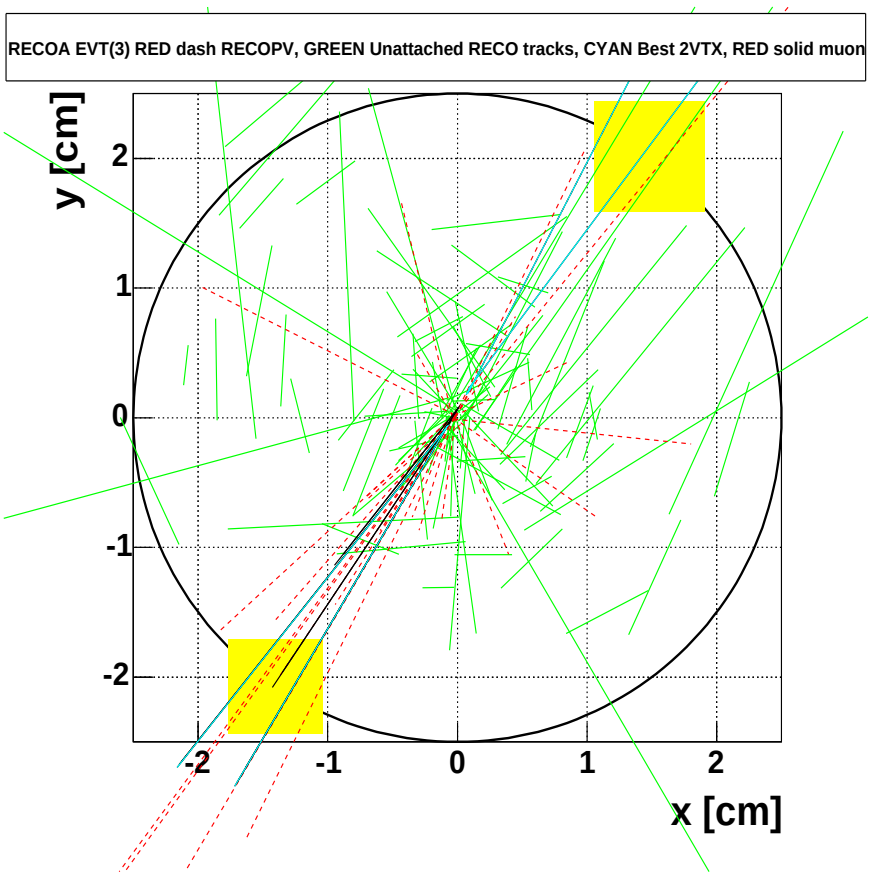

Figure 2.4. A typical double-jet event at DØ shown with the event display in $(x-y)$ plane. Yellow squares represent the energy measured by the calorimeter. Based on dØroot analysis package.

to the total production cross section into account causes collinear divergences when forming parton density functions. In case of jet analysis, we assume that at such high $|Q^2|$ the reconstructed jets have essentially the same momentum four-vector as the parton from which they originated. There are several effects that are of relevance to jet analyses: fragmentation and hadronization [4]. Fragmentation describes the emissions and absorptions of gluons between the partons in the final stage of the collisions, and the splitting of gluons into quarks. In the hadronization stage the resulting quarks and gluons, which all carry a color charge, are forced to combine

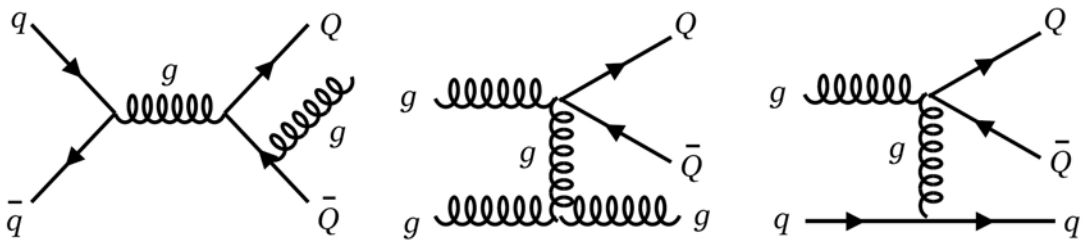

Figure 2.5. Feynman diagrams for some of the NLO corrections to heavy quark production.

to form colorless hadrons and preserve color confinement. Because the Tevatron $\sqrt{s}$ is well above the production threshold, the experimental measurement of the jet transverse momentum distribution does not depend on the particulars of the fragmentation and hadronization of the b-quark [13].

The detailed discussion on formation and measurement of jets can be found in Chapter 5. However, some basic conventions are mentioned here. In this analysis, jets are defined with particles that are clustered in (η, ϕ)-space in a cone of radius $R = 0.5$. For the purpose of standardization, a set of rules and algorithms for jet reconstruction was established. This set of rules is called the Snowmass convention [14]. However, the jet reconstruction algorithm used in this analysis differs slightly from the Snowmass standard, and will be described in Section 5.1 with moderate level of detail. In this study we only consider jets that contain one or more b or $\overline{b}$ quarks. The production mechanism is also of little importance. The b flavor may come either from direct $b\overline{b}$ production, or gluon radiation, but as long as the carrier is contained within the jet cone, it contributes to our inclusive b-jet cross section measurement.

A much more detailed explanation of jet formation and measurement is given in Chapter 5.

2.5 Motivation for Analysis

Among many unsolved issues with the Standard Model, there is one of particular interest. This issue is the nature and cause of three particle generations, each similar in gross properties, yet different among other things, including increasing mass. In a simple argument by analogy, one might compare this situation with the chemical Periodic Table, in which a similar phenomenon was successfully explained by atomic structure. Consequently a possible explanation of the problem of particle generations is the idea of quark compositeness [15]. If quarks are composite (taking the quarks with charge -1/3), then one might envision that a down quark is in the ground state, while the strange and bottom quarks are in low-lying excited states. A parallel structure would describe the +2/3 charge quarks. By this reasoning, it could be true that a study of the quarks of the third generation might exhibit deviation from point-like behavior. Thus one might choose to study the process $p\bar{p} \rightarrow X \rightarrow q\bar{q}$, where the final state quarks would be either bottom or top. Given the resources at hand, namely statistically significant b production rate at Tevatron, it was decided to study $X \rightarrow b\bar{b}$.

2.5.1 b-Jets as a Door to Top and Higgs Physics at Tevatron

The proper understanding and experimental measurement of the properties of b-jets is crucial for the detection and reconstruction of particles that decay into b-quarks, of which the most interesting are the top quark and the Higgs boson. Figure 2.6 shows the cross sections for b, t and Higgs production at hadron colliders as a function of center of mass energy. Due to the low cross section of top and Higgs production compared to the total inelastic, non-diffractive cross section, one requires b-jets as the sensitive signature needed to separate the Higgs- and top-producing events from the background.

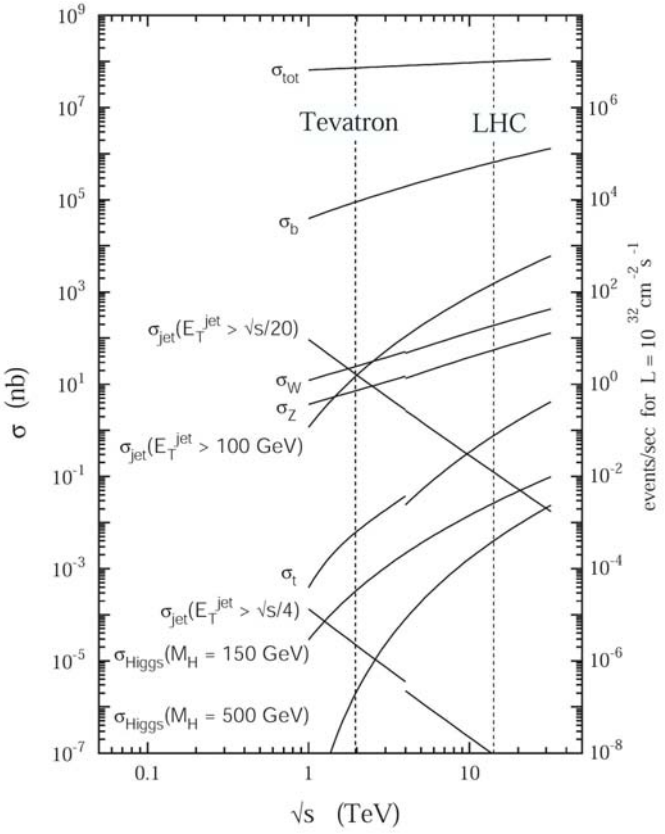

Figure 2.6. Energy dependence of interesting physics processes at hadron colliders as function of the center of mass energy. The discontinuities in the lines are caused by the change from $p\bar{p}$ collisions to pp collisions. Adopted from [13]

With the available center of mass energy of 1.96 TeV, the Tevatron currently is the only place in the world where top quark pairs can be produced directly. They decay primarily through $t\bar{t} \rightarrow (W^+b)(W^-b)$, resulting in two b-jets in the event. If properly detected, these b-jets can be used to remove backgrounds to the $t\bar{t}$ signal, which gives a considerable improvement in the signal over background ratio [13].

The best option to detect the Higgs boson at the Tevatron is the associated production of a Higgs boson with a W or Z boson. The W and Z then decay leptonically or hadronically. The Higgs boson primarily decays to a $b\bar{b}$ pair, since the

Higgs coupling to a fermion is proportional to the squared mass of that fermion, and the b-quark is almost three times heavier than the next heavy particle (the τ lepton). This gives rise to two b-jets in the event, in addition to the decay products of the W or Z boson. The detection of both the top quark and the Higgs boson therefore relies on proper detection and reconstruction of b-jets. The measurement of the b-jet cross section within the context of this dissertation improves our understanding of these jets, leading the way to a better understanding of the Standard Model as well as search for any signatures for the New Physics beyond its boundaries.

2.6 Analysis Outline

Before addressing the technical particulars of the measurement, it is prudent to outline some basic definitions and physical quantities of interest, and give a general *bird's-eye* view of how the b-jet cross section measurement is done in practice.

2.6.1 Some Basic Definitions

Physics events described in this analysis, come from $p\overline{p}$ collisions. As we have mentioned in sections above, the majority of hard-scattering events produce collimated beams of particles known as *jets*. Typically, each jet has much more transverse momentum than the particles making up the beams. Jets can be described by energy-momentum four-vectors, which are the sums of all four-vectors of all particles contained within the jet cone. It can be parameterized by the energy E and three Cartesian momentum components:

$$m = \sqrt{E^2 - p_x^2 - p_y^2 - p_z^2} \tag{2.16}$$

$$p_\perp = \sqrt{p_x^2 + p_y^2} \tag{2.17}$$

$$y = \frac{1}{2}\ln\left(\frac{E + p_z}{E - p_z}\right) \tag{2.18}$$

$$\phi \quad = \arctan\left(\frac{p_y}{p_x}\right) \tag{2.19}$$

where y is the variable called *rapidity*.

The above parameterization is practically convenient, as all of the variables except for rapidity are invariant under Lorentz boosts along z axis, which is taken to be parallel to the beam axis. However, Δy is a Lorentz invariant quantity. For a more detailed explanation of coordinate systems used, and kinematics description in the detector please refer to Chapter 3.

Luminosity $\mathcal{L}$ is a measure of the incident flux of particles leading to collisions. It is proportional to the number of proton-antiproton interactions. The higher the luminosity, the more collisions will occur, thus giving greater odds for quark production. The quantity, pb^{-1}, or *inverse picobarns*, is a convenient unit in which luminosity is measured. In order to understand this unit of luminosity, we should first discuss its inverse, the *picobarn* (pico is the prefix for 10^{-12}, or one millionth of a millionth), or better, the barn. The barn is a cross-sectional area of size 10^{-24} cm^2 and a picobarn is 10^{-12} barns. The cross section σ is proportional to the probability of producing a particular reaction when particles collide. One must note, while the luminosity measures the number of collisions, the cross section measures the probability of production. If, for instance, the cross-section for a reaction is 1 picobarn and the accelerator has accumulated a luminosity of 1 inverse picobarn (pb^{-1}), the average number of produced events for this reaction is 1.

2.6.2 Measuring b-Jet Differential Cross section

The final b-jet production cross section presented in Chapters 7 and 8 is binned as a function of transverse jet momentum, $p_\perp$:

$$\left\langle \frac{d\sigma}{dp_\perp} \right\rangle \Bigg|_{p_\perp average} = \frac{N_{jets}}{\mathcal{L} \times \Delta p_{\perp bin}} \times \frac{\mathcal{P}_{b-tagging}}{\varepsilon_{b-tagging}} \times C_{PL} \tag{2.20}$$

Here N_{jets} is the overall number of jets in a particular $p_\perp$ interval, $\mathcal{L}$ is the integrated luminosity, and $\Delta p_{\perp bin}$ is the width of the $p_\perp$ bin. This part of the formula represents the measured *inclusive* cross section, i.e. the cross section of an ensemble of jets chosen by certain loose pre-selection cuts with no explicit corrections for their flavor content. However, we are specifically interested in b-jets, so we identify them via a *tagging* procedure (Chapter 6). The tagging efficiency $\varepsilon_{b-tagging}$ associated with b-jet identification, is the fraction of b-flavored jets contained in the inclusive sample of N_{jets}. The purity $\mathcal{P}_{b-tagging}$ is the quantity establishing how many identified b-jets are true b-jets, or how pure our jet selection is. So in order to get the cross section for b-jets, we have to divide the inclusive cross section by the tagging efficiency, and multiply by the purity of the b data sample.

The factor C_{PL} connects our experimentally measured detector-level cross section σ_{det} to the true (particle-level) cross section, and is determined through the procedure called *unsmearing* (Section 7.5). This procedure is intended to remove the effect of the finite detector resolution with which the calorimeter measures the jet energy for the measured cross section, and correct the cross section in such a way that it will correspond to the true particle-level cross section.

In the course of the measurement description given in Chapter 7, we will go through the steps of identifying and determining all of the individual components of Equation 2.20, and will obtain the final b-jet cross section measurement.

CHAPTER 3

THE EXPERIMENTAL APPARATUS

This analysis is based on data collected at Fermi National Accelerator Laboratory (FNAL or Fermilab). The two primary instruments at Fermilab that produced this data are the Tevatron accelerator and the recently upgraded DØ particle detector. The Tevatron accelerator creates proton and anti-proton beams colliding with the center of mass energy of 1.96 TeV. The DØ detector is an extremely complex and potent multipurpose particle detector surrounding one of the interaction points with nearly enclosed 4π geometry and collecting data of the final state particles coming from collisions. In this chapter, these instruments are discussed with a moderate level of detail in order to clarify the experimental challenges and goals as well as to give the fullest credit to all people who have built them and made these unique machines a reality.

3.1 The Fermilab Accelerator Complex

Located in the small suburban town of Batavia, IL, and 35 miles from Chicago, on 6,800 acres of beautiful prairie land, Fermi National Laboratory (Figure 3.1) is the home for a series of machines designed to produce and deliver highly energetic beams of particles, the particle accelerators. The Tevatron, currently the largest and most powerful accelerator in the world, is only the last one in the chain of complex machines working together in combination to push the energy frontier [13].

Figure 3.1. Four miles in circumference, the Tevatron $p\overline{p}$ collider is housed in a tunnel about 30 feet below the big ring you see in this aerial view of the Fermilab. The ring to the left of it is the Main Injector. Photo is courtesy of Google Earth$^{\text{TM}}$.

The Tevatron is built as a *collider* machine, which accelerates both protons (p) and anti-protons ($\overline{p}$) to an energy of 980 GeV and then smashes them against each other, providing the center of mass energy $\sqrt{s}$ of 1.96 TeV. Until the Large Hadron Collider (LHC) at CERN (abbreviation of the French for European Nuclear Research Centre), Switzerland, starts in 2007, the Tevatron will remain the highest energy collider and a tool for discovery. As with all modern-day high-energy accelerators, the Fermilab Accelerator Complex consists of many integral parts created (and now operating) with great precision. This succession of machines includes the preaccelerator and Cockroft-Walton accelerator, the linear accelerator (LINAC), the Booster synchrotron, the Main Injector, the Antiproton Souce, the Tevatron, and the Recycler (Figure 3.2). In the following subsections we are going to take a virtual

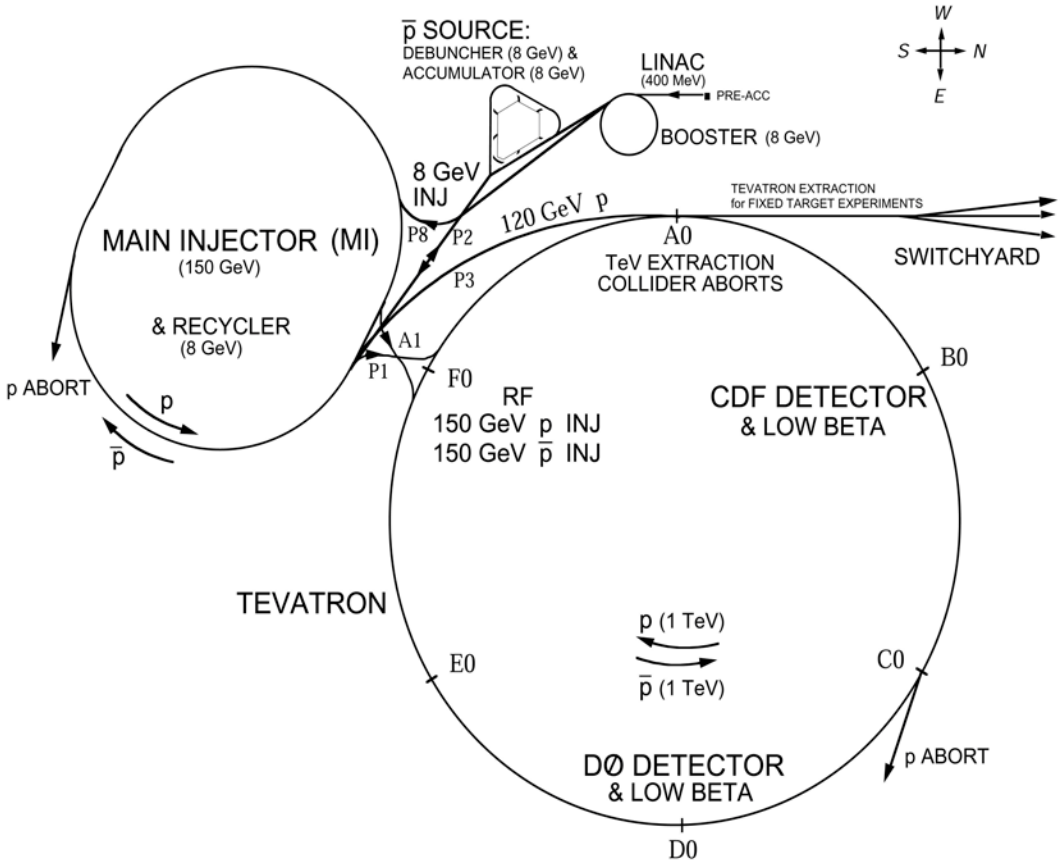

Figure 3.2. Schematic view of the accelerator complex at Fermilab. Figure is adopted from [17].

tour, and familiarize ourselves with each stage leading to $p\overline{p}$ collisions [16].

3.1.1 The Preaccelerator

The first step to Tevatron accelerator is creating the beam of protons. Protons ending up in the main ring originate at the device called preaccelerator. The process begins with hydrogen gas being pulsed into a magnetron surface-plasma source. During the operating cycle, a pulsed arc voltage (150 V) is applied to the cathode to create an electric discharge between the cathode and anode. The resulting electric field strips off electrons from the hydrogen atoms, producing H^+ ions. The free

protons are then attracted to the Cesium cathode's surface. Because of the relatively low work function of Cesium, protons can quite easily free up the electrons from the cathode's surface. Every so often it happens that a proton captures not one but two electrons thus becoming H^- ions. The electromagnetic field causes them to drift to the opposite side of the magnetron source. An extractor plate accelerates the ions to a kinetic energy of 18 keV. A schematic view of the negative ion source is shown at Figure 3.3. Further acceleration of the H^- ions is done by using an electrostatic

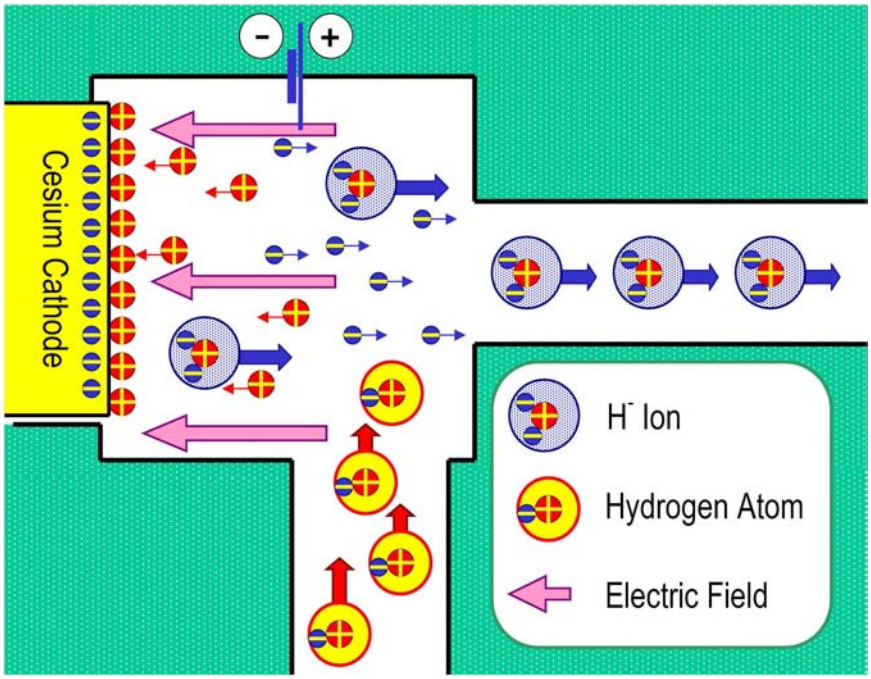

Figure 3.3. The schematic view of H^- ion source operation principle.

Cockroft-Walton accelerator. Using a system of rectifiers to create a high-voltage gap, the potential difference of the Cockroft-Walton propels the H^- ions further to the next acceleration stage with energies of 750 keV.

3.1.2 The Linac

At the next stage, H^- ions are taken to the linear accelerator called the *Linac*. The Linac consists of a 130-meter long series of cylindrical cavities, and its acceleration principle can be defined through two stages (Figure 3.4). An electric field

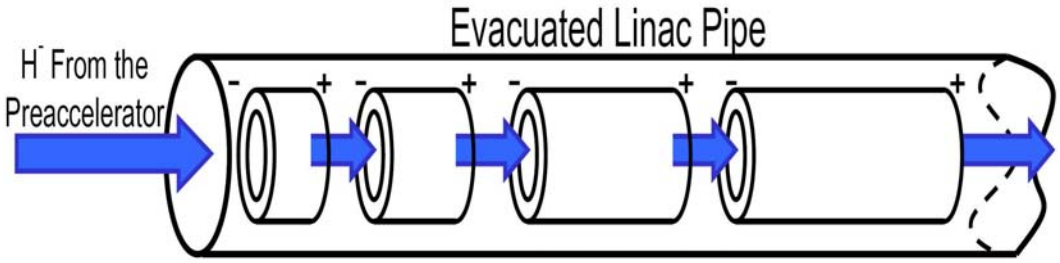

Figure 3.4. The operation principle of *Linac* linear accelerator.

pulls the H^- ions inside the starting cavity of the Linac's beam pipe. When these ions then enter a shielded region, the polarity of the electric field is simultaneously reversed. This prevents other ions outside of the cavity from entering. Upon exiting the shielded region the electric field is reversed again, which gives the ions another boost of acceleration. With this cycles repeated over and over, the ion stream becomes structured in localized bunches as opposed to a steady ion flow from the preaccelerator. By the end of their travel along the Linac, ions reach an output energy of 403 MeV.

3.1.3 The Booster Synchrotron

After the Linac, the Booster (Figure 3.5) is the first synchrotron accelerator that the H^- beam encounters. Just before injection into the Booster, a debuncher is used to remove the 805 MHz momentum spread structure formed by the Linac. Upon debunching the H^- ion beam passes through a thin carbon foil. As ions pass through the foil, the atoms of the foil interact with the two ion's electrons and strip

Figure 3.5. Inside the Booster ring. Figure courtesy of Fermilab.

them from the ion. Thus the electrons are discarded, leaving only the bare beam of protons to pass through.

The Booster is housed in a ring tunnel of 1570 feet in circumference. Dipole magnets in a synchrotron accelerator are used bend the trajectories of the protons and constrain them to a circular orbit, and the quadrupole magnets are used to focus the proton beam. The accelerating electric fields are formed by a set of Radio Frequency (RF) cavities, which gradually add momentum to the proton beam as it circles around the ring. The basic idea behind all synchrotron accelerators is both the RF frequency and magnetic field strength are increased in a synchronous manner while maintaining the same circular orbit with increasing beam momentum. After approximately 20,000 revolutions around the Booster ring in just 0.033 seconds, the

proton beam attains an energy of 8 GeV. In the Booster, the proton beam is again bunched into a pulse train of about five to seven bunches. Each bunch contains about $5 \sim 6 \times 10^{10}$ protons.

3.1.4 The Main Injector

The Main Injector synchrotron is the primary upgrade to the Fermilab accelerator complex for Run II. Two miles in circumference, this accelerator utilizes the former Main Ring tunnel that was used in Run I. With the addition of the Main Injector there is a factor of three increase in the number of protons that can be delivered to the Tevatron over what was possible in Run I. Also, the Main Ring was located in the same enclosure as the Tevatron, leading to significant beam halos and other backgrounds in the detectors at the collision points. This issue now has been resolved by locating the Main Injector outside the Tevatron. The Main Injector accepts seven bunches of 8 GeV protons from the Booster and accelerates them to 120-150 GeV. The Main Injector performs several functions: delivery of the 150 GeV proton beam to the Tevatron, delivery of the 120 GeV proton beam to the anti-proton production farm and a 120 GeV proton beam for fixed-target experiments. It also accelerates the anti-proton beam produced at the farm to 150 GeV and then injects that beam into the Tevatron [18].

3.1.5 The Anti-proton Source

As has been mentioned above, the Tevatron is a $p\overline{p}$ collider. The method of colliding a beam of particles with its antimatter counterpart in the same accelerator allows for the doubling of the center of mass energy. While protons are relatively easy to produce, the production of comparably large quantities of anti-protons is a complicated task. The intensity of the anti-proton beam is one of the primary limitations for the Tevatron. Anti-protons (or $\overline{p}$) are produced by bombarding a pro-

duction target with a high energy proton beam. Anti-protons are produced by using the 120 GeV proton beam from the Main Injector. This proton beam is directed to strike a target of a 10×2 cm nickel disk [19]. It creates a multitude of secondary particles from the proton-Ni collision, with anti-protons among them. Immediately after the nickel target is a cylindrical collection lens made of Li. Lithium is used because of its conductive and low absorbing properties. A large current (peaked at 670 kA) is applied to the lens, thus setting up a solenoidal magnetic field. This field tends to bend the secondary particles so that they travel in collinear paths. The schematic anti-proton source setup is shown in Figure 3.6. Following the collection lens is a pulsed dipole magnet that specifically selects 8 GeV negatively charged particles from all of the secondaries.

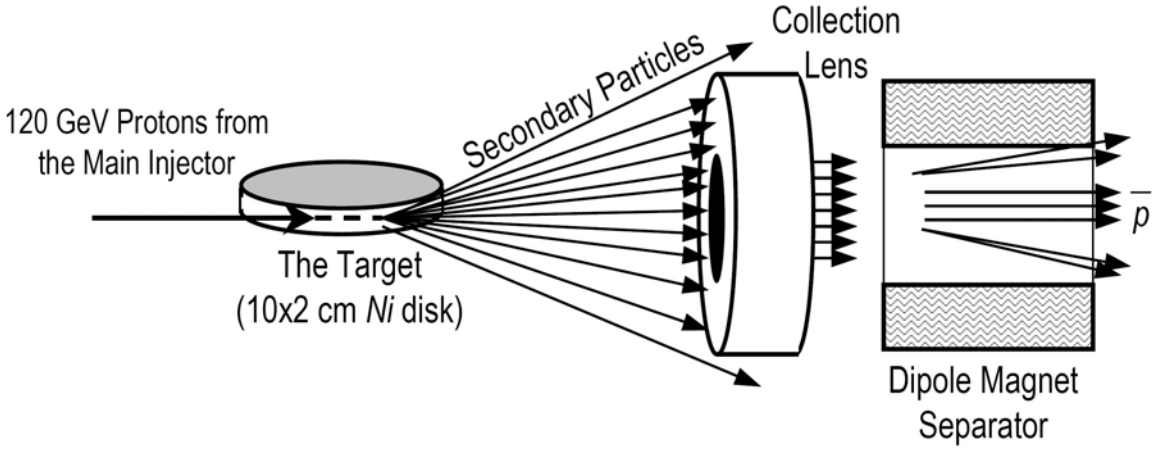

Figure 3.6. Illustration of $\overline{p}$ production.

3.1.6 The Debuncher and Accumulator

The 8 GeV anti-protons from the source are sent to two anti-proton storage rings, the Debuncher and the Accumulator, contained in the same tunnel. The tunnel housing these storage rings has rounded triangle type geometry with a cir-

cumference of roughly 1700 ft. Both the Debuncher and the Accumulator contain sets of magnetic and RF devices. The Debuncher RF cavities cause the anti-protons to feel different RF phases depending on their energies. The low energy anti-protons are accelerated and the high energy anti-protons are decelerated. This process repeats over and over, causing the spread in energy to be reduced. Applying so-called stochastic cooling to anti-protons restricts their transverse oscillations and helps keep them on an optimal orbit around the ring. The stochastic cooling and momentum manipulations allow the Debuncher to achieve greater efficiency transferring anti-protons to the Accumulator [19].

The Accumulator stores the anti-protons and arranges them into bunches with the same structure as the protons in the Main Injector. This is accomplished by stacking successive pulses of anti-protons from the Debuncher by their momentum, using RF cavity and stochastic cooling systems. This process takes several hours or even days to get accumulating stacks of 10^{12} antiprotons for use in Run IIa. The stack of the antiprotons is then transferred into the Main Injector for acceleration to 150 GeV and subsequent injection into the Tevatron ring.

3.1.7 The Tevatron

The Tevatron synchrotron ring is the final stage of particle acceleration. It uses superconducting magnets with a field strength of 4.2 Tesla (at a beam energy of 980 GeV) to bend the protons and antiprotons around the tunnel of 2000 meters in diameter. The proton beam traverses the Tevatron clockwise, with the anti-proton beam moving in the opposite direction. The beams can meet at six interaction points of the smallest transverse beam dimensions, which are named AØ through FØ. At two of these points, particle collision detectors are located. The Collider Detector Facility (CDF) detector is located at BØ and the DØ detector is located at

TABLE 3.1

TEVATRON COLLIDER PARAMETERS FOR RUN IIa

Parameter	Run IIa Values
Beam Energy	980 GeV
Bunches	36×36
Protons / bunch	27×10^{10}
Antiprotons / bunch	7.5×10^{10}
Antiproton stacking	2×10^{10} / hour
Luminosity	2.1×10^{32} cm^{-2}s^{-1}
Bunch spacing	396 ns
Interactions per crossing	5.8

DØ (Please refer to Figure 3.2). The longitudinal position of the interaction point has a Gaussian shaped distribution around the center of the DØ detector with a width of approximately 25 cm. In the transverse plane the position distribution also has a Gaussian shape but with a width of 30 μm. Some characteristic parameters of the Tevatron for Run IIa are given in Table 3.1.

As it has been mentioned above, the final Tevatron beams are not continuous. The Tevatron beams have protons and antiprotons grouped into bunches with a certain timing. The Tevatron operates in a 36×36 $p\overline{p}$ bunches mode, with a bunch spacing of 396 ns during Run IIa.

The Tevatron operating parameters have changed significantly from the previous Run I to maximize the output of interesting physics events for Run II. Most notably, the design luminosity is increased tenfold to 2.1×10^{32} cm^{-2}s^{-1}. This was achieved by increasing the number of bunches from 6 to 36 while simultaneously lowering the bunch crossing time from 3.6 μs to 396 ns, and by increasing the number of protons and anti-protons per bunch, using the Main Injector and the Recycler (Please refer to Subsection 3.1.4).

3.2 Coordinate Systems and Other Conventions at DØ

Before we proceed with the description of the DØ detector, we have to define some conventions in terms of which we can better understand its construction and application to this analysis. DØ uses a standard orthogonal right-handed coordinate system with the positive z axis in the direction of the proton beam, from detector North to South. The positive x axis is defined to be a vector pointing radially outward from the center of the DØ detector in the East direction. As DØ has nearly-hermetic 4π geometry, it is convenient to use a combination of cylindrical and spherical coordinates (z, ϕ, θ) to describe it. The polar angle θ is defined from positive z axis direction, while the azimuthal angle ϕ is the angle around the z axis with zero being the positive x direction and $\phi = \pi/2$ is the positive y direction. Figure 3.7 illustrates the described choice of coordinate system.

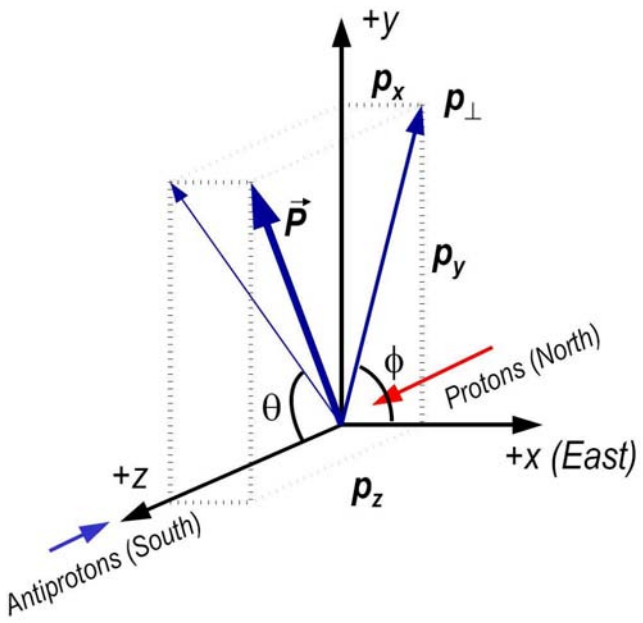

Figure 3.7. DØ coordinate system and $p_\perp$ definitions.

Besides the DØ coordinate system, there are several kinematic variables introduced. While a brief note on the variables was made in the Introduction (Chapter 1), there are some details that require a more thorough explanation. The rapidity y, is convenient to use instead of the polar angle θ, because Δy would have then a Lorentz invariant construction. It is defined to be:

$$y = \frac{1}{2} \ln \left(\frac{E + p_z}{E - p_z} \right), \tag{3.1}$$

However, at the Tevatron we operate with energies far exceeding the proton mass, so instead of rapidity y, pseudorapidity is often used, where $E = \mid \vec{p} \mid$:

$$\eta = -\ln(\tan \frac{\theta}{2}) \tag{3.2}$$

There is also a distinction between pseudorapidity relating to an actual collision event versus pseudorapidity defined within the detector's coordinate system. While the precision of measuring x and y coordinates is quite high, the z coordinate of the primary interaction point of collisions is not well constrained. The position of the interaction point is distributed along the z axis following a Gaussian distribution. Since z of the primary vertex in a particular event generally is not located at zero, the detector-related pseudorapidity η_d and η are distinct.

Other kinematic variables commonly used at DØ are transverse energy ($E_\perp$) and transverse momentum ($p_\perp$) defined as $E_\perp = E \sin\theta$ and $p_\perp = p \sin\theta$. These are used instead of total energy E and momentum p partly because of ease of measuring ability and partly because of the fact that in $p\overline{p}$ collisions the center-of-mass energy $\sqrt{s}$ is often not a relevant variable [20]. According to the Parton Model, partons carry only a fraction of the total nucleon energy. Therefore the scattering of these partons (of different energies) results in their center-of-mass frame not coincident with the lab frame.

3.3 The Run II DØ Detector

The 5500 ton, 40 foot tall DØ detector is a huge monster of a machine designed to record extremely complicated processes on a minute scale with an impressive degree of accuracy and detail. It is a multipurpose detector used to study various phenomena resulting from high center-of-mass energy ($\sqrt{s}$= 1.96 TeV) $p\overline{p}$ collisions. The detector is geared primarily toward the investigation of large $p_\perp$ phenomena and high mass states. Observation of the top quark, precision measurements of W and Z bosons, production of b-quark hadrons, testing of perturbative QCD and the search for new physics beyond the standard model were all within the design goals. In order to successfully study such processes, the detector was designed to provide excellent identification of electrons and muons along with good measurement of high $p_\perp$ jets and missing transverse energy which indicates the presence of non-interacting particles like neutrinos.

The DØ experiment was proposed in 1983 and performed very well during Run I of the Tevatron in 1992-1996, leading among many successfully accomplished physics analyses to the discovery of the top quark. Along with the Tevatron, the DØ detector has gone through a major upgrade for the start of Run II in order to further increase its performance. Essentially, by the end of the upgrade, the DØ detector was in many respects a different instrument. A completely new tracking system was installed along with a new superconducting solenoid magnet. The muon systems have both new hardware and new readout electronics installed. In addition, the data acquisition system was completely upgraded. Even older elements such as the calorimeter system have new readout electronics installed in order to accommodate the increased physics needs and higher event rates. You can see the general overview plot of detector components in Figure 3.8. In this chapter, the details of the various systems of the Run II DØ Detector are described.

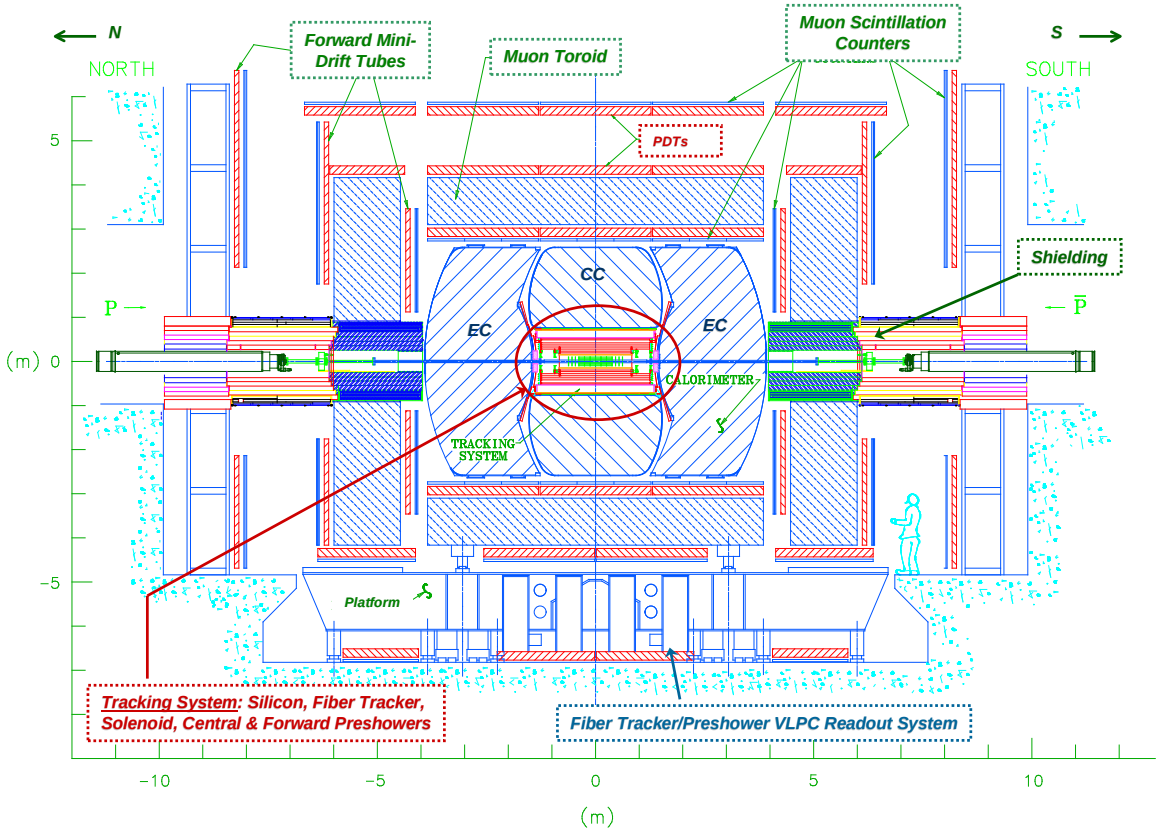

Figure 3.8. Cross section view of the DØ detector for Tevatron Run II. Figure adopted from [21]

The recent upgrade made it possible for the members of DØ collaboration to expand and broaden their physics goals. The new tracking system opened up the potential for a vigorous B-physics program. The studies with the DØ data include top quark, W and Z bosons, as well as perturbative and non-perturbative QCD. The upgrade also enhanced the ability to search for new particles, including searches for the Higgs boson, gravitons, and other signatures of new phenomena beyond the Standard Model.

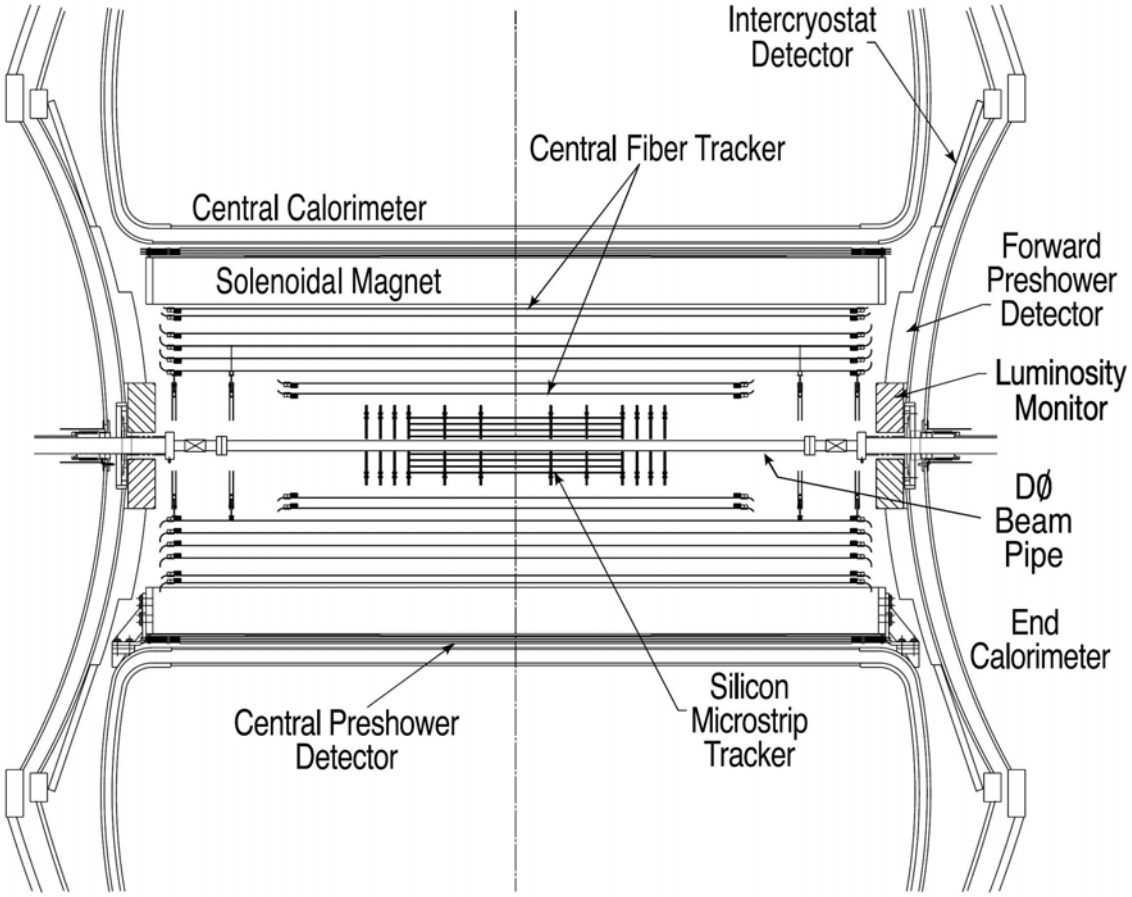

Figure 3.9. Central tracking volume of the DØ detector for Tevatron Run II. Figure adopted from [22]

3.3.1 Central Tracking System

The central tracking volume of DØ is shown in Figure 3.9. Excellent tracking in the central detector region is essential for studies of top quark, electroweak, and B physics and to search for new phenomena, including the Higgs boson. The upgraded DØ detector uses a completely new central tracking system, which consists of several parts: the Silicon Microstrip Tracker (SMT) and the Central Fiber Tracker (CFT), and a superconducting solenoid magnet, which provides a magnetic field of 2 Tesla parallel to the beam direction. With the solenoid added for Run II, the charge

and momenta of charged particles can be measured from the curvature of their trajectories in the new central tracking system. Below we will discuss each of these subsystems in more detail.

3.3.2 The Silicon Microstrip Tracker

The innermost (and the closest to the interaction point) layer of the DØ detector is the Silicon Microstrip Tracker [23]. The choice for the Silicon detector has a number of advantages, such as low ionization energy, fast signal collection time, good signal efficiency, and low rates of multiple scattering within such devices. Silicon-based detectors are an increasingly popular choice among tracking designs, as they also provide excellent spatial resolution. Indeed, the SMT has the highest resolution of all sub-detectors of DØ. While its position inside DØ can be viewed at Figure 3.9, the SMT design schematics are given by Figure 3.10.

The SMT provides both tracking and vertexing over nearly the full η coverage of the calorimeter and muon systems. Design of the detector, electronics, and cooling are, in large part, dictated by the existing space and environment. The length of the interaction region ($\sigma \approx 25$ cm) sets the length scale of the device. With a long interaction region, it has been a challenge to design the detector in which the majority of tracks in a wide η range will be perpendicular to its surfaces. This requirement led to a design of barrel modules interspersed with disks in the center and assemblies of disks in the forward regions. The barrel detectors primarily measure the $r - \phi$ coordinate and the disk detectors can also measure $r - z$ coordinate. Vertices for particles at high η are reconstructed in three dimensions by the disks, and vertices of particles at small values of η are measured in the barrels and by the CFT.

Structural support for the SMT is provided by Beryllium bulkheads. These bulkheads also provide cooling water to the detector through channels machined

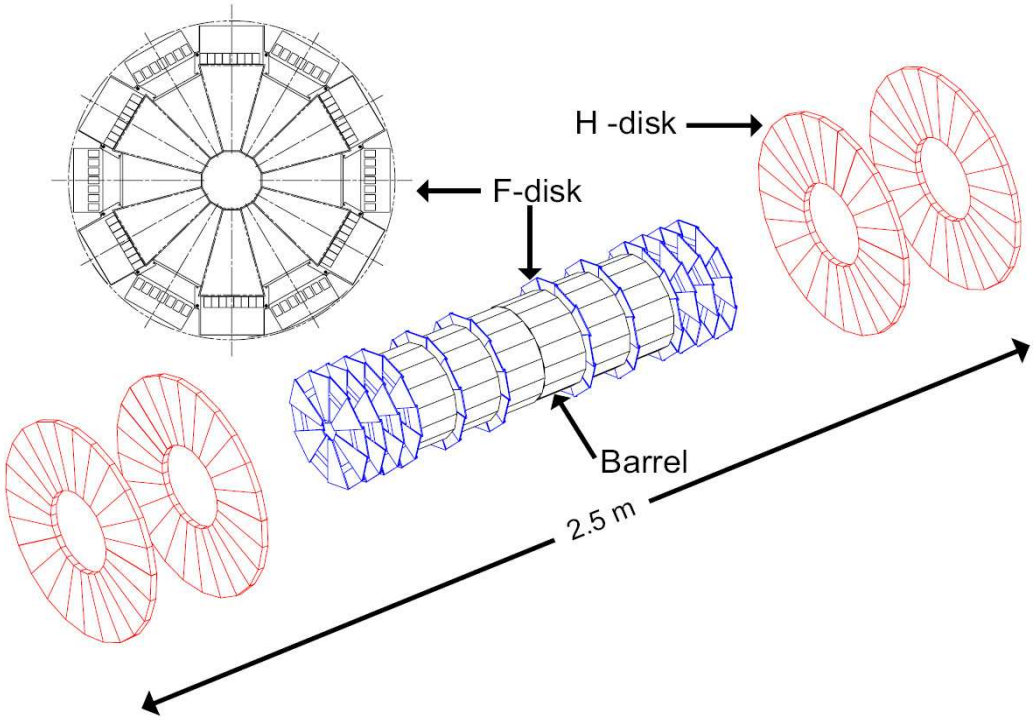

Figure 3.10. The Silicon Microstrip Tracker (SMT) construction overview. Figure courtesy of Fermilab and DØ collaboration.

into them. The beryllium bulkheads are mounted on half-cylinders made of carbon fiber, and provide further support for the sensitive parts of the SMT detector.

The barrel structure of the detector is formed by six sections each 12 cm long in z. There are four concentric layers of barrels, made with Silicon ladders. Each ladder is made from two 300 μm-thick wafers. Layers two and four of all barrel modules are double-sided detectors with a 62.5 μm pitch and positioned at a 2° stereo angle. The first and the third layers of the central four barrels have double-sided detectors with a pitch of 153.5 μm and positioned at a 90° stereo angle. Layers one (closest to the beam pipe) and three of the outer two barrels consist of single-sided axial detectors pitched at 50 μm.

Alternating the barrels in the perpendicular plane, there is a structure of twelve disks, called F-disks. Each F-disk is 8 mm thick and is composed of twelve overlapping double-sided detector wedges. The readout strips on the two sides are laid out with angles of ± 15 degrees with respect to the symmetry axis of the wedge, which gives an effective stereo angle of 30° to the detectors. These detectors have a pitch of 50 μm for the p-doped side of the Silicon and a pitch of 62.5 μm for the n-doped side of the Silicon.

The four disk assemblies with larger areas are called H-disks. These four disks are located further out from $z = 0$ two-by-two on both sides to the extreme ends of the DØ detector. H-disks are constructed with 24 single-sided silicon wedges with a pitch of 81 μm. The H-disks help to maintain a uniform momentum resolution and to extend tracking coverage to large η region.

The SMT consists of a grand total of 912 readout modules, with 792,576 channels, and collects electron/hole pairs produced by particles passing through the radially arranged modules described above. To collect the flow of electrons, a potential difference of ≈ 100 volts applied across the silicon wafer. With $r - \phi$ coordinate resolution of approximately 10 μm, a hit is determined by measuring the amount of charge deposited on each strip. Spatial resolution of this scale helps achieve two goals for the experiment. First, it allows the identification and reconstruction of vertices displaced from the primary vertex (please refer to Chapter 6.1), especially important for this analysis. Figure 3.11 shows an illustration of displaced vertex finding. Secondly, the hit resolution helps the momentum resolution for very high $p_\perp$ tracks. Secondary vertex finding is very important for any physics involving b or c quark decays, while good resolution at high momentum is important for physics searches involving high-mass particles.

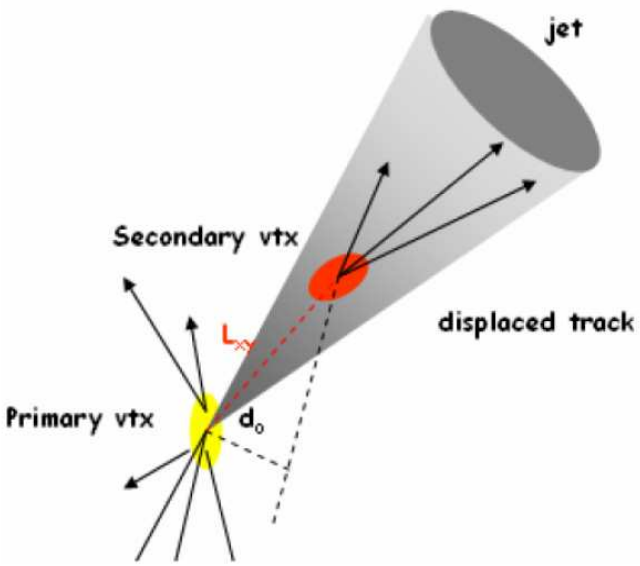

Figure 3.11. Displaced (secondary) decay vertex finding using tracking information. Here denoted the impact parameter d_o. For a more detailed explanation, please refer to Chapter 6.

3.3.3 The Central Fiber Tracker

The Central Fiber Tracker (CFT) is located just outside and surrounding the SMT, occupying the cylindrical radial space between 20 and 52 cm from the center of the beam pipe. The main function of the CFT is to measure the $p_\perp$ of charged particles passing through the detector. By measuring the curvature of tracks in the magnetic field of the solenoid, the CFT provides the information to determine the $p_\perp$ and the charge of the particle tracks crossing the detector.

The CFT consists of scintillating fibers mounted on eight concentric supporting cylinders [24]. To accommodate the larger diameter forward SMT H-disks, the two innermost cylinders are shorter than the outer six cylinders. The fibers are double clad and are 835 microns in diameter. The fibers are arranged into ribbons of 256 fibers, composed of two 'singlet' layers of 128 fibers each. Each cylinder supports one 'doublet' layer of fibers parallel to the beam direction (axial layers),

and a second stereo 'doublet' layer at an angle ϕ of $+3°$ (stereo u-layer) or $-3°$ (stereo v-layer). From the smallest cylinder outward, the fiber doublet orientation is $zu-zv-zu-zv-zu-zv-zu-zv$. Figure 3.12 shows a cross section quarter view of the CFT as well as a schematic for the doublet layer structure. The detector is

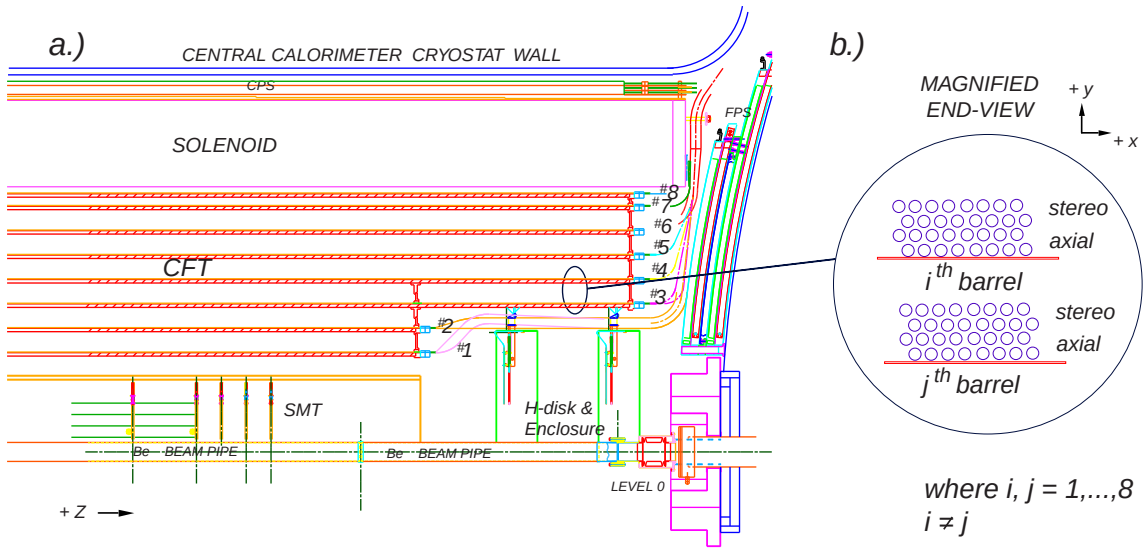

Figure 3.12. a) A quarter $r-z$ view of the CFT detector. Concentric nested barrel construction is shown. b) An extended $r-\phi$ end view of the two ribbon doublet layer structure for two different barrels. Adapted from [21].

logically divided into 80 sectors in ϕ. Each pie-shaped slice has 896 fibers and the entire detector has 71,680 channels.

The scintillating fibers are coupled to clear fiber wave guides of 7.8 to 11.9 m long, which carry the scintillation light to Visible Light Photon Counters (VLPCs) for read out. An end-on view of a CFT ribbon and the curved end connector are shown in Figure 3.13. Scintillation light is being collected from only one end of each scintillating fiber. The readout end for the axial ribbons is at the south end of the CFT, while the stereo ribbon readout is on the north end. The opposite end of each of the scintillating fibers was mirrored with a highly reflective aluminum

coating. The scintillating fiber is structurally and chemically similar to the clear fiber, but contains fluorescent dyes which emits light when a charged particle passes through it. The CFT uses about 200 km of scintillating fiber and 800 km of clear fiber.

During assembly, the scintillating fibers were grouped into 256 channel ribbons which were mounted onto the carbon cylinders with an accuracy better than 40 μm [22]. In order to achieve such an accuracy, precisely spaced grooves were machined into long, 1/16-thick pieces of acetal. The spacing between the grooves varied between 928 and 993 μm and was defined by the radius of the cylinder on which it was mounted. The grooved plastic was inserted into a rigid, curved backing plate of the desired radius, and the scintillating fibers were laid in and glued together to form the doublet ribbon structures described above. By design, the two layers of fibers are offset by one-half of the fiber spacing. Studies using a subset of representative CFT ribbons in a cosmic ray test stand have shown a doublet position resolution of better than 100 μm (Figure 3.14) for single muons.

Travelling through the clear waveguides onto the readout platform, light is detected by the VLPCs. VLPCs are silicon-avalanche based photon detectors operating at temperatures of 9 K to reduce the noise. These tiny detectors (Figure 3.15) jointly developed by Fermilab and Boeing engineers over the course of 10 years [26]. VLPCs have a quantum efficiency of about 80 percent, a gain of 20,000-50,000, a

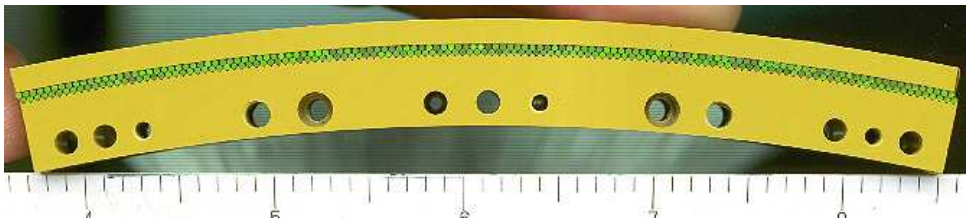

Figure 3.13. End-on view of a CFT ribbon and the curved end connector.

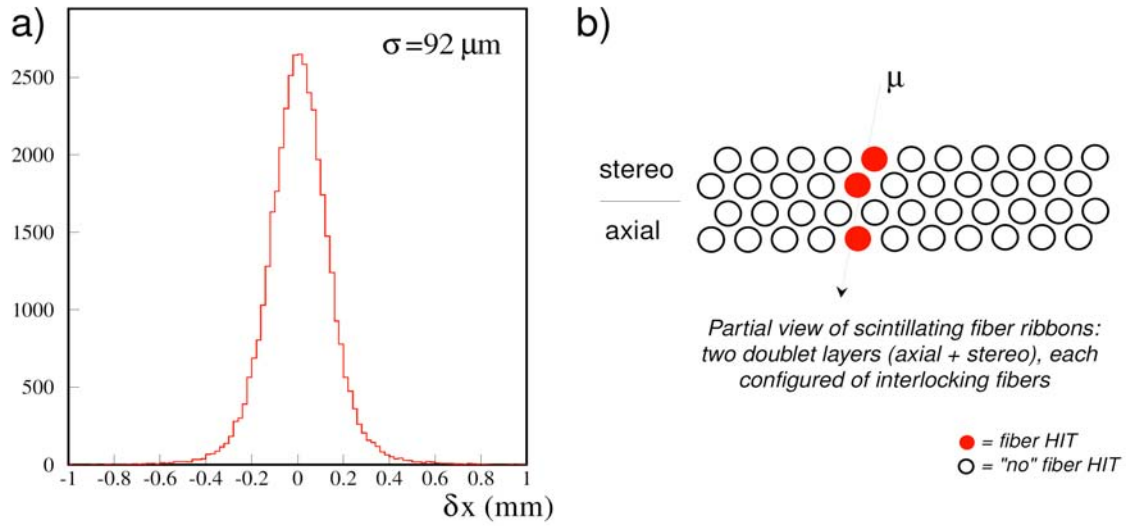

Figure 3.14. a) Distribution for the coordinate resolution measured in the CFT cosmic ray system test. b) An interlocking doublet ribbon structure (described in the text). Figures and results adopted from [25]

rate capability of at least 20 MHz, and a noise rate of less than 0.1 percent. The light coming from the CFT fibers is converted into an electrical signal by VLPCs and sent to front-end electronics boards for digitization and readout.

The front-end electronics are custom printed Analog Front End circuit boards (the AFEs) approximately 14" tall and 18" long which are mounted on top of the cassettes, that house the VLPCs and are inserted into cryostat [26]. On the readout AFE boards, the VLPC signal is sampled by a discriminator called the SiFi Trigger (SIFT) chip. From SIFT, the VLPC signal is simultaneously sent to a Silicon VerteX (SVX) chip and to the CFT triggering system. Figure 3.16 shows a typical spectrum fit for LED light in a single VLPC channel for an axial CFT fiber. Every channel is fit automatically and the parameters of the fit are extracted and used for monitoring. Typically, more than 97% of the axial channel signals fit successfully. This signal is stored in the SVX chip within an analog pipeline until a trigger decision is made,

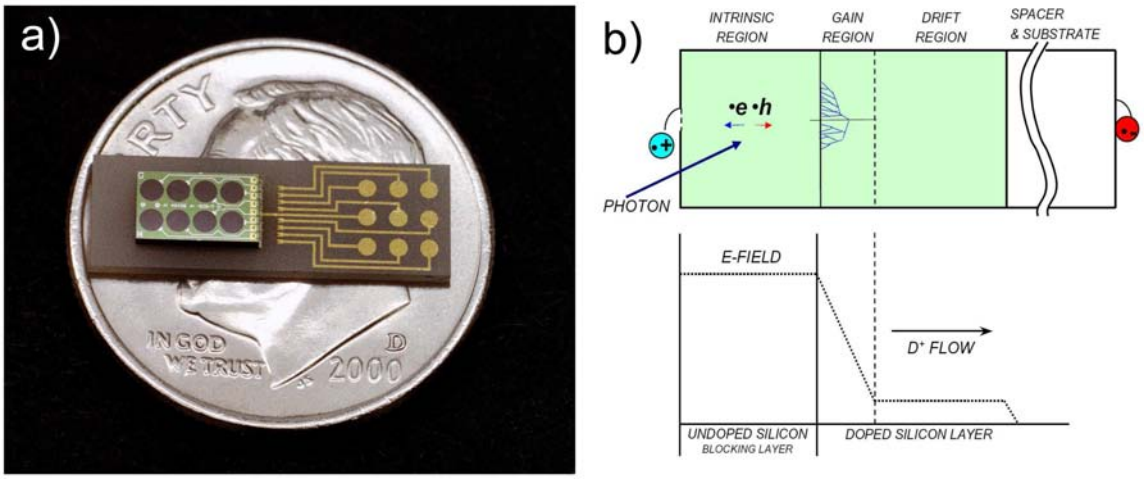

Figure 3.15. A scale view of Visible Light Photon Counters (VLPC) on a dime (a), and its basic operating principle diagram (b).

or 32 beam crossings have occurred since the signal was produced. If the trigger system issues an accept, then the SVX digitizes the signal and reads it out. The SIFT discriminator pattern which caused the SVX to readout is also appended to the SVX information. If no trigger decision is made or 32 beam crossings have passed, the signal information is discarded.

The CFT trigger (see also in Section 4.1.1) is implemented by using the SIFT output and hardware utilizing Field Programmable Gate Arrays (FPGAs) [27]. At first, only signals from axial layers are used as hits for the trigger, and coincidences are established among hits on all eight layers forming a track. Then tracks are combined with triggers from other parts of the detector, such as the Central PreShower (CPS) clusters to form an electron trigger, or the muon system to form a muon trigger. With the Trigger Level 1 acceptance, all of the CFT fiber layers are being read out. There will be a more detailed discussion on the DØ trigger system in Chapter 4.

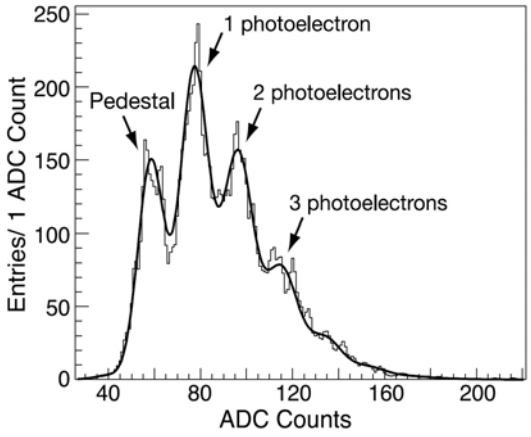

Figure 3.16. A typical fitted LED spectrum for a single VLPC for an axial CFT fiber. The histogram represents the data, and the smooth curve is the fit.

3.3.4 The Central and Forward Preshower Detectors

The Central and Forward preshower detectors are instrumented around the CFT within the central tracking volume of DØ. These subsystems are completely new additions to DØ and they are designed to take part in electron identification and background rejection during both triggering and offline reconstruction. Preshower detectors serve a double function as calorimeters and tracking detectors, improving the spatial matching between tracks and calorimeter showers [29].

The preshower detectors share common elements with the central fiber tracker, beginning with the waveguides and continuing through the entire readout electronics systems. Both preshower detectors are made from triangular strips of scintillator, as shown in Figure 3.17. Since the triangles are interleaved, there is no dead space between strips and most tracks traverse more than one strip, allowing for strip-to-strip interpolations and improved coordinate resolution. Wavelength-shifting fibers that collect the light are embedded at centers of each of the triangular strips [28].

The Central Preshower Detector (CPS) covers the central part of the detector

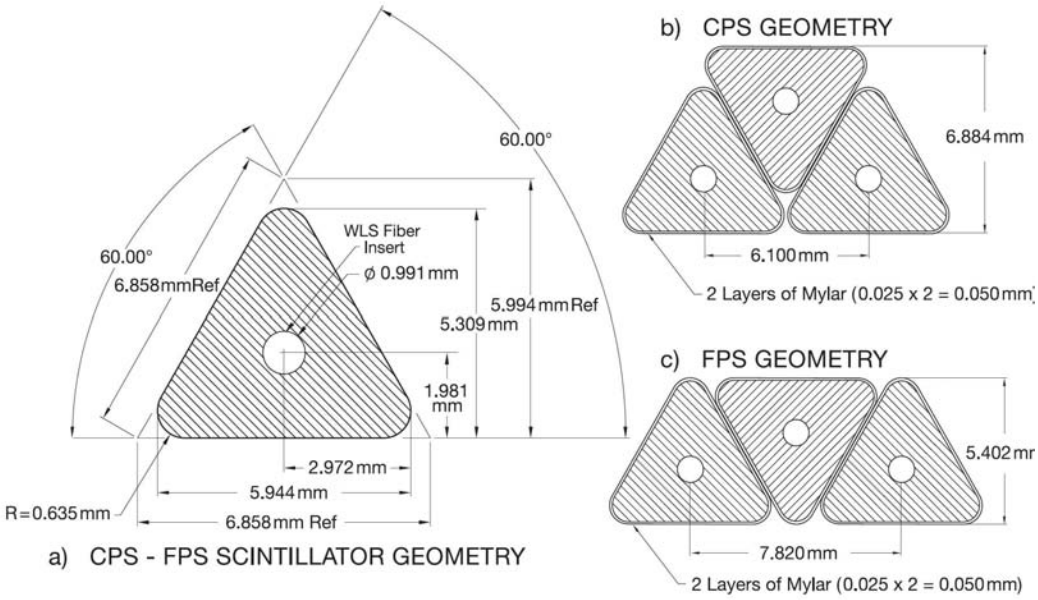

Figure 3.17. Scintillator strips geometry and structure of preshower detectors. Adopted from [22]

of $-1.2 < \eta < 1.2$ [17]. As stated above, the CPS functions as both a calorimeter and a tracker. This detector is mounted on a cylinder with a radius of 72 cm, and resides just around the solenoidal magnet and the central calorimeter cryostat. The CPS consists of three layers of scintillating strips. The innermost layer is an axially arranged layer, while the two outer layers are interleaved at stereo angles of $\pm 23°$. Similarly to the CFT, clear fiber waveguides transmit scintillation light from the CPS to the VLPCs located on the readout platform below the DØ detector. The CPS has a total of 7680 channels of readout. Data acquisition from the CPS axial layer is integrated with the CFT readout, and treated by Level 1 electron trigger as a ninth layer of the CFT.

To cover the forward regions of DØ between $(1.4 < |\eta| < 2.5)$, the Forward Preshower Detectors (FPS) are built (Figure 3.18). The two FPS detectors, north and south, are mounted on the corresponding spherical heads of the end calorimeter

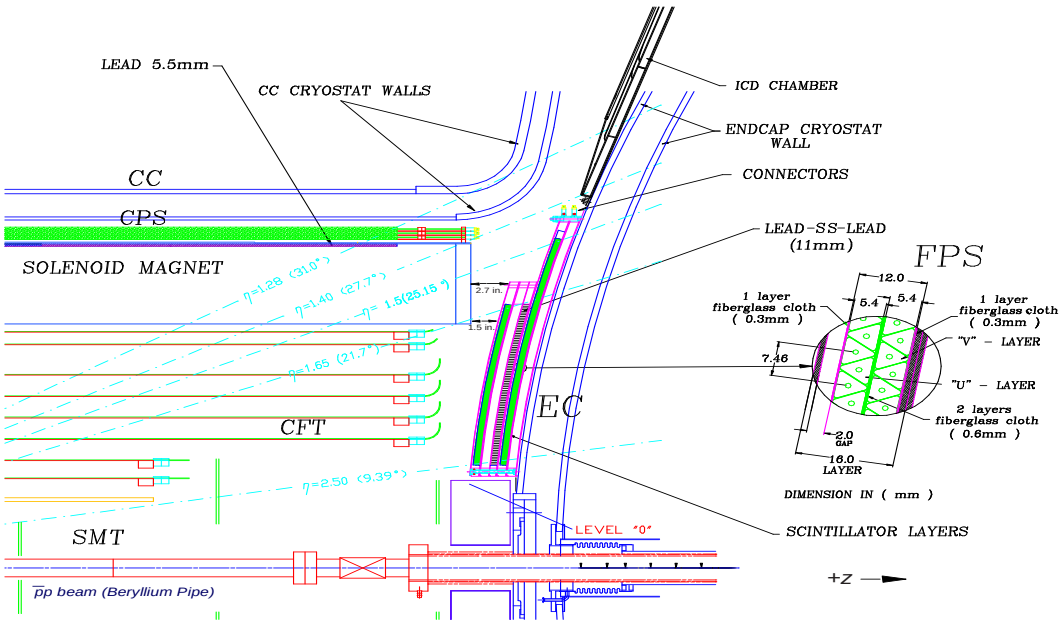

Figure 3.18. A quarter cross section view of the FPS detector. The inset shows details of the $u - v$ scintillator layer structure. Adopted from [17]

cryostats. Geometrically they are occupying the region between the luminosity monitor (Section 3.3.9) at the inner edge and the intercryostat detectors (Section 3.3.6) at the outer edge. These detectors consist of a lead absorber of two radiation lengths thick, sandwiched between two scintillation planes. Each plane is composed of one u and one v sub-layer. Each FPS detector has four measuring planes: two MIP (standing for Minimum Ionizing Particle) u and v planes and two shower u and v planes. The upstream layers (those nearest the interaction region) are known as the minimum ionizing particle, or MIP, layers while the downstream layers behind the absorber are called the shower layers. Charged particles passing through the detector will register minimum ionizing signals in the MIP layer, allowing measurement of the location (in η, ϕ, and z) of the track. Electrons will readily shower in the absorber, leading to a cluster of energy, typically on the order of three strips wide, in the shower layer that is spatially matched with the MIP layer signal. Heavier

charged particles are less likely to shower, typically producing a second MIP signal in the shower layer. Photons will not generally interact in the MIP layer, but will produce a shower signal in the shower layer [22, 29].

Readout of the FPS detectors, together totaling 14,968 channels [21], is done similarly to CFT and CPS, using the same VLPC system described above in Subsection 3.3.3.

3.3.5 The Calorimeter

The calorimeter is another crucial system for the analysis described in this dissertation, as it measures the energy of particles entering it. While certain readout components of the DØ Run II calorimeter have been upgraded, the calorimeter volume itself is unchanged from Run I [30]. It is designed to measure the energies of electromagnetic (electrons, photons) and hadronic objects (pions and other hadronic constituents of jets) accurately by completely or a partially absorbing it within the material. The calorimeter system also assists in identification of electrons, photons, jets, and muons and measures the transverse energy of the events. The DØ calorimeter system consists of three sampling calorimeters with primarily a uranium/liquid-argon medium, and an intercryostat detector. The overview of DØ calorimetry is pictured in Figure 3.19.

The electromagnetic (EM) and hadronic (HC) objects interacting with the calorimeter matter produce showers with distinct properties. EM objects interact primarily with the uranium in the detector via the following two processes: pair production ($\gamma \rightarrow e^+ + e^-$) and bremsstrahlung ($e \rightarrow e + \gamma$), while HC objects interact with the uranium nuclei via the strong nuclear force producing hadronic showers. In the case of the EM showers, the number of secondary particle increases but the average energy per particle decreases for each successive interaction. For the HC showers,

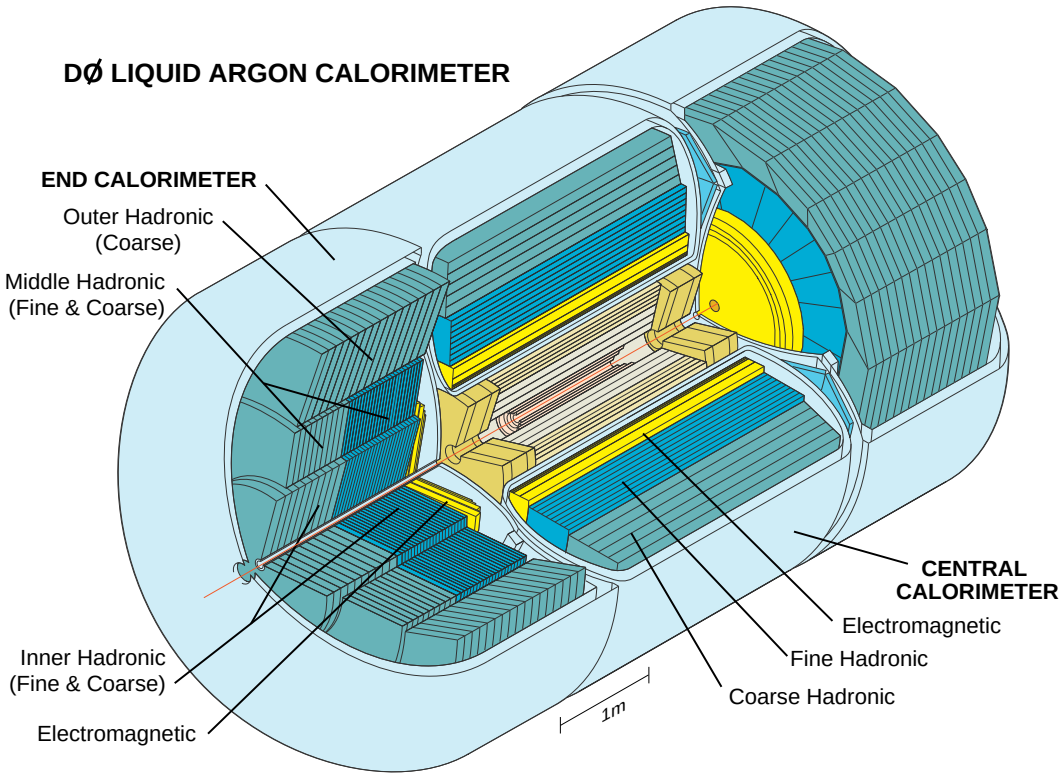

Figure 3.19. An isometric view of DØ calorimeter system. Adopted from [17]

the interactions produce secondary particles, approximately a third of which are neutral pions subsequently decaying in two photons ($\pi^\circ \rightarrow \gamma\gamma$). These photons also produce secondary electrons and photons which interact electromagnetically. The other $\frac{2}{3}$ of the hadronic showers are charged pions, and they continue to interact strongly. Hadronic showers are wider than purely electromagnetic showers, and typically develop slower over longer distances. This fact is utilized in the design of the DØ calorimeter.

The calorimeter system is enclosed by three cryostat volumes, one for the central, and two for the forward detector regions. The Central Calorimeter (CC) weights ≈330 tons, and the End ones (ECs, North and South) are ≈240 tons each. Within the CC and ECs, there are three sections arranged in order of increasing distance

from the collision point. These are the electromagnetic section (EM), the fine hadronic section (FH), and the coarse hadronic section (CH). The EM sections consist of four separate layers (EM1, EM2, EM3, and EM4). For the CC these EM subsections are layered radially, while for the ECs they are layered in increasing z. The electromagnetic sections use thin plates (3 or 4 mm in the CC and EC, respectively), made from nearly-pure depleted uranium. The fine hadronic sections are made from 6-mm-thick 2% uranium-niobium alloy. The coarse hadronic modules contain relatively thick (46.5 mm) plates of copper (in the CC) or stainless steel (in the EC).

In terms of logical organization, each layer represents a discrete set of readout cells. Radial conglomerates of cells, one cell from each of the layers, aligned in an outward direction from the interaction point, constitute calorimeter towers. This readout tower geometry is shown in Figure 3.20.

Each readout cell is a combination of several adjacent elementary unit cells. A schematic view of two typical calorimeter unit cells is given in Figure 3.21. As is seen, there is a gap between the adjacent absorber plates which is filled with liquid argon. Electron-ion pairs created via ionization of the liquid argon by charged particles from a shower are collected by electrodes in the unit cell. Metal absorber plates are used as ground electrodes (cathodes) and the resistive coats located at centers of the gaps on the readout board at a voltage of +2.0 to +2.5 kV, are used as anodes [22]. Signal boards (for all but the EM and small-angle hadronic modules in the EC) are made from two 0.5 mm thick G-10 plastic sheets serving as high voltage electrodes for gaps. The charge from the electrons deposited on the anode induces a charge on the copper readout pads via capacitive coupling. Electronics receive the analog signal from the readout pad proportional to the energy deposited by the shower in the liquid argon active media. The signals are carried out of the

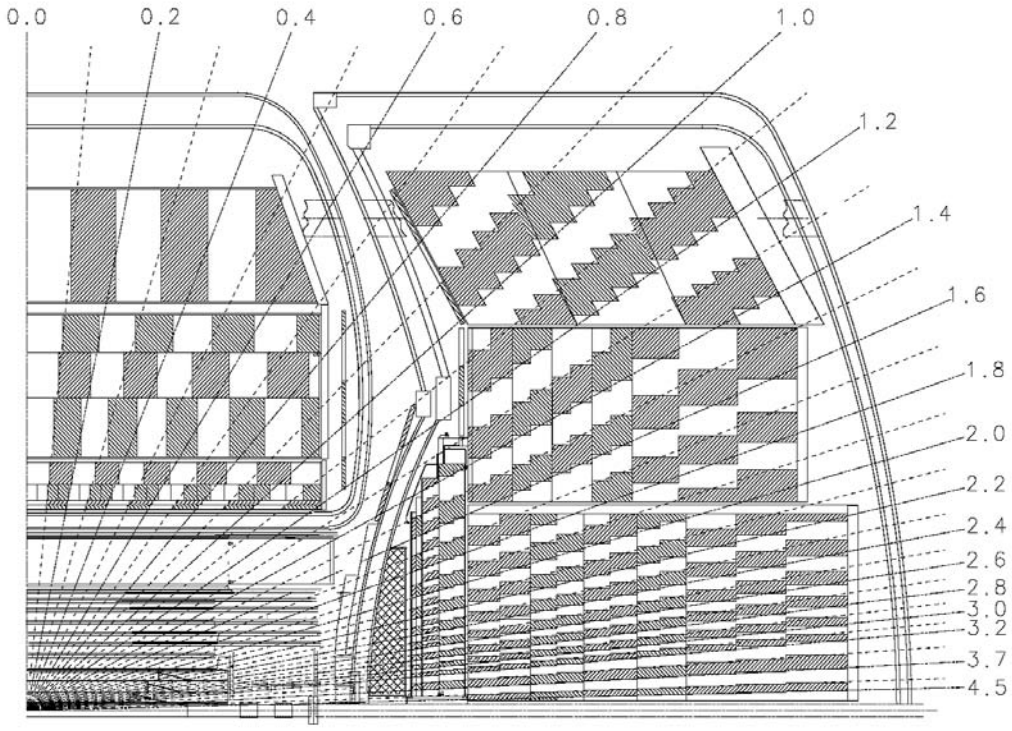

Figure 3.20. Schematic view of a portion of the DØ calorimeters showing the transverse and longitudinal segmentation pattern. The shading pattern indicates groups of cells merged together for signal readout. The rays indicate η intervals from the center of the detector. Adopted from [17]

detector via coaxial cables to several electronics boards that logically reorganize the outputs from the module structure into a tower arrangement. After this, the signal is sent to preamplifiers and signal shaping electronics and then is split and sent down two different paths. One path goes to the Level 1 calorimeter trigger. The other path leads to the baseline subtraction system, which cleans and removes noise from the signal before it gets digitized. The baseline subtraction system uses the signal from the previous interaction, which is taken as a baseline. Subtracting the baseline value from the current signal reduces noise caused by long time constants existing in some of the electronics used within the calorimeter readout system. Following a

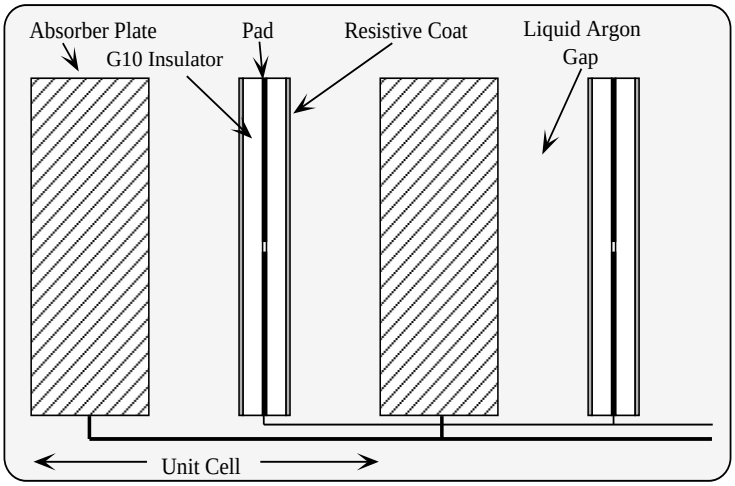

Figure 3.21. Schematic view of two calorimeter cells. Adopted from [31]

positive trigger decision, the output is read out and digitized by Analog-to-Digital Converters (ADCs). This digitized signal is then incorporated with signals from other DØ detector subsystems to form an event [32].

3.3.6 Intercryostat and Massless Gap Detectors

To augment the energy measurement in the intercryostat space between the central and forward calorimeters, InterCryostat Detectors (ICDs) are placed in this region (see Figures 3.18 and 3.20). They consist circular structures made of scintillating material 1.25 cm thick, divided into 16 sections and covering $1.1 < |\eta| < 1.4$. The 16 pieces are further divided into 384 segments (tiles) of the size $\Delta\eta \times \Delta\phi = 0.1 \times 0.1$, which are being read out by photomultipliers through embedded wavelength shifting fibers that collect and transport the light. In addition, separate single calorimeter-like readout cell structures, called massless gaps, are installed in both the EC and CC calorimeters. The readout electronics for the ICDs and massless gap detectors are similar to that of the main DØ calorimeters.

3.3.7 The Muon System

Muon identification is an essential part of a multitude of physics analyses [33]. It is particularly important within the context of this dissertation, as muons are used as one of the signatures of possible b flavor presence in the event. DØ has a large muon detection subsystem as the outermost detection layer. In general, it is constructed using wire chambers for precise track position resolution, and scintillators with photomultiplier tubes for fast triggering. Muons are much heavier than electrons, and therefore they do not lose as much energy via bremsstrahlung as electrons do. Muons lose energy due to ionization of the detector media, which is an absorption process with relatively low energy loss. Therefore, muons above a certain energy threshold ($\sim$ 3GeV) pass through the entire DØ detector with frequently negligible energy losses. The muon detector consists of three major parts, as is shown in Figures 3.8 and 3.22:

- The Wide Angle Muon Spectrometer (WAMUS) with $|\eta| < 1$ coverage;

- The Forward Angle Muon Spectrometer (FAMUS), covering $1 < |\eta| < 2$;

- A solid-iron 1.8 Tesla toroidal magnet.

The toroidal magnet is a square annulus made of iron, 109 cm in thickness and weighing 1973 tons. With the coils of the magnet running at 1500 A, the magnet generates a magnetic field of 1.8 Tesla. The magnetic field lines run in a plane perpendicular to the beam axis, vertically in the side parts of the magnet and horizontally in the top and bottom of the magnet. The iron of the central magnet also serves as the return yoke for the solenoid magnetic field. The magnet is split in the central system, covering the WAMUS region, and the two forward systems, covering the FAMUS region. In Run I there was no magnetic field in the central tracking region, subsequently the muon momentum measurement was done using

exclusively the toroid. After DØ upgraded with the solenoid, the muon momentum is predominantly found using the upgraded central tracking system discussed above in 3.3.1, but the muon system toroid still allows for an independent measurement. A possibility of combining the muon momentum information from the toroid with that from the central tracking systems can further improve the overall muon momentum resolution of the DØ detector.

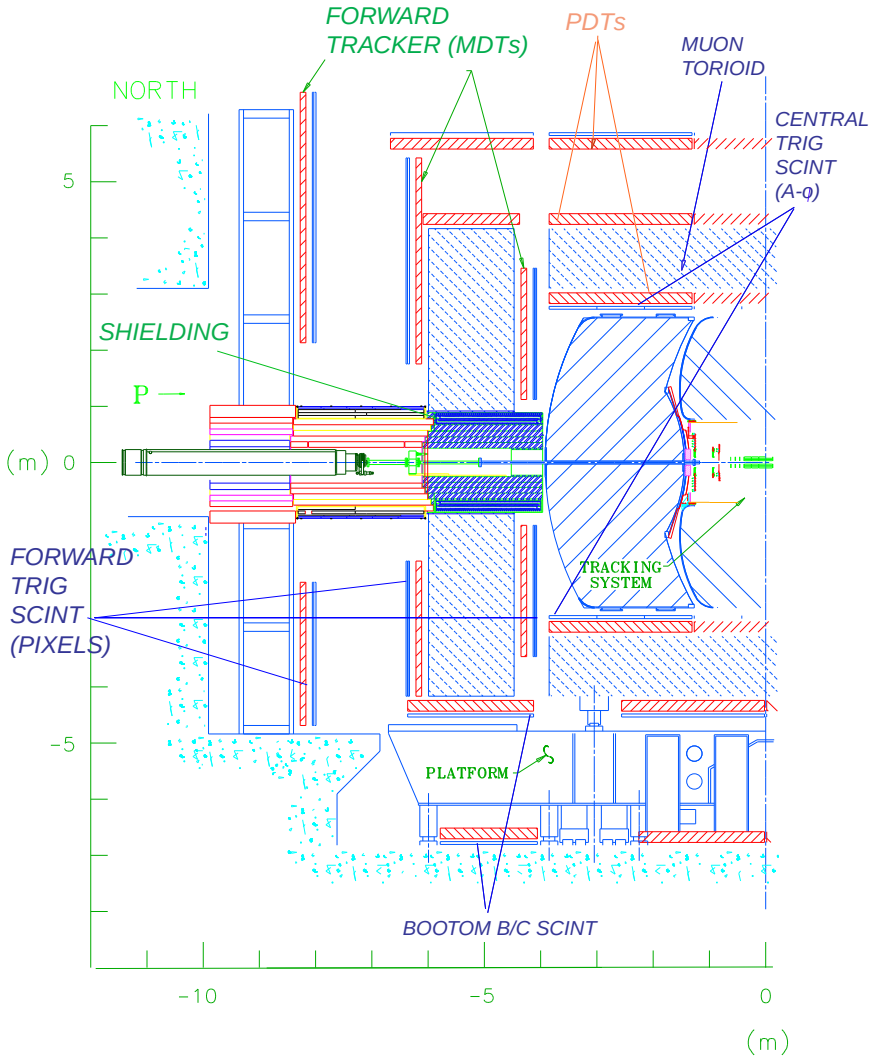

Figure 3.22. One quarter side view of DØ muon system. Adopted from [17]

The WAMUS consists of three layers of detectors, extending radially outward and labeled as layers A, B and C [22]. Layer A is located between the calorimeter and the toroidal magnet, while the B and C layers are placed outside the toroid. Each WAMUS layer is made of proportional drift tube chambers (PDTs) and scintillator/photomultiplier combos. The three planes of PDTs are located on each of the layers and cover $|\eta| \leq 1$. About 55% of the central region is covered by three layers of PDTs, and close to 90% is covered by at least two layers. The drift chambers are large (typical size 2.8×5.6 m^2), rectangular aluminum tubes. The PDTs outside of the toroid (layers B and C) have three decks of drift cells. Layer A has four decks of cells, with the exclusion of the bottom A-layer PDTs which have three decks. The cells are 10.1 cm across, and typical chambers are 24 cells wide and contain 72 or 96 cells. Inside each tube is an anode wire at its center which runs the full length of the tube. These wires are collinear with the magnetic field lines in order to provide a position measurement for momentum calculation. To obtain information on the hit position along the wire, vernier cathode pads are located above and below the wires. Each tube is filled with a non-flammable gas mixture of 80% argon, 10% CH_4 and 10% CF_4. At the operating voltage of 2.5 kV for the pads and 5.0 kV for the anode wire, the drift velocity in this gas mixture is about 10 cm/s, with a maximum drift time of 500 ns. Hit position uncertainty due to diffusion deviation in the gas is around 375 μm.

Scintillator detectors for the WAMUS are broken up into two categories, the $A - \phi$ counters and the Cosmic Caps. The cosmic cap and bottom counters are installed on the top, sides and bottom of the outer layer of the central muon PDTs. An important technical detail is that there is a difference between the top and sides (cosmic cap) and bottom counters. The bottom counters are positioned with their narrow dimension along ϕ and their long dimension along η. This orientation has

better matching in ϕ with the central fiber tracker trigger. With timing resolution of about 5 ns, they provide a fast timing signal to associate a muon in a PDT with the appropriate bunch crossing and discriminate against the cosmic ray background [34].

The $A-\phi$ counters cover the A-layer PDTs. They are sliced in segments in ϕ of 4.5° having a length of around 85 cm along the z direction. In a quite standard fashion, scintillator segments are embedded with wavelength-shifting fibers coupled to photo-multiplier tubes (PMTs), which are used for readout. The $A-\phi$ counters operate in a magnetic field of 200-350 Gauss due to the residual magnetic field of the toroid and solenoid, and are magnetically shielded with soft iron housings. These counters have a timing resolution of about 4 ns. This fast signal is used for triggering and rejecting out-of-time muons from cosmic rays and backscattered particles from the forward regions.

The forward muon detector, FAMUS, covers $1.0 < |\eta| < 2.0$ and consists of three main parts: the end toroidal magnets, three layers of Mini Drift Tubes (MDTs) used for muon track reconstruction, and three layers of scintillation pixel counters for triggering on events with muons [35]. As with the WAMUS, the forward muon detector also consists of A, B, and C layers. A layer consists of three (for layers B and C) or four (for layer A) planes of tubes mounted along magnetic field lines, similarly to WAMUS. All of the MDT installation contains 48,640 individual wires. The maximum length of the MDT tube is 5.8 m. Each of MDT layers is divided into eight octants, and each tube has eight individual cells. The individual cells have an internal cross-sectional area of 9.4×9.4 mm^2 and each contain a 50 μm tungsten/gold anode wire. A gas mixture of 90% CF_4 and 10% CH_4 is used in MDT cells. With this gas mixture and a cathode voltage of 3.1 kV, a maximum drift time of near 60 ns is achieved. The position resolution of the MDTs in the drift plane is on average around 0.7 mm per hit.

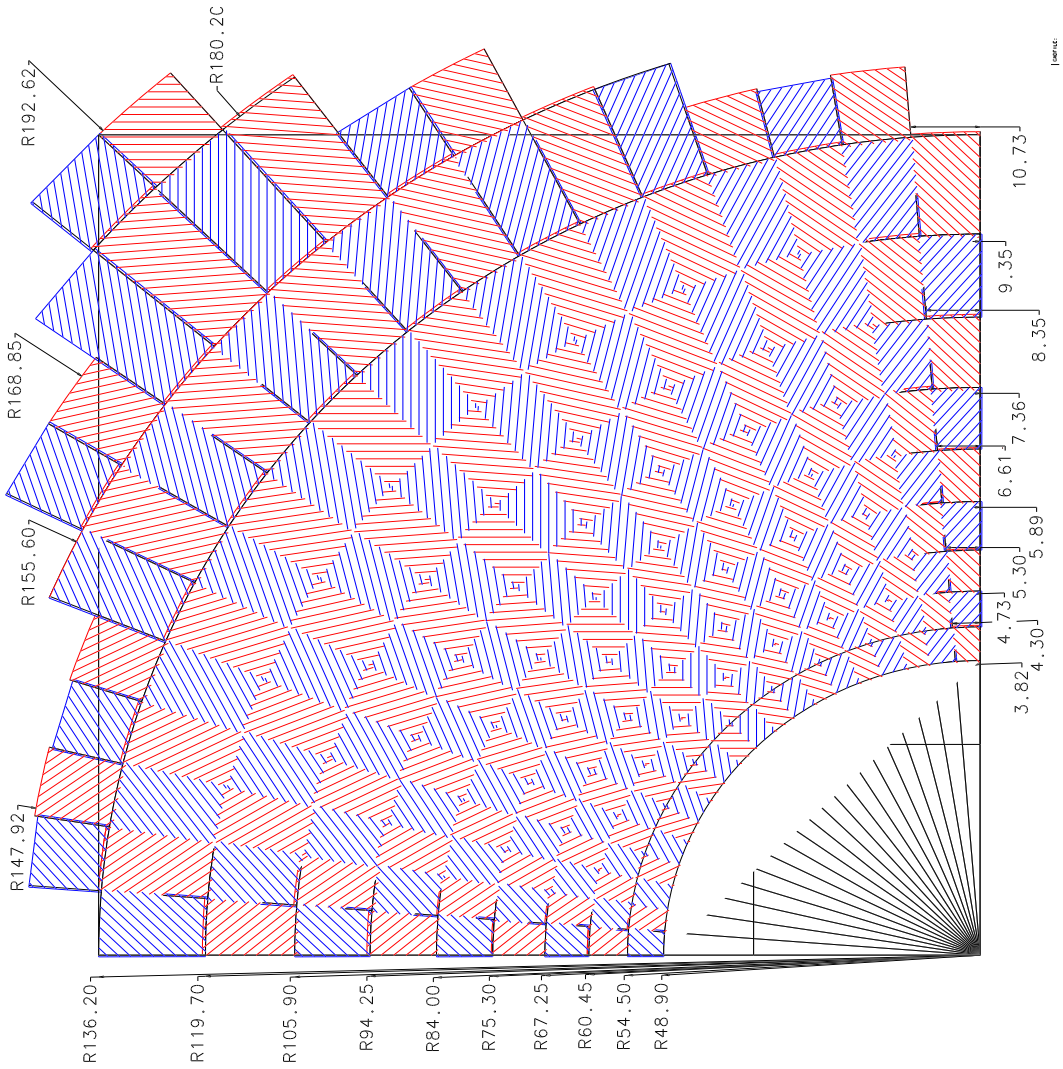

Figure 3.23. An $r - \phi$ quarter view of the segmentation structure of the FAMUS scintillator pixel counters. Adopted from [21]

The muon trigger scintillation counters [36] are mounted inside (layer A) and outside (layers B and C) of the toroidal magnet, on top of the MDTs (Figure 3.23). These are single planes of scintillator, called the pixel counters. Again, each plane is divided into eight octants with each octant consisting of 96 tiles of scintillator. The pixel counters have a ϕ segmentation of 4.5° with η segmentation varying between 0.12 (for the outer 9 rows) and 0.07 (for the inner 3 rows). The largest counters, outer counters in the C layer, are 60×110 cm^2. Similarly to WAMUS scintillators, the FAMUS pixel counters are readout with wavelength shifting scintillators and PMTs with operating voltages of 1.8 kV. The efficiency for detecting a particle with the pixel counters reaches 99.9%, and time resolution is less than 1 ns.

3.3.8 Forward Proton Detector

The Forward Proton Detector (FPD) is used to detect protons and antiprotons scattered at very small angles (on the order of 1 mrad), which escape the main DØ detector. During Run I, such diffractive events were tagged using the absence of particles in a region of the detector (a *rapidity gap*). However, data collected by the FPD is far more informative as it provides complete information about kinematics of scattered particles.

The FPD consists of a series of momentum spectrometers that are comprised of accelerator magnets in conjunction with position detectors along the beam line. The position detectors operate a few millimeters away from the beam and have to be moved out of the beam pipe during injection of p or $\overline{p}$ into the accelerator. The position detectors are housed in special stainless steel containers, called Roman pots [37]. This allows for them to function outside of the highly vacuumed accelerator pipe, but close to the beam. The scattered protons or antiprotons traverse through a thin steel window at the entrance and exit of each pot. The Roman pots

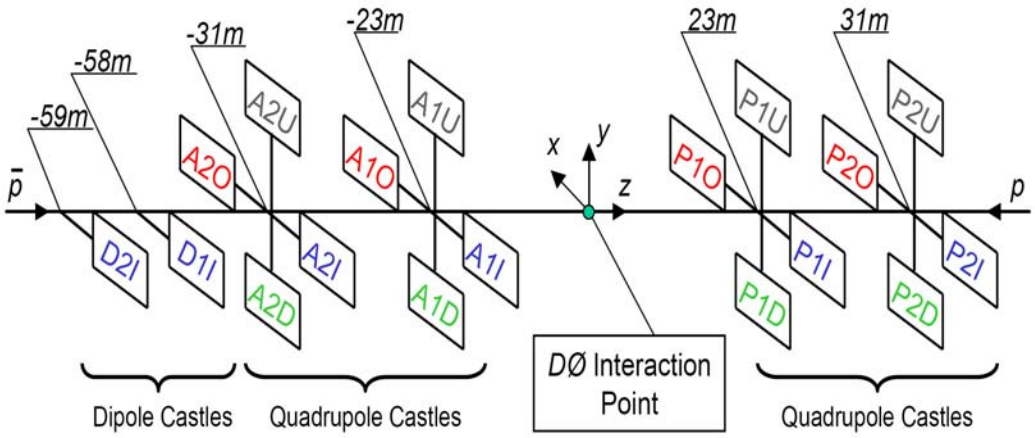

Figure 3.24. The FPD layout. Quadrupole castles are designated with a leading P or A when placed on the p side or the $\overline{p}$ side, respectively. The number designates the Roman pot location. The final letter indicates pot potition (U for up, D down, I inside, O outside). *D1I* and *D2I* are dipole castles.

are remotely controlled and can be moved closer to the beam during stable running conditions.

There are eighteen Roman pots in total, arranged in six castles. The castles are located at various distances from the DØ interaction point. Their locations are determined so that the castles do not interfere with the accelerator devices. The arrangement of the FPD detector subsystem is shown in Figure 3.24. Four of the castles are located behind the quadrupole magnets on each side of the collision point: two on the proton beam side (*P1* and *P2*) and two on the antiproton beam side (*A1* and *A2*). Each of these quadrupole castles contains four Roman pots arranged to practically surround the beam. Two castles (*D1* and *D2*) are located on the outgoing $\overline{p}$ side after the dipole magnet. Each of these dipole castles contains only one Roman pot.

Each position detector located within the Roman pot is made of 0.8-mm-thick

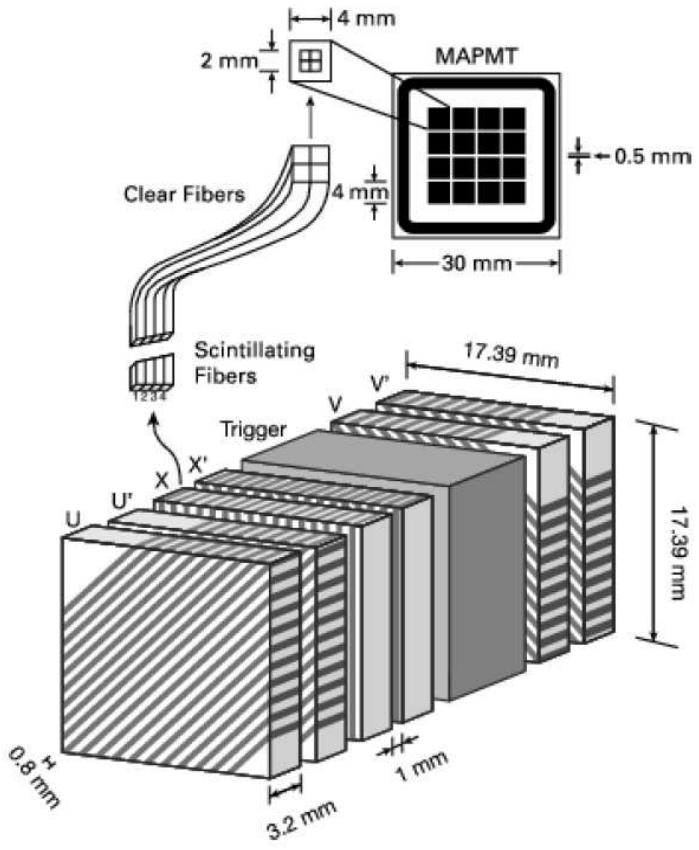

Figure 3.25. FPD Position detector fibers and the MAPMT.

double-clad square scintillating fibers bundled in groups of four to form scintillating structures measuring 0.8×3.2 mm. One end of the detector element is covered by a 3 mm thick aluminum/mylar foil to increase the light yield. The other end of each scintillating fiber is spliced to a double-layered clear fiber of square cross section with the same dimensions. The use of square fibers gives an increase of about 20% in light output compared to round fibers. The scattered p or $\overline{p}$ goes through 3.2 mm of scintillating material. The four clear fibers deliver the light of each detector element to a single channel of the 16-channel multi-anode photomultiplier (MAPMT), each yielding in average about ten photoelectrons.

A position detector (Figure 3.25) consists of six planes in three directions (u, x

and v). Each view is made of two planes ($u - u'$, $x - x'$, and $v - v'$). The primed layers have an offset by two-thirds of a fiber width with respect to the unprimed layers. The u and v planes are oriented at 45° angle with respect to the horizontal plane, while the x plane is mounted at 90° angle. There are 20 channels in each layer of the u and v planes and 16 channels in each of the x layers, which gives the grand total of 2016 channels for all eighteen Roman pots. The FPD uses CFT electronics for the scintillating fiber signal read out, luminosity monitor electronics (Section 3.3.9) for the trigger read out, and the muon LED system for calibration. A much more detailed description of the FPD detector is provided in [37].

3.3.9 The Luminosity Monitor

The DØ detector overview within this dissertation's context concludes with the description of the luminosity monitors. The luminosity monitors are designed to assess the integrated luminosity [38]. Two symmetrical luminosity monitors (shown in Figure 3.26 (a)) are located perpendicularly to the beam pipe at $z = \pm 135$ cm from the DØ coordinate origin. The detectors cover a region in pseudorapidity of $2.7 < |\eta| < 4.4$. During inelastic $p\overline{p}$ collisions, showers of particles nearly collinear with the beam axis are produced. The luminosity monitors can detect them, and based on that data, an assessment of the current luminosity can be made.

The monitors are constructed of wedges made of scintillator, with photo multiplier tubes attached to them. The general view and arrangement of the luminosity monitors is shown in Figure 3.26 (a,b).

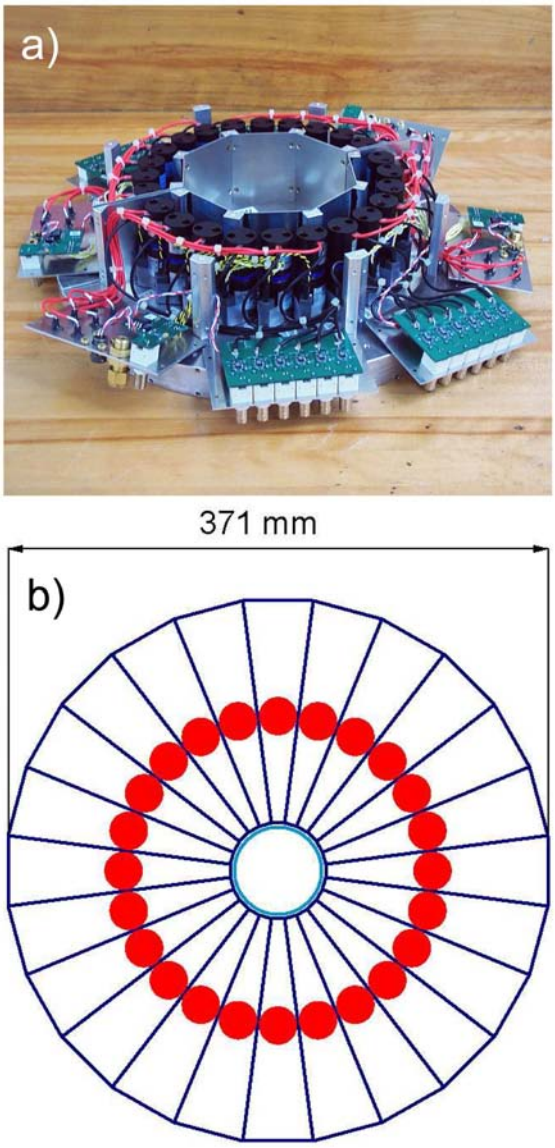

Figure 3.26. The general view (a) and wedges arrangement (b) of the luminosity monitors.

CHAPTER 4

DØ TRIGGER SYSTEM

The Tevatron provides a very high rate of collisions at DØ, but in a million of events there are only a handful of physics interest. Among those are, for instance, events in which a W or Z boson or even a top quark are produced. Even a smaller fraction of interesting events is expected in searches for Higgs and other new phenomena. The majority of events coming from $p\overline{p}$ collisions are due to low-$p_\perp$ non-diffractive $p\overline{p}$ scattering and parton scattering. These kinds of processes have been comprehensively studied in many previous experiments, being therefore of little interest at DØ [32]. Events containing particle jets are the central topic of this analysis, and the way of identifying these events is of outmost importance in this context. While the triggering system is an integral part of the detector, it deserves a more detailed discussion initiated in this chapter.

The frequency of beam crossings at the DØ detector is about 2.5 MHz. At the design luminosity of 2.1×10^{32} cm^{-2}s^{-1}, this results in approximately 6 overlapping events per beam crossing. This event rate, combined with the average event size of 300 kilobytes, results in data flow of more than 500 gigabytes per second. This amount of data is much greater than what is technically possible to write to tape or analyze. Therefore a dedicated system of filters, called triggers, is needed to keep interesting physics events and reject background events. Three levels of triggers have been designed to reach this goal:

- Level 1: A pipelined hardware stage using signals from CFT fibers, preshower detectors, calorimetry and the muon system to reduce the 2.5 MHz input rate to about 2 kHz (with maximum designed output rate of 10 kHz);

- Level 2: A second hardware stage refining and combining the Level 1 output with multiple preprocessors and a global processor to reduce the 2 kHz rate to an output rate of about 1 kHz;

- Level 3: Partial event reconstruction using sophisticated software algorithms running on multiple microprocessors, delivering a final event rate of 50 Hz to tape.

With each progressive trigger level, the trigger system is examining fewer events with growing attention to detail and with increasing complexity, which is reflected by decreased output rates at each of the three trigger levels (Figure 4.1). These trigger levels are explained in more detail below. Special emphasis is placed on the Level 1 jet triggers, since those triggers have been used to select the data for this analysis. The Level 2 and Level 3 trigger systems are discussed in a more general fashion.

4.1 Level 1 Trigger

The Level 1 trigger is a hardware based system filtering the 2.5 MHz trigger rate to an output rate of about 2 kHz as input to Level 2, with minimal dead time. The time available for the Level 1 trigger decision is 4.2 μs. The system consists of a number of hardware components [40]:

- Trigger Subsystems;
- Trigger Managers;

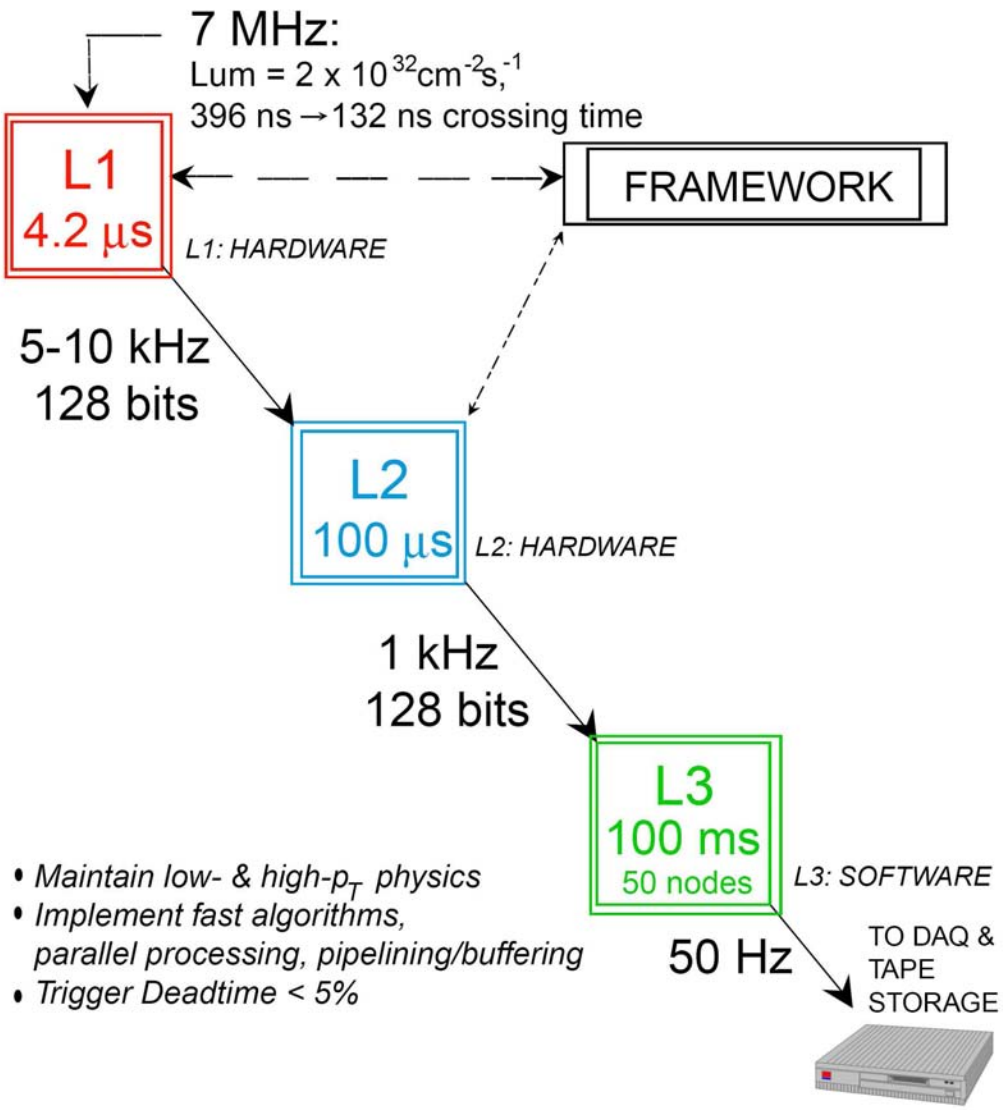

Figure 4.1. The DØ trigger layout and typical trigger rates. Adapted from [39].

• Trigger Framework.

The Level 1 trigger is implemented with hardware devices called Field Programmable Gate Arrays (FPGAs), embedded on electronics boards, in which the trigger logic is implemented. Each of the Trigger Subsystems processes the data for each of the subsystems of the DØ detector. The calorimeter trigger (L1CAL) looks for energy deposition patterns exceeding programmed limits on transverse energy deposits. The central track trigger (L1CTT), comprising preshowers and CFT, and the muon system trigger (L1Muon) compare tracks, separately and together, to see if they exceed preset thresholds in transverse momentum. The L1 forward proton detector trigger (L1FPD) is used to select events produced by diffraction: it triggers on p or $\overline{p}$ scattered at very small angles. Schematic overview of trigger levels 1 and 2 is shown in Figure 4.2).

The Trigger Subsystem reports the physics results to a subsystem-specific Trigger Manager. This Trigger Manager evaluates these results, and produces And-Or Input Terms which are sent to the Trigger Framework. These input terms are flags which represent information about the event. This can be physics information such as a found muon, but it can also be beam indicator signals, cosmic background vetoes or any information about the event that is required for a Level 1 Trigger decision. The entire trigger system contains a maximum of 256 of these And-Or Input Terms, which are combined in And-Or combinations in the Trigger Framework (e.g. a found muon in the muon Trigger Subsystem with a matching track in the L1CTT Trigger Subsystem). For every beam crossing, the Trigger Framework can evaluate 128 of these And-Or combinations.

When at least one of these 128 combinations is positive, and the DAQ system is ready for acquisition of data, the Level 1 Trigger Framework issues an accept, and the event data is digitized and moved into a series of 16 event buffers to await a

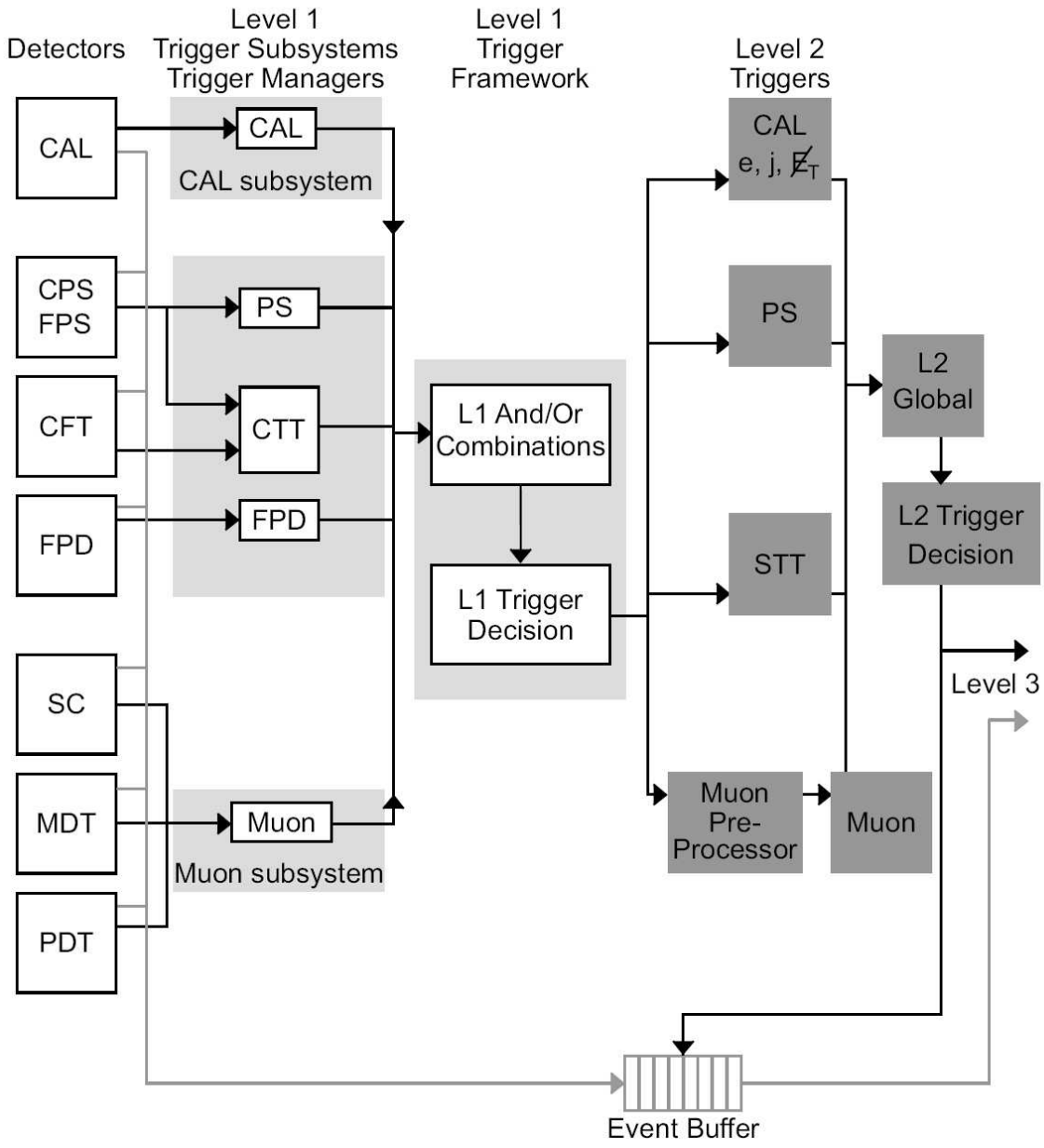

Figure 4.2. Level 1 and Level 2 trigger system overview. The abbreviations are explained in Chapter 3 and in the text.

Level 2 trigger decision. Each of the Trigger Subsystems is discussed in more detail in the following sections.

4.1.1 Central Track Trigger

The Level 1 Central Track Trigger (L1CTT) produces Level 1 acceptance decisions otherwise known as *trigger terms*. It uses the information from the following detector elements [27]:

- Axial fibers of the Central Fiber Tracker;
- Axial strips of the Central Preshower;
- Forward Preshowers strips;
- Forward Proton Detectors.

At Level 1, no information is available from the CFT stereo fibers and the CPS stereo strips. The trigger is split into a central part, using the Central Fiber Tracker and the Central Preshower, and a forward part, consisting of the Forward Preshower strips and the Forward Proton Detectors.

The central trigger is divided in 80 sectors in ϕ. For each of these sectors, the central trigger determines the number of tracks per $p_\perp$ interval, as well as the number of fibers hit. There are four $p_\perp$ intervals available:

- 1.5 - 3 GeV/c;
- 3 - 5 GeV/c;
- 5 - 11 GeV/c;
- 11 - 1000 GeV/c.

In addition, the trigger also reports the number of tracks that have been successfully matched with a cluster in the central preshower. The tracks found are reported to the Trigger Manager, the Level 1 Muon Trigger and Level 2 preprocessors. A typical Level 1 trigger that uses a CTT term will fire on the presence of a track that matches

with a muon object, on a single high $p_\perp$ track or multiple low $p_\perp$ tracks. At the time the data set under consideration for this analysis was taken, the CTT was partially inactive.

The forward trigger combines clusters in the backward u- and v-layers of the FPS with hits in the forward layer of the FPS to tag the clusters as electron- or photon-like. The number of electron and photon candidates per quadrant is reported to the L1FPS Trigger Manager. In each of the FPS detectors, track segments are reconstructed and matched to form tracks [22]. The number of tracks found is reported to the L1FPS Trigger Manager. Typically, a L1FPS trigger will require one or two diagonally opposed tracks found in the FPS detectors in combination with one or two trigger towers found by the calorimeter trigger.

4.1.2 Forward Proton Detector Trigger

The FPD trigger manager selects events in which the outgoing beam particles pass through one or a combination of the nine FPD spectrometers. Three FPGAs containing between 600,000 and 1.5 million gates store generated L1 hit patterns for these spectrometers. L1FPD Trigger Manager searches for coincidences between the discriminated hit signals of both position detectors of any of the FPD spectrometers to trigger on events in which both outgoing beam particles leave the interaction region intact in back-to-back configurations (elastic diffractive triggers) and in the larger set of other two-spectrometer configurations (double pomeron triggers) [41]. To reduce the contribution from beam halo particles that can accidentally produce a trigger signal, events with large hit multiplicities are rejected. The FPD information can be combined with timing information from the FPD scintillator photomultiplier tubes, veto counters, and the Luminosity Monitor.

4.1.3 Calorimeter Trigger

The Calorimeter Trigger inputs consist of electromagnetic (EM) and hadronic (HC) trigger tower energies made up from sums of energies in depth and transverse segments. The calorimeter is divided in 1280 projective towers, with 32 divisions in ϕ and 40 in η, resulting in a segmentation of 0.2×0.2 in (η, ϕ) for each tower [22]. In depth, these towers are divided in three sections: an inner electromagnetic section, followed by a hadronic section and a coarse hadronic section [42]. The electromagnetic section is divided in 7 segments in depth, while the hadronic section is divided in 3 segments with some variation depending on the position of the tower. Only the EM and HC sections are used for the Level 1 trigger decision since the coarse hadronic section typically generates too much noise at Level 1 [43]. The inputs for the trigger are the transverse energies deposited in each of the 1280 electromagnetic and 1280 hadronic sections. These transverse energies are combined in the trigger manager into quantities, which are then compared to various trigger criteria to pass or reject the event. Typically the trigger criteria require one or more towers with an energy higher than a certain threshold energy (generally 3, 5, or 7 GeV per tower).

The trigger towers are small relative to the size of jets, thus some of the partial $E_\perp$ sums are required to calculate $\not\!\!E_T$ to trigger on jets. It is convenient to use sums covering 4×8 trigger towers in (η, ϕ). For generating trigger bits for EM and HC large tiles combined, four reference sets are available with two count thresholds for each set.

4.1.4 Muon Trigger

The Level 1 muon trigger looks for patterns consistent with muons using hits from muon wire chambers, muon scintillation counters, and additional information about tracks from the L1CTT. The FPGAs are utilized to process various hit combinations

on roughly 60,000 muon channels and up to 480 tracks from L1CTT for every bunch crossing. The detector information is used in two different trigger algorithms to detect muon tracks. The first combines tracks that are found by the L1CTT with hits in the scintillators of the muon system. The segmentation of the scintillators matches the segmentation of the CTT in ϕ, and tracks that are found in a ϕ slice of the CFT are matched with hits in the scintillators in the same ϕ slice. A timing gate of 25 ns is used in the scintillators to reject background hits, while a 50 ns timing gate defines cosmic ray veto hits. In the central system, high $p_\perp$ CFT tracks are matched with an A-layer scintillator hit, as well as with a B- or C-layer scintillator hit, since these tracks penetrate the iron core of the magnet between the A- and the B- and C-layers. In the forward system, all three planes of scintillating counters are used to match the CTT track with scintillator hits.

The other algorithm uses a binary readout (i.e. no drift time information, but solely hit/no-hit information) of the wires to find combinations of hits in different planes, compatible with a straight line track (centroids), and verifies these with matching hits in the scintillating counters. In the central system, the timing information of the scintillating counter hit is needed because the maximum drift time in the PDTs (500 ns) is greater than the bunch crossing time (396 ns). This is not needed in the forward system, where the maximum drift time is 60 ns. A low $p_\perp$ trigger is defined using only centroids found in the A-layer, while a high $p_\perp$ trigger is defined using correlations between centroids found in the A-layer and the B- or C-layer. For both algorithms, four $p_\perp$ thresholds (2, 4, 7 and 11 GeV/c) are defined.

The information for each octant in each region is combined in the muon Trigger Manager, which produces global muon trigger information. The muon trigger manager makes a trigger decision based on the $p_\perp$ threshold (2, 4, 7 and 11 GeV/c), pseudorapidity region ($|\eta| < 1.0,\ |\eta| < 1.5$ and $|\eta| < 2$), quality and multiplicity

information. This trigger decision is sent to the Level 1 Trigger Framework where it is included in the global physics trigger decision. Depending on the trigger list, the trigger will fire on a single high $p_\perp$ muon, multiple low $p_\perp$ muons, or muons in association with other physics objects (jets, electrons etc.). In case of an accept, the Level 1 Muon Trigger reports the results to the Level 2 Muon Trigger, and on a Level 2 Accept, to the Level 3 Muon Trigger.

4.2 Level 2 Trigger

The Level 2 trigger provides preprocessing engines specific to individual subdetectors, and a global stage to search for correlations in physics signatures across all of the detector subsystems. The L2 trigger system was designed to handle input rates as high as 10 kHz with a maximum acceptance rate of 1 kHz for the input to Level 3. The Level 2 trigger was originally running on 500 MHz Alpha processors residing in Versa Module Europa (VME) standard crates. Early in Run II these processors were replaced by so-called L2βeta processor cards. The L2βeta processors are composed of commercially produced Single Board Computers (SBCs) mounted on VME adapter cards. Each SBC provides dual 1 GHz Pentium processors. The SBC connects to the adapter via a 64-bit, 33/66 MHz PCI bridge. Each VME adapter card, controlled by the SBC, implements all DØ-specific protocols for custom-built Magic Bus interfaces which provide data transfer rates up to 320Mb/s. The L2βeta processors run GNU/Linux operating system, and all of the processing software is written in C++. Events processed and passed by the Level 2 trigger system are tagged for complete readout and further analysis by the Level 3 trigger.

There are two distinct stages in Level 2 trigger: a preprocessor stage, which processes data from each of the Level 1 triggers for use in the second stage, which is a global processor that combines this data to make a trigger decision (L2Global).

There is a one-to-one correspondence between mapping of Level 1 trigger bits and Level 2 trigger bits (see figure 4.2). The subsystems work in parallel, and trigger decisions are made in the L2Global stage based on physics objects reconstructed by the preprocessors. There are preprocessors for the following subsystems:

- Central tracker;
- Preshower detectors;
- Calorimeter;
- Muon tracker.

For each subsystem, the Level 1 information is collected and transformed into physical objects like hits, clusters and tracks. These individual preprocessors will be briefly discussed below. The maximum time budget for preprocessing is about 50 μs. After the physical objects are formed, they are transmitted to L2Global processor. The global processor correlates the information from the different detector systems to make physics objects like jets, electrons and muons, and produces a trigger decision in less than 75 μs. The total deadtime introduced by the Level 2 trigger system is 5%.

4.2.1 Silicon Track Preprocessor

The Silicon Track Preprocessor (L2STT) performs online pattern recognition in the data from the SMT. It reconstructs charged particle tracks found in the CFT at Level 1 with increased precision by utilizing the much finer spatial resolution of the SMT. The L2STT improves the momentum measurement of charged particle tracks at this trigger level. Requiring hits in the SMT helps to reject Level 1 triggers caused by accidental track patterns in the CFT. The primary purpose of the L2STT is to measure the impact parameter of tracks with high precision in order to tag the decays of long-lived particles such as B hadrons.

4.2.2 Central Track Preprocessor

The Central Tracker preprocessor (L2CTT) collects the tracks found by the Level 1 CTT trigger and creates Level 2 tracks [45, 46]. It performs the following tasks for each track:

- It converts the Level 1 binned $p_\perp$ information into a real $p_\perp$ value;
- Using the ϕ position at the innermost CFT layer and the measured $p_\perp$, the ϕ direction at the vertex is calculated;
- Using the above, the ϕ direction at the third layer of the electromagnetic calorimeter is calculated;
- The isolation of the track is measured.

The tracks are then ordered in $p_\perp$ and sent to the L2Global processor. The tracks are maintained in memory for Level 3 readout in case of a positive Level 2 trigger decision.

Another mode of L2CTT operation utilizes input tracks from L2STT which receives its inputs from the L1CTT and SMT barrels. In this mode, input data are provided by the L2STT along with refined L2 track $p_\perp$ values. The separate list of Level 2 tracks sorted by the determined value of the impact parameter is passed to L2Global.

4.2.3 Preshower Preprocessor

Both the central and the forward preshower detectors are designed to provide high electron detection efficiency, $e - \gamma$ separation and high background rejection rate at the trigger level. This is accomplished by providing evidence for early shower development and by refining spatial resolution of clusters or tracks detected in the

calorimeter. At Level 2, the CPS and FPS are treated as separate detectors and their data are preprocessed independently.

At Level 1, the central tracks found by the central track trigger are matched to preshower clusters in η only. The larger time budget at Level 2 allows the preshower preprocessor to improve this match [47]. To accomplish this, it uses the stereo information from the u- and v-layers of the preshower to calculate the global η- and ϕ-positions of the clusters. These clusters can then be matched with the tracks found by the Level 2 Central Track preprocessor and with calorimeter objects found by the calorimeter preprocessor, to identify different physics objects.

Forward tracks are processed with functionality similar to CPS, except for the FPS being the only source of forward tracking information available before the Level 3 trigger.

4.2.4 Calorimeter Preprocessor

The calorimeter preprocessor system identifies jets, electrons and photons, and calculates missing transverse energy $\not\!\!E_T$ in the event for the L2Global processor. The calorimeter preprocessor runs three algorithms in parallel:

- Jet reconstruction;
- Photon and electron reconstruction;
- Calculation of missing transverse energy $\not\!\!E_T$.

As it was discussed in Section 3.3.5, the calorimeter is logically divided in 2560 calorimeter trigger towers. These towers are defined as groups of calorimeter cells with the same η- and ϕ-position, at increasing radial distance from the DØ interaction point [48]. Around the towers that fired the Level 1 calorimeter trigger, 5×5 groups of neighboring towers are clustered. The total $E_\perp$ of all the towers in such a group must pass a minimum $E_\perp$ cut of 2 GeV to be considered a jet candidate.

The $E_\perp$ of the clusters is calculated assuming that the interaction point is at $z = 0$. Jets that pass a minimum $E_\perp$ cut, as defined in the trigger list, are passed to the Level 2 global processor.

The photon and electron reconstruction algorithm processes the electromagnetic towers given by the Level 1 calorimeter trigger and turns them into seed towers with minimum $E_\perp$ above 1 GeV. For each seed tower, it determines which of its nearest four neighbors contains the largest $E_\perp$, and the total electromagnetic and hadronic energy in the seed tower and the nearest neighbor with highest $E_\perp$ is calculated. Based on the total electromagnetic energy, and the ratio of electromagnetic energy compared to hadronic energy, the electromagnetic tower is considered an electromagnetic candidate and passed to the Level 2 global processor.

The missing transverse energy algorithm calculates the vector sum of the $E_\perp$ in individual trigger towers passed to it from the Level 1 calorimeter trigger. and reports it to the Level 2 global processor if it exceeds a certain value. The missing $E_\perp$ algorithm is capable of evaluating the $\not\!\!E_T$ for various minimum tower $E_\perp$s and η ranges.

4.2.5 Muon Preprocessor

The muon preprocessor (L2Muon) uses calibration and refined timing information to improve the quality of the Level 1 muon candidates. It receives the L1Muon output and data from the PDTs, MDTs, and the scintillation counters. The muon candidates contain the track $p_\perp$, η and ϕ coordinates, hit and timing information.

The preprocessing begins with the Level 2 Muon Trigger attempting to detect muon tracks using all the wire hits and scintillator hits of the muon system [22, 48]. It starts with a pattern recognition step in which straight track segments are reconstructed in each layer of the muon detector. The pattern recognition is done by

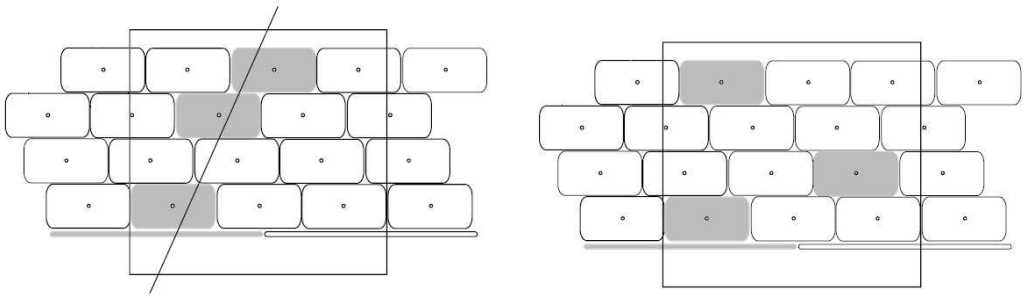

Figure 4.3. The Level 2 muon pattern recognition uses a three-tube wide window to find track segments. The left plot shows a situation in which the trigger fires: three wire hits and a scintillator hit (grey), compatible with possibility of having a straight line track. The plot on the right shows a situation incompatible with a straight line track, which therefore does not pass the trigger.

shifting a 3-tube wide window over all the cells in an octant, looking for wire triplets with a matching scintillator hit (if a scintillator layer is present), as illustrated in Figure 4.3. Combinations of hits are compared with a hit-map to determine which 3-tube combinations are compatible with a straight track segment. This hit-map is created offline using Monte Carlo samples. After this pattern recognition step, found track segments in the A-layer are then combined with track segments found in the band C-layers to form Level 2 objects which contain η, ϕ, and $p_\perp$ information.

The pattern recognition step is implemented in an extra sub-level of preprocessing in the stochastic pipeline sequence. This additional level runs before the actual Level 2 Muon Trigger. This sub-level incorporates 80 Digital Signal Processors (DSPs) running in a parallel scheme, in which each DSP finds track segments in a small region of the muon detector. This way the total execution time of the recognition algorithms is independent of the number of hits. The combination of the track segments into tracks is performed in the Level 2 Muon Preprocessor, which reports the found tracks to the Level 2 global processor. The L2βeta boards use the track segments to construct integrated muon candidates with an associated $p_\perp$

and quality. Upon a Level 2 Accept, the Level 2 muon objects are sent to Level 3 to serve as seeds for a more precise muon track reconstruction [48].

4.3 Level 3 Trigger

The Level 3 system is a software-based, fully programmable trigger characterized by parallel data-paths which transfer data from the detector front-ends to a group of computers called *nodes*. This trigger level reduces the input rate of 1 kHz to an output rate of 50 Hz in an available time of 100 ms. The Level 3 Trigger decisions are based on complete analysis of input physics objects as well as on the relationships between such objects. For instance, the rapidity or azimuthal angle separating physics objects or their invariant mass are among the parameters used to form these relationships.

Upon a Level 2 accept, the data arrives from each of the detector subsystems independently through the data system over the data pathway, and is assembled at the assigned Level 3 processor node. A software program, called the Event Tag Generator, then uses the Level 1 and Level 2 trigger bits to assign the event to a certain event class, for example having a high $p_\perp$ muon, or two jets. The nodes are running high level software algorithms to reconstruct those parts of the event that are interesting for that particular event class, such as electrons, muons and jet candidates, or interesting event topologies. Because of the increased time budget with respect to Level 2, this reconstruction can use information with a higher precision. For instance, drift distances for the wire hits in the muon system can be utilized instead of modest binary information, and calibration constants can be used to improve the quality of the reconstructed physics objects. In addition, the SMT information can be used at this stage to further improve the central track reconstruction. The event is then accepted or rejected, based on this comprehensive

reconstructed information [40].

4.4 Inclusive Jet Triggers

As we have seen, a trigger corresponds to a list of requirements at each level. In certain triggers, one or more levels have no requirement. Every event that is written to tape includes a list of the triggers that fired. Each trigger has a name that reflects its requirements, for example, "JT_45TT" selects events with at least one jet candidate with a transverse momentum in excess of 45 GeV/c, "EM_MX" selects events with high energy photons or electrons (Electromagnetic objects), and "zero_bias" selects events with no requirement other than being in time with a beam crossing. If an event passes a Level 1 requirement, then that trigger's Level 2 requirements are checked, and similarly for Level 3. If an event passes Level 1 because it meets the requirements for something other than a jet trigger, then it will not be checked for jets at levels two or three [31].

Some triggers are prescaled. If a trigger has a prescale value of 15, then only one randomly-selected event in fifteen that passes that trigger is written to tape. This is accomplished by considering only one out of every fifteen events for that trigger at Level 1. In essence, that trigger gets only one fifteenth of the luminosity that an unprescaled trigger gets. Triggers that fire only on rare events are not prescaled (have prescale values set to 1), but triggers that fire often must be prescaled. Prescale values are changed frequently, depending on the instantaneous luminosity in a particular run. When the instantaneous luminosity is low, there are fewer rare events, and so the prescales on more common events can be reduced to keep the rate of events recorded on tape at $\approx$50 Hz. Doing this allows us to never miss rare events, and make the best use of the time when the Tevatron is providing low instantaneous luminosity.

The zero bias trigger is satisfied at every bunch crossing. This trigger is used primarily to study the detector and has an enormous prescale factor to keep its rate to ≈0.5 Hz. The minimum bias trigger is similar to zero bias, but it also requires hits in the luminosity monitors. It too is usually greatly prescaled to achieve a rate of ≈0.5 Hz to tape.

The specific triggers that were used for measuring the inclusive and b-jet cross section are JT_125TT, JT_95TT, JT_65TT, JT_45TT, JT_25TT_NG, and JT_15TT. The "JT" part of their names refers to jets. "TT" means that they are triggered with trigger towers at Level 1 (as described above in 4.1). The number is the transverse energy in GeV required at L3 to fire the trigger. The "NG" in JT_25TT_NG means "no gap" to distinguish it from other 25 GeV jet triggers that require rapidity gaps for studying diffractive physics.

To produce a jet trigger, certain sets of requirements are imposed on every trigger level. For instance, JT_45TT trigger on Level 1 has to satisfy CJT(2,5) requirement, which calls for two calorimeter trigger towers (both EM and hadronic) with $E_{\perp} > 5$ GeV. So in the abbreviation for the Level 1 trigger term CJT(2,5) the first number corresponds to the number of objects required, while the second number provides the threshold value for the simple jet trigger requiring one calorimeter tower.

On Level 2, the trigger term for JT_45TT trigger is *unrestricted*. For this kind of trigger term the trigger framework does the following: it disables the Level 1 accept signal for a pre-programmed time after it has been issued in order to give the Level 1 system time to make a decision. This time delay is fixed. This particular term is included in every Level 1 trigger and reflects the minimum Level 1 trigger inherent dead time of the experiment. This practically means no specific requirements were imposed on trigger Level 2, and the event is passed through after the delay has been invoked.

On Level 3, there are two trigger terms for JT_45TT trigger. The first trigger term passes one out of 400 events entering it at Level 3, marking this event as *unbiased* in the event record. The corresponding trigger bit is set to be true in the event record only if it is set to be true by passing all other filters at this level. Events selected by this rule are likely used for monitoring and/or offline data quality assessment. The next Level 3 requirement is of main importance. It is a jet filter requiring at least one jet with $E_{\perp} > 45$ GeV found using a simple cone algorithm with supplied parameters. This term invokes several algorithms called *tools*. Different tools perform individually specialized tasks such as unpacking raw data, locating hits, forming clusters, applying calibration, and reconstructing electrons, muons, taus, jets, vertices, and $E_{\perp}$. The particular tools running in case of JT_45TT trigger at Level 3 unpack raw calorimeter information, assume the primary interaction vertex to be at the center of the coordinate system, and run a simple cone algorithm with $\Delta R = 0.7$ and minimum $E_{\perp} = 0.5$ GeV. Jet reconstruction algorithms will be discussed in more detail in Chapter 5.

Analogously to JT_45TT trigger, JT_125TT, JT_95TT, JT_65TT, JT_25TT_NG, and JT_15TT triggers are defined. These are the jet triggers that were used in this analysis, and will be referred to in Chapter 7.

CHAPTER 5

JETS AT DØ

The events that pass all three levels of trigger criteria are reconstructed offline by the DØ event reconstruction package, *d0reco*. This program uses an object-oriented approach to reconstruct events by identifying various physics objects in each sub-detector separately. Over the course of data collection, several versions of d0reco were used. Data which was processed with older versions of the program were brought to correspondence with the latest version available ($fixed$). Further discussion of data processing is given in Section 7.1. The reconstruction of jets is of interest in this analysis, and is discussed in detail in this chapter.

At the Tevatron, final state partons produced in hard collisions between protons and anti-protons hadronize into collimated streams of particles that are defined as jets. Particles in jets deposit their energies in the calorimeter cells. Jet events are easy to identify just by looking at the overall topology of these energy depositions. In jet reconstruction, inclusion of particles close to the edges of jets would be an issue without well-defined criteria imposed. For this reason jet identifying algorithms were created to search for jets in every event and to reconstruct their properties [49, 50].

5.1 Jet Reconstruction Algorithm

At the beginning of Tevatron Run II, the DØ and CDF collaborations jointly developed a jet reconstruction algorithm called the "Improved Legacy Cone Algo-

rithm", or ILCA [51, 52]. This algorithm implements various improvements to the Snowmass algorithm [14]. While setting a common standard in jet reconstruction techniques, this algorithm still had several shortcomings which became apparent as demand for better quality of data reconstruction increased. The original ILCA scheme was further modified independently by the DØ collaboration to better address the most problematic issues. General features and highlights of this modified scheme are briefly described in this chapter. This modified algorithm was used at DØ, and was utilized for jet reconstruction in this analysis.

The jet reconstruction algorithm starts with the clustering of energy depositions in the calorimeter cells (generically called *objects*) into towers, which are then assembled into jets. The general idea is to try to circle all the objects in two-dimensional (y, ϕ) space, which corresponds to cones in three dimensions [53]. An energy deposit is added to a jet if its distance to the jet axis in (y, ϕ) space is less than a cone size R, where R is given by:

$$R = \sqrt{(\Delta y)^2 + (\Delta \phi)^2} \tag{5.1}$$

with $\Delta\phi$ and Δy being the distance of the energy deposit to the jet axis in ϕ and rapidity y, respectively.

The particles are specified by their 4-vectors $\mathbf{p}^i = (E^i, p_x^i, p_y^i, p_z^i)$ with angles (ϕ^i, θ^i) given by the direction from the interaction point with unit vector $\hat{\mathbf{p}}^i = \mathbf{p}^i/E^i$, and rapidity y^i. For a certain geometric center for the cone (y, ϕ) the particles i within the cone obey the relation:

$$i \subset C : \sqrt{(y^i - y^C)^2 + (\phi^i - \phi^C)^2} \leq R. \tag{5.2}$$

The algorithm starts with a trial geometric center (or axis) for a cone in (y, ϕ) space, the energy-weighted centroid is calculated including contributions from all particles within the cone. This new point in (y, ϕ) is then used as the center for

a new trial cone. As the calculation is iterated, the new cone center "flows" until a "stable" solution is found (the angle between the center of the cone and the four-vector comprised from the sum of all objects in the cone is sufficiently small). This solution also must be unique, meaning that it has not been found starting from another seed. Intuitively, these stable cones (and the particles inside) can be identified as jets, $J = C$. To complete the jet finding process we require a recombination scheme. The definitions for the (y, ϕ) direction of the reconstructed jet are defined by means of constructing four-vector-like variables as follows:

$$p_x^i = E_\perp^i \cdot \cos\left(\phi^i\right), \tag{5.3}$$

$$p_y^i = E_\perp^i \cdot \sin\left(\phi^i\right), \tag{5.4}$$

$$p_z^i = E^i \cdot \cos\left(\theta^i\right), \tag{5.5}$$

and with jet energy defined as $E^J = \sum_{i \subset J=C} \sqrt{\left(p_x^i\right)^2 + \left(p_y^i\right)^2 + \left(p_z^i\right)^2 + \left(m^i\right)^2}$, we have:

$$\mathbf{p}^J = (E^J, p^J) = \sum_{i \subset J=C} \left(E^i, p_x^i, p_y^i, p_z^i\right), \tag{5.6}$$

$$\theta^J = \tan^{-1}\left(\frac{\sqrt{\left(p_x^J\right)^2 + \left(p_y^J\right)^2}}{p_z^J}\right). \tag{5.7}$$

The transverse jet momentum $p_\perp^J$ is defined as:

$$p_\perp^J = \sum_{i \subset J=C} p_\perp^i = p_\perp^C. \tag{5.8}$$

Finally, for this particular version of the algorithm, η^J, ϕ^J and y^J are defined as:

$$\eta^J = -\ln\left(\tan\left(\frac{\theta^J}{2}\right)\right), \tag{5.9}$$

$$\phi^J = \tan^{-1}\left(\frac{p_y^J}{p_x^J}\right), \tag{5.10}$$

$$y^J = \frac{1}{2}\ln\left(\frac{E^J + p_z^J}{E^J - p_z^J}\right). \tag{5.11}$$

While η^J variable is a good approximation for massless objects, y^J is used in this algorithm as generalization.

The reconstruction of the jet proceeds in two main stages, clustering and reconstruction of the jet. Having the main principles and key parameters of the algorithm described above, the process of building jets can be schematically outlined as follows.

1. The energy deposits are segmented in towers with a size of 0.1×0.1 in (η_{det}, ϕ_{det}). Towers with $E_\perp < 0.5$ GeV are ignored to reduce the contamination by noisy cells. Then, starting with the tower with the highest transverse energy as a seed, preclusters are formed in a cone of $R_{precluster} = 0.3$ around this seed. Only preclusters with $E_\perp > 1$ GeV are kept, and form *pre-protojets*.

2. Using all preclusters with $E_\perp > 1$ GeV in a cone of size R, where R is the final cone size, the jet direction and energy are estimated by equations (5.6 - 5.11), where i then runs over the preclusters, and *pre-protojets* become *protojets*. If the distance is too large, the new seed is formed and another *pre-protojet* is defined. In this analysis, $R = 0.5$ is used.

3. Around this jet direction, all energy deposits within a cone of size R are accumulated, and the new (y, ϕ) direction of the jet is calculated.

4. Step 3 is repeated until the direction is stable. At this point, a *jet* is reconstructed.

5. In the case that two stable reconstructed jets are separated by more than R but by less than $2R$, a new jet axis is defined at the midpoint of the two stable jets. This new axis is then used as a precluster to possibly reconstruct a jet around it.

6. If two jets share energy in clusters, they are merged if the shared energy is higher than half of the energy of the lowest energy jet. If the shared energy is lower, each of the shared clusters is assigned to the closest jet.

7. Jets with $E_\perp < 8$ GeV are rejected.

5.1.1 Jet Reconstruction Efficiency

According to the outline given above, the jet reconstruction requires a calorimeter tower with $E_\perp > 0.5$ GeV be a starting point from which the jet precluster is formed. This precluster itself is required to have $E_\perp > 1$ GeV. The absence of such a tower with $E_\perp > 0.5$ GeV or precluster with $E_\perp > 1$ GeV will cause the energy that is deposited in the calorimeter not to be assembled into a jet, resulting in an inefficiency. To investigate this possible inefficiency, the distributions of transverse energies of towers and preclusters which are used to serve as seeds to jets are studied. To calculate the inefficiency resulting from not finding the tower, the distribution of the energy of the highest energy tower in the jet cone and at different energy ranges is parameterized using a Gaussian fit F with a logarithmic argument:

$$F = e^{-(x-\mu)^2/\sigma^2}, \; x = \log_{10}(E_\perp) \tag{5.12}$$

with μ the mean of the distribution, σ the width and $E_\perp$ the tower energy. The efficiency to find a 0.5 GeV tower in a particular energy range can then be expressed as the area under this fit above the 0.5 GeV cut, divided by the total area under the fit. This is then equal to the probability for a jet of a given $E_\perp$ to contain a tower above 0.5 GeV. The energy distributions for two jet energy ranges are shown in Figure 5.1, with the Gaussian fit applied. For transverse jet energies below 20 GeV, the 0.5 GeV cut causes some inefficiency. With increasing transverse jet energy, the tower energy distribution shifts up, and the cut does not cause any inefficiency. For

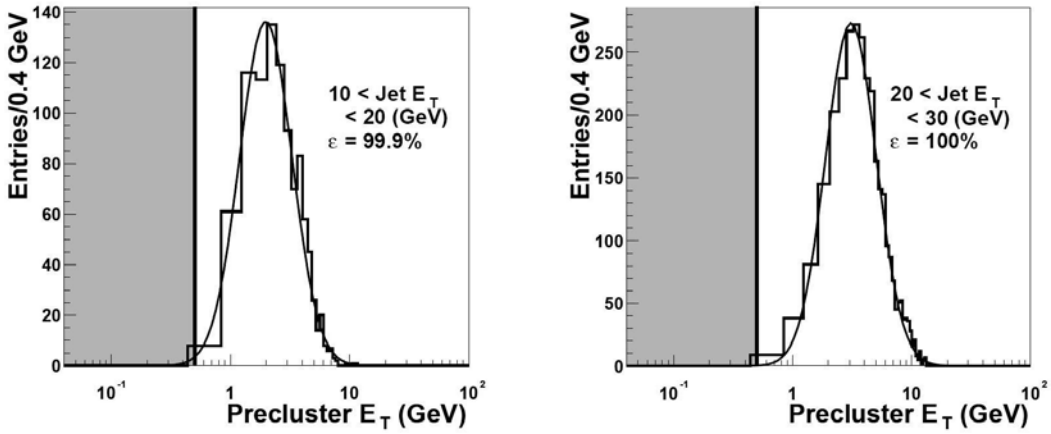

Figure 5.1. Tower transverse energy distributions for jet transverse energies between 10 and 20 GeV (left) and between 20 and 30 GeV (right). The vertical line represents the 0.5 GeV cut on the tower transverse energy, as it is used in the reconstruction algorithm. Adapted from [40].

the jets under consideration in this analysis ($E_\perp > 20$ GeV), this yields a 100% efficiency [40].

The inefficiency resulting from not finding a precluster with $E_\perp > 1$ GeV is found in a similar manner. The distribution of the precluster energy shifts up with increasing jet transverse energy, also yielding an efficiency close to 100% for jets above 20 GeV. Jets in the Monte Carlo simulation show a similar behavior as jets in the data, reaching full efficiency for jets above 20 GeV.

5.1.2 Jet Energy Scale

As the algorithm above permits, reconstructed jets can contain different kinds of particles. Most commonly jets consist of photons, pions, kaons, (anti-)protons, and neutrons, for each of which the calorimeter response is different. Moreover, there can be energy deposited in the calorimeter by products of spectator interactions (additional parton-parton interactions in the same $p\overline{p}$ event), multiple perturbative interactions, electronic noise, and noise due to radioactive decay of the calorimeter

material, uranium. In addition, not all particles in a jet always deposit their energy within the cone defined by the algorithm. All these effects can lead to discrepancies in the measured jet energy, for which a correction must be applied [13].

The particle-level jet energy E_{ptcl} can be obtained from the measured jet energy E_{det} by using the following relation [54]:

$$E_{ptcl} = \frac{E_{det} - E_{offset}}{R_{jet} \times R_{cone}} \tag{5.13}$$

where the calorimeter response is denoted as R_{jet}, which includes the ratio of observed signal to incident energy, and takes into account any variations due to any non-linear effects, dead or hot channels, uninstrumented areas of the detector and so on. R_{cone} is the fraction of particle jet energy contained within the algorithm cone, which compensates for the effects of physical showering in the detector and accounts for the fact that some of the energy inside the detector cone may have come from the outside, and vice versa. E_{offset} is a certain energy offset which includes bias coming from multiple interactions, underlying event energy, electronic noise, uranium noise, and pile-up effects from previous bunch crossings.

These three parameters generally depend on the jet energy and its position inside the detector, and constitute the Jet Energy Scale correction (JES). The JES parameterization for this analysis has been determined via methods relying only on the jet energy, luminosity and η_{det}, and are described in detail in [54, 55, 56]. In addition, correction factors needed for heavy flavor jets containing muon and neutrino from semileptonic decays are required. Below are outlined the results and general strategies used to determine the Jet Energy Scale corrections utilized in this analysis.

Figure 5.2 shows the energy scale corrections (E_{ptcl}/E_{det}) for jets with cone of $R = 0.5$, as well as the uncertainties associated with these corrections.

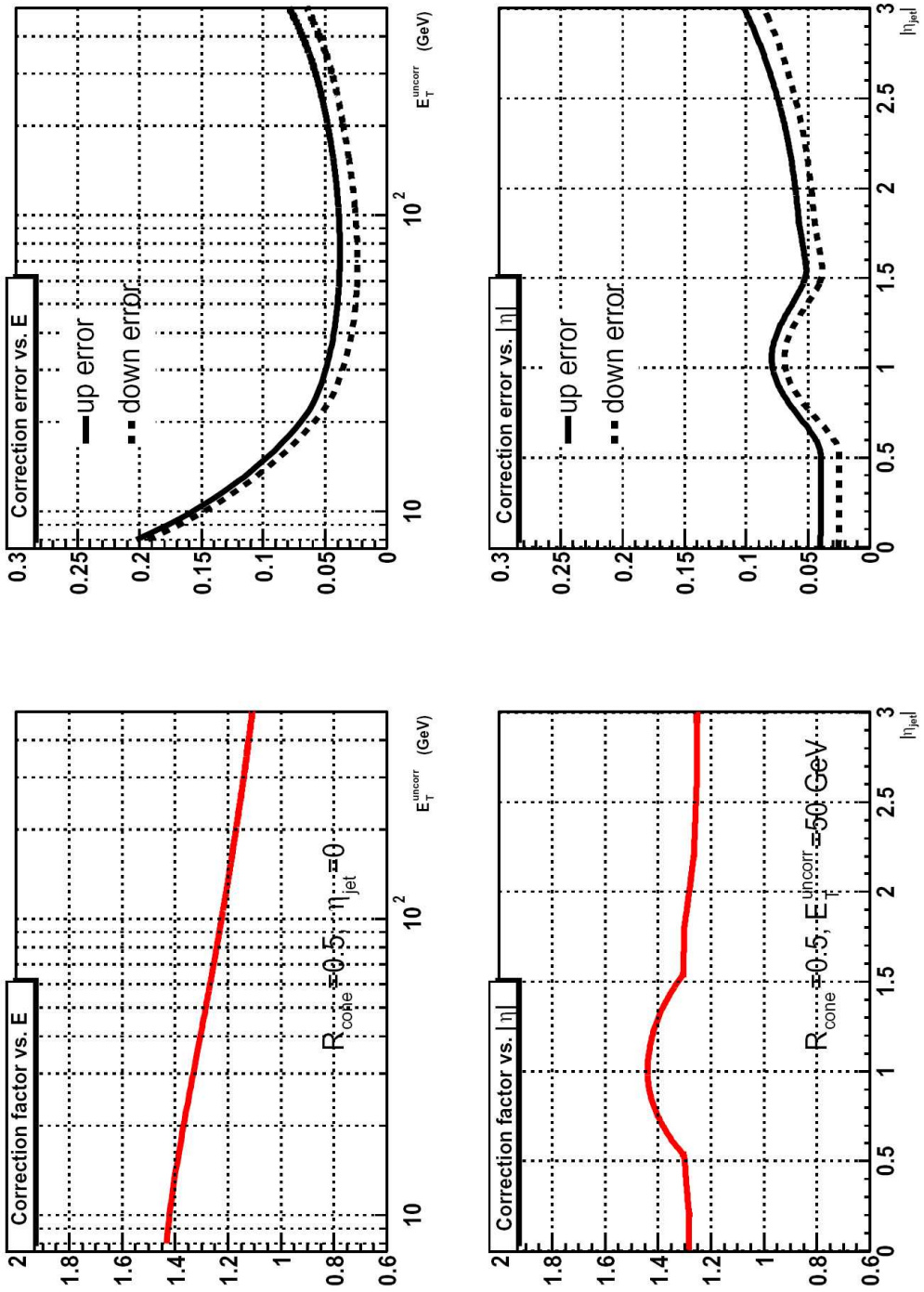

Figure 5.2. The JES (version 5.3) correction factors (E_{ptcl}/E_{det}) and their uncertainties for $R = 0.5$ jets as functions of jet uncorrected energy and pseudorapidity η. Adopted from [54]

To calculate the Jet Energy Scale correction, events containing jets and photons are used. There is no requirement on having just one jet in these events, but $\Delta\phi$ between the photon and jet axes should exceed 2.8 [56]. The energy of a photon can be measured more precisely than the jet energy, since it is mostly contained within one or at most two towers. Electromagnetic showers do not have much event-to-event fluctuation, and typically more than 95% of the energy is contained within four EM calorimeter layers. EM layers are well-calibrated using known masses of the Z° and J/ψ particles via reconstructing their $e^{+}e^{-}$ decays.

Since the energy of a γ can be measured well, the jet energy can then be deduced from the conservation of transverse momentum. Using this technique, the corrections for jets with relatively low momentum (on the order of 10 GeV) is determined. The reason that the statistical error gets very large at high energy is that the range of $p_{\perp}$ accessible by this approach is limited and the rate of jet+γ events drops rapidly with increasing jet $p_{\perp}$.

Some non-(γ+jet) events may be indistinguishable from true γ+jet events, such as single π^0+jet events. This occurs because the main decay of the π° is into two γ's which cannot be resolved by the calorimeter. This means that the energy of neutral pions is measured as well as of photons, and they also can be used to balance $p_{\perp}$ of the jets [54].

The showering correction R_{cone} is found by looking at how the $p_{\perp}$ of a photon is being balanced by the jet's transverse momentum as a function of the jet's radius. The response R_{jet} is determined in a similar fashion except the $p_{\perp}$ balance is expected at a fixed jet's radius. The energy offset E_{offset} is calculated using events that fired a *minimum_bias* trigger. The energy deposited in the calorimeter in these events does not come from a hard scattering processes so it should be subtracted from the jet's energy.

TABLE 5.1

JET QUALITY CUTS SUMMARY

Variable	Cut
Coarse Hadronic Fraction (CHF)	CHF < 0.4
Electromagnetic Fraction (EMF)	$0.05 <$ EMF < 0.95
"Hot" Fraction (HotF)	HotF < 10
Number of towers containing $> 90\%$ jet $E_{\perp}$	n90 > 1
Correlated two-dimensional cut	F90 < 0.5 or CHF < 0.15

In this analysis, the Jet Energy Scale was applied to the data at the reconstruction stage. More detail on the dataset and reconstruction will follow in Section 7.1. The Jet Energy Scale version applied was JES 5.3, and details on it are discussed in [56]. The effect that the Jet Energy Scale correction has on the systematic uncertainty of this analysis is given in Section 8.1.7.

5.2 Jet Quality

As can be seen from the discussion of reconstructing jets given in Section 5.1, the reconstruction algorithm can mistake noise or instrumental and physics backgrounds for jets. To ensure a good quality of reconstructed jets and to remove the fakes, some additional requirements (*jet quality cuts*) are imposed on several variables relevant to jets. A summary of the standard jet quality cuts that were made is given in Table 5.1. Each of the variables on which quality cuts are made as well as the cut values will be discussed below [57].

These jet quality requirements are not specifically tuned for the b-jet cross section analysis described. Indeed, while not optimized and often overridden by a more stringent multivariate Neural Net requirement, these cuts are made because the Jet Energy Scale corrections described in Section 5.1.2 relied on these cuts and we

therefore consistently apply it to the final b-jet cross section. Inefficiencies caused by this combination of cuts will be studied and taken into account while determining the final b-jet cross section measurement.

The **Coarse Hadronic Fraction (CHF)** is the fraction of the jet's uncorrected energy deposited in coarse hadronic layers of the calorimeter. Normally the CHF takes values between zero and one, but occasionally the calorimeter can read out negative values for energy due to noise, detector sparking, or flaws in calibration. Only a very small portion of jet's energy is expected to be found here. If a large fraction occurs, this jet is likely a fake from noise in electronics, and is removed by the CHF < 0.4 requirement.

The **Electromagnetic Fraction (EMF)** is the fraction of jet's energy registered in the electromagnetic layers of the calorimeter. This variable can take on a wide range of values for good and fake jets. If we imagine jets with high content of π^0's which decay predominantly into pairs of γ's, these jets will shower mostly electromagnetically. Some other jets could shower mostly hadronically. Jets with values of EMF that are extremely close to either one or zero are likely to be fakes coming from a few noisy calorimeter cells, or extremely energetic photons or electrons. The EMF cut in this analysis is $0.05 <$ EMF < 0.95.

The **HotF** variable is defined to be the ratio of the uncorrected energy detected by the most energetic cell and the next to most energetic cell. A typical energy distribution in a jet spreads over many cells and no single cell should contain a major part of the energy. This is only likely to happen when there is noise in this cell of the calorimeter. By construction, we expect the ratio of the two most energetic cells to be close to unity. A higher ratio points to the fact that most of the energy of the jet was released in one cell, which suggests that the highest energy cell is probably a noisy, or *hot* cell. The quality cut was HotF < 10.

The **n90** variable is defined as the minimum number of calorimeter towers to contain at least 90% of the jet's uncorrected $E_{\perp}$. If this number is close to one, it suggests that we have an unusual concentration of the energy of the jet within one tower, which in turn is likely a fake jet. If the value of this variable is large, this could mean that the jet consists of a large number of noisy cells with little energy depositions in each one. The probability of the latter case to occur is extremely small, so there is no upper cut on n90 variable is made.

The **Correlated two-dimensional cut** is made on two variables, one of which is CHF described above, and the other one is the F90 variable. The F90 is defined as the fraction of towers which contain at least 90% of the jet's uncorrected $E_{\perp}$ relative to the total number of the jet's towers. On average, about 2% of all found jets are generated from noise in the coarse hadronic layers of the calorimeter. These jets can acquire more energy beyond the hadronic layers through the merging process, and pass the CHF cut. Consequently, if the number F90 is more than a half of all the towers, we have a wide-spread reconstructed jet that is likely a fake. The CHF < 0.15 requirement makes sure that it was not a mostly hadronic jet.

One of the questions of interest for this analysis is the efficiency of these jet quality cuts. All the cuts combined remove around 2% of all jets [57], and the following Neural Net tagging requirement described in the next chapter is usually a far more stringent requirement practically overriding the jet quality cuts. The final efficiency was estimated to be close to unity, and was set as $99\pm1\%$.

5.3 Muons in Jets

In this analysis, muons associated with jets are used to determine the b-tagging efficiency as described in detail in section 7.4.1. In this section, some more general information is given about the muon quality standards used at DØ.

Muons at DØ are reconstructed using both the central tracking (Section 3.3.1) and the muon (Section 3.3.7) systems. Depending on the particulars of these subsystem responses, muons are divided into three quality groups. The type of muon is given by the parameter *nseg*. A positive value of *nseg* indicates that the muon reconstructed in the muon system ("local muon") was matched to a track in the central tracking system. A negative value of *nseg* indicates that the local muon could not be matched to a central track. The absolute value $\mid nseg \mid = 1$, 2, or 3 respectively indicates that the local muon is made up of A-layer only hits, B- or C-layer only hits (outside the toroid), or both A- and B- or C-layers hits. The requirements for each of the three muon quality groups are outlined below [58].

• **Tight Muons**

Only $\mid nseg \mid = 3$ muons can be Tight. A muon is Tight if it has:

- at least two A layer wire hits;

- at least one A layer scintillator hit;

- at least three BC layer wire hits;

- at least one BC layer scintillator hit;

- a converged local fit ($\chi^2_{loc} > 0$).

• $\mid nseg \mid = 3$ **Medium/Loose Muons**

When an $\mid nseg \mid = 3$ muon fails the Tight criteria, it still can be qualified as Medium or Loose, if it has:

- at least two A layer wire hits;

- at least one A layer scintillator hit;

- at least three BC layer wire hits;

- at least one BC layer scintillator hit (except for central muons with less than four BC wire hits).

• An $\mid nseg \mid = 3$ **Loose muon** is defined as a Medium muon but allowing for one

of the above tests to fail, with the A wire and scintillator requirement treated as one test and requiring always at least one scintillator hit.

• $nseg = +2$ **Loose/Medium Muons**

Muons with $\mid nseg \mid < 3$ can only be Loose or Medium if they are matched to a central track. Loose criteria requires:

- at least one BC layer scintillator hit;

- at least two BC layer wire hits.

An $\mid nseg \mid = 2$ muon can be Medium if in addition to the above requirements it is located at the bottom of the detector, where the muon system has less coverage (octants 5 and 6 with $\mid \eta_{det} \mid < 1.6$).

• $nseg = +1$ **Loose/Medium Muons**

Muons with $nseg = +1$ have A segment matched to a central track. An $nseg = +1$ muon is considered Loose if it has:

- at least one scintillator hit;

- at least two A layer wire hits.

An $\mid nseg \mid = 1$ muon can also be Medium if in addition to the above requirements it is located at the bottom of the detector.

A muon is associated with the jet if the reconstructed muon track is collinear with jet axis with maximum separation of 0.5 in (η, ϕ) space, and ΔZ of less than 1.5 cm. In addition, the $p_{\perp}$ of muons was required to exceed 5.0 GeV in order to eliminate punch-through. A more detailed discussion is given in relation to the muon-in-jet cross section analysis in [59].

5.4 Jet Energy Resolution

The transverse jet momentum measured with the detector has an uncertainty associated with it. This uncertainty propagates and affects the measured differential

cross section for b-jet production. In order to be able to take this into account and compensate for these resolution effects in the final result, the jet energy resolution has to be studied.

One widely used way to determine the jet $p_\perp$ resolution is to look at the $p_\perp$ balancing of jets in clean di-jet events. At DØ there are two types of jets (with the 0.5 algorithm cone) useful for this study: so-called JCCB (jets with $\Delta R < 0.5$ cone and no JES corrections applied), and corrJCCB (those 0.5 cone jets with jet quality cuts and only hadronic JES corrections applied). In order to have a di-jet sub-sample, some requirements on events are imposed. The cuts are that two and only two jets exist at both the JCCB and the corrJCCB level. These two jets need to be separated by $\Delta\phi > 2.84$. Both jets need to be central $|y_{jet}| < 0.8$. Then one of the jets is required to be b-tagged with the Neural Net, and the other may have any tagging status. It was important to require two and only two jets at the JCCB level, since what occasionally occurred was that there were three JCCB jets, two normal and balancing and one other jet. One of the leading jets failed the jet quality cuts, giving only two corrJCCB level jets with highly imbalanced $p_\perp$. These occurrences produce a false asymmetry while measuring the jet resolution.

With these di-jet events, the asymmetry variable defined below is calculated in different $(p_{\perp_1} + p_{\perp_2})/2$ bins:

$$A = \frac{|p_{\perp_1} - p_{\perp_2}|}{p_{\perp_1} + p_{\perp_2}} \tag{5.14}$$

The usual jet quality cuts discussed in this chapter were applied to these jets as well. The jet $p_\perp$ resolution is directly related to the asymmetry variable:

$$\frac{\sigma_{p_\perp}}{p_\perp} = \sqrt{2}\sigma_A \tag{5.15}$$

The obtained resolution is then fitted via the following analytical ansatz function:

$$\frac{\sigma_{p_\perp}}{p_\perp} = \sqrt{\frac{N^2}{p_\perp^2} + \frac{S^2}{p_\perp} + C^2} \tag{5.16}$$

The parameters of this fitted function are then used to correct for resolution effects in the final measured cross section in Section 7.5.

When assessing jet resolution for this study, it was decided to use a subset of data with a different and more stringent b-tagging requirement, the presence of a displaced (secondary) vertices in jets. While that was done for technical reasons (the information requited to do this resolution study was not available in the original dataset tagged with the Neural Net), it is not expected to bias the resolution as the cuts on jets with secondary vertices are more stringent.

The procedure for evaluation of jet resolution for jets tagged with a secondary vertex departs slightly from the general method described in the beginning of this section. Upon reconstruction, jets are recorded according to the descending order of their $p_\perp$. The asymmetry variable for this study was constructed similarly to (5.14):

$$A_{2VTX} = 2\,\frac{p_{\perp_1} - p_{\perp_2}}{p_{\perp_1} + p_{\perp_2}}, \tag{5.17}$$

The above asymmetry function of the two leading jets with highest $p_\perp$ values was compared to transverse momentum of the third jet. One of the two leading jets was required to contain a secondary vertex. The topology of the events was preselected by the cut $\Delta\phi_{Jet1,Jet2} > 2.84$ (the two leading jets were opposite to each other). By design, the asymmetry in $p_\perp$ between the two leading jets has to be compensated by $p_\perp$ of the third jet. At the limit $p_{\perp,Jet3} \to 0$ the imbalance of transverse momentum between the two leading jets can be interpreted as due to jet resolution. An example of the above process of determining jet resolution for jets tagged with a secondary vertex is shown by Figure 5.3 (a-c). In case there was two and only two jets in the event, the resolution was represented by the width of the Gaussian describing the asymmetry function (Figure 5.3 (d)).

The results for jet resolution determined in this analysis for jets tagged with a secondary vertex as well as the standard jet resolution determined by the DØ

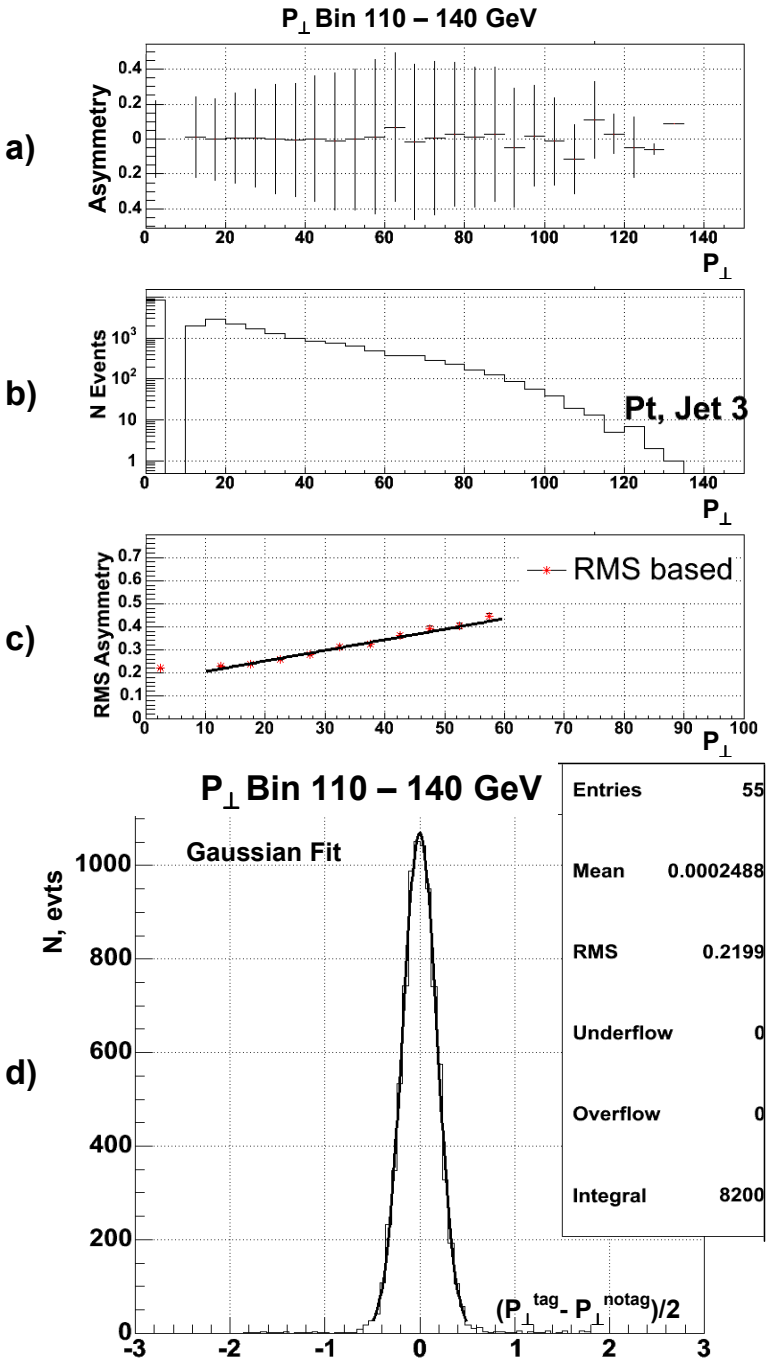

Figure 5.3. The procedure of determining jet resolution for secondary vertex-tagged jets in 100-140 GeV $P_\perp$ bin. a) Asymmetry variable with its RMS. b) The corresponding number of events for each of the asymmetry bins. c) Asymmetry RMS values are projected to the vertical axis to obtain the resolution. d) The resolution for uncorrected jets evaluated by fitting the asymmetry function distribution via the Gaussian.

collaboration [60] are shown in Figure 5.4.

The comparison shows that jet resolution for vertex-tagged jets is in overall in agreement with the standard jet resolution result. The process of evaluating the RMS for the asymmetry variable for one of the experimental points, corresponding to the 100 - 140 GeV bin in $p_\perp$ shown in Figure 5.4, and is explained in more detail by Figure 5.3. In Figure 5.4, the red stars correspond to resolution values obtained by projecting the RMS of the asymmetry variable, and red squares correspond to values described by widths of Gaussian fits when only two jets were present.

Resolution for jets tagged with the Neural Net is not expected to differ from the inclusive jet resolution, so the resolution result should be considered with the study done in [60]. This conventional approach to evaluating jet resolution was described briefly at the beginning of this section by (5.14) - (5.16). As the study of jet resolution for jets tagged with secondary vertex has shown overall agreement with the standard inclusive jet resolution [60], it was decided to use the latter in this analysis.

As the result for the inclusive jet resolution is available for two central rapidity regions, $|y| < 0.4$ and $0.4 < |y| < 0.8$, the average between these two resolution results was used. The jet resolution used in this analysis along with the results for inclusive jets is shown in Figure 5.5.

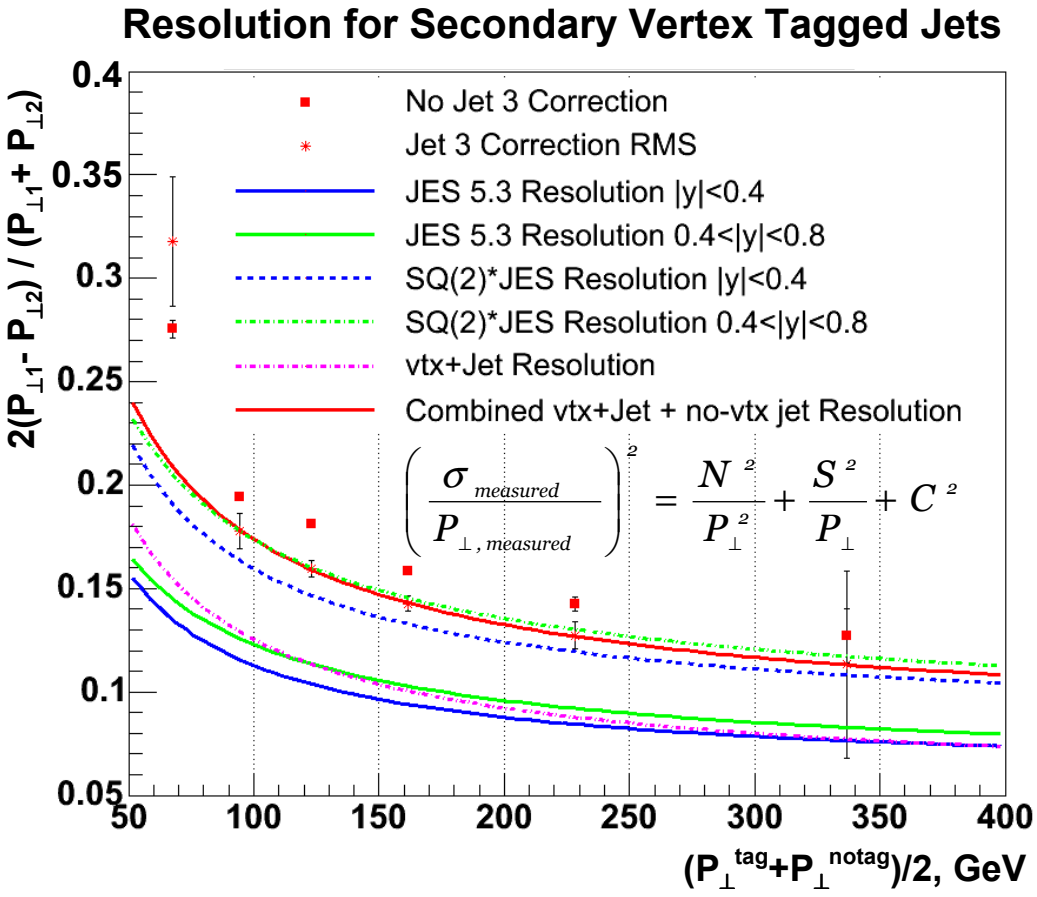

Figure 5.4. Jet resolution determined for jets tagged with a secondary vertex. The leftmost data bin was poorly determined and was excluded from the ansatz fitting. The resulting evaluation for jet resolution in this analysis is represented by the lowest dashed line. Comparison with the standard inclusive jet resolution for $|y| < 0.4$ and $0.4 < |y| < 0.8$ rapidity regions (represented by the two lowest solid lines) can be made.

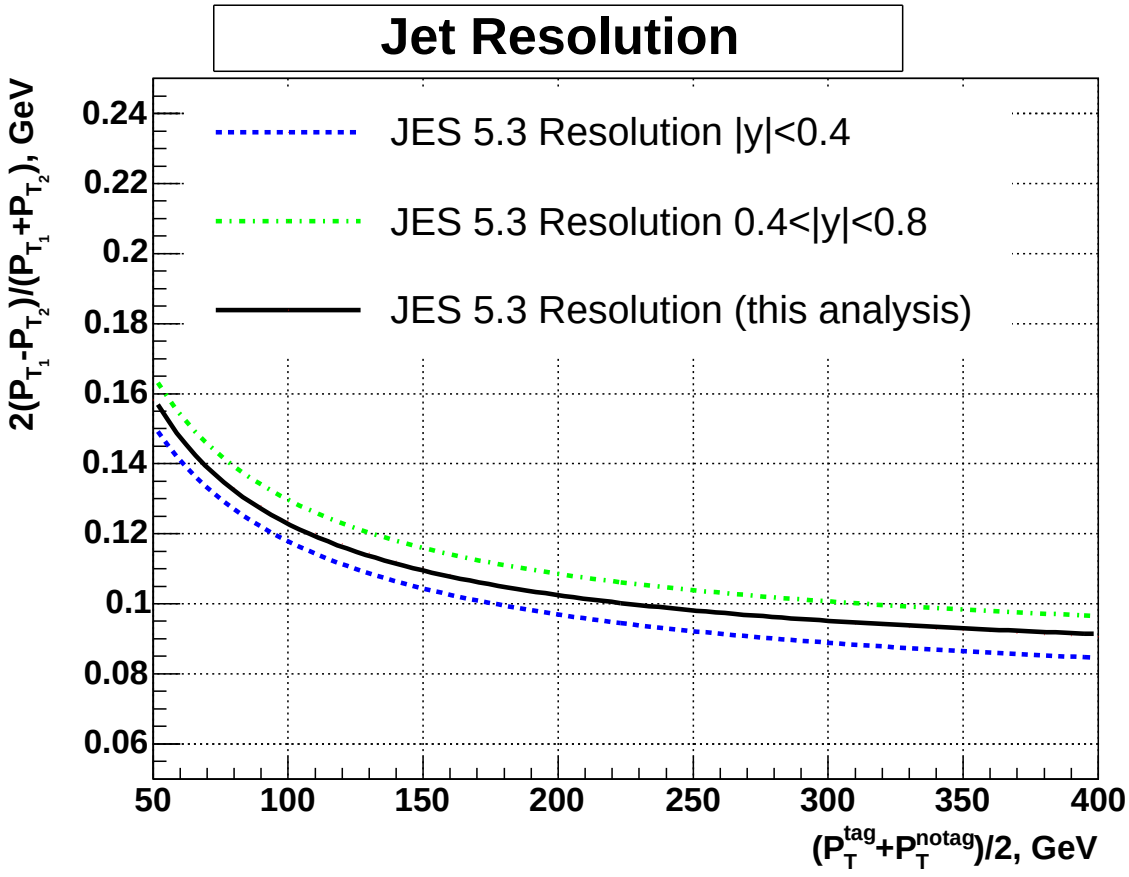

Figure 5.5. Jet resolution used in this analysis (solid black curve), and resolution established in [60] for different pseudorapidity ranges in central $|y|$ region.

CHAPTER 6

b-JET TAGGING

This chapter concentrates on the problem of identifying the flavor content of jets once they are formed. As the final goal of this analysis is to obtain the differential cross section for b-flavored jet production, the flavor identification, or *tagging* task, is most important. There have been a variety of tagging methods developed over the years, but none of these methods targeted the identification of jets with very high transverse momentum. An extensive search was done to address the tagging problem. The method used in this analysis has emerged from a number of methods, and utilizes a Neural Net to help distinguish jets of different quark flavors. These methods are briefly outlined, and the general description of the Neural Net tagging tool [61] and its performance [62] is given.

6.1 Current b-tagging Methods

Heavy flavor identification is a very important experimental task for many analyses, and is absolutely essential for this study. In certain analyses the b-content is an integral part of the process, while in other cases it produces an unwanted background. In general, tagging algorithms exploit certain characteristic signatures associated with the process of interest, and distinguish these processes by identifying traces of these signatures. For instance, b-hadrons have relatively long lifetime and on average travel several millimeters before decaying. These distances are large

enough to resolve a decay vertex from the production vertex by modern-day particle detectors. The presence of a decay vertex in the event suggests the presence of b-hadrons.

There are three main ways to identify a b-flavored jet.

- Explicitly reconstruct secondary b-hadron decay vertices using charged particle tracks.

- Identify charged particle tracks with a non-zero distance of closest approach (also called *impact parameter*) with respect to the primary vertex.

- Identification by the presence of a muon. About 11% of the time, b quarks decay semi-leptonically via the muon channel. Because of the high mass of b quarks, the transverse momenta of such muons relative to the jet axis ($p_{\perp}^{rel}$) will be much larger than a muon from one of the lighter quarks.

There are currently four b-tagging algorithms certified for use at DØ. Three of these methods are based on variations of track-based signatures, while the fourth one utilizes the presence of a muon. The basic principles of these methods are outlined below.

1. Secondary Vertex Tagger (SVT). This tool uses charged particle tracks substantially displaced from the primary vertex to reconstruct a secondary (decay) vertex [63, 64]. A jet is considered to contain a secondary vertex if the latter is located within $\Delta R < 0.5$ distance from the jet axis.

2. Jet Lifetime Probability Tagger (JLIP). This method combines the information from all the tracks seen in Silicon Microstrip Tracker, and based on their impact parameters, calculates the probability of these tracks as

originating from the primary vertex [65]. If this probability is close to zero, this means that it is likely there was a c or a b quark decay and that a secondary vertex distinct from the primary vertex is present. This output variable having discriminating power on b-jets is called the Jet Lifetime Probability.

3. Counting Signed Impact Parameters (CSIP) b-tagging algorithm relies on the fact that tracks produced by charged decay products of long-lived b-hadrons have a non-zero impact parameter with respect to the primary vertex [66]. The sign of the impact parameter is determined by the sign of the impact parameter projection on the jet axis (based on calorimeter information). Impact parameter significance is defined as the impact parameter divided by its uncertainty. The uncertainty comes from individual errors on track parameters returned by the track finding algorithm. A jet is considered to be tagged by CSIP if two or more tracks associated with this jet have signed impact parameter significance greater than 3, or three or more tracks have signed impact parameter significance greater than 2 [67].

4. Soft Lepton Muon Tagging (SLT) uses the identification of a muon within a jet to tag the jet, as most of light-flavored hadrons (and hence jets) do not decay semileptonically, or even do not decay within the detector volume due to their long lifetimes. Thus the requirement of a muon to be associated with the jet is a good signature of presence of b flavor and can be used to tag b jets [68].

Each of these algorithms assesses several variables which contain valuable information on the possibility of the jet to have originated from a b-quark. These tools

have been optimized for the best b-content extraction within their power. Used individually, these variables provide powerful discrimination between light jets and b-jets. However combining the variables using a multi-variant technique has the potential to provide much more discrimination than any of the constituent parts can achieve by itself.

The tagging algorithm used in this analysis is designed to be able to use the discrimination of all methods currently in use at DØ by combining all of the algorithms used to detect the b flavor in the jet by means of a powerful analytical construct called a *Neural Network*.

6.2 Neural Networks

The idea of Neural Networks is rooted in Artificial Intelligence research, one of the key tasks of which is to attempt to reproduce the fault-tolerance and capacity to learn of biological neural systems. Essentially, Neural Networks is an attempt to model the low-level structure and functionality of the brain. To reproduce the processing functions of the brain, neural networks are principally composed of a set of simple processing units called *neurons* with their individual inputs and outputs massively interconnected with *synapses*. Each neuron acts according to a specialized function which can propagate or reject certain types of inputs from and to other neurons. However, the living organism's brain is an extremely complex structure counting on order of 10^{10} neurons and a myriad of interconnections, and it is technically impossible to create such a model. There is a very high level of complexity in the brain that is far beyond the scope of this discussion, but it is fascinating that artificial neural networks can achieve some remarkable results using a model not at all this complex.

In order to replicate the functionality of biological neural systems, an artificial

neuron functions as follows:

- It receives a certain number of inputs coming either from original data source, or from the outputs of other neurons in the neural network. Each input is implemented via a connection that has a strength (or weight). These connections are designed to model synapses, and weights correspond to synaptic capability in a biological neuron. Each neuron also has a single threshold value. The weighted sum of the inputs is formed, and the threshold subtracted, to compose a single characteristic number called *activation* value of the neuron.

- The activation number is passed through an *activation function* (also known as a *transfer function*) to produce the output of the neuron.

A simple network has a *feed-forward* structure: from the inputs, synapses transfer signals forward through *hidden units* (or *hidden nodes*), eventually reaching the output nodes. The response for this kind of structure is very stable. There are numerous implementations of Neural Network algorithms available, for instance the ROOT analysis package based *multilayer perceptron* (MLP). The Neural Network used in this analysis is a simple feed-forward network which consists of a layer of input nodes, one or more layers of hidden nodes, and one layer of output nodes. The input layer is not really neural at all - these units simply serve to introduce the values of the input variables. The hidden and output layer neurons are each connected to all of the units in the preceding layer. Again, it is possible to define networks that are partially-connected to only some units in the preceding layer. However, for most applications, fully-connected networks are better. A graphical schematic of such network is given in Figure 6.1.

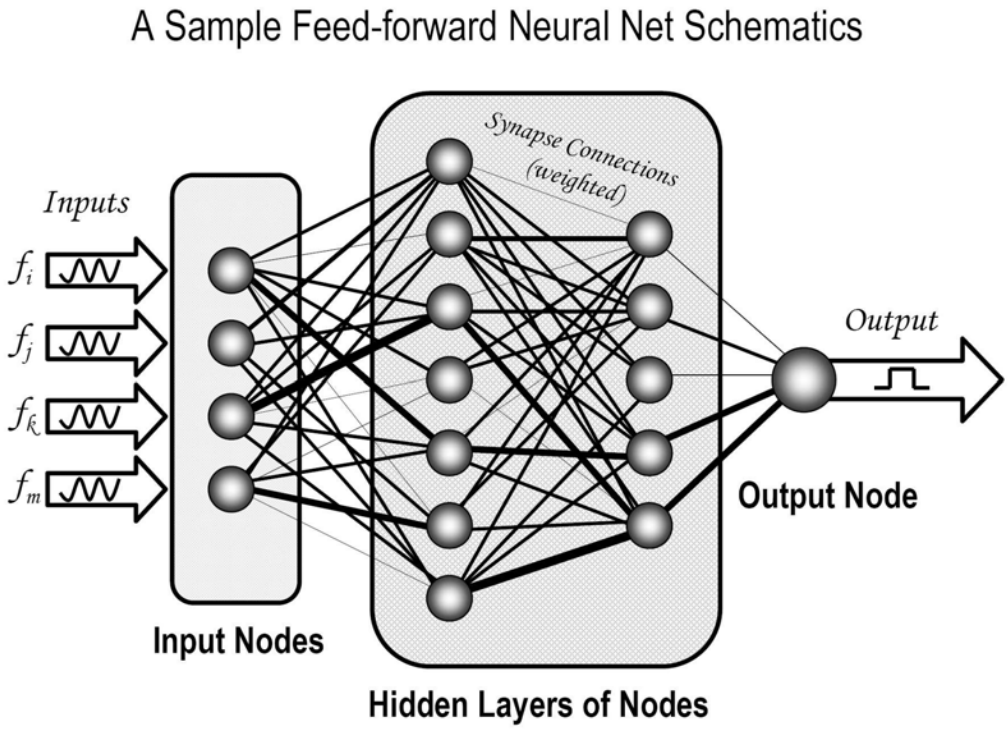

Figure 6.1. Schematic view of the main components of a simple feed-forward neural network with four input nodes, two layers of hidden nodes, and a single output node. The thickness of the lines representing synapses reflects relative weights, or strengths of correlation between internal functions of the nodes.

When the neural network (NN) is operated, the input nodes are supplied with their corresponding variable values, and then the hidden and output layer nodes are progressively executed. Each neuron calculates its activation value by taking the weighted sum of the outputs of the nodes in the preceding layer, and subtracting the threshold. The activation value is passed through the activation function to produce the output of the neuron. When the entire network has been executed, the outputs of nodes in the output layer serve as the output for the entire network. Initially the weights for each of the synapses are set randomly between -0.5 and 0.5. The NN output is compared to the desired output on a set of known examples. The

training algorithms try to minimize the error on the training samples by altering the weights. Variables have different effect on the NN output, so typically they can be ranked by their relative *power*. One can find a much more comprehensive description of the principles and structure of neural networks in [69]. We will concentrate our attention on the particular Neural Net implementation to b-jet tagging in the following sections.

6.3 Tagging Variables

Based on both data and Monte Carlo studies, several variables have been identified as being potentially good discriminators between b-jets and lighter c- and $u, d, s, (g)$-jets. Each particular tagging algorithm has its own specific physics objects and pre-selections with which to operate, so the Neural Net input variables have been chosen and optimized in such way that they will give a simple yet efficient tagging tool. The summary of input variables of the b-tagging Neural Net ranked by their relative power is given in Table 6.1, and each one of them will be discussed in a little more detail in the following subsections.

6.3.1 Jet Lifetime Probability

Generally, all jets originate from the primary vertex, unless there is only one heavy flavor hadron in the event. There is one output variable for the JLIP tagger - the probability that the jet originated from the primary vertex. The closer this probability is to 0, the more likely that it is a b-quark. If there was not enough information in the event to calculate a probability, this output value was set to 1. The distinction between the probability spectra for b-jets and light jets is illustrated in Figure 6.2. More information on this tagging algorithm can be found in [65].

TABLE 6.1

INPUT VARIABLES FOR THE NEURAL NET TAGGER

Rank	Variable	Short Description
1	$SVT_{SL}DLS$	Secondary Vertex (Super Loose): Decay Length Significance
2	$CSIPComb$	CSIP Tagger Output
3	$JLIPProb$	JLIP Tagger Probability
4	$SVT_{SL}\ \chi^2/DoF$	χ^2/DoF of Found Secondary Vertex
5	$SVT_{L}N_{tracks}$	Secondary Vertex (Loose): Number of Tracks used in Primary Vertex
6	$SVT_{SL}M_{VTX}$	Reconstructed Mass of the Secondary Vertex (Super Loose)
7	$SVT_{L}Num$	Secondary Vertex (Loose): Number of Found Secondary Vertices

6.3.2 Secondary Vertex

The presence of reconstructed secondary vertex (or multiple vertices) within the jet is a powerful signature for b-flavor. Several variables are of importance and have been included in the Neural Net. In order to properly define these variables, a few things about secondary vertex finding algorithm should be mentioned [64].

The Secondary Vertex finding algorithm employs a Kalman Filter [64] which takes the following steps to find displaced vertices:

I. Finds track clusters using simple cone algorithm of radius $R = 0.5$;

II. Selects tracks not associated with the Primary Vertex;

III. Finds vertices with the *build-up* approach:

- Finds seeds formed by two tracks with the best χ^2 within clusters. Fitting procedure uses Kalman Filter algorithm utilizing all track infor-

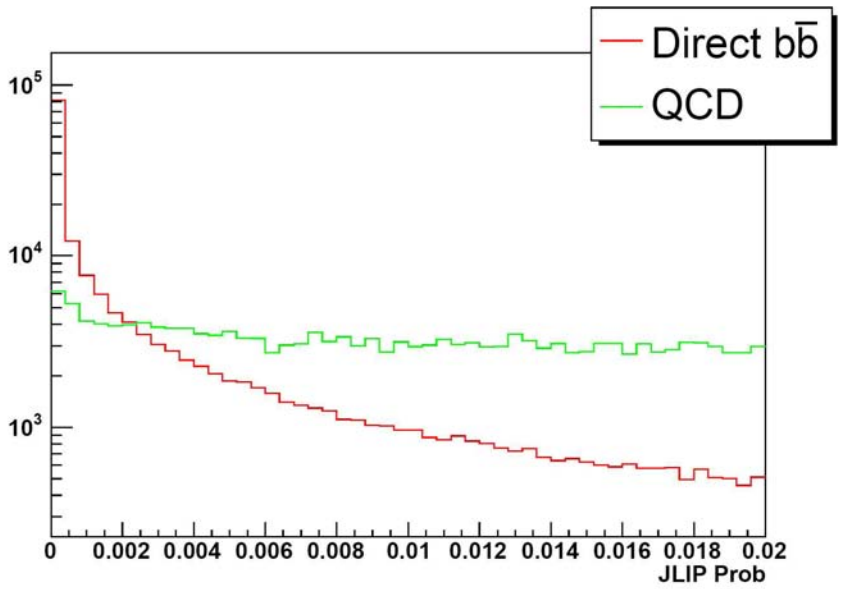

Figure 6.2. *JLIP Probability* variable spectrum for b-jets and light QCD jets (Adopted from [61]). Clear distinction in shape of the spectra is visible.

mation (both impact parameters and momentum) [64].

• All tracks (not only those belonging to a cluster) are attached to a seed if their χ^2 contribution is relatively insignificant.

IV. Selects vertices based on kinematic criteria such as cuts on decay length, opening angle, track $p_\perp$ and track multiplicity parameters.

V. Resolves possible multiple associations between found vertices and tracks by keeping the secondary vertex with the tightest opening angle, and removing all the other vertices that happen to share one or more tracks with it.

The exploration of the variables associated with secondary vertices has shown that one of the most powerful discriminating variables is two-dimensional decay length significance (DLS), or the ratio of the decay length to its uncertainty. As there may

be more than one secondary vertex found in the jet, the vertices with the highest DLS were considered.

The other variables of interest are the ratio of secondary vertex χ^2 to the number of degrees of freedom ($SVT\ \chi^2/DoF$), the number of tracks used in SVT reconstruction ($SVT\ N_{tracks}$), reconstructed secondary vertex mass ($SVT\ M_{VTX}$), and the found SVX multiplicity found in the jet ($SVT\ Num$).

In order to increase tagging efficiency, there was one important modification made to the settings of the SVT tagger. As the Neural Net operates best if more information is available, it was a disadvantage to have tight secondary vertex tagger settings. When SVT failed to find a vertex, no information at all was accessible, and the tagging rate was lower than when a loose criteria was applied and a vertex was found. Thus it was decided to loosen the SVT criteria from the standard loose SVT_L to a *super loose* criteria SVT_{SL}. The tagging efficiency for Monte Carlo b-jets was measured to increase from around 65% up to 90%. This is very important as the SVT_{SL} tagger provides by far the greatest number of variables (the distinctive features of which are shown in summary Figure 6.3) and having information present for these variables to successfully tag b-jets is essential.

6.3.3 Counting Signed Impact Parameters

The Counting Signed Impact Parameters (CSIP) tagger provides four variables that are used to distinguish b-jets. These are the numbers of tracks with decay length significances greater than 2 or 3 (named 2s and 3s, which identify the signal jets), and the numbers of tracks with *negative* decay length significances greater than 2 or 3 and $\Delta\phi < \frac{1}{15}$ with respect to the jet (named 2w and 3w, which identify the background jets).

All the CSIP variables are small integer values which are not ideal inputs for

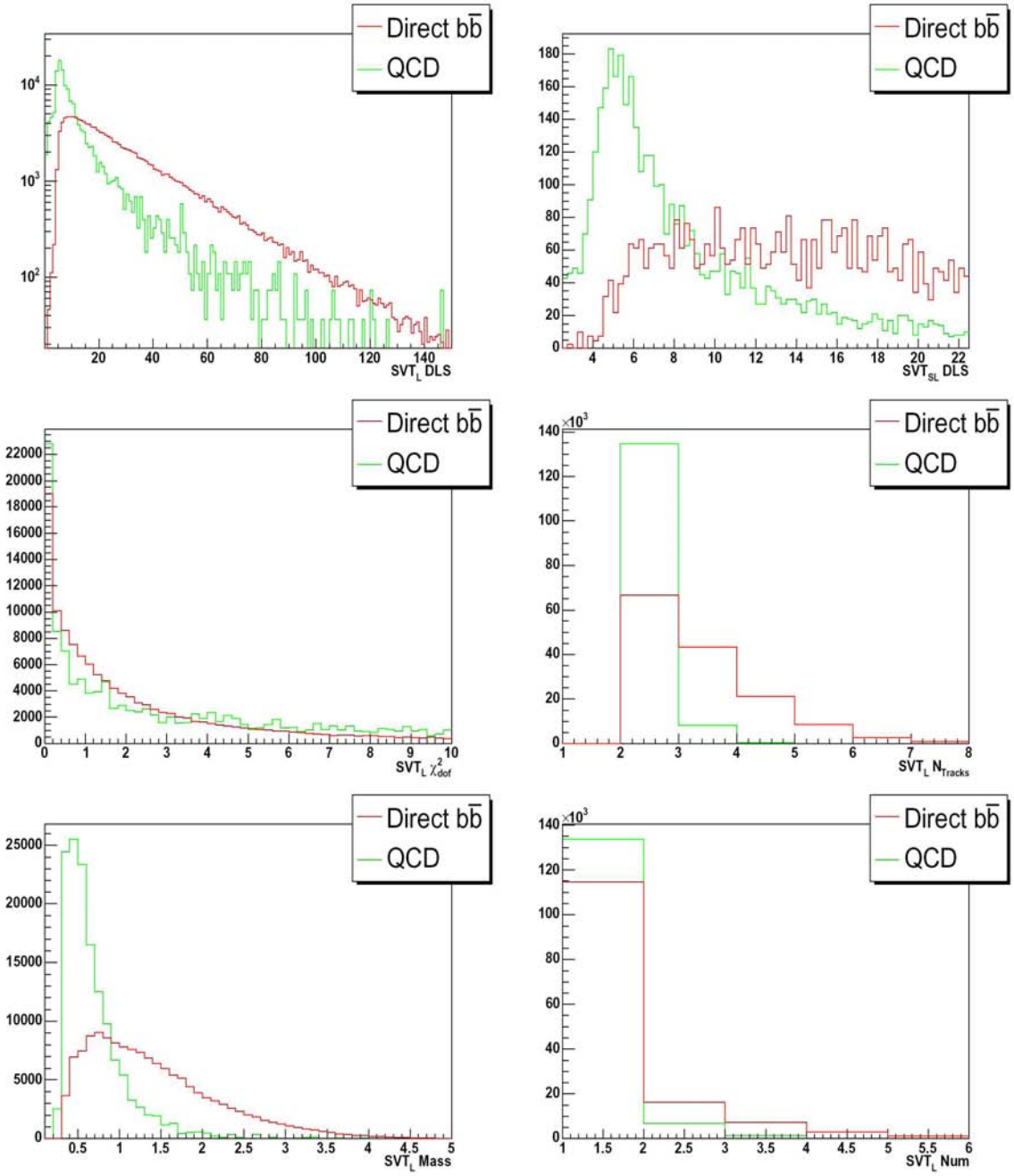

Figure 6.3. Variables for the loose SVT tagger, DLS (top left and right), χ^2/DoF (middle left), N_{Tracks} (middle right), Mass M (bottom left) and number of vertices (bottom right) in direct bbbar and QCD light jet Monte Carlo jets (Plots adopted from [61]). Please see the description of these variables in the text

a NN which works best with continuous values spread over a range. So the CSIP variables were used to create a single variable which was spread over a greater range. Replacing four variables with one also simplifies the Neural Net structure by reducing the number of input variables. The four CSIP tagger variables are combined as follows:

$$\text{CSIPComb} = 6 \times 3\text{s} + 4 \times 2\text{s} + 3 \times 3\text{w} + 2 \times 2\text{w} \tag{6.1}$$

The spectra for individual CSIP tagger variables, and the combined variable given by (6.1) is shown in Figure 6.4.

6.3.4 Soft Lepton Tagger

There was no output of the SLT tagger included in the Neural Net, and there are several reasons for such a decision. First of all, the method used to determine the tagging efficiency in data called *System 8* [70] uses jets with muons to assess the efficiency, and the tagger must be uncorrelated to use it correctly. If SLT inputs were included, that would introduce a bias in the *System 8* calculation. Secondly, there is a relatively small fraction of events that can be tagged using a lepton tag, so for the majority of the events there will be no input from the SLT. And finally, the method used by the SLT is mainly targeted at the lower jet $p_\perp$ kinematic region. At high $p_\perp$ (over 100 GeV/c), the $p_\perp^{rel}$ variable loses its distinguishing power as all the tracks become highly collinear with the jet axis. A more detailed and illustrated discussion on the failure of $p_\perp^{rel}$ method at high jet $p_\perp$ can be found in [59].

6.4 Neural Net Structure and Performance

The final version of Neural Net tagger used in this analysis, has seven input variables discussed above and listed in Table 6.1. The structure is 7:24:1:1, where there is 7 inputs, two layers of hidden nodes of 24 and 1, and one output node with

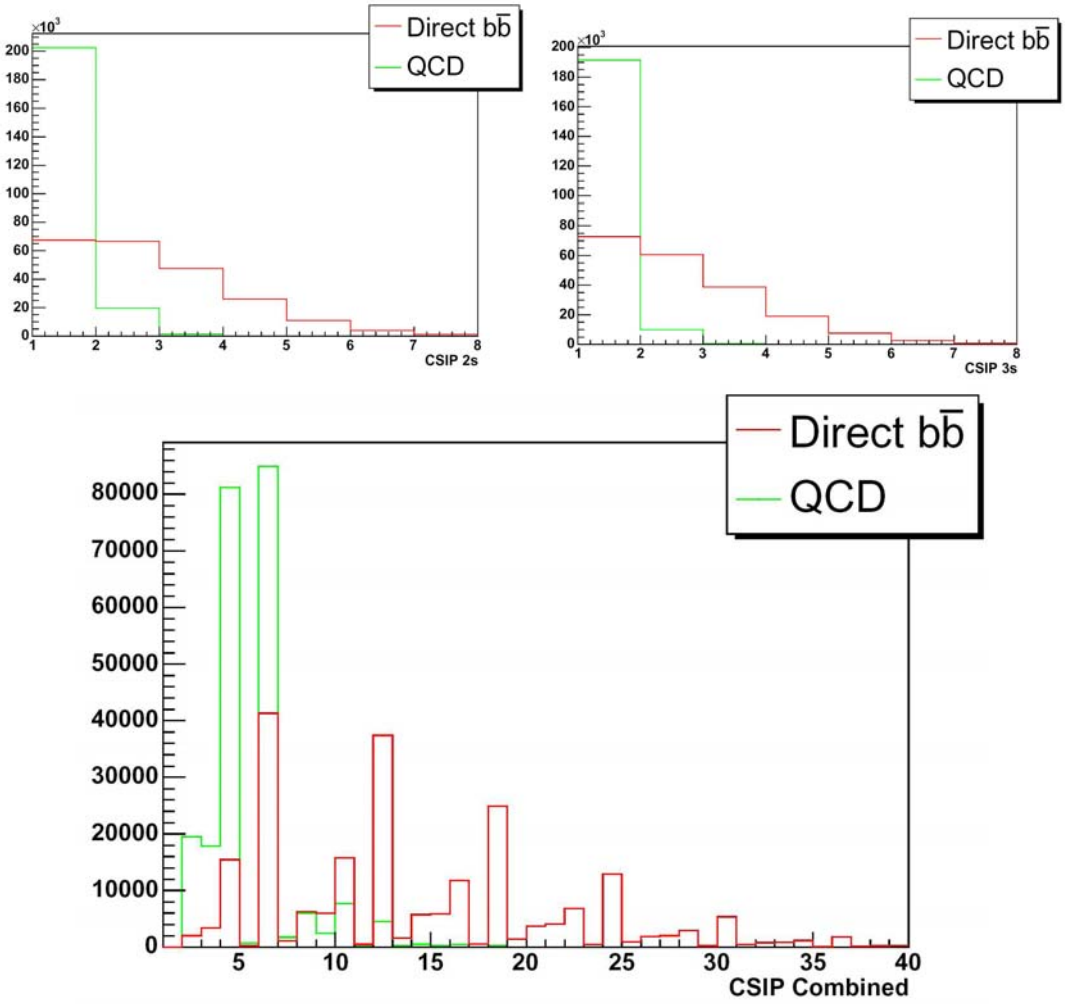

Figure 6.4. CSIP tagger output variables, and the combined variable spectra for signal in direct bbbar and QCD light jet Monte Carlo jets (Plots adopted from [61]).

the signal and background separated (NN output variable). The hidden layer of just one node does not provide any additional functionality other than normalization of the output variable to be in the range between 0 and 1 (Figure 6.5, [61]).

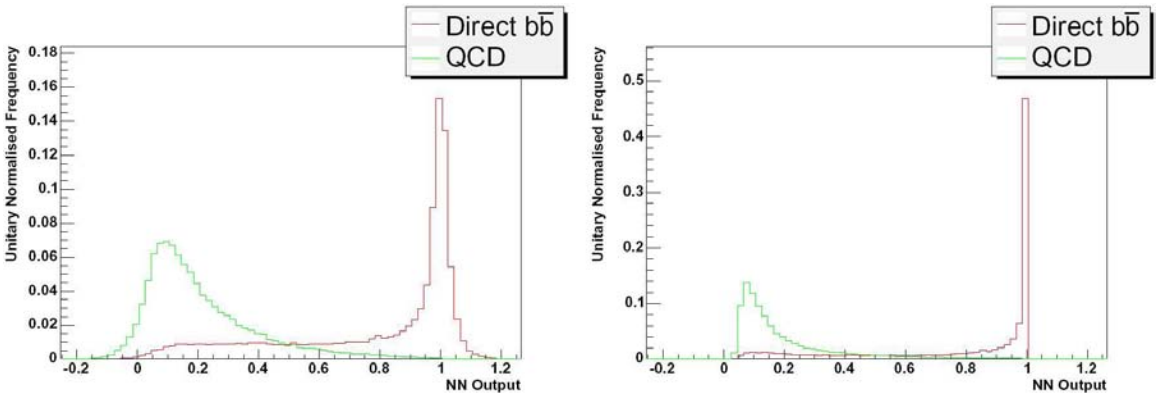

Figure 6.5. The NN output for the case of a single hidden layer 1:24:1 (left) and double hidden layer 1:24:1:1 (right). The extra hidden layer of one node helps to constrain the NN between 0 and 1. (Plots adopted from [61]).

The initial input pre-selections are summarized by Table 6.2:

TABLE 6.2

INPUT VARIABLE PRE-SELECTIONS FOR THE NEURAL NET TAGGER

Variable	**Selection (OR requirement)**
$SVT_{SL}DLS$	> 2.5
$JLIPProb$	< 0.02
$CSIPComb$	> 8

The performance of the NN tagger is discussed in detail in [62]. The relative performance comparison to the JLIP tagger illustrates the advantages of the Neural Net tagger (Figure 6.6).

By the multiple tests discussed in [61, 62] the NN tagger demonstrates a remarkable performance and achieves an efficiency of $\approx 70\%$ with the fixed fake rate of $\approx 1\%$. Although the tagging performance of the NN tagger deteriorates somewhat at high jet $p_\perp$ values, the NN tagger has been shown to have a substantially lower fake rate than the SVT and CSIP taggers at high $p_\perp$.

This Neural Net that combines the existent track-based b-tagging tools at DØ is a highly sophisticated and advantageous method to identify b-jets, and it was decided to use this tool in extracting the b-jet component in this analysis. For the detailed description of the Neural Net please refer to [61], and for the particulars of performance see [62].

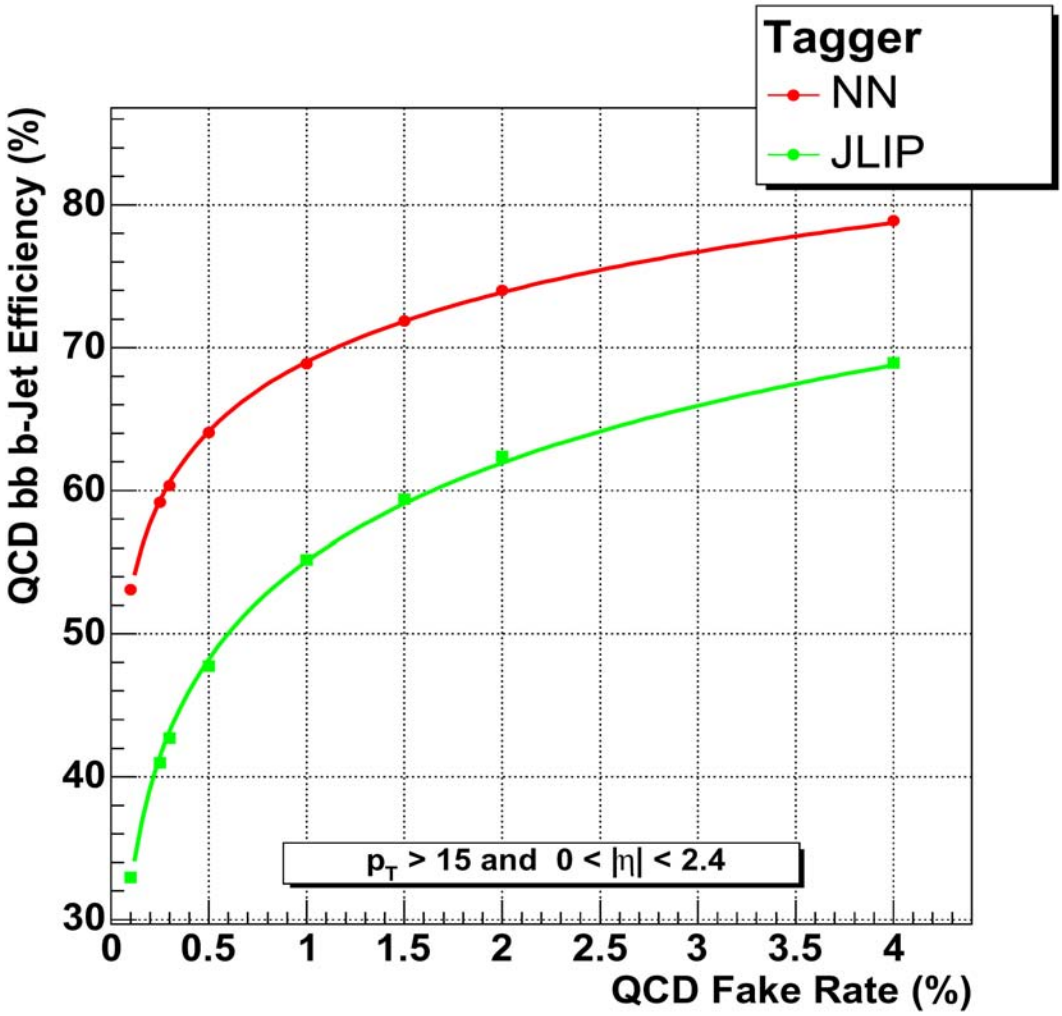

Figure 6.6. Performance curves ($b\bar{b}$ efficiency vs. fake rate) for the NN tagger and the JLIP tagger on the same MC sample. Plots adopted from [61].

CHAPTER 7

b-JET CROSS SECTION MEASUREMENT

This chapter presents the particulars of the b-jet cross section measurement. The data and Monte Carlo samples used in this analysis are introduced. The steps necessary to obtain the b-jet cross section (outlined earlier in 2.6.2) are carried out, and the detector-level measurement is obtained.

In $p\overline{p}$ collisions, b-jets are produced with a transverse momentum that follows a certain underlying distribution. The experimental goal is to measure this distribution. However, this $p_{\perp}$ cannot be measured directly due to events such as b$\rightarrow x + \nu$, in which the undetected neutrino carries away energy from the jet. Detector resolution and acceptance effects also distort the distribution. To measure the true $d\sigma/dp_{\perp}$ distribution with which the b-jets are produced, we correct the detector-level measurement for these effects, obtaining the particle-level b-jet cross section.

7.1 Data Set and Selections

The results of this analysis are based on data collected with the DØ detector in Tevatron Run II from April 27, 2002, to June 28, 2004. The corresponding detector run numbers span 148600 - 194566. Data has been processed with several versions of the DØ reconstruction software (DØreco) such as p14.03.xx, p14.05.00, p14.05.02, p14.06.00. The dataset also contained duplicate events that were removed.

Due to the sizeable amount of data at hand, it was convenient to use a loosely preselected dataset of a reduced size, called the *skim*. Skims are created and handled by a special working group at DØ, the Common Sample group. The data for this analysis originates from the common skim done for the QCD group. More details on this data can be obtained in [71]. In the process of skim creation, the data was corrected (or *fixed*) for the differences caused by the variety of the reconstruction software versions. The selection criteria for creating this subset was the requirement that at least one of the jet triggers (CJT5, JT_8TT, JT_15TT, JT_25TT_NG, JT_45TT, JT_65TT, JT_95TT or JT_125TT) conditions were met in each event.

The skimmed data at DØ is stored in a compressed format called a *thumbnail*. In order to process files with the DØRoot analysis package [72, 73], all the data was processed with the software called *dØcorrect* version v00-00-06a in order to convert the thumbnail to *TMBTree* format, an object-oriented container class suitable for accessing with the DØRoot analysis software. The Physics objects recorded in thumbnails and TMBTrees can be accessed via the ROOT analysis package directly, but the convenience of numerous pre-built functions and methods of the DØRoot package makes it advantageous. Duplicate events totaling 1,445,600 were identified and removed at this point. With the duplicates removed, the dataset containing 43,681,935 events was successfully processed into *TMBTree* format retaining all the event information. At this stage, the jet energy scale corrections (Section 5.1.2) are applied to correct the jet transverse energy $p_\perp$.

At the next processing stage, the following set of selections have been made to further reduce the dataset to a manageable size:

- require at least two jets reconstructed in each event;
- remove inefficient trigger data via imposing $p_\perp$ thresholds (discussed in more detail later in 7.1.2), so each of the jet triggers is $\geq 90\%$ efficient;

- tag events using a Neural Net (see 6.4) requirement on each jet, requiring that either one of the two leading jets have a Neural Net output greater than zero;

- confine pseudo-rapidity range of tagged jets to be within the central region of $|y_{jet}| \leq 0.8$.

In order to facilitate the analysis and reduce the processing turn-around time, it was convenient to manipulate the data even further. For that purpose, a custom container class called *jettree* based on DØRoot objects, was created. The benefits of converting to the custom-tailored analysis class include the $\times 20$ increase in processing speed and simplifying access to the information by keeping only the jet-analysis-specific data in that class.

7.1.1 Luminosity

In order to produce a good cross section measurement, all of the DØ detector subsystems involved in the tagging process must function properly. However one expects occasional detector malfunctions, and the data taken at the times of any major detector sub-system malfunction must be removed from the dataset. In order to do this, the list of bad runs was created using the Offline Run Quality Database [74]. The database was queried against malfunctions of the calorimeter, SMT, CFT, and muon sub-systems. In addition detector runs claimed as bad by the Missing-$E_{\perp}$ and Jet Working groups were removed. The final list of bad runs consists of 1764 runs out of the total of 30393 Physics runs taken. The luminosity calculation was done taking into account all of the bad-run data reductions.

The total delivered luminosity for this data sample is $\mathcal{L}$= 426.5 pb^{-1}. However, the luminosity for each trigger must reflect the trigger pre-scale value to properly normalize the jet spectra. The luminosity summary for each trigger is given in

TABLE 7.1

INTEGRATED LUMINOSITY SUMMARY

Trigger by name	Recorded, pb^{-1}	Recorded w/good quality, pb^{-1}
JT_8TT	0.025	0.0219
JT_15TT	0.1135	0.0975
JT_25TT_NG	2.216	1.836
JT_45TT	38.51	29.2
JT_65TT	189.05	146.4
JT_95TT	378.23	309.5
JT_125TT	381.9	312.3

Table 7.1. Also, not all the luminosity was collected effectively due to detector down-times and/or data acquisition problems that prevented recording of some data. This fact is reflected by the luminosity number recorded is being 381.9 pb^{-1} instead of 426.5 pb^{-1} delivered.

7.1.2 Trigger Turn-on Curves and Thresholds

In this analysis data is coming from several QCD jet triggers. The luminosity weighted detector-level inclusive jet $p_\perp$ spectra are shown in Figure 7.1 for each of the triggers. In order to combine and normalize jet spectra, and to exclude the data which has been collected with inefficient triggers, thresholds were imposed on jet $p_\perp$. This requirement assures that the efficiency in the data is essentially 100%. This cut reduces the dataset size by approximately a factor of three. Trigger turn-on points in $p_\perp$ were obtained by comparing the distribution of the raw jet $p_\perp$ cross section for that trigger with the same distribution using the trigger with the next lower $p_\perp$. The ratio of jet $p_\perp$ spectra from two subsequent triggers (JT_45TT and JT_65TT) described in Figure 7.2a, is shown in Figure 7.2b. To determine the turn-on points with greater accuracy, these ratios were fitted via the following

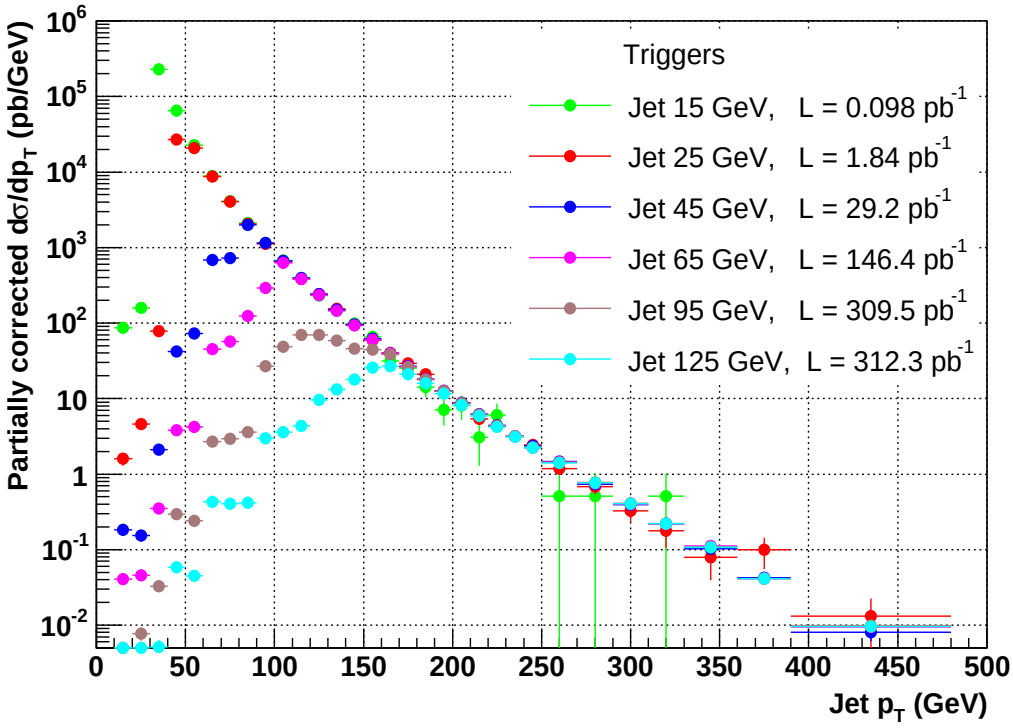

Figure 7.1. Partially corrected inclusive jet $p_\perp$ spectra.

three-parameter functional form:

$$f_{TrigTurn} = \frac{p_2}{1 + \exp\left((p_1 - x)/p_0\right)} \tag{7.1}$$

where p_i $(i = 1, 2, 3)$ are parameters. The turn-on point for the particular trigger is taken to be the $p_\perp$ value for which the corresponding ratio of trigger spectra (trigger efficiency) is 99%.

During high luminosity runs, the lower $p_\perp$ jet triggers have higher prescales than in the low luminosity runs. The spectra were corrected for jet energy scale (the offset correction depends on instantaneous luminosity) and for non-linearity effects in the Luminosity Monitor electronics [38].

Trigger turn-on points for other triggers were determined in the same fashion (Figure 7.3). The relative trigger efficiency for all triggers in most cases is within 1-

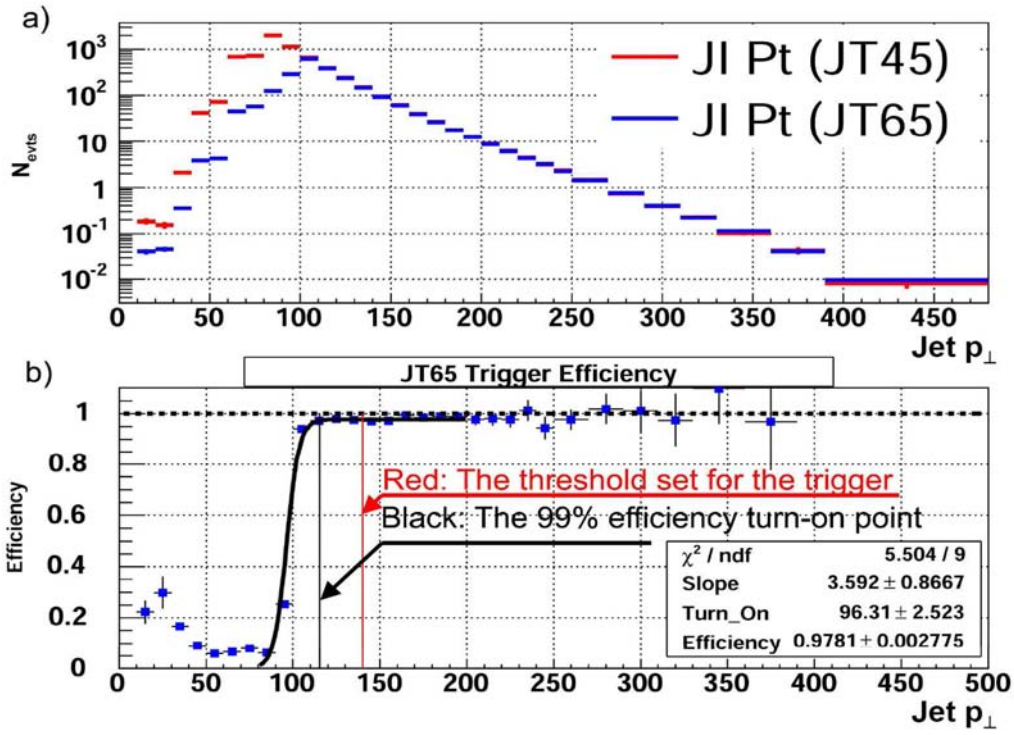

Figure 7.2. Ratio of the $p_\perp$ spectra for triggers JT_45TT and JT_65TT. The black line shows the 99% efficiency value. The red line shows the $p_\perp$ bin that was set to be the threshold for JT_65 trigger.

3% of 100% efficiency. No fit was performed in the case of trigger JT_15TT because the relative efficiency with respect to trigger JT_8TT decreases with increasing jet $p_\perp$. This behavior is explained by the noise in measuring low $p_\perp$ jets and/or to the differences in Level 1 conditions of trigger JT_8TT and JT_15TT. JT_8TT requires one Level 1 trigger tower with $E_\perp > 5$ GeV, whereas JT_15TT requires two Level 1 trigger towers with $E_\perp > 3$ GeV. However, the $p_\perp$ range for data coming from JT_15TT trigger used in this analysis is well above the turn-on point for this trigger, so the threshold was conservatively set at 50 GeV mark (please see more in [57]).

The obtained jet $p_\perp$ threshold values as well as the actual $p_\perp$ ranges used in the analysis are given in Table 7.2. As can be seen, the ranges used are well above

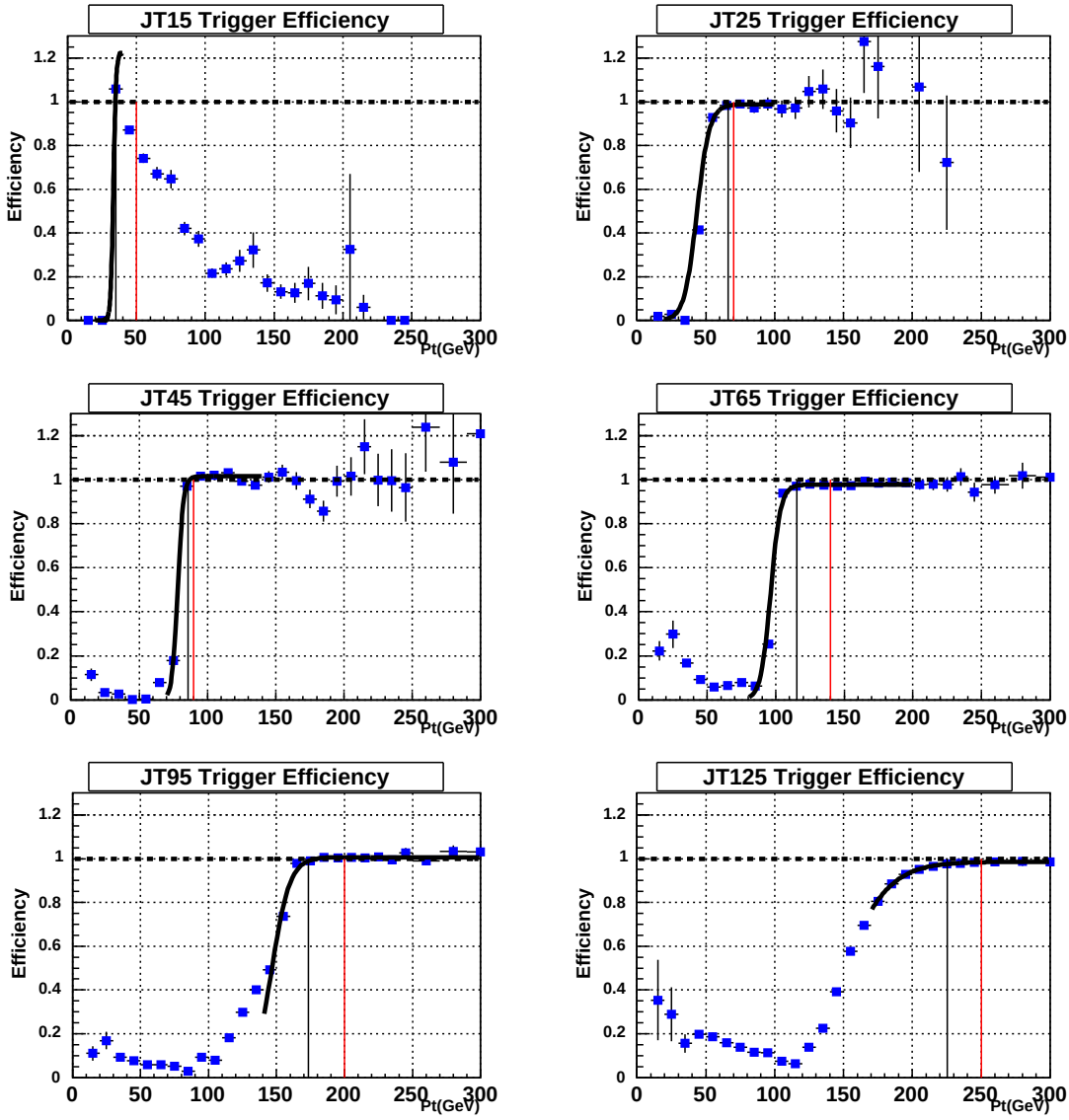

Figure 7.3. Turn-on curves for all jet triggers used in the analysis. Turn-on for trigger JT_15TT is not well-defined for the reasons discussed in the text. In this analysis, the $p_\perp$ cutoff was placed above the 100% turn-on for this trigger based on the results of previous comprehensive inclusive jet studies done at DØ [31, 57].

TABLE 7.2

JET TRIGGERS THRESHOLD VALUES AND $p_\perp$ RANGES USED IN ANALYSIS

Trigger by name	$p_\perp(\varepsilon_{trig} = 90\%)$, GeV	$p_\perp(\varepsilon_{trig} = 99\%)$, GeV	Range Used, GeV
JT_15TT	37.8	38.3	50-70
JT_25TT_NG	43.5	50.2	70-90
JT_45TT	74.4	84.7	90-140
JT_65TT	99.4	126.1	140-200
JT_95TT	156.4	174.7	200-250
JT_125TT	179.8	233.0	>250

the trigger turn-on point. This is done for several reasons. Using data well above threshold ensures us that any additional requirements such as Neural Net tagging that make trigger turn-ons higher, will not bias the data in such a way that it would come from an inefficient trigger interval. Secondly, the jet energy scale correction has a considerable uncertainty, and data taken from a $p_\perp$ region well above threshold ensures that the data is efficient within this uncertainty. Because of the choice of trigger thresholds, the trigger efficiency can be assumed to be 100%.

7.1.3 Jet Quality Cuts

The jet quality cuts imposed were the standard DØ cuts that are applied to attain a good jet quality, as was discussed in detail in 5.2. The standard quality cuts applied were:

- Hot Fraction (HotF) < 10;
- Number of calorimeter towers in jet (n90) > 1;
- Coarse Hadronic Fraction (CHF) < 0.4;
- Electromagnetic Fraction (EMF) is between 0.05 and 0.95;

• Either the fraction of all jet towers with 90% of the scalar $E_\perp$ commonly abbreviated as (f90) < 0.5 or Coarse Hadronic Fraction (CHF) < 0.15.

These cuts remove less than 2% of all jets [59]. The non-zero Neural Net output requirement applied later to jets has a very high correlation with these cuts, so in this analysis the effect of these quality cuts is extremely small, and the efficiency of jet quality cuts is estimated to be 99±1%.

7.1.4 Missing $E_\perp$ cut

Most of the events from the jet inclusive sample are produced through the standard QCD interactions. Therefore the events should be $p_\perp$-balanced. A cut on missing $E_\perp$ removes events with large missing $E_\perp$ (events with missing $E_\perp$bigger than 70% of the leading jet's uncorrected $p_\perp$). This cut becomes especially important at high $p_\perp$, where the imbalance can be very large, and we intend to keep only those jets whose energy was measured well in order to produce a cross section result [57]. The main purpose of the cut is to remove non-physical background, when the energy deposition occurred only in one part of the calorimeter. A typical example of such events are cosmic events.

The distribution of the leading jet $p_\perp$ over missing $E_\perp$ is smooth for jets with $p_\perp$ < 90 GeV in the central rapidity bin [57]. There is no evidence of any background in this domain of transverse momenta. An excess of events around $p_\perp \sim \not\!\!E_T$ starts to appear at higher transverse momenta. The relative height of the peak, with respect to the total number of events in the jet inclusive sample, increases with jet $p_\perp$. This is demonstrated in Figure 7.4, which shows as an example the distribution of ($p_\perp$/missing $E_\perp$) variable for the events which fulfill all selection criteria except the cut on missing $E_\perp$.

The requirement for the Neural Net variable to exceed zero in the jet in order

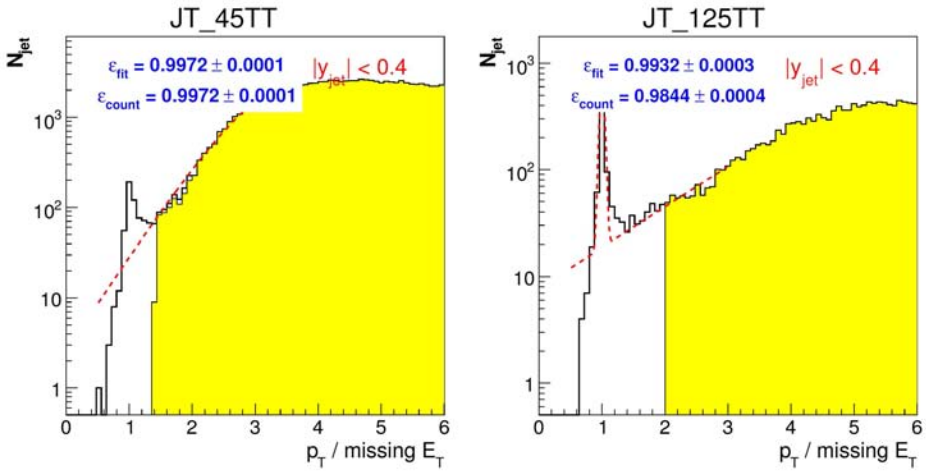

Figure 7.4. Distributions of the leading jet $p_\perp / \not{E}_T$ for two regions of transverse momenta (JT_45TT for $90 < p_\perp < 120$ GeV and JT_125TT for $p_\perp > 220$ GeV) for the central $|y| < 0.4$ inclusive sample. Solid lines represent the distribution for events where all selection criteria were applied except the cut on missing $E_\perp$. Shaded regions then correspond to events that satisfied the missing $E_\perp$ criterion as well and are kept. Dashed lines represent a double gaussian fit (adopted from [57]). The difference in cut values arises from the fact that the cut is imposed on uncorrected jets, while the effect is shown after JES corrections have been applied.

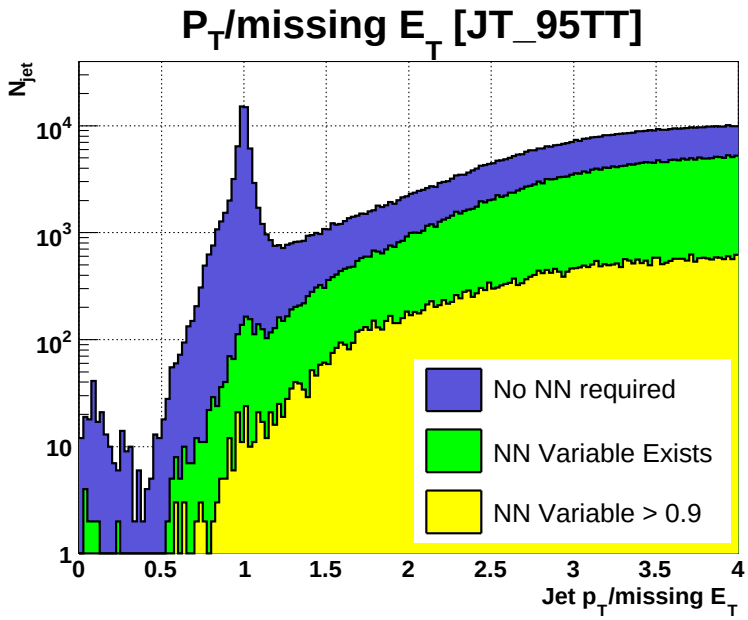

Figure 7.5. Missing $E_\perp$ cut does not have any significant impact on jet quality with Neural Net requirement present.

to tag it imposes an additional and quite tight requirement on jet quality (as was mentioned in 7.1.3). This reduces the significance of the $\not\!\!E_T$ cut even further, as shown in Figure 7.5.

The $p_\perp$ over missing $E_\perp$ cut was studied in detail [79] and was shown to have efficiency very close to 100% up to the highest energies. The missing $E_\perp$ cut efficiency was taken to be 99±1%.

7.2 Monte Carlo Samples

Initially, twenty thousand events were requested at three different $p_\perp$ ranges: 80-160, 160-320, and 320-980 GeV. Separate requests in these $p_\perp$ ranges were made for direct b-quark production, direct c-quark production, and the standard inclusive jet production to have light quark simulation. Samples generated previously for b-tagging and QCD working groups have been used as well. Table 7.3 provides the summary of Monte Carlo samples used in this analysis.

7.3 b-flavor Extraction

In order to measure b-jet cross section, the following measurement strategy is utilized. As it was discussed earlier in Chapter 6, the Neural Net has an impressive b-flavor separating power, and a cut on the Neural Net output variable can be used to discriminate the backgrounds consisting of c-flavored and light quark containing jets from our objects of interest, the b-flavored jets. However, the cut does not provide definitive information about the purity of the events remaining after the cut with respect to the b-jets as the signal. All the tagging tools are typically tuned in such way that they maximize the signal efficiency. However, to measure b-jet cross section the purity of b-jets must be determined.

As this analysis is exploring the b-jet tagging problem at extremely high $p_\perp$,

TABLE 7.3

MONTE CARLO SAMPLES USED IN ANALYSIS

# MC Request	MC Type	# Events	SAM Dataset Definition
13334	$b\bar{b}$ 80-160	20000	req-id-13334-tmb-good
13383	$b\bar{b}$ 80-160	18490	req-id-13383-tmb-good
13336	$b\bar{b}$ 160-320	18193	req-id-13336-tmb-good
13385	$b\bar{b}$ 160-320	27000	req-id-13385-tmb-good
13338	$b\bar{b}$ 320-980	18297	req-id-13338-tmb-good
13387	$b\bar{b}$ 320-980	17259	req-id-13387-tmb-good
13335	$c\bar{c}$ 80-160	20500	req-id-13335-tmb-good
13384	$c\bar{c}$ 80-160	20397	req-id-13384-tmb-good
13337	$c\bar{c}$ 160-320	21000	req-id-13337-tmb-good
13386	$c\bar{c}$ 160-320	20000	req-id-13386-tmb-good
13339	$c\bar{c}$ 320-980	20140	req-id-13339-tmb-good
13388	$c\bar{c}$ 320-980	20750	req-id-13388-tmb-good
13369	QCD 40-80	106000	req-id-13388-tmb-good
13370	QCD 40-80	38000	req-id-13388-tmb-good
13371	QCD 40-80	49500	req-id-13388-tmb-good
15406	QCD 40-80	104000	req-id-13384-tmb-good-genuine
13327	QCD 80-160	51000	req-id-13327-tmb-good-genuine
13328	QCD 80-160	50500	req-id-13328-tmb-good-genuine
13330	QCD 80-160	50500	req-id-13330-tmb-good-genuine
13372	QCD 80-160	51000	req-id-13372-tmb-good
13373	QCD 80-160	51000	req-id-13373-tmb-good
13374	QCD 80-160	50500	req-id-13374-tmb-good-genuine
13375	QCD 80-160	51000	req-id-13375-tmb-good-genuine
15407	QCD 80-160	115000	req-id-15407-tmb-good-genuine
13331	QCD 160-320	46789	req-id-13331-tmb-good-genuine
13376	QCD 160-320	33500	req-id-13376-tmb-good
13377	QCD 160-320	24108	req-id-13377-tmb-good
15408	QCD 160-320	101000	req-id-15408-tmb-good-genuine
13378	QCD 320-980	20000	req-id-13378-tmb-good
15409	QCD 320-980	72358	req-id-15409-tmb-good-genuine

there were no initial purity studies made for the Neural Net tagging in this kinematic region. It was decided to use Monte Carlo driven shape templates for the Neural Net output variable to fit the Neural Net output distribution in data. This gives the purity information needed for this measurement. After that, the b flavor-enriching cut on the Neural Net is imposed, and the purity of the enriched subsample is recalculated.

The efficiency of tagging b-jets can be determined either by having tagged an unbiased pure b-jet sample, or by using Monte Carlo simulation of the b-production and hadronization to tag simulated b-jets, and then correcting for the differences between simulation and real detector data. Pure b-flavored data samples come from direct b-hadron reconstruction, and are not applicable in this study because of low statistics and a kinematic range being much different than targeted by this study. Moreover, clean b-flavored data samples are usually comprised of b-quark content produced only by certain specific modes, which will introduce bias in the inclusive measurement. Thus the only sensible option was to use Monte Carlo tagging efficiency, and to find a scale factor that will correctly map Monte Carlo to data. This procedure is described in greater detail later on in Section 7.4.

7.3.1 Neural Net Output Templates

The general features of the Neural Net output variable distribution were discussed in Section 6.4. Initial studies of the templates had to be done to determine the overall feasibility and details of the fitting procedure. Three types of templates were studied: b-jet signal, c-flavored jets, and jets containing only light quarks (u,d,s) and associated gluons. The flavors of Monte Carlo jets were determined by looking at both leading order primary partons, and at all partons collinear with jets. The definitions for the Monte Carlo associations are as follows.

For Monte Carlo simulation, the *Pythia* event generator was used [75]. This is a leading order (LO) pQCD event generator, in which parton showers are modeled according to Lund String Model [76]. A universal fragmentation function is used in Pythia to describe all collision systems. As in the Pythia Monte Carlo simulation used, the two leading order partons are generated which are subsequently modified by parton shower models. When this study began, there was no method to precisely determine the original partons in MC, so the following simple algorithm was derived. The program loops over all partons in the event (including ones coming from parton showers). It finds the parton with the largest $p_\perp$ and declares it to be a leading-order parton. It then loops again over the remaining partons, and finds the highest $p_\perp$ parton which also has a $\Delta\phi$ from the highest $p_\perp$ parton of more than (π - 0.7). This parton is assumed to be the second leading order parton. These two potential leading order partons are then compared to the two leading jets. The partons and jets are associated if they match in (η, ϕ) space with a ΔR of less than 1.0 and a ΔZ of less than 100 cm. This matching criteria was intentionally left loose to enhance efficiency and, since there are only two leading order partons allowed, this can be done without much effect on fake matches.

The Monte Carlo *truth* particles are **all** truth particles collinear with the calorimeter jet, even if the particle subsequently decays into other particles that will also be listed as collinear with the calorimeter jet. Then these particles are restricted to the only stable ones with the methods of *JetInfo* analysis object. The truth particles and calorimeter jets are associated if they match in (η, ϕ) space with a ΔR of less than 0.5 [59].

The Monte Carlo *truth* partons are **all** truth partons that are collinear with the calorimeter jet, even if the parton subsequently showers into other partons that will also be listed as collinear with the calorimeter jet. The truth partons and calorimeter

jets are associated if they match in (η, ϕ) space with a ΔR of less than 0.5. Note this is distinct from the leading order parton, as it provides another way to look at b and c quark content [59] by including possible higher order QCD processes in the consideration.

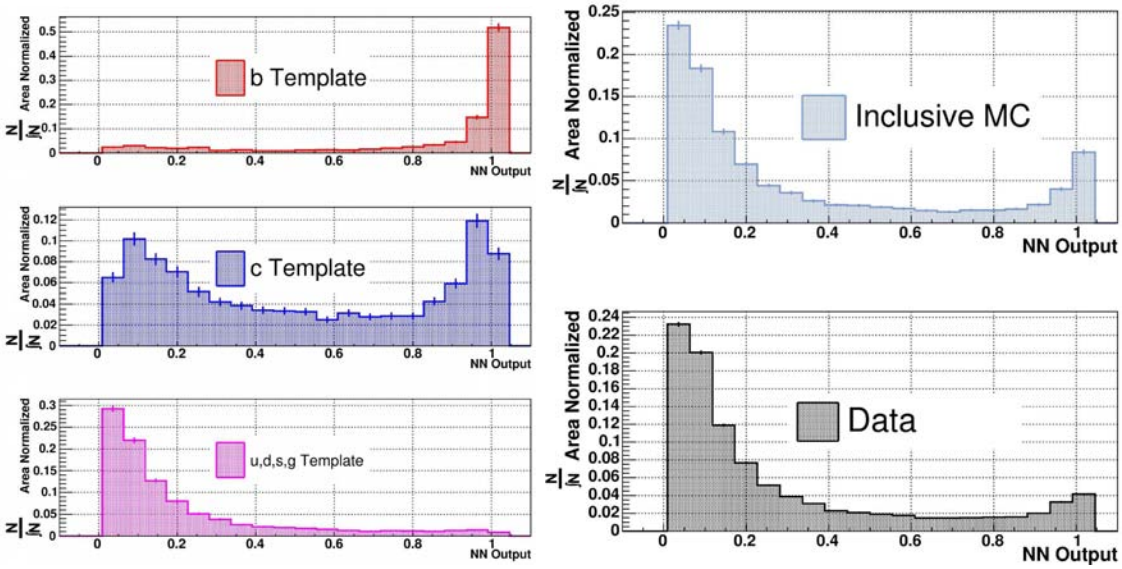

Figure 7.6. Characteristic Monte Carlo template shapes for the Neural Net output variable for three kinds of MC jets (b-jets, b-jets, and jets containing light quarks u,d,s), inclusive simulation, and data.

Having these associations in place, Monte Carlo shape templates of the Neural Net output variable for jets of three distinct flavors were made. For the b-flavor extraction procedure to be successful, all of the templates must be substantially distinct. The characteristic shapes of these templates that are shown in Figure 7.6 do have this character. A number of additional features of these templates is important for successful fits for the b-fraction. The most important of these is the $p_\perp$ dependence of these shapes, and there was one (as noted in Figure 7.7).

Because of the slight $p_\perp$ dependence it was decided to split the data into several $p_\perp$ ranges (as statistics in Monte Carlo and data allows), and use $p_\perp$-specific

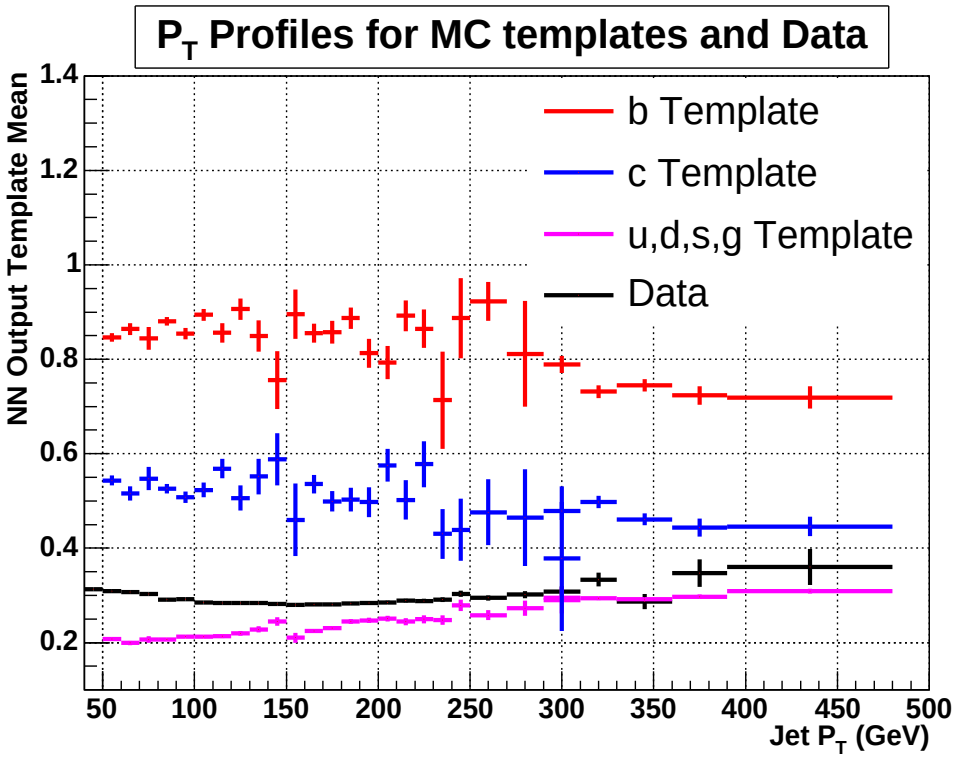

Figure 7.7. Neural Net output mean as a function of jet $p_\perp$ for Monte Carlo (b, c, *light*) and data.

templates to fit each range separately. The shape comparisons between the Neural Net output variable in Monte Carlo and in data for all 17 $p_\perp$ bins can be found in Appendix A.

The Monte Carlo jet flavor content-matching procedure allows for several sources for a particular flavor, such as direct $b\bar{b}$ production and b-flavor coming from gluon radiation in the fragmentation stage. As Figure 7.8 suggests, it was established that there was no difference in template shapes depending on which source of flavor particular jets have. Since this analysis is intended to measure the inclusive b-jet cross section, all jets containing b-flavor are accepted, and the templates can utilize all the flavor sources.

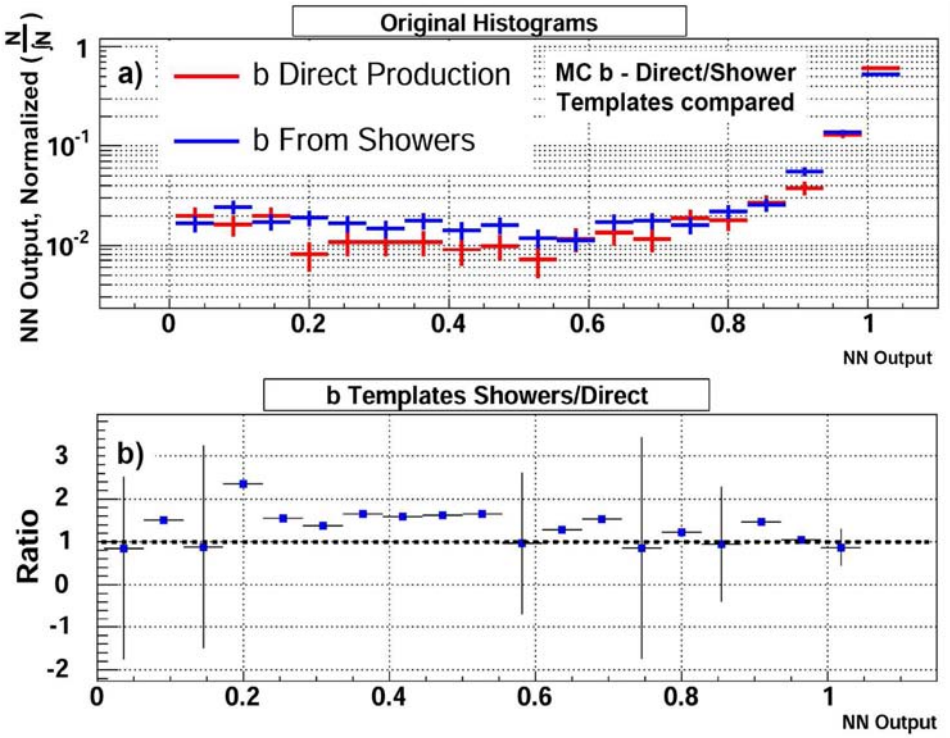

Figure 7.8. a) Spectra for the Neural Net output variable for MC b-jets coming from direct and shower production. b) Ratio of the Neural Net output templates (above) for b-jets originated by direct and shower b production shows that the shapes are similar.

7.3.2 Fitting for the b-fraction

In order to obtain the b-jet cross section, we need to extract the b-jet component out of the inclusive sample using the Neural Net output variable. It was decided to divide the data in 17 $p_\perp$ bins determined by the statistics at hand ($p_\perp$ bins were chosen so as to have at least 1000 events in each bin to ensure good quality fits). For each $p_\perp$ bin, templates of Neural Net output shapes were produced after ensuring all of the cuts in MC and data were the same. To ensure that, Monte Carlo simulations were processed with the same code as the data. Two fitting algorithms were utilized: a least-squares fit with a χ^2 minimization, and a maximum likelihood

fit. Both methods gave the same results. It was decided to use likelihood fits to extract the b-jet fraction, and the χ^2 method to use as a fit quality-control criterion. An example of a sample fit in one of the $p_\perp$ bins is shown in Figure 7.9.

The fitting function $\mathcal{F}$ minimized to fit the templates is a two-parameter function constructed in the following way:

$$\mathcal{F} = (p_0 \times f_b + p_1(1-p_0) \times f_c + (1-p_0)(1-p_1) \times f_q) - f_{Data} \qquad (7.2)$$

Here p_0 and p_1 are the parameters representing b and c fractions ($0 < p_0, p_1 < 1$), and f's are the functions for the Neural Net output variable for different MC flavors and data represented by the corresponding templates. The quality of the fits may be assessed by looking at the two-dimensional χ^2 contours also plotted in Figure 7.9.

The fitting procedure described above depends on choices made for a number of parameters such as choice for the binning of the variable, starting fit values and constraints on fit parameters and fitting ranges. Establishing these settings is very important, as they will be used to perform many repeated fits for each $p_\perp$ bin in order to estimate the systematic uncertainty associated with the purity extraction process. The reasonable ranges in which it is safe to vary fit parameters have to be well-established prior to actual fitting. While this question will be covered in more detail in the discussion of systematic uncertainties, we describe how these choices were made here.

Despite the fitting process takes many assumptions and choices made by researcher as inputs, the effects of these choices on the final result must be minimized to have the least impact on the analysis. Listed below are the choices made while extracting the b-jet component, and steps made to reduce their impact on the results.

The choice of binning: It is true that most spectra measured in nature can be presented with continuous functions. In other words, nature does not know about binning. Binning is used it to facilitate the measurements. By introducing binning,

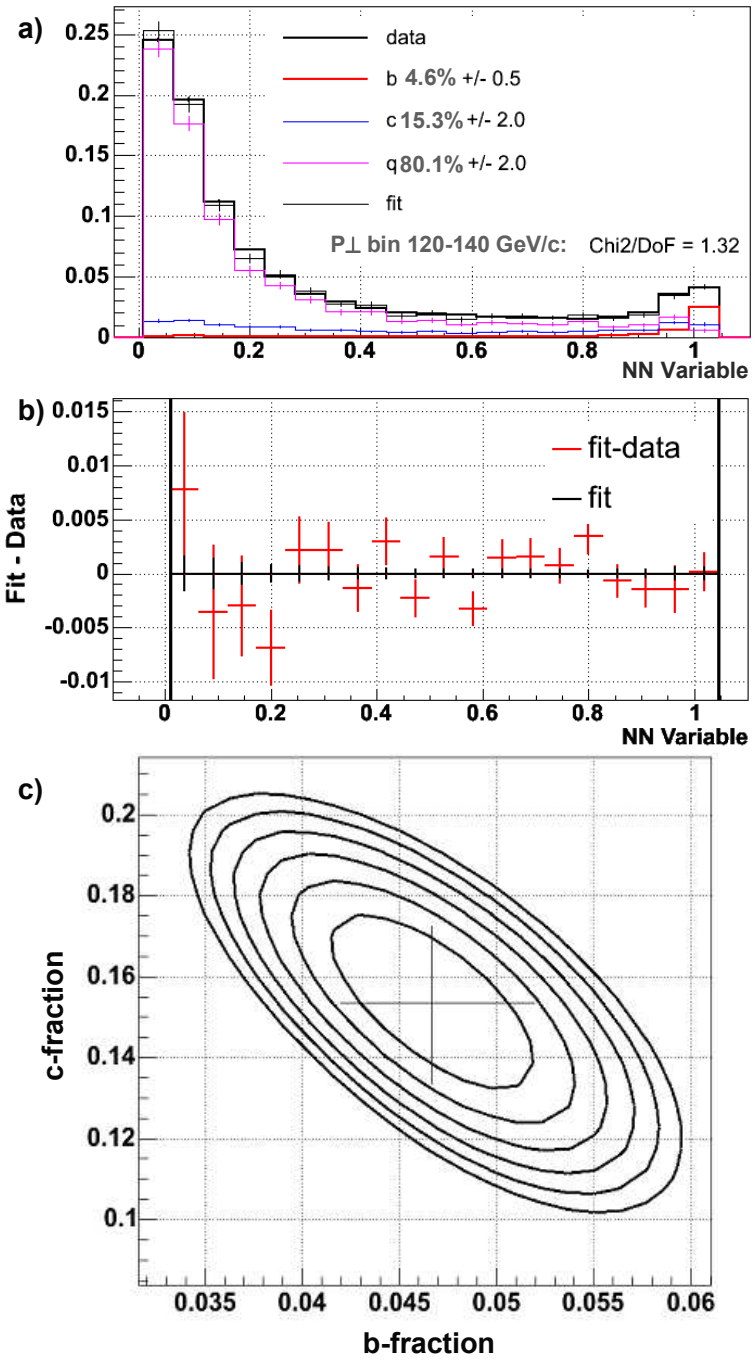

Figure 7.9. a) Sample fit for the b-jet fraction in 120-140 GeV $p_\perp$ bin with the templates for the Neural Net output. b) Expanded view for the (Data-Fit) difference. c) The χ^2 contours for this fit.

we reduce the amount of information available. The reduction can be crucial if we choose the width of the bins too coarse and some real physical effect is lost in a single wide bin. Followed by this logic one could come to the conclusion that it is best to have the binning as fine as is technically possible. While ultimately true, this conclusion does not work well in practice as another important constraint, the statistics, comes into play.

While measuring some physical quantity, one has only a limited capacity of determining the values of that quantity, and there is statistical error inevitably associated with the measurement. If the bins are made finer, the statistical uncertainty in each bin becomes higher as the number of bin entries is reduced thus depreciating the measurement and hiding physical information within the errors.

To avoid these two extremal binning choices, the *comfortable range* has been determined while fitting for the b-jet fraction in this analysis. The choice of binning was considered to be in the *comfortable range* of values according to some basic criteria:

- Flavor fractions obtained are within physical range. This means that none of the fractions, b, c, or *light* jets, is negative or is equal to unity, as we expect all of them to be present in the inclusive jet sample.

- Fitting results must vary within the fitting errors while making transition to another bin size.

- Internal consistency must be preserved while fitting b, c, and *light* MC templates to the inclusive MC. In other words, the fitting procedure must give the same numerical answer as MC internal "generator-level" information (within the uncertainties) about flavor fractions.

Followed by these basic rules, the range of binning choices was surveyed, and with the results shown in Figure 7.10 the *comfortable range* for the binning choices was determined.

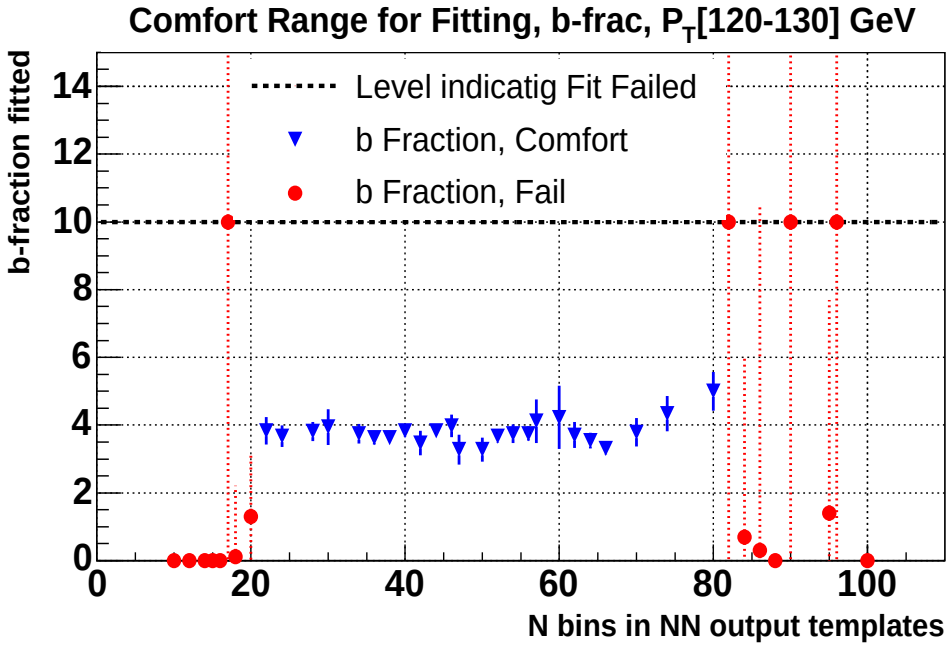

Figure 7.10. An example of determining the number of bins of Neural Net templates to fit for the b-fraction. A similar procedure was repeated for all seventeen $p_\perp$ bins where fits were done. Dashed line indicates that for results equal to that level fitting procedure failed to converge, or other problems exist.

For every one of 17 $p_\perp$ bins, 24 fits within the *comfortable range* of bin choices were made (**the total of 408 individual template fits!**), and the averaged results of these fits were taken to be b-jet fraction (or *purity*) for that $p_\perp$ bin. These binning choices are called comfortable for the simple reason that they provide consistent and systematically similar results for the purity. Without a careful choice of settings for all of these fits the results would have been erratic and unphysical. Individual fitting attempts would have had a multitude of failures, preventing us from establishing the purity with any confidence. It should become clear why we have bothered

to understand the fitting parameters and their ranges, and constrain ourselves to varying these parameters only within the reasonable boundaries.

The choice of starting points and parameter constraints: Fit parameters (flavor fractions) were allowed to take values from 0 to 1 to determine the approximate starting points. Once starting points were established (0.03 for b, 0.12 for c, and 0.95 for light jets), fit parameters were allowed to take any values. Unphysical results such as negative fraction values were treated as fit failure. However within the chosen binning ranges this never happened, supporting the general stability of the fitting procedure.

The choice of variable value range: It was decided to keep the full range of the Neural Net output variable in all fits, since throughout the entire spectrum this variable displays different features which are equally important for the purity determination. Narrowing the range was explored, but this was an unnecessary deprivation of physically useful information stored in template shapes and led to de-stabilizing fitting procedure.

I cannot stress more the importance of the fitting settings established above. The extraction of purity of the sample and establishing the systematic uncertainty associated with the purity is one of the most important tasks in this analysis.

7.3.3 Cut on Neural Net variable

Fitting for b-jet purity was done over the full range of the discriminating variable, the Neural Net output variable, *NN Output*. Since we would like to have our data sample as clean as possible and keep the efficiency for b-jets up while suppressing the backgrounds, we then required $NNoutput > 0.9$ in order to increase the purity. The relative b-jet fraction was recalculated knowing the b-jet content before the cut just by finding the relative ratio of the fitted number of b events to all of the

events above the cut. The final purity for the Neural Net tagged data sample with $NNoutput > 0.9$ is shown in Figure 7.11.

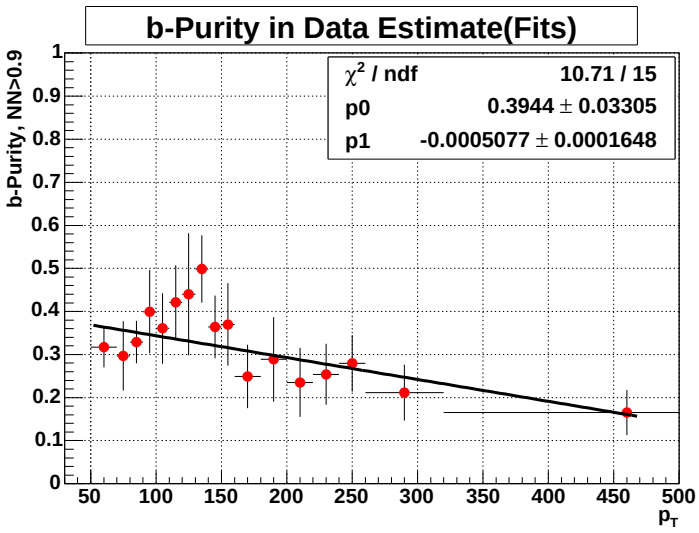

Figure 7.11. Purity for the Neural Net tagged b-jet sample with $NN_{out} > 0.9$ based on template fits. Solid line represents the linear fit.

Figure 7.11 is the cumulative plot of the fitting results, where the value for purity in each $p_\perp$ bin is the averaged result of 24 different template fits for that bin. This is done in order to establish the most reliable value for purity, as well as to address the determination of the systematic uncertainty. Error bars are the width of the Gaussian that was fitted over the purity spectra for that bin. An example of establishing one of the experimental points for purity and a Gaussian fit are shown in Figure 7.12. A much more detailed strategy of systematic uncertainty evaluation will be discussed in 8.1.2.

7.4 b-tagging Efficiency

For the evaluation of Neural Net b-jet tagging efficiency the same $p_\perp$ bins are used as for the purity fits. The procedure is to determine the tagging efficiency for

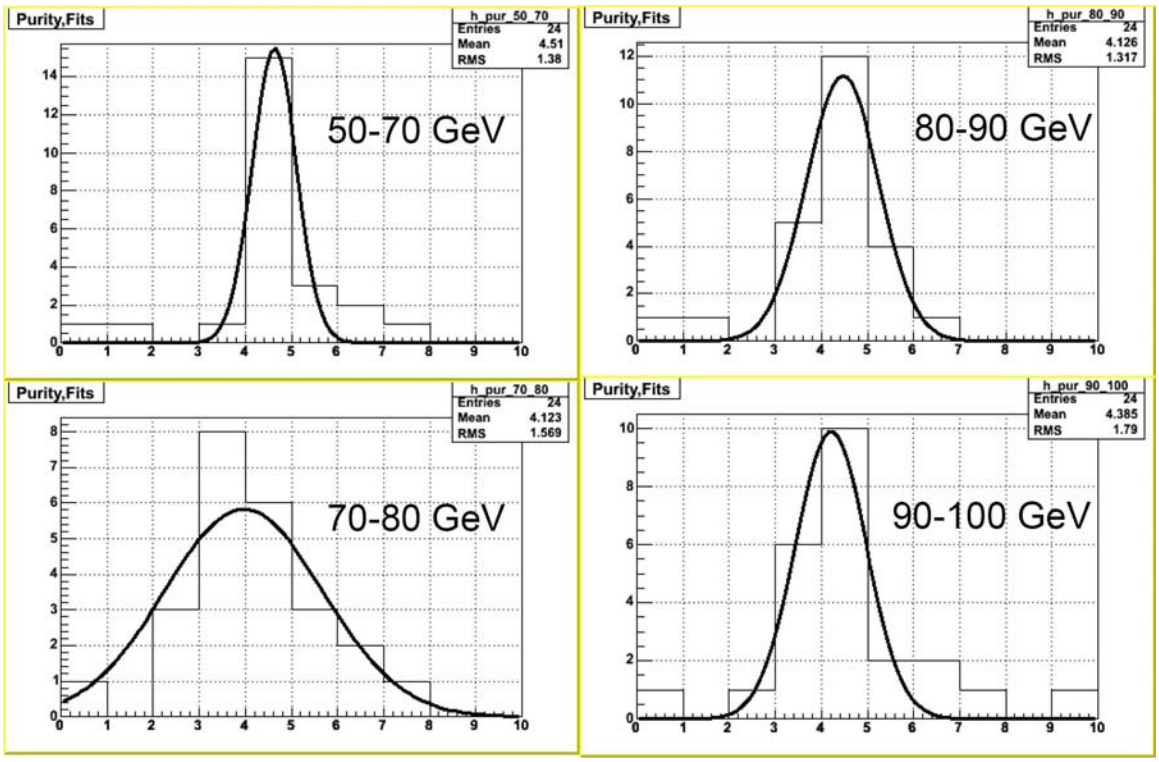

Figure 7.12. An example of purity extraction for four of the $p_\perp$ bins in Figure 7.11 with Gaussian fits over 24 fit values for each of these four $p_\perp$ bins.

the Monte Carlo samples and then to correct for the differences between data and simulation. While the task of finding Monte Carlo tagging efficiency is straightforward knowing the underlying information, correcting it to data is less obvious. Indeed, while intended to reproduce the data, simulation still has such differences as: different errors on particle tracks; different vertex finding efficiency and different flavor fractions than that of the real data. A way to correct the efficiency is to have some flavor-enhancing cut that will not bias any of the input variables of the Neural Net tagger, yet make a significant change in the b-jet content of both MC and data samples. Once found, the correction can be made utilizing differences in the relative effect of that cut on data and simulation.

7.4.1 MC to Data Efficiency Scale Factor

The idea of an independent flavor-enhancing cut was inspired by another analysis closely related to the one described in this manuscript, namely the muon-tagged jet cross section measurement, details of which can be found in [59]. The requirement of the presence of a muon inside the jet significantly increases the heavy flavor content of such a sub-sample, and makes a considerable increase in the b-jet fraction due to the 11% branching fraction $b \rightarrow c + \mu$. While being inefficient for tagging b-jets for the cross section measurement, muon tagging does not relate to or cut directly on any of the Neural Net tagging variables, although it does require a track associated with the jet. The shape studies of the additional muon tag requirement for several neural network input variables can be found in Appendix B. This fact makes the muon tagging requirement an excellent tool to use in finding the scale factor between data and Monte Carlo. The only concern in this case might be the efficiency for the presence of a muon, which has been shown to be nearly identical for isolated muons in data and Monte Carlo [77].

Reconstructed muons were associated with the *JetInfo* object if they pass a number of quality requirements. Muons get matched to the calorimeter jet if in (η, ϕ) space they are within $\Delta R < 0.5$ and $\Delta Z < 1.5$ cm. In addition, the $p_{\perp}$ of the muon was required to exceed 5 GeV. Muon quality requirements are summarized in [78], and are briefly outlined in 5.3.

Having sub-samples of events of both Monte Carlo and data requiring jets to be tagged with muons (Medium and Tight quality settings were used), the scale factor (SF) corresponding the two can be formed. In general, the ideal scale factor would be:

$$SF_{desired} = \frac{\varepsilon^{DT}_{NN,bjets}}{\varepsilon^{MC}_{NN,bjets}} = \frac{N^{DT}_{NN,b}/N^{DT}_{b}}{N^{MC}_{NN,b}/N^{MC}_{b}} \tag{7.3}$$

Here $\varepsilon^{DT}_{NN,bjets}$ and $\varepsilon^{MC}_{NN,bjets}$ are the corresponding efficiencies of the Neural Net b-jet

identification in data and MC defined through numbers of events $N^{DT}_{NN,b}$ and $N^{MC}_{NN,b}$ that passed the NN cut. As we actually do not know the true number of b-jets N^{DT}_{b} in data, we must use some approximate scale factor that we can measure, and construct it to be as close as possible to the true SF. An additional soft lepton tag will enchance the b-jet content, and it is possible to define an observable only $SF_{measured}$ as:

$$SF_{measured} = \frac{N^{DT}_{NN,\mu}/N^{DT}_{\mu}}{N^{MC}_{NN,\mu}/N^{MC}_{\mu}} \tag{7.4}$$

Denoting probabilities of a muon to be present and reconstructed in the jet for jets with and without the Neural Net requirement as $\varepsilon_{NN\mu}$ and ε_{μ} for signal (b-jets) and background, and corresponding branching ratios of signal and background as σ_{sig} and σ_{bkd}, the scale factor can be written:

$$\begin{aligned} SF &= \frac{\left.\frac{\varepsilon_{NN\mu}\varepsilon_{\mu}\sigma_{sig}+\varepsilon_{NN\mu}\varepsilon_{\mu}\sigma_{bkd}}{\varepsilon_{\mu}\sigma_{sig}+\varepsilon_{\mu}\sigma_{bkd}}\right|_{DT}}{\left.\frac{\varepsilon_{NN\mu}\varepsilon_{\mu}\sigma_{sig}+\varepsilon_{NN\mu}\varepsilon_{\mu}\sigma_{bkd}}{\varepsilon_{\mu}\sigma_{sig}+\varepsilon_{\mu}\sigma_{bkd}}\right|_{MC}} = \\ &= \left.\frac{\varepsilon_{NN\mu}\varepsilon_{\mu}\sigma_{sig}+\varepsilon_{NN\mu}\varepsilon_{\mu}\sigma_{bkd}}{\varepsilon_{\mu}\sigma_{sig}+\varepsilon_{\mu}\sigma_{bkd}}\right|_{DT} \times \left.\frac{\varepsilon_{\mu}\sigma_{sig}+\varepsilon_{\mu}\sigma_{bkd}}{\varepsilon_{NN\mu}\varepsilon_{\mu}\sigma_{sig}+\varepsilon_{NN\mu}\varepsilon_{\mu}\sigma_{bkd}}\right|_{MC} \end{aligned} \tag{7.5}$$

The requirement of simultaneously having the Neural Net and a muon tag for the background light flavor jets is extremely unlikely, so we assume the terms $\varepsilon_{NN\mu}\varepsilon_{\mu}\sigma_{bkd} \approx 0$ in both MC and data. With this assumption in place (7.5) can be rewritten as:

$$SF_{measured} = SF_{desired} \times \frac{\varepsilon^{DT}_{\mu,sig}\sigma^{DT}_{sig}}{\varepsilon^{MC}_{\mu,sig}\sigma^{MC}_{sig}} \times \frac{\varepsilon^{MC}_{\mu,sig}\sigma^{MC}_{sig}+\varepsilon^{MC}_{\mu,bkd}\sigma^{MC}_{bkd}}{\varepsilon^{DT}_{\mu,sig}\sigma^{DT}_{sig}+\varepsilon^{DT}_{\mu,bkd}\sigma^{DT}_{bkd}} \tag{7.6}$$

Here ε_{μ} for both Monte Carlo (MC) and data (DT) represents the probability of a real muon existing in the jet, and it being reconstructed. To further illustrate the concept behind the calculation of the scale factor, the above equation (7.6) can be rewritten as:

$$SF_{measured} = SF_{desired} \times \left[\frac{1+\varepsilon^{MC}_{\mu,bkd}\sigma^{MC}_{bkd}/\varepsilon^{MC}_{\mu,sig}\sigma^{MC}_{sig}}{1+\varepsilon^{DT}_{\mu,bkd}\sigma^{DT}_{bkd}/\varepsilon^{DT}_{\mu,sig}\sigma^{DT}_{sig}}\right] \tag{7.7}$$

As we can see, the equation (7.7) defines the $SF_{measured}$ by means of observables only, and at the limit of similar ratios of the efficiencies in Monte Carlo and data approaches the $SF_{desired}$.

In practice, the scale factor is determined in two steps. At first, in addition to the Neural Net tagging, the sub-samples of both MC and data tagged also with the muon are made. On the second step, tagging rate functions are parameterized in both Monte Carlo and data, and then their ratio produces the scaling factor between data and MC tagging rates. Requirement of the muon will ultimately yield different results in data and simulation, but it is going to change the b-fraction in the exactly same way, providing an observable-only variable sensitive to the tagging efficiencies in MC and data. The tighter the muon quality requirement, the closer scale factor will correct for the differences. Thus we can use the less tight muon setting to estimate the uncertainty associated with the scale factor.

For the final scale factor, evaluation with Tight and Medium muons were used. While more on the systematic uncertainty will follow in 8.1.1, the parameterized (see Appendix D) tagging rate functions between data and MC for the two muon settings are shown in Figures 7.13. Then the ratio of these curves provides the correction scale factor by which Monte Carlo efficiency should be multiplied to reflect the tagging efficiency expected in the data sample. These scale factors in case of Medium and Tight muon requirements are shown in Figure 7.14.

7.4.2 Expected Efficiency in Data

Having determined the scale factor, the efficiency in data can be attained by multiplying Monte Carlo tagging efficiency by the scale factor. The MC efficiency was found by imposing the Neural Net cut of 0.9 and relating the number of generated b-jets passed the cut to the overall number of b-jets as a function of jet $p_{\perp}$.

a)

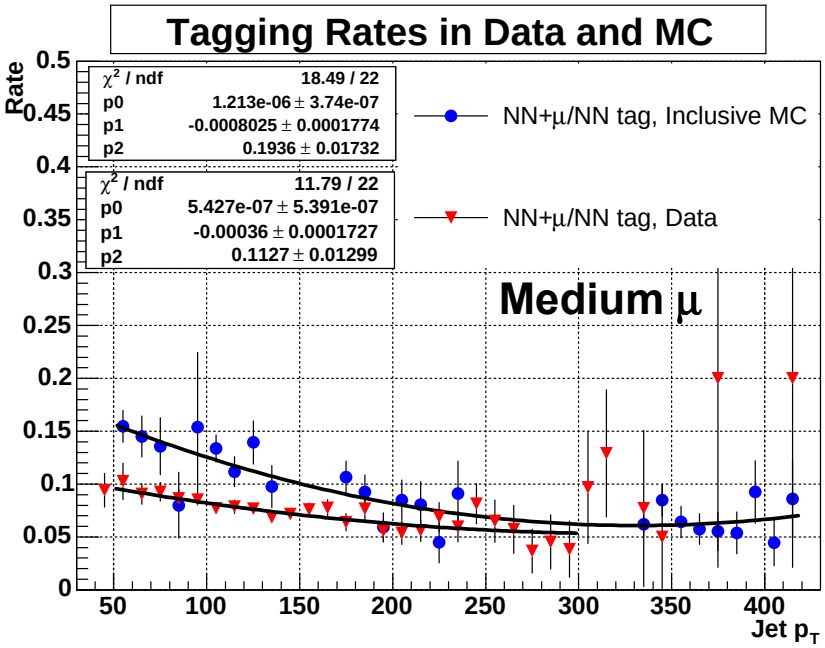

b)

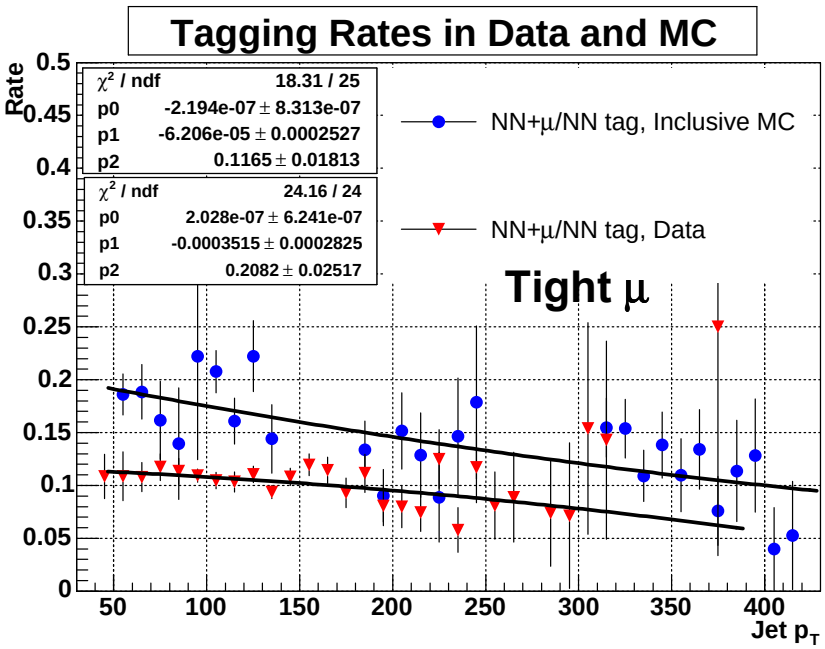

Figure 7.13. Ratios of the tagging rates with and without an additional muon tag requirement in Monte Carlo and in data. a) The above plot shows the ratios with "Medium" quality muon tag. b) The ratios corresponding to the "Tight" muon setting are pictured below.

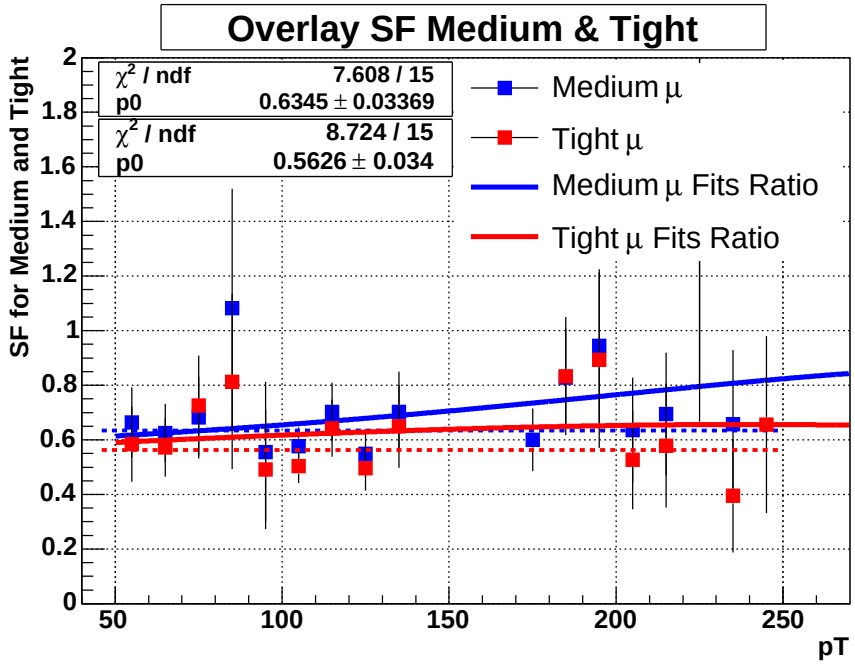

Figure 7.14. The resulting scale factors to correct Monte Carlo efficiency to match the one in data. The one corresponding to the "Tight" setting (shown in Red) was used to correct the efficiency, and the "Medium" setting (shown in Blue) was utilized to estimate the systematic uncertainty. Dashed lines represent linear fits. For the parameterizations for Medium and Tight scale factors, please see Appendix D

Then the resulting efficiency distribution is multiplied by the scale factor attained from Tight muon tagging (Figure 7.13), and expected b-jet finding efficiency in data emerges. Results are shown in Figure 7.15. The functional form and values of the parameters for efficiency in data can be found in Appendix D.

7.5 Unsmearing

With the b-jet tagging efficiency and purity as functions of jet $p_{\perp}$ in place, the b-jet cross section can be derived from the inclusive jet cross section shown in Figure 7.1. This measurement, however, will not be the true particle-level b-jet cross section. The detector resolution effects are needed to be corrected for by the

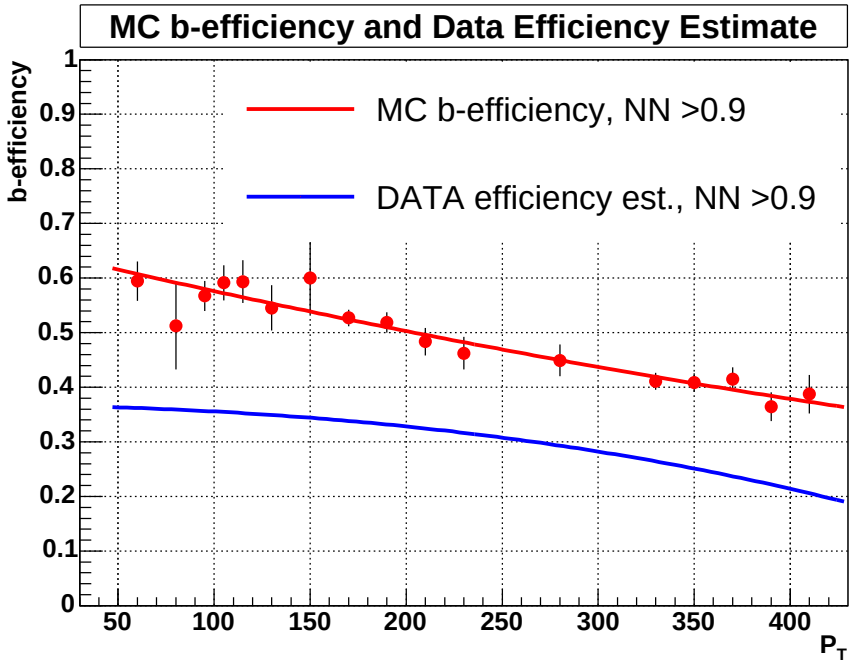

Figure 7.15. Monte Carlo b-jet tagging efficiency with the Neural Net variable cut $NN_{out} > 0.9$ represented by a linear fit, and b-jet tagging efficiency estimate in data with $NN_{out} > 0.9$ after application of the scale factor.

means of procedure called *unsmearing*.

To extract the b-jet cross section as a function of the true particle energy of the jet from the calorimeter-level measurement, we have to remove the effect of the finite resolution (discussed in 5.4) with which the calorimeter measures the jet energy. In jet analyses, the unsmearing procedure is well-established, and a general schematic is pictured in Figure 7.16. In this analysis it is done in the traditional way [40, 59]. In general, the observed spectrum can be written as $F(p_\perp)$, while the particle-level truth spectrum can be denoted as $f(p'_\perp)$. The smearing function $G(p'_\perp\text{-}p_\perp,\, p'_\perp)$ is usually taken to be a Gaussian. The observed spectrum can be written as:

$$F(p_\perp) = \int_0^{\frac{\sqrt{s}}{2}} dp'_\perp \cdot f(p'_\perp) \cdot G(p'_\perp - p_\perp, p'_\perp) \tag{7.8}$$

The particle level truth function can be parameterized in a number of ways. One

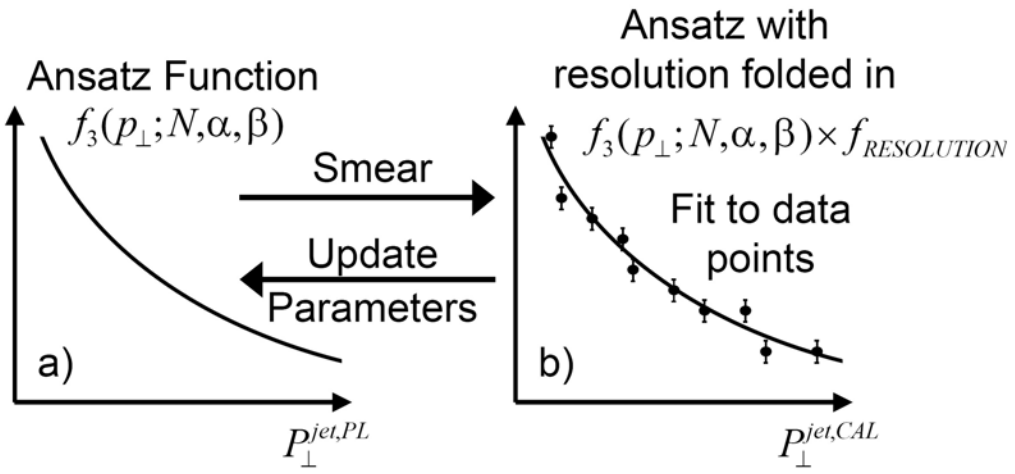

Figure 7.16. Schematic view of the procedure used to unsmear the b-jet cross section. a) The ansatz function f as function of jet $p_\perp$, which is smeared according to the jet resolution to get the distribution as function of jet ${p_\perp}^{CAL}$, which is then fitted to the measured data points, shown in b).

popular ansatz is to use a three parameter function:

$$f(p_\perp) = f_3(p_\perp; N, \alpha, \beta) = N \cdot p_\perp^{-\alpha} \cdot e^{-\frac{p_\perp}{\beta}} \tag{7.9}$$

Another ansatz tried was the following four parameter function:

$$f(p_\perp) = f_4(p_\perp; N_1, k_1, N_2, k_2) = \sum_{j=1}^{2} e^{N_j - \frac{p_\perp}{k_j}} \tag{7.10}$$

Thus one inserts this function into the smearing equation and minimizes the difference between the smeared equation and the data (after all efficiency corrections to the spectra are imposed). The data was then fitted to the smeared ansatz via the following χ^2 function:

$$\chi^2 = \sum_{i=0}^{27} \frac{1}{\Delta y_i^2} \left[y_i - \frac{\int_{x_{1,i}}^{x_{2,i}} \int_0^{\sqrt{s}/2} f(p_\perp) \frac{1}{\sqrt{2\pi}\sigma(p_\perp)} \exp\left(-\frac{\left(p_\perp - p'_\perp\right)^2}{2\sigma^2} \right) dp_\perp dp'_\perp}{x_{2,i} - x_{1,i}} \right]^2 \tag{7.11}$$

Finally, one can correct the data by the unsmearing correction factor C_{PL} defined by the ratio:

$$C_{PL} = \frac{\int_l^h f\,(p_\perp) dp_\perp}{\int_l^h F\,(p_\perp) dp_\perp} \tag{7.12}$$

where integration is performed over $p_\perp$ within the bin, and determine the corrected and unsmeared result [59]. In essence, this is the same as defining the measurement as that of $f(p_\perp)$ (assuming a good fit of $F(p_\perp)$), but with the statistical variation preserved. In Figure 7.17, we see the efficiency corrected (but not unsmeared) cross section. In Figure 7.18 we see an overlay of the data (points), point-by-point fit to the smeared function (stars, $*$), and the unsmeared parent function (black line). The figure shows a fit to the smeared ansatz of equation (7.9). A fit to equation (7.10) was performed successfully and yielded numerically similar results. This fit will be discussed in more detail in 8.1.5. The parameters of the unsmearing function are given by Table 7.4. The correlation coefficients for these parameters are given in Table 7.5. The error matrix for the unsmearing ansatz fit can be found in Table 7.6. The unsmearing correction coefficients C_{PL} and fractional differences between fit and data points are shown in Figures 7.19 and 7.20.

The unsmearing procedure produces the correction coefficients C_{PL} (please refer to Equation 2.20) which allow one to correct the measured spectrum to the particle level. Efficiency and purity have also been already determined as discussed above. If one combines all of the information included above, one can determine the final, efficiency and purity corrected cross section. The results are summarized in the next Chapter.

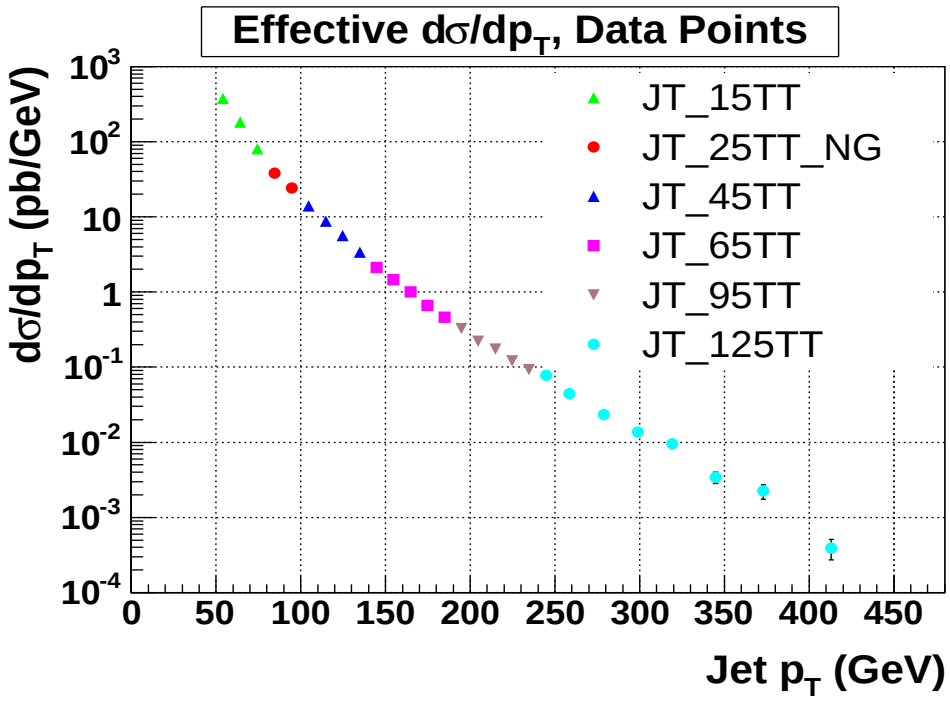

Figure 7.17. The efficiency-corrected (but not unsmeared) b-jet cross section.

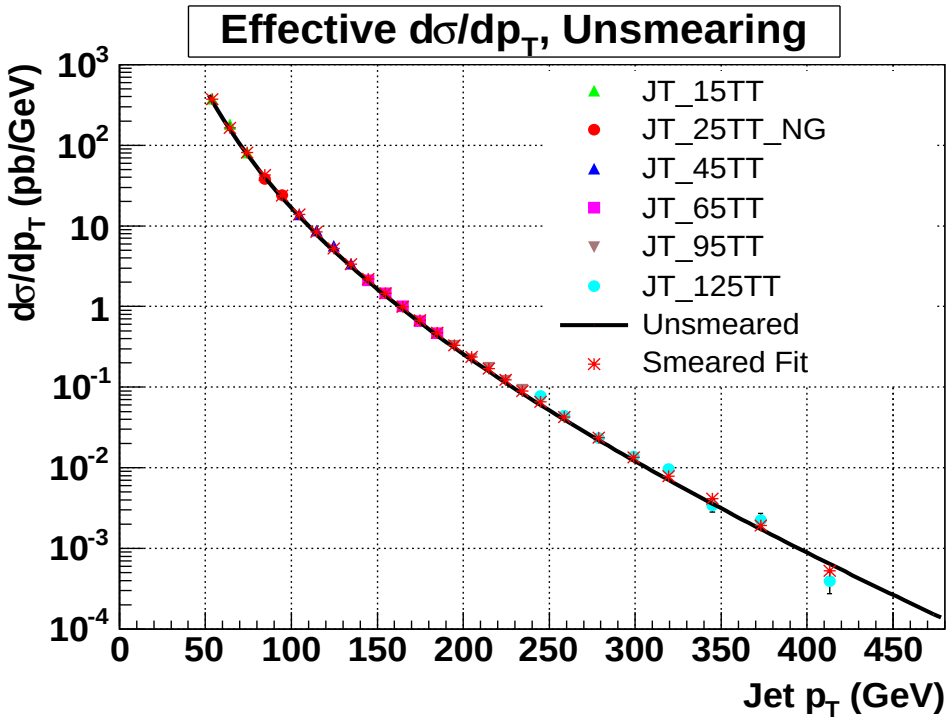

Figure 7.18. An overlay of the data (points), a point-by-point fit to the smeared function (stars, *), and the unsmeared parent function (black line) represented by equation (7.9).

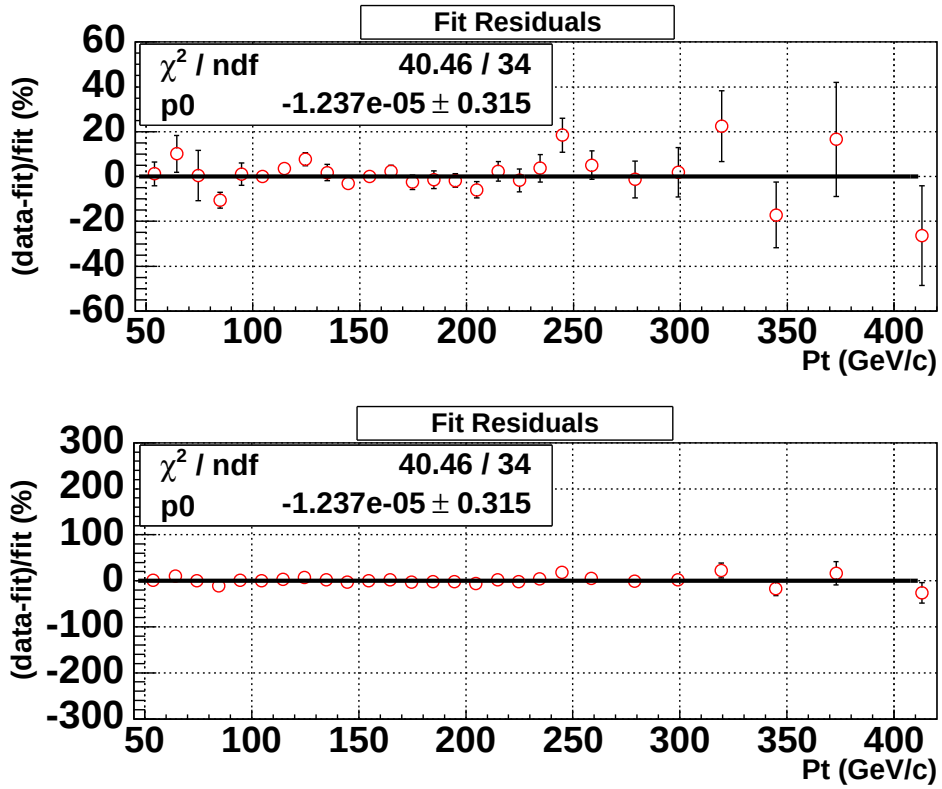

Figure 7.19. The fractional difference between the data and the smeared fit. Top and bottom are the same plots, except for top having an expanded vertical scale.

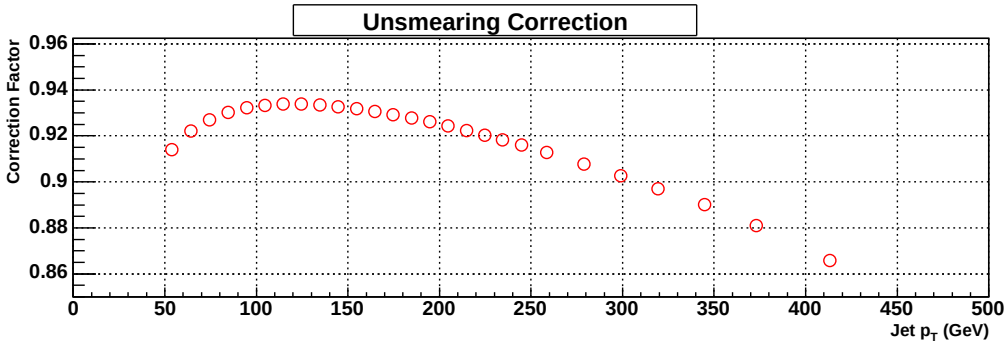

Figure 7.20. Ratio of unsmeared/smeared fit, as discussed in the text.

TABLE 7.4

UNSMEARING FUNCTION PARAMETERS

Parameter	Fitted value	Parabolic Error
N	3.786×10^{9}	1.18×10^{9}
α	3.85	5.2×10^{-2}
β	66.64	2.47

TABLE 7.5

UNSMEARING FIT CORELLATION MATRIX

	N	α	β
N	1	0.997	0.941
α	0.997	1	0.962
β	0.941	0.962	1

TABLE 7.6

UNSMEARING FIT ERROR MATRIX

	N	α	β
N	1.4×10^{18}	9.37×10^{7}	2.76×10^{9}
α	9.37×10^{7}	2.68×10^{-3}	1.89×10^{-1}
β	2.76×10^{9}	1.89×10^{-1}	6.125

CHAPTER 8

EXPERIMENTAL RESULTS

In Chapter 7, the experimental b-jet cross section measurement has been obtained, and corrected to the particle level. However, the measurement is not complete until of the systematic uncertainties are established and properly applied to the result. This chapter discusses the sources and details of the calculation of systematic uncertainties for this measurement, as well as providing cross checks by comparing the resulting b-jet cross section to Monte Carlo (*Pythia* leading order) and to the experimental result produced by the CDF collaboration.

8.1 Systematic Uncertainties

The sources of uncertainties for the presented measurement include the common statistical errors as well as systematic errors. Systematic uncertainties are associated with all of the steps associated with obtaining the final result, and include errors on the efficiencies, the error on b-content extraction, the error coming from the jet energy scale corrections and finite detector resolution, luminosity determination, and errors due to the unsmearing procedure.

8.1.1 Uncertainty on Tagging Efficiency

The main source of uncertainty in the tagging efficiency in data is the ambiguity associated with the scale factor, described in the previous chapter (Subsection 7.4.1)

and the underlying assumptions and approximation. The scale factor calculation relies on muon-tagged jets, and the MC is corrected to data using the tightest μ quality possible. A reasonable estimate for the uncertainty will be the variation of the scale factor value caused by a different choice of muon quality. Scale factors produced with using *tight* and *medium* muon quality are shown in Figure 7.14. The associated systematic uncertainty is taken to be the difference between the two (Figure 8.1).

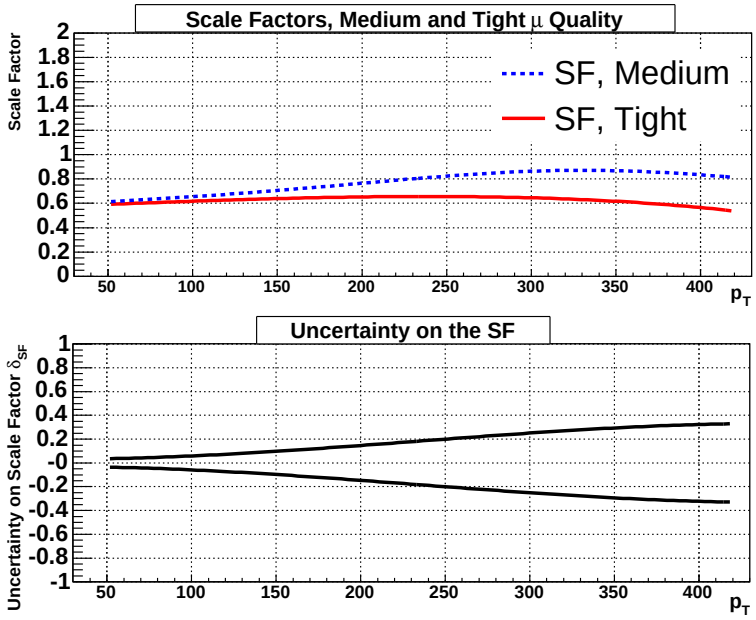

Figure 8.1. The systematic uncertainty on the tagging efficiency (below) is taken to be the variation of MC-Data scale factor *SF* determined with *tight* and *medium* quality muons (above).

As we can see, this uncertainty gets large only at high $p_\perp$, reaching about 35%. However, this is a very conservative estimate, and as we will find below, it is rather small compared to the dominant error, the Jet Energy Scale uncertainty.

8.1.2 Uncertainty on Purity

In Section 7.3 we extracted the purity of the b-jet sample by fitting the MC Neural Net output templates to the NN shape in data. To get an estimate of the uncertainty, each of 17 bins in $p_\perp$ was fitted 24 times within the stable fitting range with different choices of the NN bin width. One way to estimate the uncertainty was to place all 24 fit results in the histogram for each $p_\perp$ bin, and to fit it with a Gaussian. The width of the Gaussian then would produce the uncertainty estimate. However, 24 individual fits are barely enough to carry out this procedure. As all fits were individually checked for quality and consistency, fitting more combinations did not seem feasible. It was decided to pursue a different route, although it will tend to overestimate the purity extraction errors.

What was done is for every one of the 24 binning choices in the NN variable (for all $p_\perp$) its corresponding purity $p_{b-tagging}^{i=1-24}$ dependence from $p_\perp$ was produced. These curves are shown in Figure 8.2. In Figure 8.2a, only four sets of purities are plotted and fitted via straight lines. In Figure 8.2b, the average of all 24 sets produce the range, within which the purity results reside. The average curve was produced and taken to be final purity, while the bounding curves (which contain all of the fit results) were considered the boundaries for uncertainty. The resulting uncertainty (the difference between the median and purity boundaries) is illustrated in Figure 8.2c. This uncertainty is likely an overestimate, but since there were errors on individual fits associated with every fitting attempt, and the Monte Carlo template shapes are not treated as idealizations, this is a fair although conservative representation of the uncertainty value on purity.

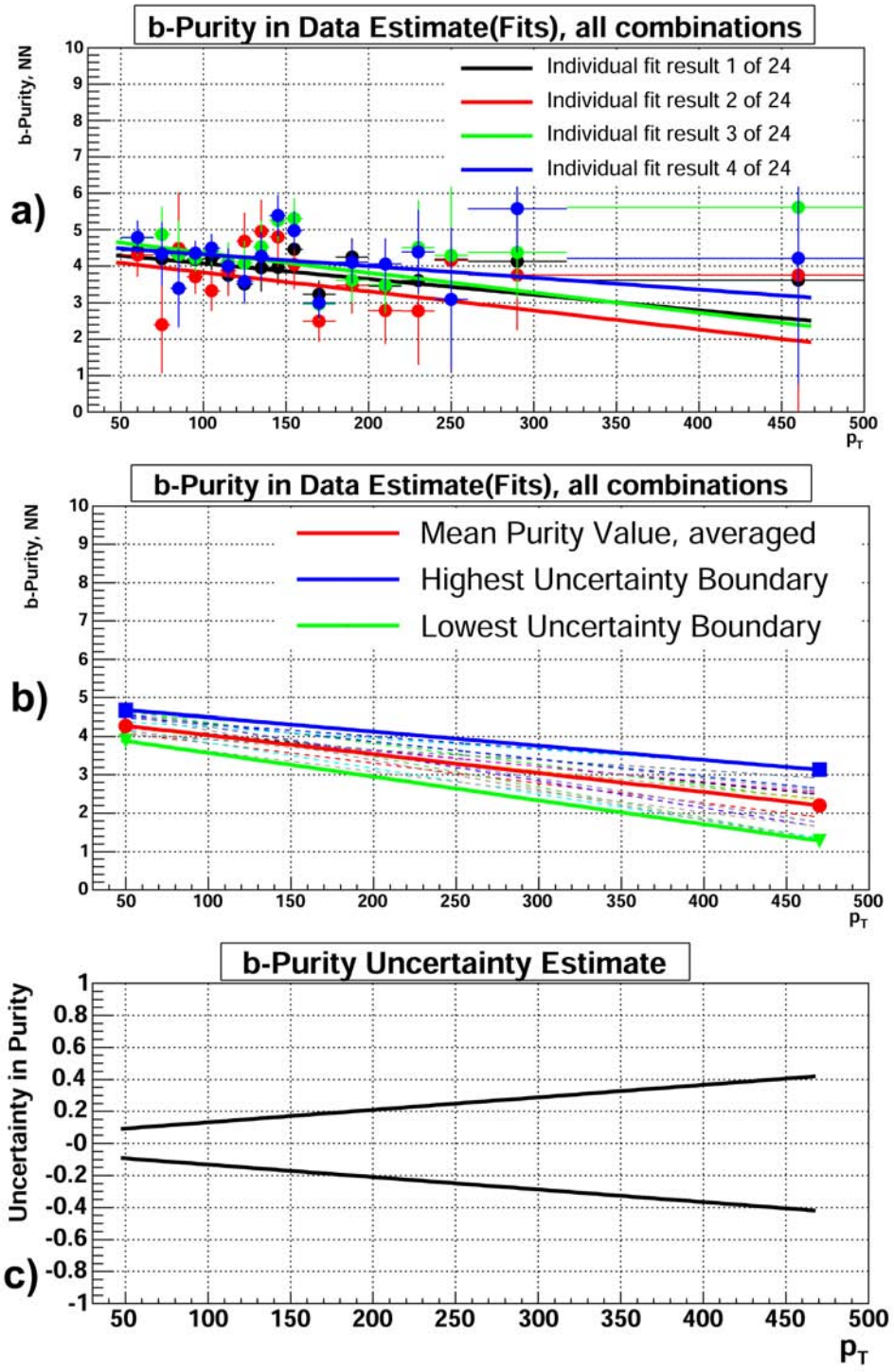

Figure 8.2. Estimate on fitting procedure to obtain purity. a) Only four sets of purity estimates plotted and fitted with the straight lines. b) All 24 lines produce the variation range. The resulting uncertainty is the difference between the median and purity boundaries and is illustrated in (c). Please see additional description in the text.

8.1.3 Uncertainty on Jet Energy Scale

As it was mentioned above, the uncertainty on JES (described in Section 5.1.2) is the leading source of systematic uncertainty in this analysis. This fact is typical for all jet-based studies, and is connected to the fact that in the photon plus jet sample that was used to calibrate jet energies, no jets exist beyond an energy of ≈300 GeV. Therefore the uncertainties are largest at highest $p_\perp$ [54, 57].

The uncertainty on JES was determined in a quite standard fashion. To incorporate the errors due to jet energy scale (JES), we determined the JES correction for each jet and increased it or decreased it by one standard deviation. Then the two new raw cross-section measurements were created, one for each $p_\perp$ bin, which is determined by the number of events for the standard JES, as well as the high and low valued of JES ($JES \pm \sigma_{JES}$). The effect due to the high and low corrected cross sections increased or decreased the number of events in each bin. The JES systematic error was delineated by the cross-sections as determined by the one-sigma variation of the JES. In all cases, the unsmearing factor C_{PL} (please refer to Equation 2.20) was taken to be the same as the central value.

The effect of this uncertainty on the cross section is presented in Figure 8.3, and its value is more clearly shown in Figure 8.4. The JES errors are relatively small at $p_\perp$ values of 100 GeV/c (about 20%) rising to (-50%, +70%) at 400 GeV/c.

8.1.4 Uncertainty on Jet Resolution

While the comprehensive study of jet resolution was done in [60], it was decided to apply these results to estimate the uncertainty on the jet resolution. While again being a conservative estimate, the following approach is intended to address the resolution uncertainty fairly, especially since the overall effect of this error is relatively small.

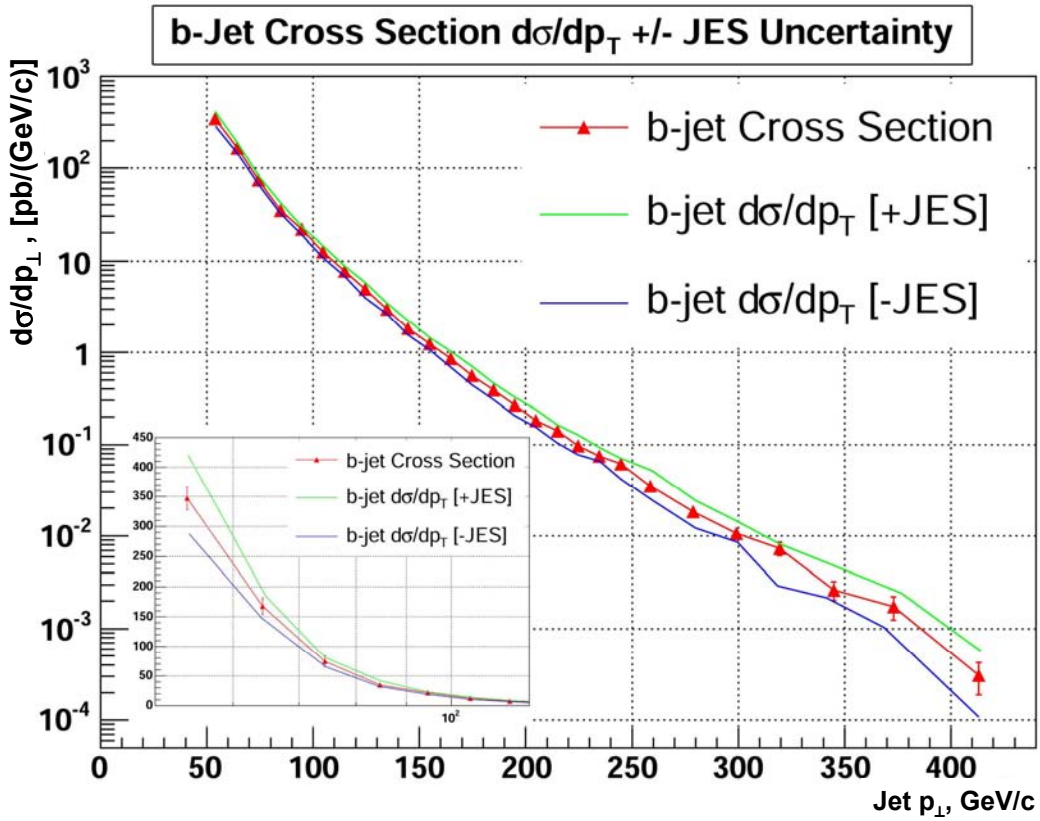

Figure 8.3. Cross section for b-jets (efficiency correction only) with the effect of varying the jet energy scale by one standard deviation. the inlay shows linear zoom on $p_\perp$ from 50 to 115 GeV.

In Section 5.4 (please refer to Figure 5.5) we discussed measurements of jet resolution for jets with $|y| < 0.4$ and $0.4 < |y| < 0.8$. Jets used in this analysis are in the $|y| < 0.8$ kinematic region. The expected resolution of these jets therefore is between the results for $|y| < 0.4$ and $0.4 < |y| < 0.8$, which were taken to be the boundaries in which resolution *may* vary. For the upper limit, the parameters N, S and C for the jet resolution function (Equation 5.16) were taken for jets with $0.4 < |y| < 0.8$ and for the lower limit, $|y| < 0.4$. The two cross section results were produced and unsmeared using the two resolution settings, thus giving the cross section uncertainty caused by the uncertainty on the varying jet resolution. The

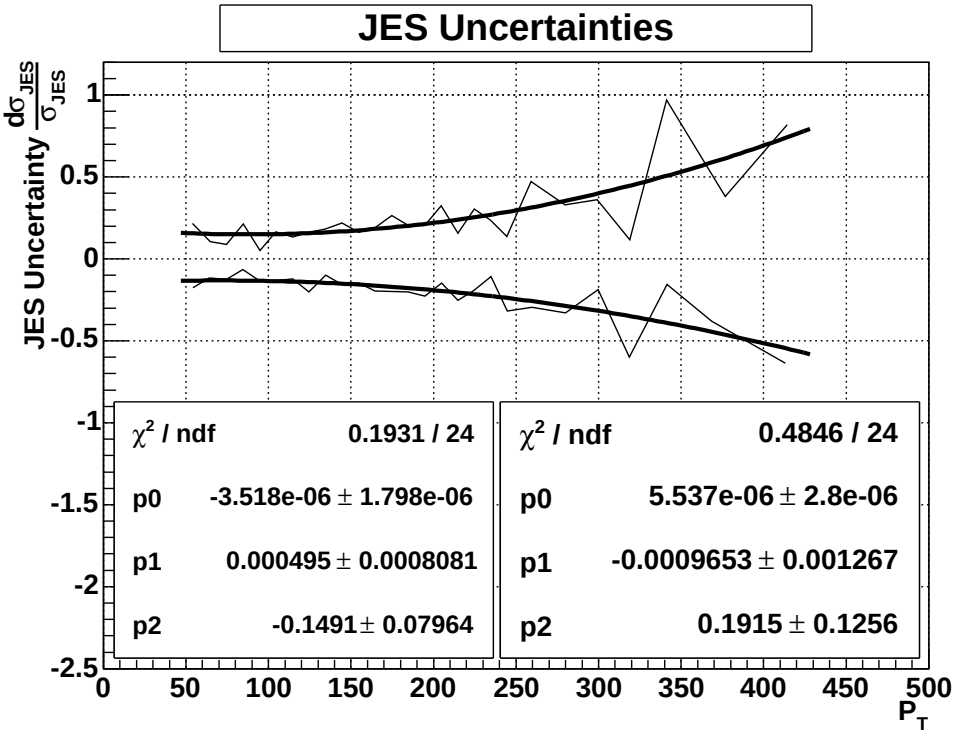

Figure 8.4. Linearized presentation of the effect of varying the jet energy scale by one standard deviation. While the statistical variation is such that occasionally one finds a fluctuation of the one-standard-deviation high JES can be below the central value, the broad trend appears to be a 20% variation at low $p_\perp$, rising slowly by 30-50% variation at 400 GeV. The thin line is the raw error values, while the thicker line denotes a quadratic fit.

resulting uncertainty is shown in Figure 8.5.

As we can see, differences in jet resolution have a relatively small effect on the resulting measured cross section result. This systematic uncertainty decreases slowly with jet $p_\perp$ from 15% at 50 GeV/c, and plateaus at about 8%.

8.1.5 Uncertainty on Unsmearing

The uncertainty on the unsmearing procedure itself (see Section 7.5) must reflect our choice of parameterization for the cross section shape. Along with the ansatz function used to unsmear data (Equation 7.9), there is another popular function

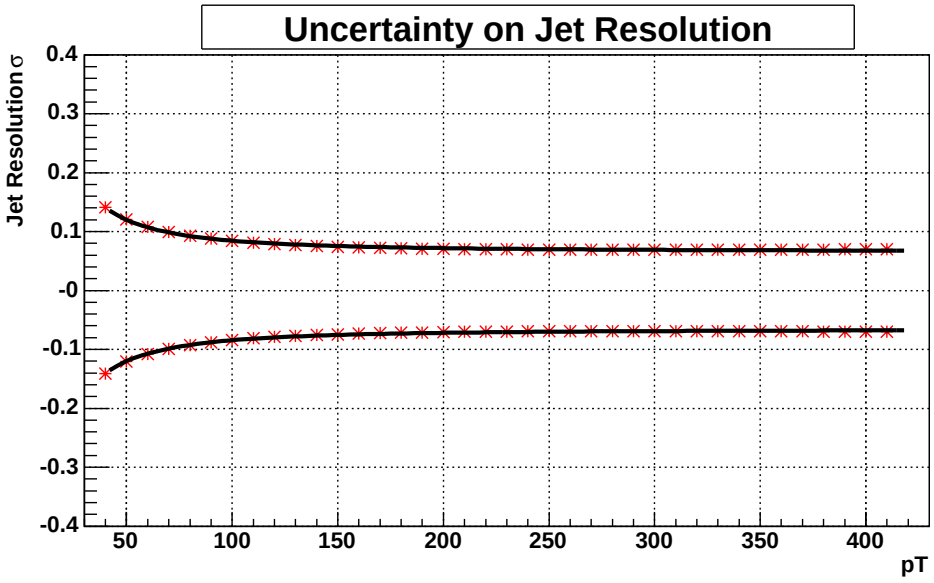

Figure 8.5. Uncertainty on jet resolution for jets within $|y| < 0.8$

that can be used to parameterize the cross section:

$$f(p_\perp) = \sum_{j=1}^{2} e^{N_j - \frac{p_\perp}{k_j}} \tag{8.1}$$

The unsmearing systematic error is determined by using the different ansatz, doing the unsmearing, and taking the variation of the unsmearing correction coefficients obtained by the two ways as the error. Fit results for both parameterizations are shown in Figure 8.6. The uncertainty produced in such way is illustrated by Figure 8.7.

8.1.6 Uncertainty due to Luminosity

The luminosity measurements done with the Luminosity Monitor (please see 3.3.9) also contain a systematic uncertainty that must be included. Since all of the luminosity measurements at DØ are done in a centralized way by the luminosity group [80], the official uncertainty value of 6.5%, independent of $p_\perp$, was taken.

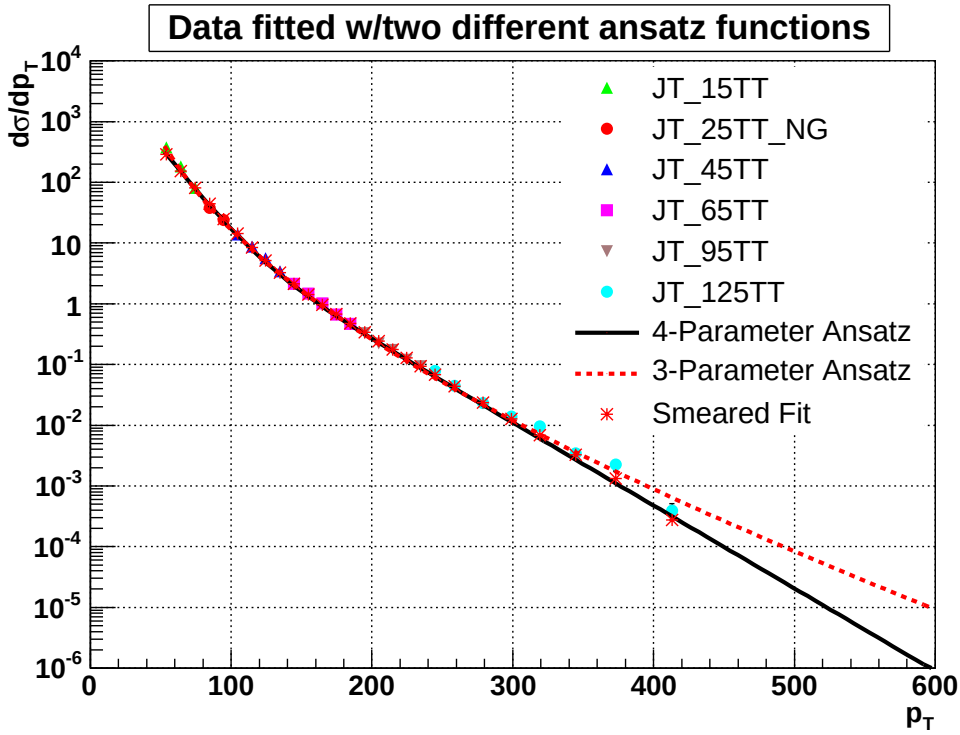

Figure 8.6. Fit results done to estimate the unsmearing systematic uncertainty. The three parameter ansatz function is given by Equation 7.9 and four parameter function is given by Equation 7.10.

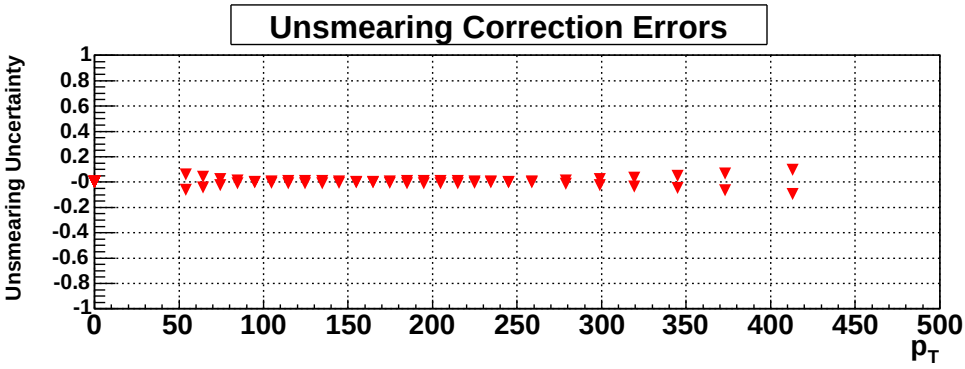

Figure 8.7. Resulting systematic uncertainty due to the unsmearing procedure.

8.1.7 Summary of the Systematic Uncertainties

Summarizing the systematic uncertainties discussed in Sections 8.1.1 through 8.1.6, the total resulting error along with the individual uncertainties mentioned is shown in Figure 8.8. The total uncertainty comes from adding the individual systematic uncertainties in quadrature.

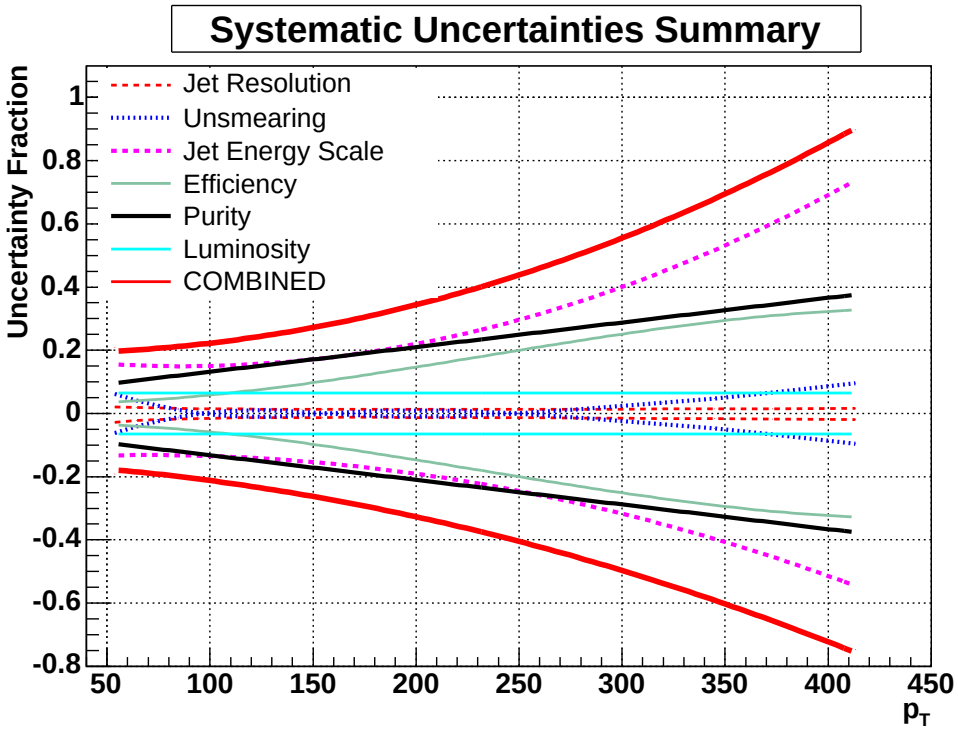

Figure 8.8. Systematic uncertainties summary for the Neural Net tagged b-jet cross section analysis.

As it can be seen, the dominant sources of errors are the Jet Energy Scale, b-purity extraction procedure, and tagging efficiency estimate using the MC/Data scale factor. Although the uncertainty is very large, it is comparable to uncertainties cited in previous jet analyses done both by DØ and CDF collaborations [31, 40, 57, 81, 82].

8.2 b-Jet Cross Section Result

There are many ways to present the measured cross section result, and since most of these representations can be easily converted to and from each other, the following representations are mainly a matter of choice and practicality. During the discussion of the measurement and uncertainties, the experimental b-jet cross section result itself has been already presented, for instance by Figures 7.18 and 8.3. The Tables C.1 and C.2 summarizing and tabulating this result and associated errors can be found in the Appendix C. In this section we compare the result with simulation and previous physics results. However, the cross section produced in this analysis was not compared to any of these results until all of the measurement and processing steps were completed. This was done to avoid any subconscious bias that could be induced by knowing the outside information.

8.3 Comparison to Monte Carlo and Experimental Results

Before we proceed with the comparing this result to others and also to the theoretical prediction, let us briefly review previous measurements. The first b-jet cross section result was obtained in the very beginning of DØ Run II (by the Summer of 2003), using only about 3.7 pb^{-1} of data, and with a muon to tag the b-jets [40]. The cross section measured in that analysis is shown in Figure 8.9. Because of the low statistics and quite inefficient tagging method utilizing muons in jets, this result was not able to explore the high $p_\perp$ kinematic region, which is one of the main aims of this present study.

Several preliminary measurements of the cross section of b-jet production including high $p_\perp$ are available from the CDF collaboration [81, 82]. The CDF result is shown in Figure 8.10 [81]. The reconstructed secondary vertex mass was used as a signature for tagging b-jets. This result was also limited in its $p_\perp$ region coverage and

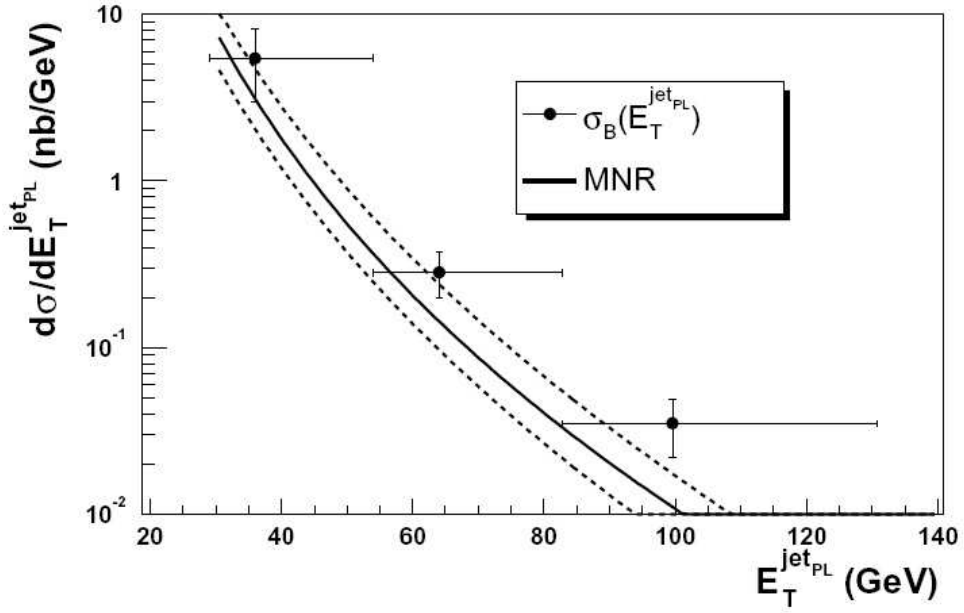

Figure 8.9. Muon-tagged b-jet cross section result obtained by DØ in Run II [40], comparison of the data to the theory is shown. The solid line shows the result of the theoretical calculation, with the dotted lines showing the error on this calculation coming from varying the b-quark mass and the factorization and renormalization scales. The black points represent the measured data.

had relatively high systematic uncertainties, as the secondary vertex mass variable spectra for b, c and light quark jets used to fit for the b fraction become less distinctive at high $p_\perp$. Another recent experimental result made by the CDF collaboration is presented in Figure 8.11 illustrating the best preliminary result obtained in these studies using about 300 pb^{-1} of Tevatron data. This result was produced using a dataset of comparable size as the analysis presented herein, and it is the most recently approved measurement of high $p_\perp$ b-jets to date. In addition, the rapidity region is very close to the one used in this analysis, and a simple correction can be made to reasonably compare the two measurements. It will be fair to compare that analysis to the measurement described in this dissertation, and the comparison will

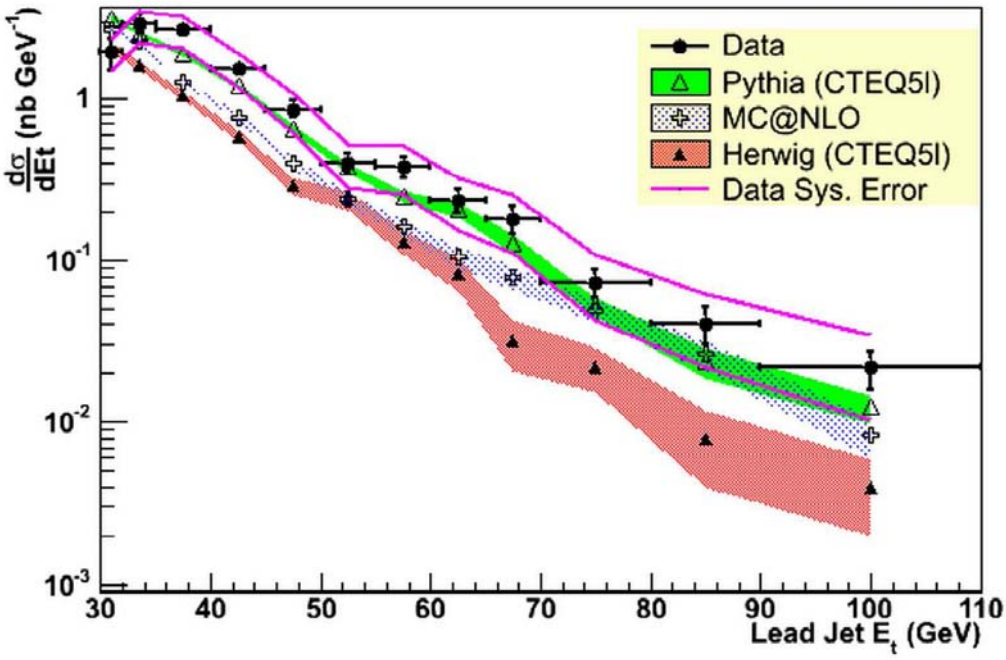

Figure 8.10. b-jet cross section result obtained by CDF in Run II [81]. Shown is the b-jet cross section as a function of corrected jet $p_{\perp}$, superimposed with various Monte Carlo predictions.

be shown shortly.

Besides the experimental measurement comparisons, which are of primary importance, it is also prudent to provide a leading order simulation comparison. The Monte Carlo simulation samples used to produce the theoretical (leading order) cross section were the same samples utilized in building the Neural Net variable templates (Summary Table 7.3). The Pythia [75] leading order generation was used. The cross section was extracted from separate inclusive MC samples using generator-level information, and the same jet algorithm and analysis code as was used to process the data (to ensure internal consistency). The present experimentally measured b-jet coss section result is compared to the Pythia and CDF Run II [82] results in Figure 8.12. The experimental CDF plot was not numerically tabulated, so the points

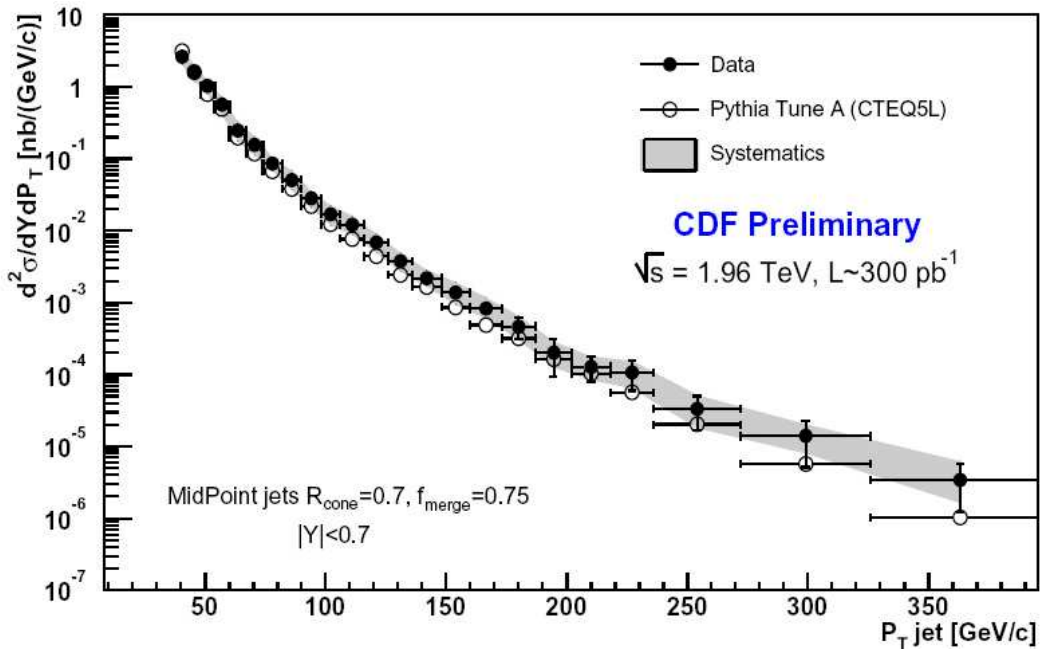

Figure 8.11. b-jet cross section result obtained by CDF in Run II [82]. Shown is the b-jet cross section as a function of corrected jet $p_{\perp}$, superimposed to Pythia Monte Carlo Leading Order prediction.

were extracted from the graph cited by Figure 8.11, and then fitted via a smooth ansatz within the approximate values for the uncertainties.

As we can see from Figure 8.12, the result is generally in agreement with CDF data, but does not correspond well to the Pythia LO prediction. This fact is likely due to Monte Carlo tuning which needs to be corrected. As we can observe in all of the experimental plots, Pythia leading order predictions for the b-jet cross section tend to be lower than the experimental measurements. In some cases, presented results are scaled to Monte Carlo to compare only the shapes of cross section distributions, making the comparison of the absolute values moot. We refrain from relative scaling in our presentation, comparing both shapes and absolute measurements. In order to illustrate better the correspondences established in Figure 8.12, we can present the result as the relative comparison constructed as $(Data - MC)/MC$, thus

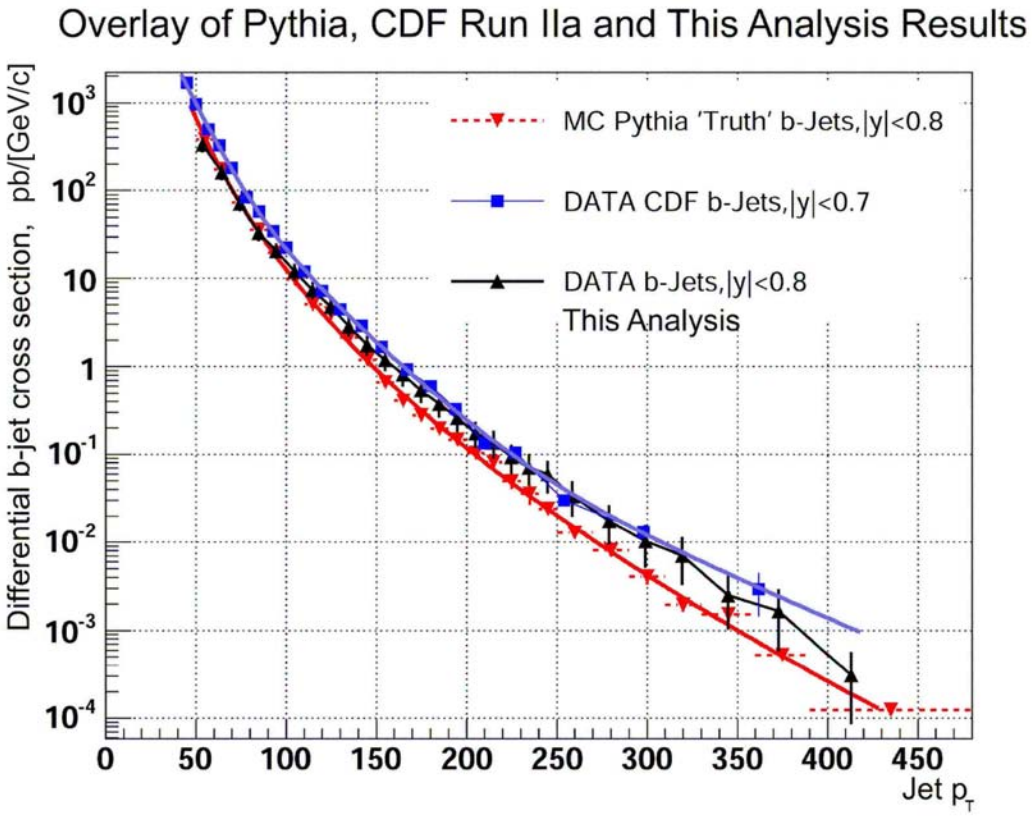

Figure 8.12. The present b-jet cross section result overlay with the CDF Run II [82] results compared to Pythia (LO) prediction.

establishing MC to be a unit measurement, and the difference between Monte Carlo and data superimposed on that scale. The result of such a comparison is shown in Figure 8.13.

While the comparisons (Figurs 8.12 and 8.13) indicate the disagreement with Pythia (LO) prediction, the data is in reasonable agreement with the previous experimental measurement. While the subsequent tuning of Monte Carlo and comparisons to the Next to Leading Order (NLO) predictions are needed, and work is being done to provide these tests, this task is a fairly complex analysis of its own, and is beyond the scope of this dissertation.

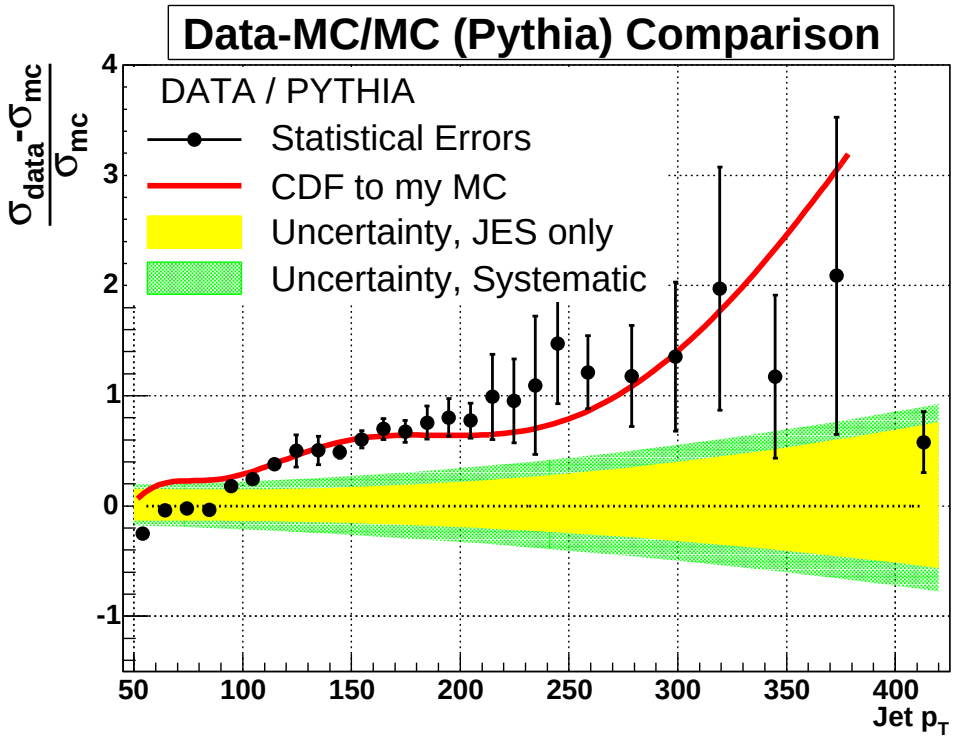

Figure 8.13. The present b-jet cross section (points with error bars) and the parameterized by the red curve CDF Run II results [82] compared to Pythia(LO) prediction. The green band represents the absolute values of the systematic uncertainty, while the yellow band is the JES uncertainty only. The error bars are statistical errors only. CDF curve is given as a parameterized approximation.

CHAPTER 9

CONCLUSION

In this analysis, the measurement of the differential b-jet cross section based on 312 pb^{-1} of Tevatron Run IIa data produced with $\sqrt{s} = 1.96$ TeV in $p\overline{p}$ collisions and collected with the DØ detector, has been presented and compared with theoretical predictions as well as previous experimental results. Jets in the central detector region ($|y| < 0.8$) were tagged using the Neural Net, and the NN output variable was fitted for the b-jet fraction with Monte Carlo driven templates. The tagging efficiency in Monte Carlo was corrected to better correspond with the data. The total b-jet cross section, fully corrected for all detector effects and lepton contributions was determined. The sources of systematic uncertainties have been identified, and values for the uncertainties have been established. The results of the present measurement are tabulated values along with the values for the statistical and systematic errors, and can be found in Appendix C.

The preliminary result is in agreement with previous experimental data, while providing an expanded coverage of b-jets with extremely high values of transverse momentum $p_\perp$. Presented results do not match to the Monte Carlo (Pythia) leading order prediction for several possible reasons. First, the leading order processes may be insufficient to explain the data. Second, the Monte Carlo was tuned using experimental data, and there were no previous measurements of the b-jet production cross section done by DØ at such a high $p_\perp$ (up to about 420 GeV) kinematic region.

This measurement came to a fruition as a result of many comprehensive studies, including b-tagging algorithms, detailed comparisons of data and Monte Carlo event structures and variables, as well as refining many of the procedures learned with help of DØ Run I results, which one can refer to as a common knowledge.

In the course of this study, several methods for identifying b-jets have been proposed and tried, and the present tagging algorithm is a convolution of the best results and efforts of many people at DØ and beyond, done in that direction.

This result has provided additional information, and some of the useful experimental answers concerning b-flavor tagging, b-jets, and b fractions to many people working on various analyses including top, τ-lepton, missing energy $\not\!\!E_T$, and b-physics.

APPENDIX A

TEMPLATE SHAPES FOR THE NEURAL NETWORK OUTPUT VARIABLE

In this section the shape for the Neural Net output variable obtained for the inclusive Monte Carlo is compared to data in corresponding $p_\perp$ bins. This comparison further illustrates the difference between the data and simulation noted in the process of determining the tagging efficiency for the b-jets (discussed in Section 7.4). The fraction of b-jets in the inclusive Monte Carlo simulation is not assumed to be the same as it is in data, and the shapes for the inclusive templates shown in Figures A.1 - A.5 are indeed different. Furthermore, the difference shown is consistently observed throughout the entire range in jet $p_\perp$. As the inclusive simulation was generated separately for several distinct $p_\perp$ ranges (for the description of the MC samples please refer to Section 7.2), the following comparison plots illustrate that there is no abnormality in generated Monte Carlo observed, and these differences in Neural Net output variable spectra are consistent in all seventeen bins in jet $p_\perp$ used in fitting for the b-flavor fraction done in Section 7.3.2.

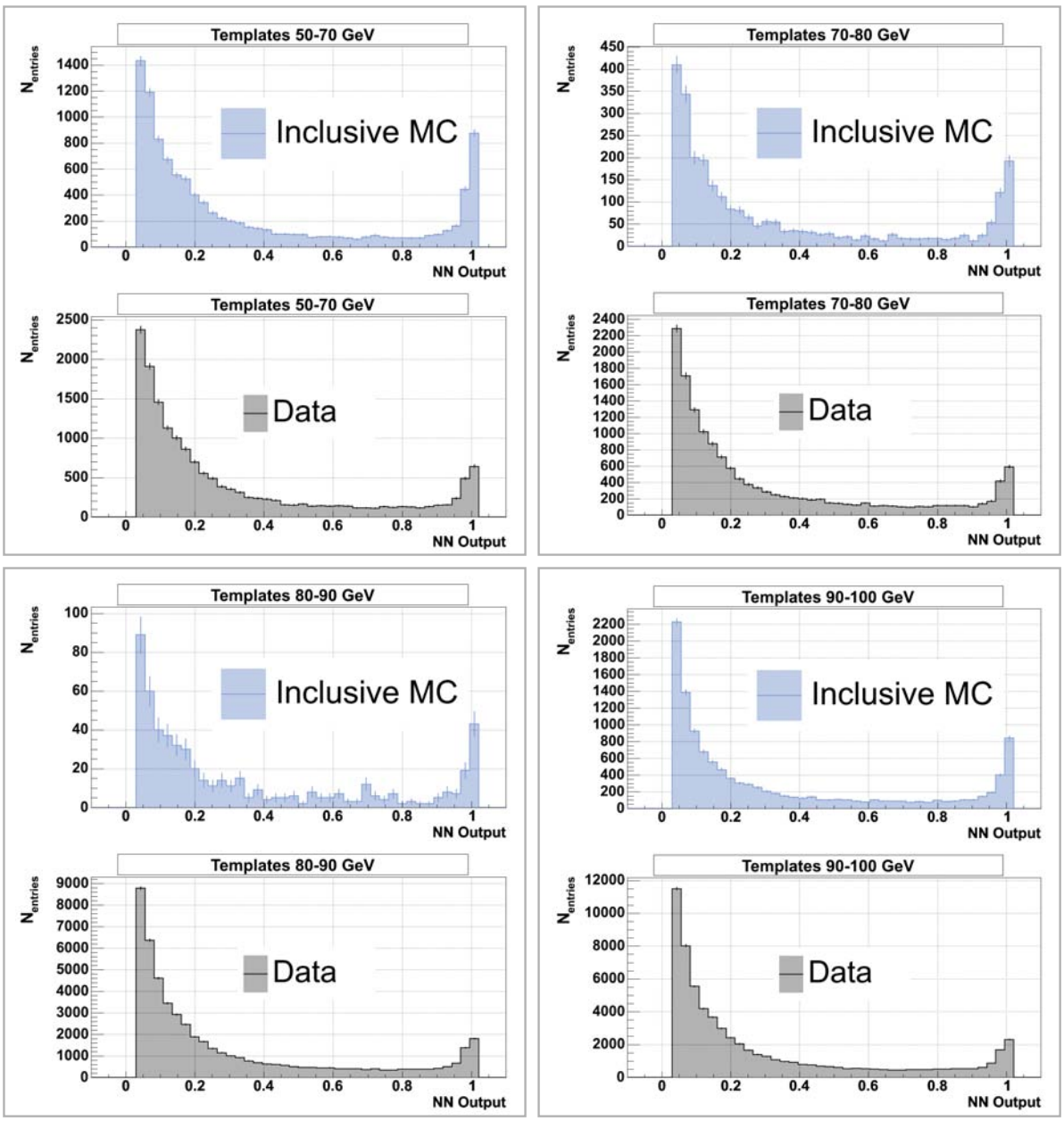

Figure A.1. Comparison of spectra between the inclusive Monte Carlo simulation and data for the Neural Net output variable. Shown are the plots in four $p_\perp$ bins: 50-70 GeV, 70-80 GeV, 80-90 GeV, 90-100 GeV.

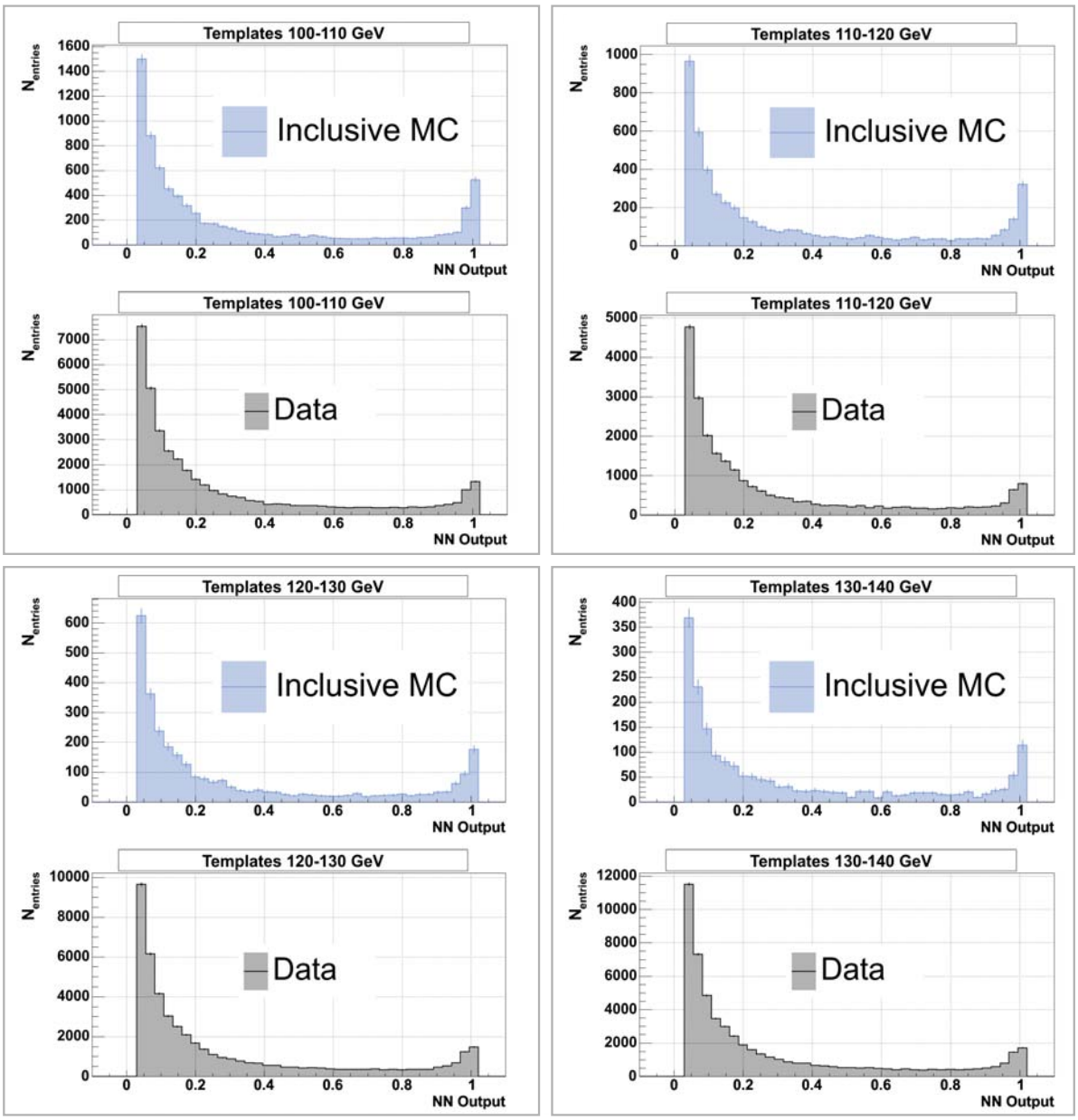

Figure A.2. Comparison of spectra between the inclusive Monte Carlo simulation and data for the Neural Net output variable. Shown are the plots in four $p_\perp$ bins: 100-110 GeV, 110-120 GeV, 120-130 GeV, 130-140 GeV.

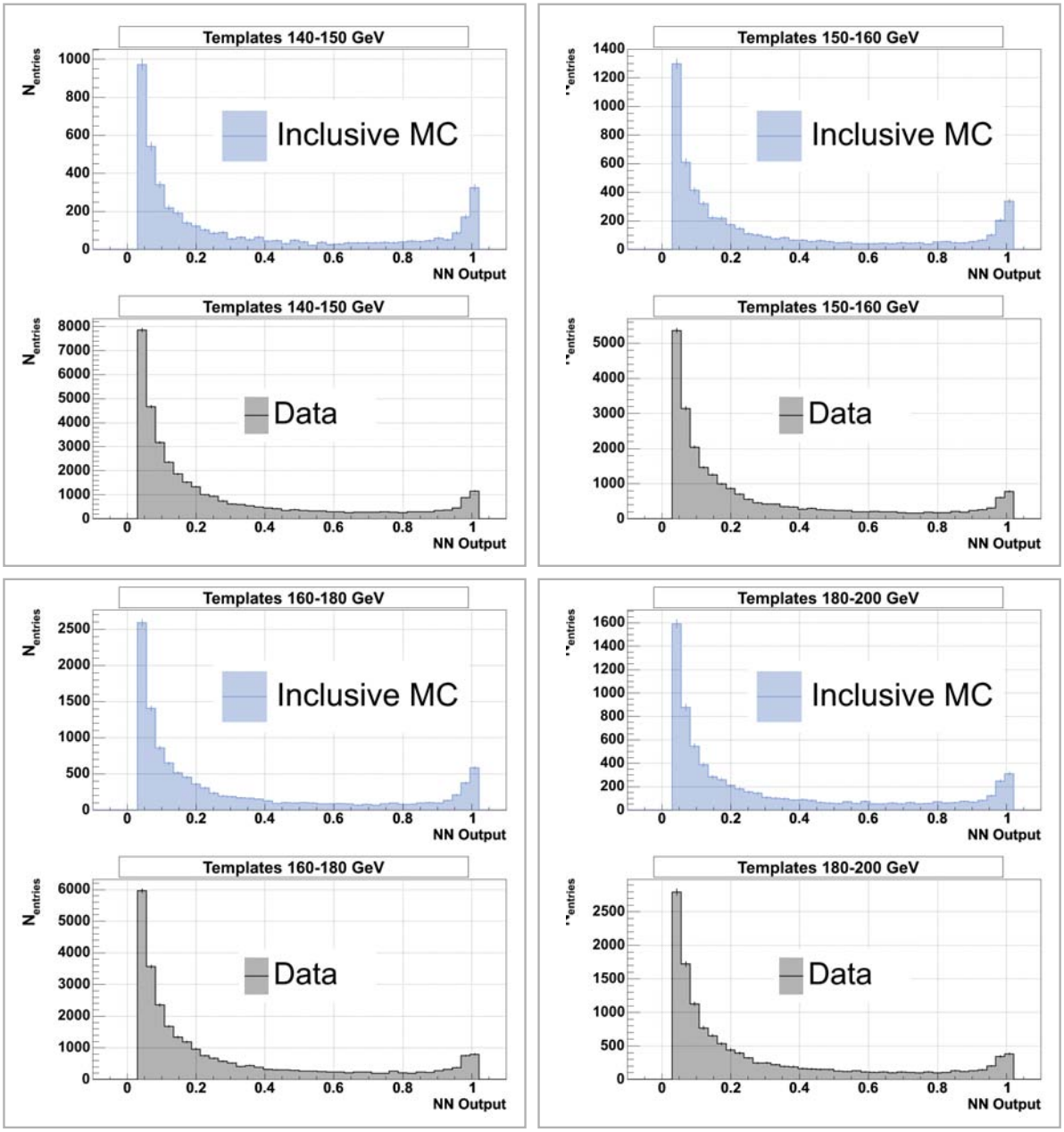

Figure A.3. Comparison of spectra between the inclusive Monte Carlo simulation and data for the Neural Net output variable. Shown are the plots in four $p_\perp$ bins: 140-150 GeV, 150-160 GeV, 160-180 GeV, 180-200 GeV.

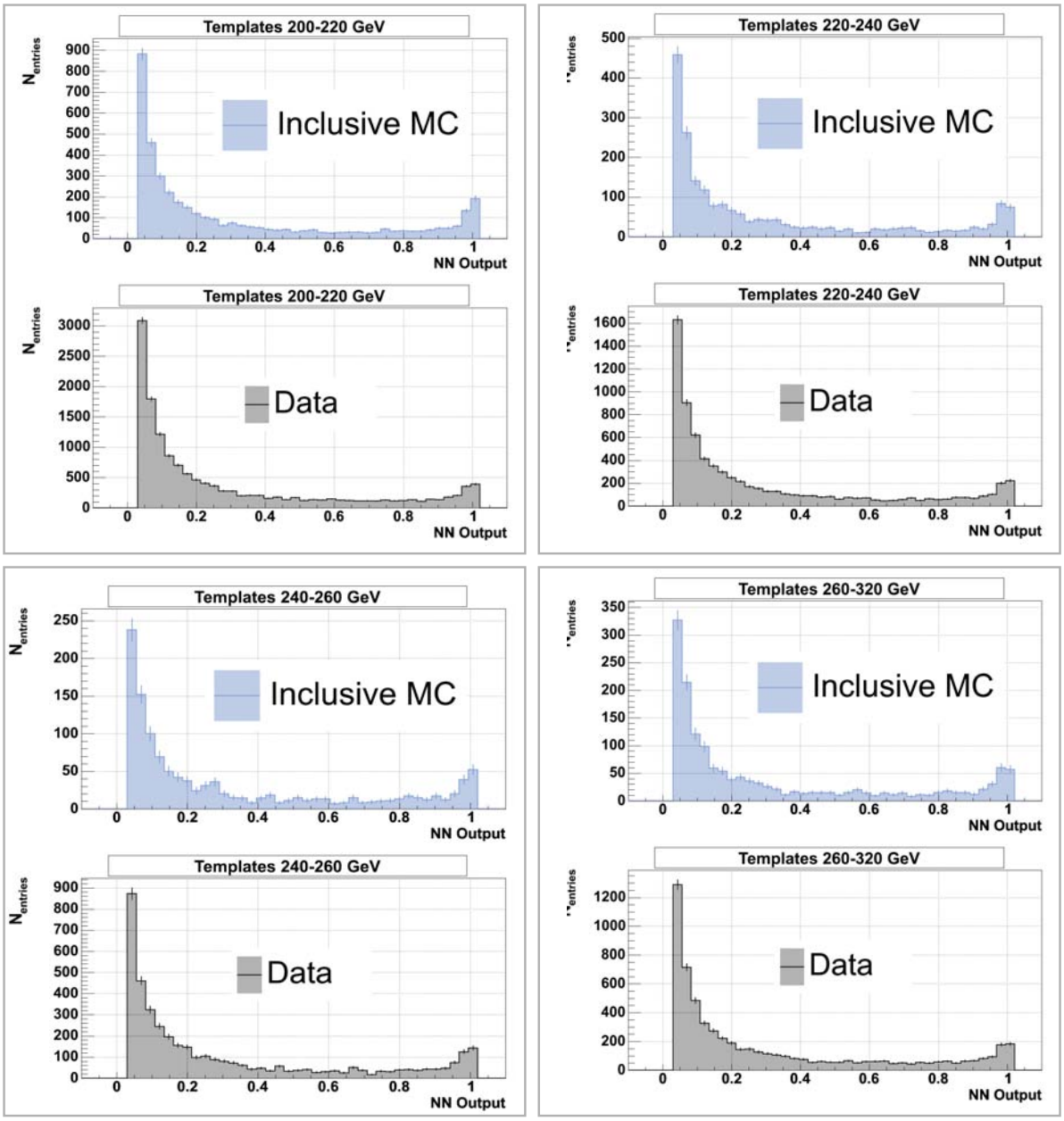

Figure A.4. Comparison of spectra between the inclusive Monte Carlo simulation and data for the Neural Net output variable. Shown are the plots in four $p_\perp$ bins: 200-220 GeV, 220-240 GeV, 240-260 GeV, 260-320 GeV.

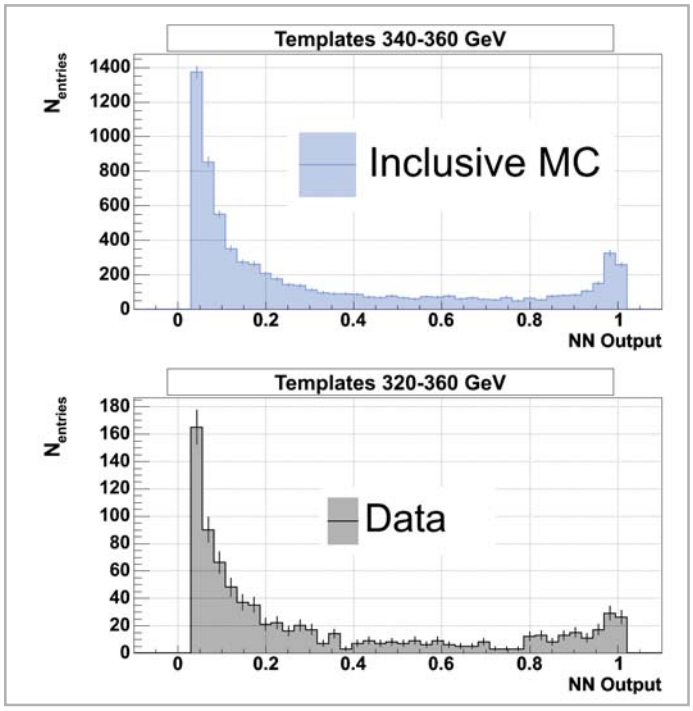

Figure A.5. Comparison of spectra between the inclusive Monte Carlo simulation and data for the Neural Net output variable. Shown are the plots in 340-360 GeV $p_\perp$ bin for MC and in 320-360 GeV $p_\perp$ bin for the data.

APPENDIX B

ADDITIONAL STUDY OF THE NEURAL NETWORK INPUT VARIABLES

The evaluation of the scale factor connecting the b-jet tagging efficiency in Monte Carlo and in data relies on the additional requirement of a muon presence in jets. An additional study of the effect of the muon tag on some of the input variables for the neural network is presented in this section.

The five variables studied in this section are χ^2 per degrees of freedom for the secondary vertices found in jets, the decay length significance of the secondary vertices (the logarithm of this variable was taken to further emphasize any possible shape features), the JLIP probability for all of the tracks in found displaced vertices to originate at the primary vertex, the number of secondary vertices found in jets, and the number of tracks constituting displaced vertices in jets. Both shape comparisons (Figures B.1 and B.3) and $p_\perp$ profile plots of the mean values for the corresponding distributions for the above variables (Figures B.2 and B.4) have been studied. The distribution shapes for the neural network input variables were compared before and after the muon cuts were applied with *medium* and *tight* muon quality settings (for the description of the muon quality requirements please refer to Section 5.3).

As it is shown by the comparisons, the additional muon tag requirement does not directly cut on any of the input variables for the neural network. The profile plots for the input variables do not show strong dependence on jet $p_\perp$. Both spectra

and profile analyses of the variables indicate that the distributions obtained with two different muon quality settings are virtually identical. However, these two muon tag requirements do shape some of the initial variables obtained just for the neural net output existence selection. Such behavior is expected because the presence of a muon in a jet significantly enhances the b-flavor content in the data sample. An example of this kind of shaping is illustrated by the spectra of the decay length significance variable shown in Figure B.1. The presence of a muon in a jet shapes the initial distribution, shifting its mean towards higher decay length significance values (red and blue shapes compared to the initial distribution shown in black). However the variation in muon quality does not affect the shape of the spectrum significantly.

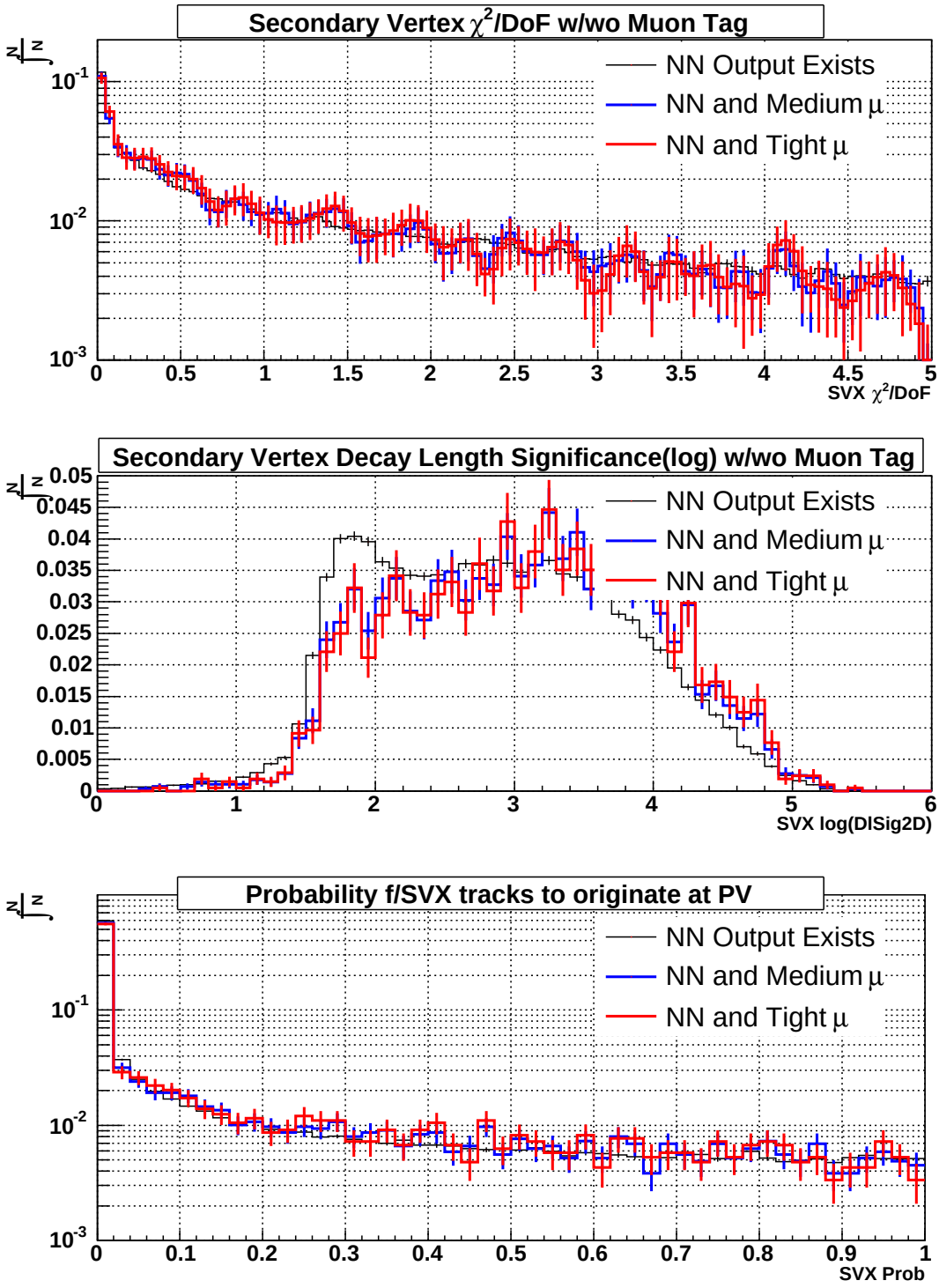

Figure B.1. Comparison of the spectra for χ^2/DoF_{SVX}, $log(DlSig)_{SVX}$, and $Prob_{SVX}$ neural network input variables for non-trivial neural net output (black), and additional *medium* and *tight* muon requirement in jet (shown in blue and red, respectively).

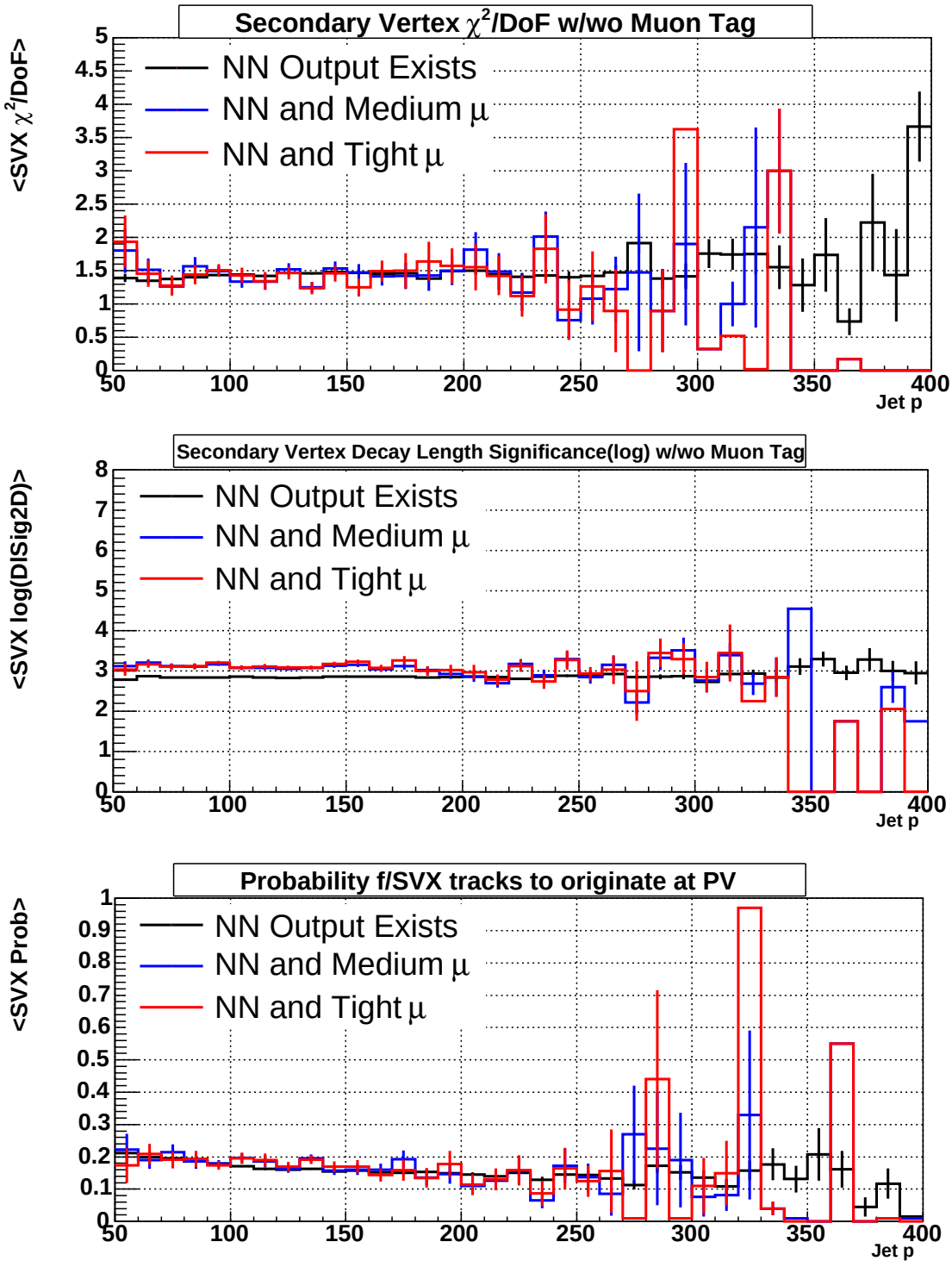

Figure B.2. Profile plots for the mean values χ^2/DoF_{SVX}, $log(DlSig)_{SVX}$, and $Prob_{SVX}$ neural network input variables against jet $p_\perp$ for non-trivial neural net output (black), and additional *medium* and *tight* muon requirement in jet (shown in blue and red, respectively). There were no abnormal differences observed between the two muon settings.

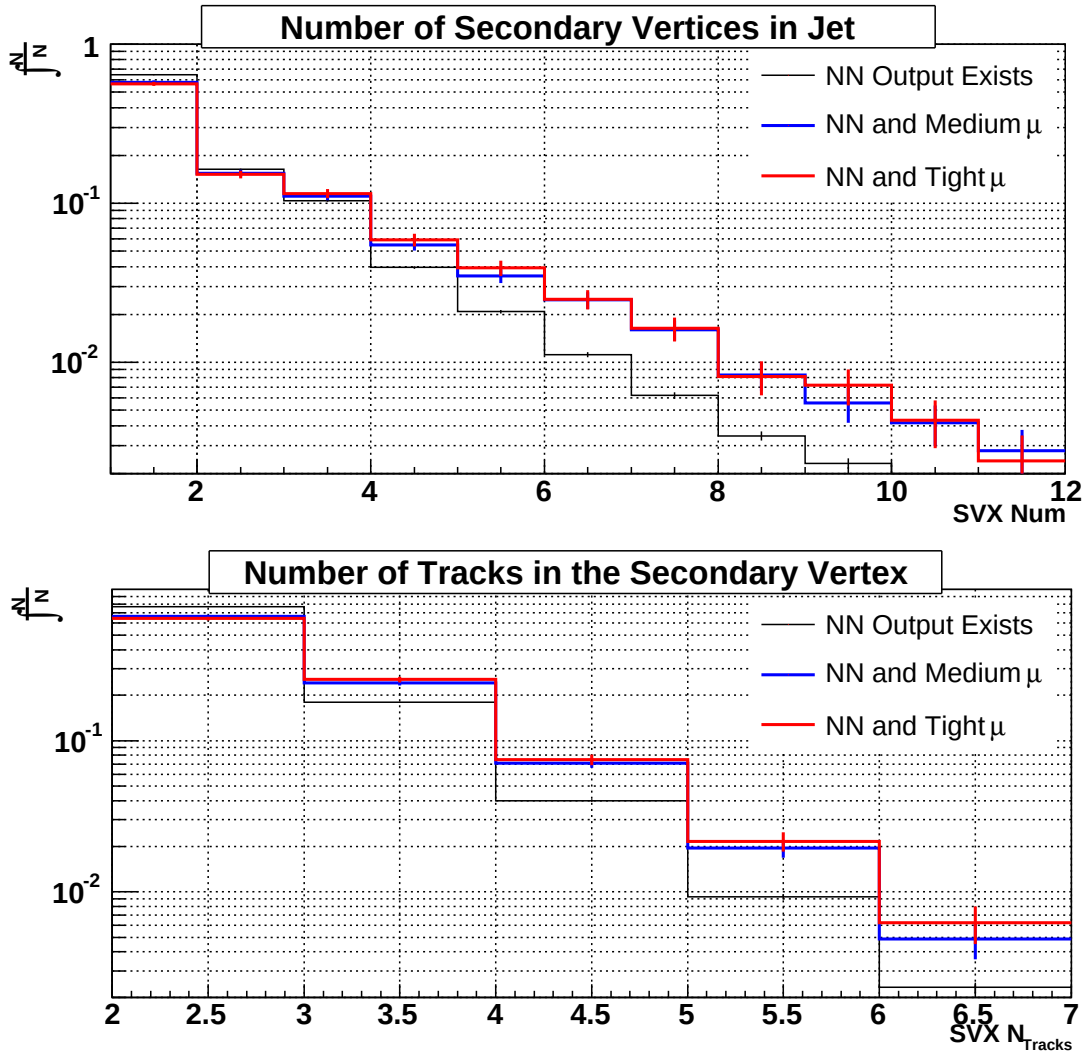

Figure B.3. Comparison of the spectra for the number of displaced vertices SVX_{num} and track multiplicity $SVX\ N_{Tracks}$ neural network input variables for non-trivial neural net output (black), and additional *medium* and *tight* muon requirement in jet (shown in blue and red, respectively).

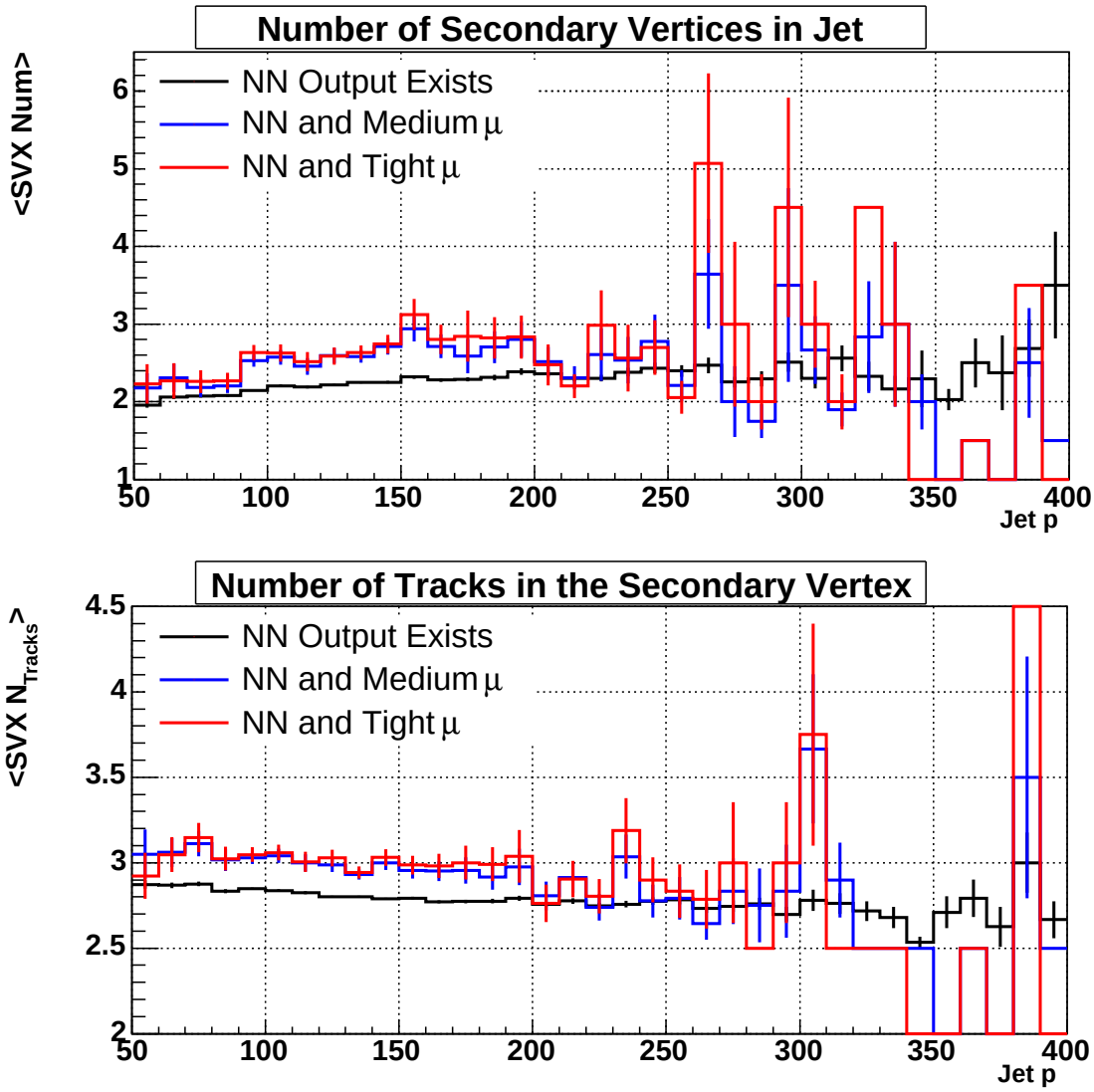

Figure B.4. Profile plots for the mean values of the number of displaced vertices SVX_{num} and track multiplicity $SVX\ N_{Tracks}$ neural network input variables against jet $p_\perp$ for non-trivial neural net output (black), and additional *medium* and *tight* muon requirement in jet (shown in blue and red, respectively). There were no abnormal differences observed between the two muon settings for these variables.

APPENDIX C

TABULATED b-JET CROSS SECTION MEASUREMENT RESULTS

On the next two pages below is given the numeric summary Tables C.1 and C.2 for the differential cross section of the b-jet production analysis, done within this dissertation. All of the constituents of the result are presented. Detailed systematic errors are presented as fractions of the corresponding final cross section value. Asymmetric uncertainties are given as a vertical column with a ($\pm$) signs against the numeric value. The final statistical and systematic uncertainties to the measured cross section value, however, are presented as absolute values. Corresponding units and representation legends can be found on top of the tables below the column descriptions.

Table C.1

TABULATED FINAL b-JET CROSS SECTION MEASUREMENT (PART I)

Bin Number	$P_\perp$ Range	N entries/bin	Luminosity	Luminosity Uncertainty	Raw Cross Section, pb/Gev/c	Efficiency		Purity		Unsmearing Correction Factor		Resolution Uncertainty	JES Uncertainty	Final b-Jet Cross Section $\frac{d\sigma}{dp_\perp} \pm$ Stat $\pm$ Syst (pb/Gev/c)		
	$\Delta P_\perp$ GeV	Count	L, Pb^{-1}	± Frac. Error	$\frac{\mathcal{N}}{\mathcal{L}\times\Delta p_\perp}$	%/100	± Frac. Error	%/100	± Frac. Error	%/100	± Frac. Error	± %/100	± %/100	$\frac{d\sigma}{dp_\perp}$ pb/(Gev/c)	± Stat. Error pb/(Gev/c)	± Syst. Error pb/(Gev/c)
0	50-60	370	0.098	0.065	375.67	0.363	0.037	0.35	0.096	0.914	0.06161	+ 0.028 - 0.021	+ 0.156 - 0.133	332	±17	+ 69 - 65
1	60-70	179	0.098	0.065	181.74	0.362	0.039	0.35	0.104	0.922	0.04107	+ 0.023 - 0.019	+ 0.152 - 0.132	160	±12	+ 32 - 30
2	70-80	80	0.098	0.065	81.23	0.360	0.044	0.34	0.112	0.927	0.02460	+ 0.019 - 0.017	+ 0.150 - 0.132	71	±8	+ 15 - 14
3	80-90	642	1. 28	0.065	38.15	0.358	0.049	0.34	0.120	0.930	0.01133	+ 0.017 - 0.016	+ 0.149 - 0.132	33.3	±1.3	+ 7.3 - 6.6
4	90-100	405	1.68	0.065	24.07	0.357	0.055	0.33	0.128	0.932	0.00118	+ 0.014 - 0.014	+ 0.150 - 0.134	21.2	±1.0	+ 4.5 - 4.3
5	100-110	3253	23.4	0.065	13.90	0.355	0.061	0.33	0.136	0.933	0.00573	+ 0.014 - 0.014	+ 0.151 - 0.136	12.0	±0.21	+ 2.7 - 2.5
6	110-120	2038	23.4	0.065	8.71	0.353	0.069	0.32	0.143	0.934	0.00936	+ 0.0134 - 0.0137	+ 0.154 - 0.139	7.4	±0.16	+ 1.7 - 1.7
7	120-130	1321	23.4	0.065	5.65	0.351	0.076	0.32	0.151	0.934	0.00998	+ 0.0130 - 0.0134	+ 0.157 - 0.142	4.8	±0.1	+ 1.2 - 1.1
8	130-140	798	23.4	0.065	3.41	0.348	0.084	0.31	0.159	0.933	0.00819	+ 0.0130 - 0.0132	+ 0.162 - 0.146	2.9	±0.1	+ 0.7 - 0.7
9	140-150	2956	139.5	0.065	2.12	0.346	0.093	0.31	0.167	0.933	0.00485	+ 0.0126 - 0.0131	+ 0.168 - 0.151	1.82	±0.03	+ 0.46 - 0.44
10	150-160	2033	139.5	0.065	1.46	0.343	0.102	0.30	0.175	0.932	0.00087	+ 0.0126 - 0.0130	+ 0.175 - 0.157	1.21	±0.03	+ 0.33 - 0.32
11	160-170	1407	139.5	0.065	1.01	0.340	0.111	0.30	0.182	0.931	0.00297	+ 0.0125 - 0.0129	+ 0.183 - 0.163	0.82	±0.022	+ 0.24 - 0.23
12	170-180	921	139.5	0.065	0.66	0.337	0.121	0.29	0.190	0.929	0.00613	+ 0.0126 - 0.0129	+ 0.192 - 0.170	0.53	±0.018	+ 0.16 - 0.16
13	180-190	648	139.5	0.065	0.46	0.334	0.131	0.29	0.198	0.928	0.00830	+ 0.0126 - 0.0129	+ 0.202 - 0. 178	0.37	±0.015	+ 0.12 - 0.11

Table C.2

TABULATED FINAL b-JET CROSS SECTION MEASUREMENT (PART II)

Bin Number	$P_\perp$ Range	N entries/bin	Luminosity	Luminosity Uncertainty	Raw Cross Section, pb/Gev/c	Efficiency		Purity		Unsmearing Correction Factor		Res.Unc.	JES Unc	Final b-Jet Cross Section $\frac{d\sigma}{dp_\perp}$ ± Stat ± Syst (pb/Gev/c)		
	$\Delta P_\perp$, GeV		L, Pb^{-1}	± Frac. Error	$\frac{\mathcal{N}}{\mathcal{L}\times\Delta p_\perp}$	%/100	± Frac. Error	%/100	± Frac. Error	%/100	± Frac. Error	± %/100	± %/100	$\frac{d\sigma}{dp_\perp}$ pb/(Gev/c)	± Stat. Error pb/(Gev/c)	± Syst. Error pb/(Gev/c)
14	190-200	1009	309.5	0.065	0.33	0.330	0.141	0.28	0.206	0.926	0.00939	+ 0.0126 - 0.0129	+ 0.214 - 0.186	0.26	8.2E-3	+ 8.7E-2 - 8.2E-2
15	200-210	687	309.5	0.065	0.22	0.327	0.152	0.28	0.214	0.924	0.00942	+ 0.0128 - 0.0129	+ 0.226 - 0.195	0.18	6.7E-3	+ 6.2E-2 - 5.8E-2
16	210-220	536	309.5	0.065	0.17	0.323	0.162	0.27	0.222	0.922	0.00848	+ .0129 - .0130	+ 0.24 - 0.21	0.14	5.9E-3	+ 5.0E-2 - 4.7E-2
17	220-230	373	309.5	0.065	0.12	0.319	0.173	0.27	0.229	0.920	0.00670	+ .0131 - 0.0130	+ 0.254 - 0.215	9.40E-2	4.8E-3	+ 3.6E-2 - 3.4E-2
18	230-240	287	309.5	0.065	0.093	0.315	0.183	0.26	0.237	0.918	0.00419	+ 0.0133 - 0.0131	+ 0.270 - 0.226	7.14E-2	4.2E-3	+ 2.9E-2 - 2.7E-2
19	240-250	243	312.3	0.065	0.078	0.310	0.194	0.26	0.245	0.916	0.00107	+ 0.0135 - 0.0132	+ 0.287 - 0.238	5.95E-2	3.8E-3	+ 2.6E-2 - 2.4E-2
20	250-270	278	312.3	0.065	0.045	0.304	0.209	0.25	0.256	0.913	0.00426	+ 0.0140 - 0.0133	+ 0.312 - 0.256	3.37E-2	2.0E-3	+ 1.6E-2 - 1.4E-2
21	270-290	146	312.3	0.065	0.023	0.294	0.230	0.24	0.271	0.908	0.01302	+ 0.0144 - 0.0136	+ 0.353 - 0.285	1.75E-2	1.5E-3	+ 8.9E-3 - 8.1E-3
22	290-310	86	312.3	0.065	0.014	0.283	0.250	0.23	0.287	0.903	0.02297	+ 0.0151 - 0.0138	+ 0.398 - 0.316	1.02E-2	1.1E-3	+ 5.7E-3 - 5.1E-3
23	310-330	60	312.3	0.065	0.0096	0.271	0.269	0.22	0.303	0.897	0.03383	+ 0.0158 - 0.0141	+ 0.448 - 0.350	7.10E-3	9.2E-4	+ 4.3E-3 - 3.8E-3
24	330-360	32	312.3	0.065	0.0034	0.255	0.290	0.21	0.323	0.890	0.04767	+ 0.0167 - 0.0145	+ 0.517 - 0.397	2.52E-3	4.5E-4	+ 1.7E-3 - 1.5E-3
25	360-390	21	312.3	0.065	0.0022	0.235	0.310	0.20	0.345	0.881	0.06643	+ .0178 - 0.0151	+ 0.602 - 0.454	1.66E-3	3.6E-4	+ 1.3E-3 - 1.1E-3
26	390-480	11	312.3	0.065	0.00039	0.203	0.328	0.18	0.376	0.866	0.09515	+ 0.02 - 0.016	+ 0.738 - 0.545	3.01E-4	9.0E-5	+ 2.7E-4 - 2.2E-4

APPENDIX D

PARAMETERIZATIONS FOR THE SYSTEMATIC UNCERTAINTIES

In this section one can find the analytical forms and parameterizations for the main sources of the systematic uncertainties used in this analysis. This is a convenient way of reproducing the individual uncertainties and comparing them to other results. Analytical functions corresponding to various systematic uncertainties along with their parameter values are given by Table D.1.

Parameterizations are done as functions of corrected jet $p_{\perp}$, denoted by x in the analytical functional forms. Parameters are denoted as P_i, where i is the number of the parameter. Positive and negative parameters for the uncertainties are given separately except for the uncertainty on jet resolution, which is supplied as a function with a ($\pm$) sign, corresponding to the positive and the negative uncertainty values, respectively.

TABLE D.1

PARAMETERIZATIONS FOR THE SYSTEMATIC UNCERTAINTIES

Functional Form	Type of the Uncertainty	Sign	Values for the Parameters
$P_0x^3 + P_1x^2 + P_2x + P_3$	Efficiency (Scale Factor)	Positive	P_0 = -8.064E-9 P_1 = 5.643E-6 P_2 = -2.454E-4 P_3 = 3.460E-2
		Negative	P_0 = 8.064E-9 P_1 = 5.643E-6 P_2 = 2.454E-4 P_3 = -3.460E-2
	Unsmearing	Positive	P_0 = -1.809E-9 P_1 = 3.189E-6 P_2 = -9.940E-4 P_3 = 8.650E-2
		Negative	P_0 = 1.809E-9 P_1 = -3.189E-6 P_2 = 9.940E-4 P_3 = -8.650E-2
$P_0x^2 + P_1x + P_2$	Jet Energy Scale (JES)	Positive	P_0 = 5.537E-6 P_1 = -9.653E-4 P_2 = 1.915E-1
		Negative	P_0 = -3.518E-6 P_1 = 4.950E-4 P_2 = -1.491E-1
	Combined (Total) Systematic Uncertainty	Positive	P_0 = 4.510E-6 P_1 = -1.408E-4 P_2 = 1.915E-1
		Negative	P_0 = -2.781E-6 P_1 = 3.113E-4 P_2 = -1.532E-1
$P_0x + P_1$	b-Fraction (Purity)	Positive	P_0 = 7.795E-4 P_1 = 5.410E-2
		Negative	P_0 = -7.795E-4 P_1 = -5.410E-2
P_0	Luminosity	Positive	P_0 = 6.5E-2
		Negative	P_0 = -6.5E-2
$\pm\sqrt{\frac{P_0^2}{x^2} + \frac{P_1^2}{x} + P_2^2}$	Jet Resolution	Positive and Negative	P_0 = 4.703 P_1 = 2.513E-1 P_2 = 6.556E-2

BIBLIOGRAPHY

[1] V. V. Ezhela, *et al.*, "Particle Physics: One Hundred Years of Discoveries", American Institute of Physics (AIP) Press, Woodbury, New York, 1996.

[2] E. D. Commins, P.H. Bucksbaum, "Weak Interactions of Leptons and Quarks", Cambridge University Press, 1983.

[3] D. H. Perkins, "Introduction to High Energy Physics", ISBN 0-201-12105-0, Addison-Wesley Publishing Company, Inc., 1987.

[4] R. K. Ellis, W. J. Stirling, B. R. Webber, "QCD and Collider Physics", ISBN 0-521-58189-3, Cambridge University Press, 1996

[5] Fermilab Top Quark Discovery Press Release, (URL:http://www.fnal.gov/pub/inquiring/physics/discoveries/pr/pr.gif), March 2, 1995.

[6] S. Abachi, *et al.*, "Observation of the Top Quark", PRL 74 (2632), arXiv:hep-ex/9503003, v1, March 3, 1995.

[7] B. Roe, "Particle Physics at the New Millennium", Springer, New York (1996).

[8] Bill Carithers (LBL, Berkeley, Fermilab) , P. Grannis (SUNY, Stony Brook), "Discovery of the top quark", Published in SLAC Beam Line 25N3:4-16,1995, SLAC Beam Line 25:4-16,1995 (No.3)

[9] B. C. Hall, "Representations & Characters of Groups", ISBN 0-521-392-X, Cambridge University Press, 2001.

[10] G. Sterman, *et al.*, "Handbook of Perturbative QCD", (URL: http://www.phys.psu.edu/ cteq/handbook/v1.1/handbook.pdf), 2003.

[11] D. Griffiths, "Introduction to Elementary Particles", John Wiley and Sons, New York (1987).

[12] F. Halzen, A. D. Martin, "Quarks and Leptons: An Introductory Course in Modern Particle Physics", John Wiley & Sons, New York, 1987.

[13] K. Anikeev, *et al.*, "B Physics at the Tevatron: Run II and Beyond", FERMILAB-Pub-01/197, hep-ph/0201071, December 2001.

[14] J.E. Huth, *et al.*, Proc. of the 1990 DPF Summer Study on High Energy Physics, Snowmass, Colorado, edited by E.L. Berger, World Scientific, Singapore (1992) 134.

[15] K. Lane, "Electroweak and Flavor Dynamics at Hadron Colliders", arXiv:hep-ph/9605257, 1996.

[16] B. Evanger, *et al.*, "Accelerator Concepts Rookie Book", *Unpublished*, (URL: www-bdnew.fnal.gov/operations/rookie_books/Concepts_v3.pdf), 1995-2002.

[17] R. J. Hooper, "A Search for Large Extra Spatial Dimentions and Z^o Bosons in the Di-Muon Final State in $\sqrt{s} = 1.96$ TeV $p\overline{p}$ Collisions at DØ, Ph.D. Thesis, University of Notre Dame, Notre Dame, IN, (URL: http://www-d0.fnal.gov/results/publications_talks/thesis/hooper/thesis.pdf), 2004.

[18] Fermi National Accelertor Laboratory, Batavia, Illinois (USA), "Tevatron Run II Handbook", Internal FNAL Note, (URL: http://www-bd.fnal.gov/runII/index.html).

[19] Elvin Harms and Jim Morgan, "The Antiproton Source Rookie Book", (URL: http://www-bdnew.fnal.gov/pbar/documents/PBAR_Rookie_Book.pdf).

[20] E. Byckling, K. Kajantie, "Particle Kinematics", ISBN 0-471-12885-6, John Wiley & Sons, Ltd., 1973.

[21] A. Patwa, "The Forward Preshower System and a Study of the J/ψ Trigger with the DØ Detector", Ph.D. Thesis, Stony Brook University, (URL: http://www-d0.fnal.gov/results/publications_talks/thesis/patwa/thesis.ps), 2002.

[22] V. M. Abazov, *et al.*, "The Upgraded DØ Detector", arXiv:physics/0507191, v1, 2005.

[23] V. M. Abazov, *et al.* [DØ Collaboration], "DØ Silicon Tracker Technical Design Report, DØ Note 2169, 1994.

[24] Central Fiber Tracker Online Documentation, (URL: http://d0server1.fnal.gov/projects/SciFi/cft_home.html)

[25] A. Bross, *et al.*, "The DØ scintillating fiber tracker", Prepared for SCIFI97: Conference on Scintillating and Fiber Detectors, South Bend, Indiana, 2-6 Nov 1997, Published in AIP Conf.Proc.450:221-228,1998.

[26] A. Bross, *et al.*, "Central Fiber Tracker Technical Design Report", (URL: http://d0server1.fnal.gov/users/stefan/www/CFT_TDR/CFT_TDR.ps), 1997, Unpublished.

[27] F. Borcherding, *et al.*, "CTT Technical Design Report for the Upgrade L1/L2 Tracking Trigger, DØ Note 3551, 1998.

[28] A. Gordeev, *et al.*, "Technical Design Report of the Forward Preshower Detector for the DØ Upgrade, DØ Note 3445, 1998.

[29] P. Baringer, *et al.*, Nucl. Instrum. Methods Phys. Res. A 469 (2001) 295.

[30] S. Abachi, *et al.*, Nucl. Instrum. Methods Phys. Res. A 338 (1994) 185.

[31] G. A. Davis, "First Measurement of the Differential Inclusive Cross Section for Jet Production at DØ Run II", Ph.D. Thesis, University of Rochester, Rochester, NY, (URL: http://www-d0.fnal.gov/results/publications_talks/thesis/davisg/thesis.ps), 2004.

[32] A. Melnitchouk, "Search for non-SM Light Higgs Boson in the $h \rightarrow \gamma\gamma$ Channel", Ph.D. Thesis, Brown University, (URL: http://www-d0.fnal.gov/results/publications_talks/thesis/melnitchouk/thesis.ps), 2003.

[33] T. Diehl, *et al.*, "Design of the Central Muon System", DØ Note 3365, 1997.

[34] B. Acharya, *et al.*, Nucl. Instrum. Methods Phys. Res. A 401 (1997) 45.

[35] G. Alexeev, *et al.*, "Technical Design Report for the DØ Forward Muon Tracking Detector Based on Mini-Drift Tubes", DØ Note 3366, 1997.

[36] V. Abramov, *et al.*, "Technical Design Report for the DØ Forward Trigger Scintillation Counters, DØ Note 3237, 1997.

[37] A. Brandt, *et al.*, "A Forward Proton Detector at DØ", Fermilab-Pub-97/377, 1997.

[38] C. Miao, "The DØ Run II Luminosity Monitor", DØ Note 3573, 1998.

[39] Nguyen Phuoc Xuan, "Search for Quark-Lepton Compositeness in the Dimuon Final State", Ph.D. Thesis, University of Notre Dame, Notre Dame, IN, (URL: http://www-d0.fnal.gov/results/publications_talks/thesis/xuan/thesis.pdf), 2005.

[40] O. Peters, "Measurement of the b-jet cross section at $sqrts = 1.96$ TeV", Ph.D. Thesis, Universiteit van Amsterdam, (URL: http://www-d0.fnal.gov/results/publications_talks/thesis/peters/OnnePeters_thesis.pdf), 2003.

[41] A. Brandt, "Triggering with the Forward Proton Detector, 1998.

[42] J. Drinkard, "The DØ Level 1.5 Calorimeter Trigger," DØ Note 2274, 1994.

[43] D. Edmunds, *et al.*, "A DSP Based Calorimeter Trigger for the DØ Experiment", IEEE Nuclear Science Symposium Volume 2, pp. 819-823, 1994.

[44] D. Edmunds, *et al.*, "Technical Design Report for the Level 2 Global Processor", DØ Note 3402, 1998.

[45] B. Abbott, *et al.*, "Specification of the Level 2 Central Tracking Trigger Preprocessor Gate", DØ Note 3645, 1999.

[46] M. Bhattacharjee, "Technical Design Report, Level 2 Preprocessor for Central and Forward Preshower Triggers", Unsubmitted DØ Note, 1999.

[47] Yuan Hu, *et al.*, "The Level 2 CPS Trigger", DØ Note 4688, 2005.

[48] R. Schwienhorst, *et al.*, "The DZero Run II Trigger System", DØ Note 4638, 2004.

[49] V.D. Barger and R.J.N. Phillips, *Collider Physics*, Addison-Wesley, 1987.

[50] M. Shochet, "The Physics of Proton Antiproton Collisions", *Lectures from Les Houches Summer School*, Les Houches, France, 1991.

[51] B. Andrieu, "Jet Finding Algorithms at Tevatron", DØ Note 5168, 2006.

[52] E. Busato, B. Andrieu, "Jet Algorithms in D0 RunII Software: Description and User's Guide", DØ Note 4457, 2004.

[53] A.R.Baden and N. Hadley, "Jets and Kinematics", DØ Note 957, 1993.

[54] J.-L. Agram, *et al.*, "Jet Energy Scale at DØ Run II", DØ Note 4720, 2005.

[55] Sarosh N. Fatakia, Ulrich Heintz, "Correcting the reconstructed jet's 4-vector to the parton level", DØ Note 4247, 2003.

[56] A. Magerkurth, "Parton Level Corrections for Jetcorr 5.3", DØ Note 4708, 2005.

[57] A. Kupco, C. Royon, M. Voutilainen, "Measurement of the Inclusive Jet Cross Section in $p\overline{p}$ Collisions at $\sqrt{s}$=1.96 TeV", DØ Note 5087, 2006.

[58] C. Clement, *et al.*, "MuonID Certification for p14", DØ Note 4350, 2004.

[59] D. Lincoln, *et al.*, "High $p_\perp$ Cross Section for μ-Tagged Jets at $\sqrt{s}$ = 1960 GeV", DØ Note 4754, 2005.

[60] M. Agelou, J.L. Agram, C. Royon, "Jet $p_\perp$ Resolution With Jetcorr 5.3", DØ Note 4775, 2005.

[61] T. Scanlon, "A Neural Network b-tagging Tool", DØ Note 4889, 2005.

[62] T. Scanlon, M. Anastasoaie, "Neural Network b-tagging Tool on Pass 2 Data", DØ Note 4890, 2005.

[63] L. Feligioni, M. Narain, P. Schieferdecker, A. Schwartzman, "Update on b-quark Jet Identification with Secondary Vertex Reconstruction Using DØReco version p14", DØ Note 4414, 2004.

[64] A. Schwartzman, M. Narain, "Secondary Vertex b-tagging Using the Kalman Filter Algorithm", DØ Note 3909, 2001.

[65] D. Bloch, *et al.*, "Performance of the JLIP b-tagger in p14", DØ Note 4348, 2004.

[66] R. Demina, A. Khanov, F. Rizatdinova, E. Shabalina, "Measurement of b-tagging efficiency and mis-tagging rates with CSIP method", DØ Note 4432, 2004.

[67] DØ b-Id Working Group web page. URL: http://www-d0.fnal.gov/phys_id/bid/d0_private/certification/p14-certification.html

[68] K. Hanagaki, J. Kasper, "Identification of b-jet by Soft Muon", DØ Note 4867, 2005.

[69] K. Gurney , "An Introduction to Neural Networks", ISBN 1-857-28503-4, UCL Press, 1997.

[70] B. Clement, *et al.*, "SystemD or How to Get Signal, Backgrounds and Their Efficiencies With Real Data", DØ Note 4159, 2003.

[71] DØ Common Sample Group web page. URL: http://www-d0.fnal.gov/Run2Physics/cs/skimming/pass1.html

[72] DØroot HEP Analysis Framework. URL: http://www-d0.fnal.gov/∼ sch/d0root/rootVertex.html

[73] T. Adams, "A Study of Highly Displaced, Detached Vertices with K_s Using DØRoot", DØ Note 4761, 2005.

[74] DØ Online Run Quality Database. URL: http://d0db.fnal.gov/qualitygrabber/qualQueries.html

[75] T. Sjeostrand, S. Mrenna, P. Skands, "PYTHIA 6.4 Physics and Manual", FERMILAB-PUB-06-052-CD-T, hep-ph/0603175, 2006.

[76] B. Andersson, *et al.*, "Parton Fragmentation and String Dynamics", Phys. Rep. 97 (2 & 3), pp 31-145, 1983.

[77] F. Deliot, G. Hesketh, P. Telford, B. Tuchming, "Measurement of $\sigma(p\overline{p}\rightarrow WX) \times Br(W \rightarrow \mu\nu)$ at $\sqrt{s}$=1.96 TeV", DØ Note 4749, 2005.

[78] C. Clement, *et al.*, "MuonID Certification for p14", DØ Note 4350, 2004.

[79] A. Kupco, C. Royon, M. Voutilainen, M. Wobisch, "Measurement of the Inclusive Jet Cross Section in $p\overline{p}$ Collisions at $\sqrt{s} = 1.96$ TeV", DØ Note 4751, 2005.

[80] A. Askew, M. Titov, M. Voutilainen, "Available Luminosity for Winter Conferences", DØ Note 5079, 2006.

[81] A. Gajjar, "Measurement of the inclusive $b\bar{b}$ jet cross section at the Collider Detector at Fermilab", Ph.D. Thesis, University of Liverpool, (URL: http://www-cdf.fnal.gov/htbin/cdfnoteSelNum?number=8002), 2005.

[82] M. D'Onofrio [CDF and DØ collaborations], "Beauty Production Cross Section Measurements at $E_{cm} = 1.96$ TeV", arXiv:hep-ex/0505036, v1, 2005.